STRUCTURAL STUDIES OF NANOPARTICLES INTERACTIONS WITH DIFFERENT MACROMOLECULES

By

SUGAM KUMAR

Enrolment No. PHYS01201204013

Bhabha Atomic Research Centre, Mumbai, India

A thesis submitted to the
Board of Studies in Physical Sciences

In partial fulfillment of requirements
for the Degree of
DOCTOR OF PHILOSOPHY
of
HOMI BHABHA NATIONAL INSTITUTE

December, 2014

Homi Bhabha National Institute

Recommendation of the Viva Voce Committee

As members of the Viva Voce Committee, we certify that we have read the dissertation prepared by Shri Sugam Kumar entitled "Structural Studies of Nanoparticles Interactions with Different Macromolecules**"** and recommended that it may be accepted as fulfilling the dissertation requirement for the award of Degree of Doctor of Philosophy.

_____Date:
Chairman- Dr. S. L. Chaplot

_____Date:
Guide- Dr. V. K. Aswal

_____Date:
External Examiner- Prof. V. A. Raghunathan

_____Date:
Member-1- Prof. P. Ayyub

_____Date:
Member-2- Dr. S. Basu

Final approval and acceptance of this dissertation is contingent up on the candidate's submission of the final copies of the dissertation to HBNI.

I hereby certify that I have read this dissertation prepared under my direction and recommend that it may be accepted as fulfilling the dissertation requirement.

Date: 27-05-2015

Place: Mumbai

Dr. V. K. Aswal
(Guide)

STATEMENT BY AUTHOR

This dissertation has been submitted in partial fulfillment of requirements for an advanced degree at Homi Bhabha National Institute (HBNI) and is deposited in the Library to be made available to borrowers under rules of the HBNI.

Brief quotations from this dissertation are allowable without special permission, provided that accurate acknowledgement of source is made. Requests for permission for extended quotation from or reproduction of this manuscript in whole or in part may be granted by the Competent Authority of HBNI when in his or her judgment the proposed use of the material is in the interests of scholarship. In all other instances, however, permission must be obtained from the author.

(Sugam Kumar)

DECLARATION

I, hereby declare that the investigation presented in the thesis has been carried out by me. The work is original and has not been submitted earlier as a whole or in part for a degree / diploma at this or any other Institution/University.

(Sugam Kumar)

DECLARATION

I, hereby declare that the queries raised by the examiners of the thesis have been incorporated as suggested.

Dr. V. K. Aswal

(Guide)

List of Publications

In Refereed Journal:

Related to Thesis

1. *Tuning of Nanoparticle–Surfactant Interactions in Aqueous System*
   Sugam Kumar and V. K. Aswal
   J. Phys.: Condensed Matt., **2011**, *23*, 035101 (1-8).

2. *SANS and UV-Vis Spectroscopy Studies of Resultant Structure from Lysozyme Adsorption on Silica Nanoparticles*
   Sugam Kumar, V. K. Aswal and J. Kohlbrecher
   Langmuir, **2011**, *27*, 10167-10173.

3. *Size-Dependent Interaction of Silica Nanoparticles with Different Surfactants in Aqueous Solution*
   Sugam Kumar, V. K. Aswal and J. Kohlbrecher
   Langmuir, **2012**, *28*, 9288-9297.

4. *Block-Copolymer Induced Long-Range Depletion Interaction and Clustering of Silica Nanoparticles in Aqueous Solution*
   Sugam Kumar, M.-J. Lee, V. K. Aswal and S.-M. Choi
   Phys. Rev. E, **2013**, *87*, 042315 (1-8).

5. *pH-Dependent Interaction and Resultant Structures of Silica Nanoparticles and Lysozyme Protein*
   Sugam Kumar, V. K. Aswal and P. Callow
   Langmuir, **2014**, *30*, 1588-1598.

6. *Structure and Interaction in the Polymer-Dependent Reentrant Phase Behavior of a Charged Nanoparticle Solution*
   Sugam Kumar, D. Ray, V. K. Aswal and J. Kohlbrecher
   Phys. Rev. E, **2014**, *90*, 042316 (1-10).

7. *Tuning of Electrostatic vs. Depletion Interaction in the Phase Behavior of Nanoparticle-Polymer System*
   Sugam Kumar, V. K. Aswal and J. Kohlbrecher (Under preparation)

8. *Nanoparticle Interaction with Different Block Copolymers and Resultant Structure*
   Sugam Kumar and V. K. Aswal (Under preparation)

In Other Areas

9. *Interactional and Aggregation Behavior of Twin Tail Cationic Surfactants with Pluronic L64 in Aqueous Solution*
   R. Kaur, **Sugam kumar**, V. K. Aswal and R. K. Mahajan
   Coll. Poly. Sci. **2012**, *290*, 127-139.

10. *Small-Angle Neutron Scattering Study of Structure and Interaction of Nanoparticle, Protein, and Surfactant Complexes*
    S. Mehan, A. J. Chinchalikar, **Sugam Kumar**, V. K. Aswal and R. Schweins
    Langmuir **2013**, *29*, 11290-11299.

11. *Influence of Headgroup on the Aggregation and Interactional Behavior of Twin-Tailed Cationic Surfactants with Pluronics*
    R. Kaur, **Sugam Kumar**, V. K. Aswal and R. K. Mahajan
    Langmuir, **2013**, *29*, 11821-11833.

12. *Transition from Long Micelles to Flat Bilayers Driven by Release of Hydrotropes in Mixed Micelles*
    G. Verma, **Sugam Kumar**, R. Schweins, V. K. Aswal and P. A. Hassan
    Soft Matter, **2013**, *9*, 4544-4552.

13. *Solubilization of Hydrophobic Alcohols in Aqueous Pluronic Solutions: Investigating the Role of Dehydration of Micellar Core in Tuning the Restructuring and Growth of Pluronic Micelles.*
    V. Patel, J. Dey, R. Ganguly, **Sugam Kumar**, S. Nath, V. K. Aswal and P. Bahadur
    Soft Matter, **2013**, *9*, 7583-7591.

14. *Additive Induced Core and Corona Specific Dehydration and Ensuing Growth and Interaction of Pluronic F127 Micelles*
    J. Dey, **Sugam Kumar**, S. Nath, R. Ganguly, V. K. Aswal and K. Ismail
    J. Colloid Interface Sci., **2014**, *415*, 95-102.

15. *Small-Angle Neutron Scattering Study of Differences in Phase Behavior of Silica Nanoparticles in the Presence of Lysozyme and Bovine Serum Albumin Proteins*
    I. Yadav, **Sugam Kumar**, V. K. Aswal and J. Kohlbrecher
    Phys. Rev. E. **2014**, *89*, 032304 (1-9).

16. *Effect of Ethylene Glycol on the Special Counterion Binding and Microstructures of Sodium Dioctylsulfosuccinate Micelles*
    J. Dey, **Sugam Kumar**, A. Srivastava, G. Verma, P. A. Hassan, V. K. Aswal, J. Kohlbrecher and K. Ismail
    J. Colloid Interface Sci., **2014**, *414*, 103-109.

17. *Butanol solubilization in aqueous F127 solution: Investigating the enhanced micellar solvation and consequent improvement in gelation characteristics*
    P. Parekh, J. Dey, **Sugam Kumar**, S. Nath, R. Ganguly, V. K. Aswal, P. Bahadur
    Colloids and Surfaces B: Biointerfaces, **2014**, *114*, 386-391.

18. *Tetraalkylammonium ion induced micelle-to-vesicle transition in aqueous sodium dioctylsulfosuccinate solutions*
    U. Thapa, J. Dey, **Sugam Kumar**, P. A. Hassan, V. K. Aswal and K. Ismail
    Soft Matter, **2014**, *9*, 11225-11232.

In Conferences and Symposia:

Related to Thesis

1. *Direct Observation of Nanoparticle-Surfactant Interactions using Small Angle Neutron Scattering*
   Sugam Kumar and V. K. Aswal
   AIP Conf. Proc. **2010**, *1313*, 183-185.

2. *Fractal Aggregation in Silica Nanoparticle and Surfactant Composites*
   Sugam Kumar and V. K. Aswal
   AIP Conf. Proc., **2011**, *1349*, 214-215.

3. *SANS Study of Protein Adsorption on Nanoparticles*
   Sugam Kumar, V. K. Aswal and J. Kohlbrecher
   AIP Conf. Proc., **2011**, *1349*, 222-223.

4. *Size Dependent Fractal Aggregation Mediated through Surfactant in Silica Nanoparticle Solution*
   Sugam Kumar and V. K. Aswal
   AIP Conf. Proc., **2012**, *1447*, 155-156.

5. *SANS Study of Lysozyme vs. BSA Protein Adsorption on Silica Nanoparticles*
   Sugam Kumar and V. K Aswal
   AIP Conf. Proc., **2012**, *1447*, 181-182.

6. *Tuning of Adsorption vs. Depletion Interaction in Nanoparticle-Polymer System*
   Sugam Kumar, A. J. Chinchalikar, V. K. Aswal and R. Schweins
   AIP Conf. Proc., **2013**, *1512*, 152-153.

7. *Probing interaction of charged nanoparticles with uncharged micelles*
   Sugam Kumar, V. K. Aswal and J. Kohlbrecher
   AIP Conf. Proc., **2013**, *1512*, 124-124.

8. *Tuning structure of oppositely charged nanoparticle and protein complexes*
   Sugam Kumar, V. K. Aswal, and P. Callow
   AIP Conf. Proc., **2014**, *1591*, 161-163.

9. *Modeling of adsorption of nonionic Surfactant on Silica Nanoparticles*
   Sugam Kumar and V. K. Aswal
   3rd International Symposium on Materials Chemistry, held at BARC, Mumbai, **2010**.

10. *Salt-induced Cold Gelation of Bovine Serum Albumin (BSA) Protein*
    Sugam Kumar, A. J. Chinchalikar and V. K. Aswal
    Indo-US Conference on Self-Assembled Fibrillar Gels, held at Trivandrum, **2011**.

11. Contrast Variation SANS Study of Surfactant Adsorption on Nanoparticles
Sugam Kumar, V. K. Aswal and J. Kohlbrecher
2nd International Symposium on Neutron Scattering, held at BARC, Mumbai, **2013**.

12. Temperature Enhanced Adsorption of Block Copolymer on Silica Nanoparticles
Sugam Kumar, V. K. Aswal and J. Kohlbrecher
4th Interdisciplinary Symposium on Material Chemistry, held at BARC, Mumbai, **2013**.

13. SANS Study of Fractal Aggregation in charged nanoparticles systems
Sugam Kumar, A. J. Chinchalikar**,** V. K. Aswal and J. Kohlbrecher
4th Interdisciplinary Symposium on Material Chemistry, held at BARC, Mumbai, **2013**.

14. Observation of Polymer Dependent Reentrant Phase Behavior in Charged Nanoparticle System
Sugam Kumar, V. K. Aswal and J. Kohlbrecher
Conference on Neutron Scattering held at IISER, Pune, **2014**.

15. SANS Study of Complexes of Silica Nanoparticles with Lysozyme Protein
Sugam Kumar and V. K. Aswal
Organic Devices: The Future Ahead held at BARC, Mumbai, **2014**.

In Other Areas

16. *Co-existence of Monomers and Clusters in Concentrated Protein Solutions*
A. J. Chinchalikar, **Sugam Kumar**, V. K. Aswal, P. Callow, and A. G. Wagh
AIP Conf. Proc., **2012**, 1447, 161-162.

17. Role of electrostatic interaction on surfactant induced protein unfolding
Sumit, **Sugam Kumar**, and V. K. Aswal
AIP Conf. Proc., **2013**,1512, 160-161.

18. SANS study of understanding mechanism of cold gelation of globular proteins
A. J. Chinchalikar, Sugam Kumar, V. K. Aswal, J. Kohlbrecher, and A. G. Wagh
AIP Conf. Proc., **2014**, 1591, 186-188.

19. Observation of two different fractal structures in nanoparticle, protein and surfactant complexes
S. Mehan, Sugam Kumar, and V. K. Aswal
AIP Conf. Proc., **2014**, 1591, 167-169.

20. Temperature Induced Solution Behavior of Surfactants: A SANS Study
A. Bhadoria, **Sugam Kumar**, V. K. Aswal, S. Kumar
15th International Small-Angle Scattering Conference held at Sydney, Australia, 2012.

(Sugam Kumar)

Dedicated

To

My Parents

ACKNOWLEDGEMENTS

I would first like to express my sincere gratitude to my guide Dr. V. K. Aswal, Solid State Physics Division, Bhabha Atomic Research Centre, for his guidance, constant support, motivation, constructive criticism and valuable advices. I am also thankful to Dr. S.L. Chaplot, Director, Physics Group and Dr. R. Mukhopadhyay, Head, Solid State Physics Division, Bhabha Atomic Research Centre, for their support and encouragement. Thanks are due to Prof. P. Ayyub and Dr. S. Basu whose useful suggestions as doctoral committee members have been very helpful.

I also wish to thank Dr. P.A. Hassan, Chemistry Division, Bhabha Atomic Research Centre, for many fruitful discussions and help during dynamic light scattering measurements as well as zeta potential measurements. My thanks are also attributable to Dr. J. Kohlbrecher, Paul Scherer Institute, Switzerland, Dr. S.-M. Choi, Korea Advanced Institute of Science and Technology, Republic of Korea and P. Callow, Institut Laue Langevin, France for their help in carrying out SANS experiments.

Special thanks to Dr. D. Sen, Dr. D. Ray and Dr. A. J. Chinchalikar with whom I shared discussions of my research work. I am also thankful to Dr. P. U. Sastry, Dr. R. Mittal, Mr. A.K. Patra, Dr. J. Bahadur and Dr. S. Abbas, for their constructive support during the period of my thesis work.

I take the opportunity to thank all my friends, Arvind, Neetika, Mayank, Ripendeep, Swapnil and others who directly or indirectly have helped me in achieving my goals. My sincere thanks are due to all my colleagues in Solid State Physics Division, Bhabha Atomic Research Centre, for helping me in different ways.

Last but not the least, I would like to thank my parents, my wife, sisters and all the family members for being supportive in my endeavour and extending encouragement throughout the work. Without their support and encouragement this would not have been easy.

CONTENTS

Homi Bhabha National Institute

Ph. D. Programme

1. **Name of the Student:** Sugam Kumar
2. **Name of the Constituent Institution:** Bhabha Atomic Research Centre
3. **Enrolment No.:** PHYS01201204013
4. **Title of the Thesis:** Structural Studies of Nanoparticles Interactions with Different Macromolecules
5. **Board of Studies:** Physical Sciences

SYNOPSIS

Nanoparticles display unique and distinct characteristics from those of their constituent atoms and bulk materials, which are being employed in wide range of applications from medicine to electronics and energy to environment. Many of these applications require adjoining of nanoparticles with macromolecules such as proteins, polymers and surfactants to obtain functional objects [1]. The interaction of surfactants with nanoparticles is utilized extensively for technical and industrial applications associated with colloidal stability, detergency and design of nanostructured functional interfaces [2]. Nanoparticle-protein complexes are of great importance in controlling enzymatic behavior, targeted drug delivery and developing biocompatible materials [3]. Nanoparticle-polymer composites have attracted attention for engineering flexible materials exhibiting enhanced macroscopic performance with improved sustainability and multi-functionality [4]. The interaction of macromolecule with nanoparticles is a cumulative effect of a number of forces such as electrostatic force, covalent bonding, hydrogen bonding, depletion interaction, hydrophobic interactions etc. The interactions deciding the nature of nanoparticle-macromolecule system, strongly depend on the characteristics of both the nanoparticles (size,

shape, charge density etc.) and macromolecules (type, size, charge etc.) used. For example, if the two components have similar charge nature (anionic or cationic), strong electrostatic repulsion prevents them from direct adsorption [5]. However, the non-adsorbing nature of macromolecules can give rise to attractive depletion force in these systems. The role of the size ratio of the particle to macromolecule becomes important in such cases as it influences effective depletion potential [6]. When two components are oppositely charged, nanoparticles may destabilize and undergo macromolecule mediated aggregation. If one or both components are nonionic they interact through moderate interactions such as hydrogen bonding or hydrophobic forces or depletion interaction, if the macromolecule remains free in the solution [2, 5]. The characteristics of nanoparticle and macromolecule as well as other solution conditions may be used to tune the degree of their interactions in order to achieve the desirable system properties. This thesis provides understanding of the interaction of model silica nanoparticles with different macromolecules (surfactant, protein, block copolymer and polymer) under varying solution conditions. The systems under study have been characterized by small-angle neutron scattering (SANS). The easy possibility of contrast variation in SANS makes it an ideal technique to study such multi-components systems. Both structure and interaction can be determined in in-situ and under native conditions.

The thesis consists of seven chapters. The chapter 1 gives an introduction to the nanoparticles and macromolecules, their possible interactions and applications. The details of the experimental techniques, in particular SANS, and its proficiency for studying of multi-components systems such as nanoparticle-macromolecule are discussed in chapter 2. The results of the studies of silica nanoparticles interaction with different macromolecules are described in chapters 3 to 6. Chapter 3 provides the study of tuning of nanoparticle-surfactant interaction by varying the charge state of surfactant and nanoparticles size. The protein adsorption on nanoparticles and their resultant structure have been examined in the chapter 4. The block

copolymer-induced evolution of depletion interaction between nanoparticles has been studied in chapter 5. Chapter 6 describes the polymer dependent re-entrant phase behavior in nanoparticle-polymer system. Chapter 7 gives the summary of the thesis.

Chapter 1 gives a general introduction to nanoparticles and different macromolecules of interest in the thesis. Silica nanoparticles occupy a prominent position in scientific research, because of their easy preparation, high stability, low toxicity and ability to be functionalized with a range of macromolecules [7]. Therefore, these nanoparticles are often used as model nanoparticles in many applications. On the other hand, macromolecules such as surfactant, protein, block copolymer and polymers represent different class of macromolecules with distinct properties. Surfactants are amphiphilic molecules which form self-assembled structures called micelles in aqueous solutions above a critical micellar concentration (CMC) [8]. The presence of nanoparticles in the solution may force micelles to undergo some structural transformation and hence can modify their hydrophobicity, surface charge and other key properties governing the interfacial process [2]. Unlike surfactants, proteins have a specific three-dimensional shape and a charge on them, which are crucial in controlling and regulating their stability and functionality [9]. Proteins are large chain biological molecules of amino acids connected by peptide bond. In physiological environment, proteins are known to cover nanoparticles immediately and therefore their structure and functionality may be disturbed [3]. Block copolymers are special type of non-ionic macromolecules which have two or more different monomer units linked by covalent bond. Block copolymers consists of blocks of with two dissimilar moieties (e.g. hydrophilic PEO block and hydrophobic PPO block) within the same molecule [10]. In aqueous solution, the molecules self-assemble to form micelles, formation and shapes of which can be tuned by varying the concentration and temperature. Similar to block copolymers, a simple polymer is also a large molecule, composed of many repeated subunits (monomers), but do not form self-assemble structures. This thesis presents the evolution of interaction and resultant structure of silica

nanoparticles with the above different macromolecules in order to tune the properties of their complex systems. A layout of thesis is discussed in the end of this chapter.

The details of experimental technique SANS for the characterization of nanoparticle-macromolecule systems are described in chapter 2. SANS is a diffraction experiment, which involves scattering of a monochromatic beam of neutrons from the sample and measuring the scattered neutron intensity as a function of the wave vector transfer Q (= $4\pi\sin\theta/\lambda$, where λ is the incident neutron wavelength and 2θ is the scattering angle) [11, 12]. In SANS experiment, one measures the scattered intensity as given by $I(Q) \sim (\rho_p - \rho_s)^2 \times P(Q) \times S(Q)$, where $P(Q)$ is the intraparticle structure factor and $S(Q)$ is the interparticle structure factor. $P(Q)$ is the square of the particle form factor and is decided by the shape and size of the particle. $S(Q)$ depends on the spatial arrangement of particles and is thereby sensitive to interparticle interactions. The magnitude of scattered neutron intensity in the SANS experiment depends on contrast factor $[(\rho_p-\rho_m)^2]$, the square of the difference between the average scattering length densities of the particle and the medium. Due to the fact that the scattering length is negative (= -0.372×10^{-12} cm) for hydrogen and positive (= 0.667×10^{-12} cm) for deuterium, SANS is ideally suited for studying the structural aspects in hydrogenous materials. Deuterating either the particle or the medium can easily enhance the contrast between the particle and the medium. Further, the multi-components systems can be simplified to study them by selectively contrast matching the components with the partial deuteration of the components [12].

The evolution of interaction and resultant structures of nanoparticle-surfactant complexes is studied in chapter 3 [13-15]. Surfactants are known to form micelles in aqueous solution [8]. However, in presence of nanoparticles they can form independent micelles or adsorb on nanoparticles or both. In this chapter, interaction of different sized anionic silica nanoparticles (8, 16 and 26 nm) with three types of surfactants (anionic, cationic and nonionic) has been

examined. The surfactants used comprise same hydrophobic tail and differing in the charge on their headgroups are anionic sodium dodecyl sulphate (SDS), nonionic decaoxyethylene *n*-dodecylether ($C_{12}E_{10}$) and cationic dodecyltrimethyl ammonium bromide (DTAB). It is found that there is no significant interaction evolved between like charged nanoparticles and the SDS micelles. Both the silica nanoparticles and micelles coexist individually with no significant change in the structure of the micelles with respect to that in the pure surfactant solution. On the other hand, the strong attraction of oppositely charged DTAB micelles with silica nanoparticles results in aggregation of nanoparticles. The aggregates are characterized by mass fractal structure where the fractal dimension is found constant (D~2.3) independent of the size of the nanoparticle and consistent with diffusion limited aggregation type fractal morphology in these systems. In the case of nonionic surfactant $C_{12}E_{10}$, surfactant adsorb on the individual silica nanoparticles through hydrogen bonding of ether oxygen of the ethylene oxide group and the surface OH group. The interaction is analyzed using two models: one that considers the surfactant layer coating on silica nanoparticles and the second one where the surface of nanoparticles is decorated by the micelles. The contrast variation SANS measurements confirm the uniform decoration of nonionic micelles on the nanoparticles. The effect of nanoparticle size on nanoparticle-surfactant interactions has also been examined [16]. The nanoparticle size controls the surface to volume ratio and surface curvature for its interaction with surfactant. The surfactant interaction with nanoparticle is enhanced with the increase in the surface to volume ratio and with the decrease in the surface curvature. The resultant structure is found to be decided by the competition of these two opposing effects [14].

Chapter 4 reports the study of protein adsorption on nanoparticles and modeling of the resultant structure of the complexes formed [17-19]. The silica nanoparticles and globular protein lysozyme has been studied as a model system to understand the behavior of nanoparticle-protein system. The interaction between them, both being charge stabilized, is predominantly

governed by the electrostatic interactions which are known to lead many nonspecific associations especially relevant for biological applications. The competition of attraction between two components and repulsion between individual components in these systems determines the resultant behavior of the system. The experiments were carried out with three different sized silica nanoparticles (8, 16 and 26 nm) over a wide concentration range of protein at three different pH values (5, 7 and 9). The adsorption curve as obtained by UV-visible spectroscopy shows exponential behavior of protein adsorption on nanoparticles as a function of protein concentration. The electrostatic interaction enhanced by decrease in the pH between nanoparticle and protein (iso-electric point ~ 11.4) increases the adsorption coefficient on nanoparticles but decreases the overall amount protein of adsorbtion, whereas opposite of this behavior is observed with increase in nanoparticle size. The adsorption of protein leads to the protein-mediated aggregation of nanoparticles. These aggregates are found to be surface fractals at pH 5 which change to mass fractals with increase in pH and/or decrease in nanoparticle size. The two different concentration regimes of interaction of nanoparticles with protein have been observed (i) un-aggregated nanoparticles coexisting with aggregated nanoparticles at low protein concentrations and (ii) free protein coexisting with aggregated nanoparticles at higher protein concentrations. These concentration regimes are found to be strongly depending on both pH and nanoparticle size [19].

Macromolecules may either adsorb on the nanoparticles or remain free in the solution depending on the system conditions. The non-adsorbing nature of macromolecule may induce to depletion interaction between nanoparticles. The depletion interactions are unambiguously known to arise in the mixtures of two significantly different sizes of colloidal particles, when the smaller one experiences an excluded volume interaction with the larger one [6]. The block copolymer-induced depletion attraction and resulting clustering in charged silica nanoparticles has been studied using SANS in chapter 5 [20]. The SANS experiments were carried out from

silica nanoparticles in presence of contrast-matched P85 block copolymer [$(EO)_{26}(PO)_{39}(EO)_{26}$]. The effective interaction of silica nanoparticles is modeled by a combination of two Yukawa potentials accounting for attractive depletion and repulsive electrostatic forces [21]. The depletion interaction is found to be long-range attraction whose magnitude and range increase with block copolymer concentration. The depletion interaction is further enhanced by tuning the self-assembly of block copolymer by the variation of temperature. The increase of depletion interaction ultimately leads to clustering of nanoparticles and is confirmed by the presence of a Bragg peak in the SANS data. The positioning of Bragg peak suggests simple cubic type packing of particles within the clusters. The scattering from the clusters in the low Q region is governed by the Porod scattering indicating clusters are quite large (order of micron).

The tuning of depletion interaction of silica nanoparticles in presence of polyethelene glycol (PEG) polymer is studied in chapter 6 [22-23]. The nanoparticle-polymer solution interestingly shows a re-entrant phase behavior where the one-phase charged stabilized nanoparticles undergo two-phase system (nanoparticle aggregation) and back to one-phase as a function of polymer concentration. The well established models for depletion attractions predict monotonic growth in the strength of depletion attractions with increasing polymer concentrations [6]. However, a colloidal dispersion which is destabilized at low polymer concentrations due to depletion attraction, in some cases is also observed to re-stabilize at high polymer concentrations. The evolution of depletion attraction is reasonably understood, but the formalism of stabilization effect is still a subject of study. Both of these effects (depletion attraction and stabilization) have been examined by studying the nanoparticle-polymer system over a wide range of polymer concentration. Such phase behavior arises because of the non-adsorption of polymer on nanoparticle and is governed by the interplay of polymer-induced attractive depletion with repulsive nanoparticle-nanoparticle electrostatic and polymer-polymer interactions in different polymer concentration regimes. At low polymer concentrations, the electrostatic

repulsion dominates over the depletion attraction. However, the increase in polymer concentration enhances the depletion attraction to give rise the nanoparticle aggregation in two-phase system. Further, the polymer-polymer repulsion at high polymer concentrations is believed to be responsible for the re-entrant to one-phase behavior. The SANS data in polymer contrast-matched condition have been modeled by a two-Yukawa potential accounting for both repulsive and attractive parts of total interaction potential between nanoparticles [21]. Both of these interactions (repulsive and attractive) are found to be long-range. The magnitude and the range of the depletion interaction increase with the polymer concentration leading to nanoparticle clustering. At higher polymer concentrations, the increased polymer-polymer repulsion reduces the depletion interaction leading to re-entrant phase behavior. The nanoparticle clusters in the two-phase system are characterized by the surface fractal with simple cubic packing of nanoparticles within the clusters. The effect of varying ionic strength and polymer size in tuning the interaction has also been examined [24]. The combination of these parameters (ionic strength and molecular weight of polymer) with polymer concentration decides the interaction and structure, which can be used to tune the re-entrant phase behavior in nanoparticle-polymer systems.

Chapter 7 summarizes the findings of the thesis. The thesis presents the study of the nanoparticle interactions with different macromolecules and resultant structures in tuning properties of their complex system. SANS has been used as a main technique to probe these systems. The main results of the thesis are

(i) The interaction of anionic silica nanoparticles with anionic, cationic and nonionic surfactants is very different and each case lead to different microstructures. The dominant repulsion in the case of anionic micelles prevents any physical interaction of the two components. The strong attractive interaction of nanoparticles with cationic micelles gives rise to the aggregation of

particles and is characterized by fractal structure. For nonionic micelles, the hydrogen bonding between nanoparticle and micelles leads to the adsorption of micelles on individual particles.

(ii) Adsorption of protein on nanoparticles is shown to obey an exponential behavior as a function of protein concentration. The protein adsorption leads to the protein-mediated aggregation of nanoparticles. The nanoparticle aggregates coexist with un-aggregated particles at low protein concentrations and free proteins at higher protein concentrations. The morphology of the aggregates is found to be strongly depending on both pH and nanoparticle size.

(iii) The presence of amphiphilic block copolymers induces a depletion interaction between charged silica nanoparticles leading to particle clustering. The depletion interaction has been modeled using an attractive Yukawa potential whose range has been found to be much larger than the van der Waals attraction. The magnitude and range of the depletion interaction can be tuned by the size of the nanoparticles and concentration of block copolymers as well as by the self-assembly of block copolymers by varying the solution temperature.

(iv) The nanoparticle-polymer system shows a re-entrant phase behavior where nanoparticles undergo from one-phase to two-phase system and back to one-phase system as a function of polymer concentration. This phase behavior has been explained in terms of the interplay of different interactions present in the system. The total interaction between nanoparticles has been modeled by a two-Yukawa potential accounting for attractive as well as repulsive interaction. Both the magnitude and range of attraction increase in going from one-phase to two-phase system, whereas decrease back in the re-entrant of one-phase system.

To conclude, this thesis presents investigation of evolution of interaction and resultant structure in a number of different nanoparticle-macromolecule systems. The phase behavior and microstructure in these systems is shown to be governed by the interplay of both DLVO and non-DLVO interactions. The phase behavior of nanoparticle-macromolecule system can be tuned by the choice of the macromolecule (surfactant, protein, block copolymer or polymer) as well as by

varying solution conditions (ionic strength, temperature, pH etc.). This work can be utilized in nanoparticle applications of drug delivery, phase separation process and synthesis of functional materials.

References

1. W. H. Suh, Y. H. Suh and G. D. Stucky, *Nano Today*, 4, 27 (2009).
2. R. Zhang and P. Somasundaran, *Adv. Colloid Interface Sci.*, 123-126, 213 (2006).
3. J. Leszczynski, *Nature Nanotechnology* 5, 633 (2010).
4. A. C. Balazs, T. Emrick, T. P. Russell, *Science*, 314, 1107 (2006).
5. Sugam Kumar and V. K. Aswal, *AIP Conf. Proc.*, 1313, 183 (2010).
6. C. N. Likos, *Phys. Rep.* 348, 267 (2001).
7. I. A. Rahman and V. Padavettan, *J. Nanomater.* 132424 (2012).
8. M. Daoud and C. Williams, *Soft Matter Physics* (Springer-Verlag, Berlin, 1999).
9. D. Whitford, *Proteins: Structure and Function* (John Wiley & Sons, Ltd, 2005)
10. I. W. Hamley, *Block Copolymers in Solution: Fundamentals and Applications* (Wiley, 2005).
11. J. S. Higgins and H. C. Benoit, *Polymers and Neutron Scattering* (Clarendon Press, 1994).
12. D.I. Svergun and M.H.J. Koch, *Rep. Prog. Phys.* 66, 1735 (2002).
13. Sugam Kumar and V. K. Aswal, *J. Phys.: Condens. Matter* 23, 035101 (2011).
14. Sugam Kumar, V. K. Aswal, and J. Kohlbrecher, *Langmuir* 28, 9288 (2012).
15. Sugam Kumar and V. K. Aswal, *AIP Conf. Proc.* 1447, 155 (2012).
16. G. Despert and J. Oberdisse, *Langmuir* 19, 7604 (2003).
17. Sugam Kumar, V. K. Aswal and J. Kohlbrecher, *Langmuir* 27, 10167 (2011).
18. Sugam Kumar, V. K. Aswal and J. Kohlbrecher, *AIP Conf. Proc.* 1349, 222 (2011).
19. Sugam Kumar, V. K. Aswal, and P. Callow, *Langmuir* 30, 1588 (2014).
20. Sugam Kumar, M.-J. Lee, V. K. Aswal, and S.-M. Choi, *Phys. Rev. E* 87, 042315 (2013).
21. Y. Liu, W.-R. Chen and S.-H. Chen, *J. Chem. Phys.* 122, 044507 (2005).
22. Sugam Kumar, D. Ray, V. K. Aswal and J. Kohlbrecher (submitted to *Phys. Rev. E*)
23. Sugam Kumar, A.J. Chinchalikar, V.K. Aswal and R. Schweins, *AIP Conf. Proc.* 1512, 152 (2013).
24. Sugam Kumar, V. K. Aswal and J. Kohlbrecher (Under preparation)

LIST OF FIGURES

Figure 3.2. SANS data of 1 wt% HS40 nanoparticles with 1 wt% surfactants (a) SDS (b) DTAB and (c) $C_{12}E_{10}$. Insets show the comparison of measured data of nanoparticle-surfactant system with the calculated addition of data of respective pure components.

Figure 3.3. SANS data of 1 wt% HS40 with 1 wt% SDS (a) nanoparticles are contrast-matched along with data from pure surfactant system under the same contrast condition and (b) micelles are contrast-matched along with data from pure nanoparticle system under the same contrast condition.

Figure 3.4. SANS data of 1 wt% HS40 with 1 wt% DTAB (a) micelles are contrast-matched along with data from pure nanoparticle system under the same contrast condition and (b) nanoparticles are contrast-matched along with data from pure surfactant system under the same contrast condition.

Figure 3.5. SANS data of 1 wt% HS40 with 1 wt% $C_{12}E_{10}$ (a) nanoparticles are contrast-matched along with data from pure surfactant system under the same contrast condition and (b) micelles are contrast-matched along with data from pure nanoparticle system under the same contrast condition

Figure 3.6. Autocorrelation functions of 1 wt% HS40 nanoparticles without and with 1 wt% $C_{12}E_{10}$ micelles as measured by dynamic light scattering.

Figure 3.7. Schematic of the microstructures formed as a result of interaction of anionic silica nanoparticles with different charged surfactants.

Figure 3.8. SANS data of 1 wt% SDS surfactant with 1 wt% silica nanoparticle systems (a) micelles are contrast-matched along with data from pure nanoparticle system under the same contrast condition and (b) nanoparticles are contrast-matched along with data from pure surfactant system under the same contrast condition.

Figure 3.9. SANS data of 1 wt% DTAB surfactant with 1 wt% silica nanoparticle systems (a) no component is contrast-matched, (b) DTAB micelles are contrast-matched and (c) nanoparticles are contrast-matched to the solvent.

Figure 3.10. SANS data of 1 wt% $C_{12}E_{10}$ surfactant with 1 wt% silica nanoparticle systems (a) nanoparticles are contrast-matched along with data from pure surfactant system under the

same contrast condition and (b) micelles are contrast-matched along with data from pure nanoparticle systems under the same contrast condition.

Figure 4.1. Lysozyme protein adsorption isotherm in 1 wt% LS30 silica nanoparticle solution. The variations of adsorbed protein concentration as well as % adsorbed protein are plotted as a function of protein concentration. Inset shows the protein concentration dependent adsorption of protein molecules per nanoparticle.

Figure 4.2. SANS data of 1 wt% LS30 silica nanoparticle system with (a) lower protein concentration (0.0 to 0.1 wt%) and (b) higher protein concentration (0.2 to 10 wt%) at pH 7.

Figure 4.3. A schematic of aggregation of silica nanoparticles in presence of lysozyme protein.

Figure 4.4. SANS data of 1 wt% concentration of (a) LS30 silica nanoparticles and (b) lysozyme protein solutions at three pH values (5, 7 and 9). Inset of figure 4.4(b) shows SANS data of 5 wt% protein solutions.

Figure 4.5. Lysozyme protein adsorption curve on LS30 silica nanoparticles (1 wt%) expressed as adsorbed protein vs. total protein (in wt%) at three pH values (5, 7 and 9). Inset shows the calculated variation of % adsorbed protein on nanoparticles in these systems.

Figure 4.6. SANS data of 1 wt% LS30 silica nanoparticle system at pH 5 with (a) lower protein concentration (0.0 to 0.1 wt%), (b) intermediate protein concentration (0.05 to 1.0 wt%) and (c) higher protein concentration (2 to 10 wt%).

Figure 4.7. Comparison of SANS data of 1 wt% LS30 silica nanoparticle system with (a) 0.01 wt%, (b) 0.1 wt%, (c) 1.0 wt% and (d) 10.0 wt% concentration of protein at three pH values (5, 7 and 9).

Figure 4.8. Schematic of structures of nanoparticle-protein aggregates at different pH.

Figure 4.9. Lysozyme protein adsorption curve on 1 wt% (a) SM30 (b) TM40 silica nanoparticles at three pH values (5, 7 and 9).

Figure 4.10. SANS data of 1 wt% protein with 1 wt% SM30, LS30 and TM40 silica nanoparticles each at three pH values (a) pH 5, (b) pH 7 and (c) pH 9.

Figure 5.1. SANS data of 1 wt% LS30 silica nanoparticles with varying concentration of P85 block copolymer at 20 ^{o}C. Inset highlights the variation in low Q data.

LIST OF TABLES

Chapter 1

NANOPARTICLES, MACROMOLECULES AND THEIR INTERACTIONS

1.1. Introduction

The field of nanoscience and nanotechnology describes the creation and exploitation of materials with structural features having at least one dimension in the nanometer range (1-100 nm). Nanostructures (synthetic or natural) are known to exhibit fascinating physical properties such as surface plasmon resonance, superparamagnetism, extremely high electron mobility, giant magnetoresistance etc. that are significantly different from that of the compositional atoms as well as corresponding bulk materials [1-5]. A nanoparticle, with all the three dimensions in nanoscale is the most fundamental nanostructure which represents the most widespread current form of nanomaterials. The striking features of nanoparticles have been widely used for various multidisciplinary applications in electronics, medicine, energy, catalysis etc. [1-10].

The macromolecules are large molecules having sizes corresponding to that of nanostructured materials and possess novel physico-chemical properties such as self-assembly, viscoelasticity, wide range of biological functions etc [16-19]. Depending upon the nature of interaction of macromolecules with aqueous medium, they are classified as hydrophilic, hydrophobic or amphiphilic. Polar and ionic macromolecules are said to be hydrophilic because of their interaction with water. Non-polar macromolecules are hydrophobic and they do not dissolve in water. On the other hand, amphiphilic molecules are made up of both hydrophilic and

hydrophobic components [16]. Polymers can be hydrophilic or hydrophobic based on the nature of functional group [19]. Polyethylene glycol is an example of hydrophilic polymer whereas polystyrene is a hydrophobic polymer. Other examples of hydrophobic macromolecules include alkanes, oils, fats etc. Protein, surfactant and some block copolymers are common examples of amphiphilic macromolecules.

The interaction of nanoparticles with macromolecules opens routes for the tuning of rich phase behavior of these systems as well as formation of new hybrid functional materials, which are being employed in wide range of applications. The interaction of nanoparticles with surfactants is utilized extensively for many technical applications associated with enhanced dispersion stability, emulsification, corrosion, enhanced oil recovery, chemical mechanical polishing etc [20]. Nanoparticle-protein complexes have shown their paramount importance in nanobiotechnology (enzymatic behavior, targeted drug delivery and diagnostics) [21]. Figure 1.1 shows the schematic of nanoparticle-biomolecule conjugate utilized to carry the protein drug for the targeted drug delivery. Nanoparticles-polymer composites display enhanced thermal and mechanical properties which are shown to be very useful for developing synthetic materials of high strength [13]. In order to accomplish the control over the performance of the fundamental building block of these hybrid structures, the understanding of nanoparticle-macromolecule interactions is essentially required. The interaction between the constituents participating, nanoparticle and macromolecule, is governed by cooperative effect of many forces such as van der Waals force, electrostatic interaction, hydrogen bonding etc. The resultant behavior of the complex system strongly depends on the characteristics of both the nanoparticles and macromolecules used [20-24]. For example, the adsorption of oppositely charged protein on

anionic nanoparticles has been found to be dramatically suppressed by manipulating charge at the nanoparticle surface through cationic coating on nanoparticles [24]. However, the

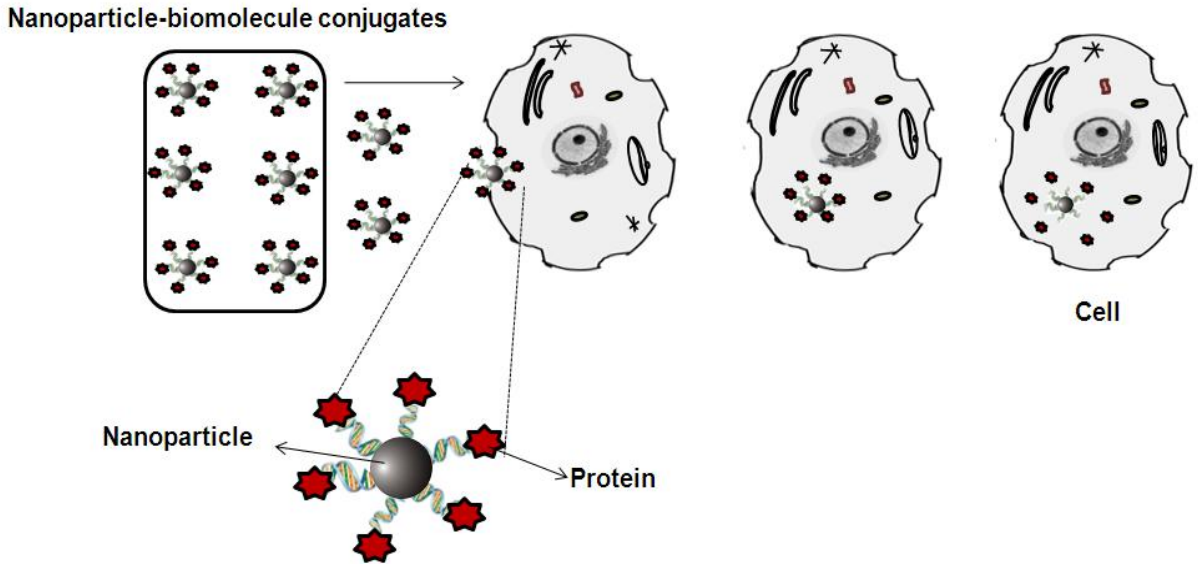

Figure 1.1. Schematic of nanoparticle-biomoleucle conjugate for targeted drug delivery.

non-adsorbing nature of macromolecules can give rise to attractive depletion force in these systems. The size difference between nanoparticle and macromolecule can be utilized to observe entropy driven depletion forces and corresponding structural changes in the system [25, 26]. When two components are oppositely charged, nanoparticles may destabilize and undergo macromolecule mediated aggregation. This phenomenon has been observed in number of oppositely charged nanoparticle and macromolecule systems, where the tuning of their electrostatic interaction can result in aggregates of different shapes, patterns and functionalities. If one or both components are nonionic they interact through moderate interactions such as hydrogen bonding or hydrophobic forces or depletion interaction, if the macromolecule remains free in the solution [20, 23, 27]. The characteristics of nanoparticle and macromolecule as well as other solution conditions may be used to tune the degree of their interactions in order to

achieve the desirable system properties. The present thesis provides understanding of the interaction of model silica nanoparticles with different macromolecules. This chapter describes the characteristics of the nanoparticles and macromolecules used, their possible interactions and applications. The layout of the thesis is also given in the end of the chapter.

1.2. Characteristics of nanoparticles

The extraordinary properties of the nanoparticles emerge largely because of two effects, quantum effect and scalable effect [1, 2, 28-32]. Quantum effects like spatial confinement can be observed in the nano size range, when the particle dimension is of the order of the de Broglie wavelength of the particle. A particle behaves as if it is confined in some potential well which otherwise feels free if the confining dimension is larger compared to its wavelength. In confined state, electronic wave function is delocalized over the entire particle and the particle may be regarded as individual atoms. In such situation, the electronic energy levels become discrete instead of continuous band (figure 1.2). Evolution of properties therefore becomes analogous to that happened with increasing atomic number in periodic table [2]. On the other hand, scalable effects are observed due to increased surface area per unit volume with decrease in particle size (figure 1.3). The surface dependent properties mostly are scalable, changes continuously with size and extrapolate slowly to that of bulk. The surface-to-volume ratio increases proportionally to the inverse of particle size and hence in the nanoscale surface atoms constitute a considerable fraction of the total number of atoms [1, 2, 29-31]. The high proportion of surface atoms suffers unsaturation in the coordination which results in an increase in the presence of dangling bonds. The higher the number of dangling bonds greater is the surface free energy. These bonds govern largely the thermodynamic, mechanical as well as chemical functions of nanoparticles.

The overall nanoparticle characteristics are determined by a combination of quantum and scalable effects. In general, quantum effects are superimposed on smoothly varying background of scalable effects for nanoparticles [2]. Nanoparticles are interesting intermediates between single atoms and bulk matter representing both ends at the middle. Some of the important properties of nanoparticles arising because of these effects are described below:

(i) Electronic properties: Electronic properties of solids in bulk depend on well defined electronic energy bands. In general, in bulk solids, there exists a valance band which is completely filled by electrons and a conduction band which is empty. The two bands are separated by an energy gap δ_E. Based on the value of δ_E, solids are classified as metals ($\delta_E \sim 0$), semiconductors ($\delta_E \sim$ 1eV) and insulators ($\delta_E \sim$ 10 eV) [29, 32]. In nanometer size range, the band structure of bulk material can no more be observed as quasi continuous, instead has to be replaced by quantum mechanical levels with a size dependent spacing and band gap (figure 1.2). Single nanoparticle display an electronic structure that corresponds to an intermediate electronic structure between the band structure of the bulk and the discrete energy levels of molecules with

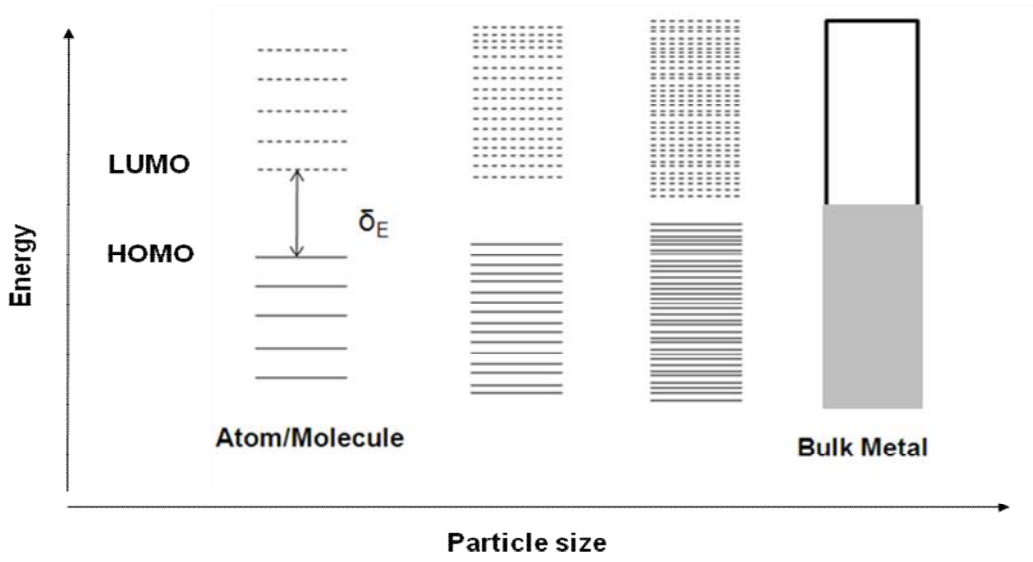

Figure 1.2. Evolution of the band gap and density of states with decreasing particle size.

characteristic highest occupied molecular orbital (HOMO) and lowest unoccupied molecular orbital (LUMO) (figure 1.2) [2, 32, 33]. Such size quantization effect may be regarded as the onset of the metal-insulator transition where the critical size at which transition occurs depends on the nature of the material. The metallic/semiconductor/insulator properties of the materials can be tuned in nanometer size range. These effects are being utilized in great extent in modern day electronics which requires miniaturization of circuit elements along with reduction in distance between them [2, 3, 28, 34]. Today's nanolithographic fabrication techniques allow scaling down to 50 nm which open up new opportunities utilizing quantum effects.

(ii) Optical properties: Nanomaterials show novel optical properties which are remarkably different from their bulk. There are two important factors determining the optical behavior of the nanoparticles, quantum confinement and surface plasmon resonance (SPR) [2, 35]. The discretization of energy spectrum in nano size range ultimately alters optical illumination of the particles. For example, the luminescence spectra of Europium doped Y_2O_3 show emergence of additional peaks in nanocrystalline phase [29]. This effect is most pronounced for semi-conductor particles where a blue shift in the light absorption can be observed because of the increase in the band gap with reduction in size. The rate of recombination of photo-excited electron hole pair is also decreased. The surface plasmon resonance is usually observed in metal nanoparticles because of which these nanoparticles exhibit particle size dependent coloring [28, 35, 36]. SPR excitation is based on the interaction of the electromagnetic field of the incoming light with conduction electrons on the metal nanoparticle surface resulting in a collective in-phase oscillation. The frequency of these oscillations depends on the free electron density, shape and size of the material as well as surrounding dielectric medium. The SPR for noble metal nanoparticles occur throughout the visible and near-infrared region of the electromagnetic

spectrum. Many applications in photonics, sensing and imaging industry, communication industry and in solar cells become possible due to the large enhancement of the surface electric field as well as increased detection sensitivity of the nanoparticles [35].

(iii) Magnetic properties: Essentially each atom with odd number of electrons can behave like a magnet. It is the electronic structure basically which determines the magnetic behavior. Therefore, the reduction in particle size can influence the magnetic properties of the system by altering the electronic structure, reducing the symmetry of the system and changing the boundary conditions [7, 29, 37-39]. In sufficiently small nanoparticles, magnetization can randomly flip direction. As a result, nanoparticle equivalent to single domain behave like superspins and show superparamagnetism where ferromagnetic particles become paramagnetic. The uncompensated surface spins at nanoscale leads to high magnetic moment even for small clusters of non-magnetic materials like Pd, Au and Pt [2]. The coercivety and saturation magnetization increases with decrease in particle size. A maximum coercive field is attained for the maximum size of a nanocluster that is of single magnetic domain [29]. Further, the possibility of inducing the room-temperature ferromagnetic-like behavior in ZnO nanoparticles without doping with magnetic impurities has been demonstrated where the electronic configuration of nanoparticles is altered by surface capping of organic molecule [40]. These interesting properties have shown useful potential in the fields like memory devices, batteries, magnetic resonance imaging, drug delivery etc [37-39].

(iv) Surface properties: The overall surface area increases with decrease in particle size for a fixed volume (figure 1.3). In chemical reactions involving a solid material, the surface-to-volume ratio becomes extremely important parameter for their reactivity. The high surface-to-volume ratio containing large portion of atoms/molecules at the surface of nanoparticles provides more

surface sites available for the higher activity [2, 29-32]. This can be understood from a simple example of ice melting where finely crushed ice melts faster than ice cubes. The excessively high reactivity of the surface originates from quantum mechanical atom-atom interaction that directs a strong driving force to speed up the process in the quest of minimizing the free energy. Immediately after generation, nanoparticle surface may get modified depending on the presence of reactants present, and solution conditions leading unpredictable behavior of them. On one hand, nanoparticles have a large functional surface which is able to bind, adsorb and carry other compounds such as drugs, polymers and proteins on the other hand, they also have a chemically more reactive surface that might enhance the catalytic promotion of reactions manyfold compared to their bulk analogues [44-46]. The important parameters governing the nanoparticle surface activity are surface composition, functional group present on surface, its termination, charge, surface strain and defects which are known to have strong impact on nanoparticle secondary size, solubility and affinity for other macromolecules [44].

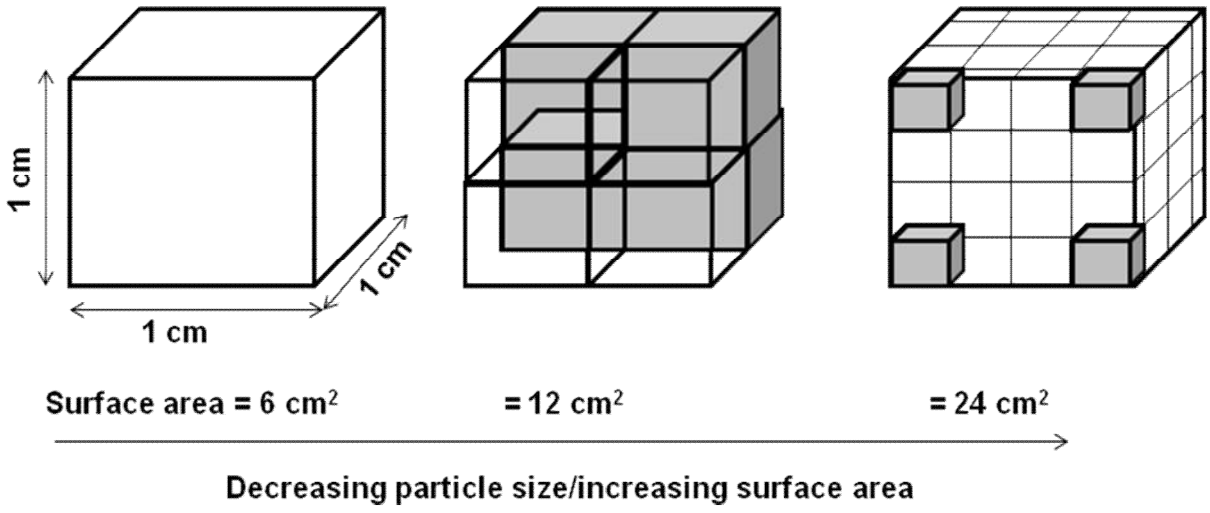

Figure 1.3. Schematic of increase in surface area with decreasing particle size.

(v) Mechanical properties: Mechanical properties of the nanoparticles have been shown to touch the theoretical limits, which are one or two orders higher than that found in bulk [1, 29]. There are basically two factors considered responsible for governing the mechanical properties at nanometer length scale (i) strong surface forces which otherwise are less relevant and (ii) reduced probability of defects like dislocations, microtwins impurities etc [1]. These two factors together modify many mechanical properties like adhesion, contact, hardness, elastic modulus, fracture roughness, scratch resistance, deformation etc. Cutting tools formed by nanomaterials such as tungsten carbide, titanium carbide are harder, more wear-resistant, erosion-resistant and long lasting compare to their conventional bulk counterpart. Ceramic materials which otherwise are very hard, ductile, brittle and difficult to machine, can be pressed and sintered into various structures if grain size is reduced in nanoscale [29]. Moreover, the nanoparticle-polymer composites show increased reinforcement, stronger plastics nature and suitability to handle higher temperature as well as mechanical stress [41, 42]. The nanoparticles impart their properties to the polymers and as a consequence, the Young's modulus and strength of nanocomposites increases with particle loading. Smart and sophisticated clothing can be achieved by attaching the nanoparticles to textile fibers. Many aircraft components require high fatigue strength for a longer time period. It has been shown that the fatigue strength as well as fatigue life can be enhanced by an average of 250% in nanodimensions [29].

(vi) Thermodynamic properties: Interesting thermal properties of nanoparticles emerge mainly because of high surface energy of the nanoparticles [43]. The nanoparticles are found to have lower melting and boiling temperature than their bulk form [2, 29]. The lowering of melting/boiling point is in general explained by the fact that the surface energy increases with the decreasing size. It has been further shown that the thermal conductivity of the nanoparticles can

be much higher. Also the nanoparticles show an intrinsic thermodynamic self-purification [1]. Any heat treatment increases the diffusion of impurities towards the nanoparticle surface causing a relatively increased perfection within the volume. Such purification has appreciable impact on other chemical and physical properties of the material. The nanoparticles provide an energy conversion through the transformation of an electromagnetic radiation into heat at the nanoscale. Therefore, the nanoparticles can also be treated as nanometric heat sources and probes for local temperature variations. For example, in plasmonic devices local heating may be used for guiding the electromagnetic wave by nanostructures. In the medical area, photo-thermal cancer therapy based on nanoparticles is a very promising technique, where nanoparticles absorb light energy, transmitted through biologic tissues and transform it into heat which diffuses toward local environment. The nanoparticles provide the possibility of sintering at lower temperatures, over shorter time scales than for larger particles [29].

Silica nanoparticles are one of the most studied model nanoparticle systems used for many applications. These nanoparticles occupy a prominent position in scientific research, because of their easy preparation, high stability, low toxicity and ability to be functionalized with a range of macromolecules [47, 48]. These are usually electrostatically stabilized suspensions of fine amorphous, nonporous, and typically spherical particles in a liquid phase. The usual particle size range is in between 10 to 100 nm in diameter. Smaller and larger particles are difficult to stabilize. Popularly, silica nanoparticles are synthesized in two ways: chemical vapor condensation (CVC) method and sol-gel process. In CVC method, silica nanoparticles are produced through high temperature flame decomposition of precursors such as silicon tetra chloride (SiCl4) with hydrogen and oxygen. Though, this method has limitations like difficulty in controlling the particle size, morphology, and phase composition but is efficiently used for

(a)

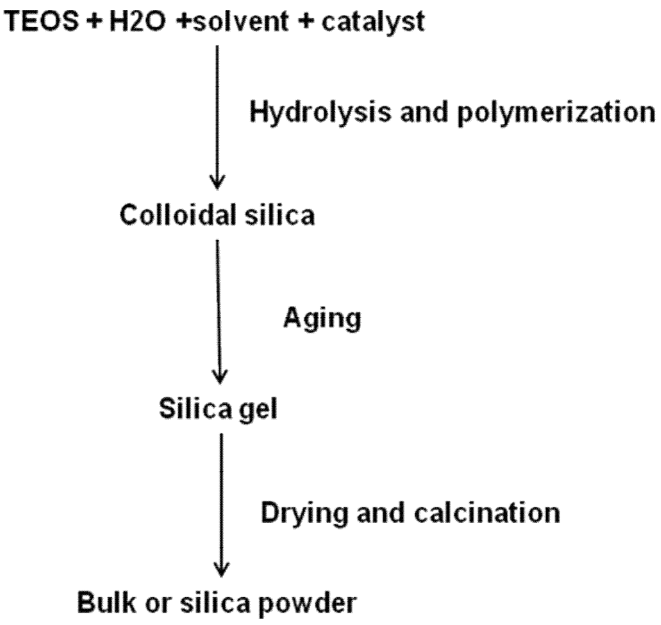

(b)

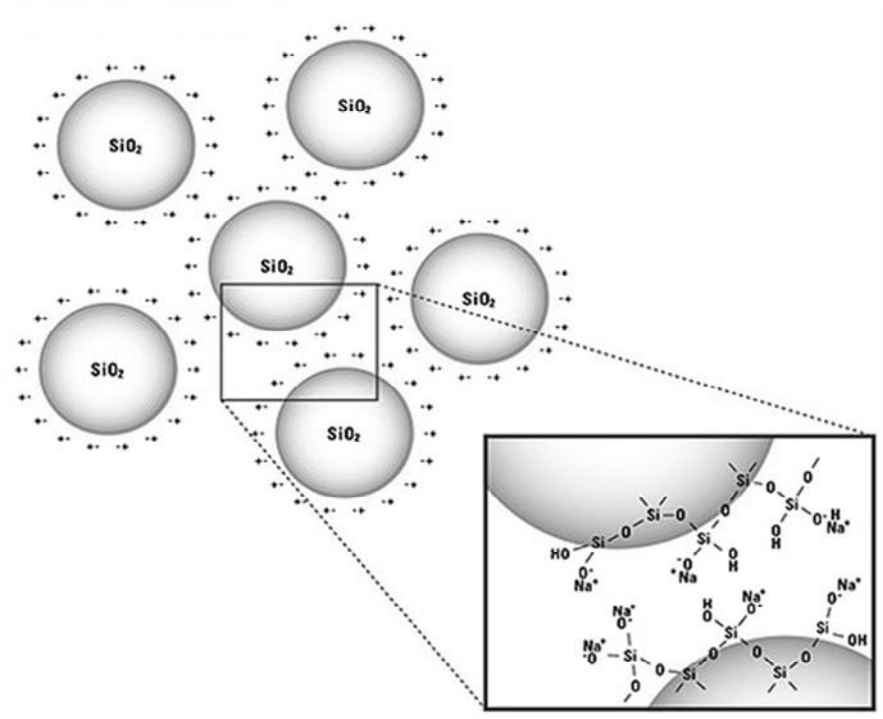

Figure 1.4. (a) A typical sol-gel process for synthesis of colloidal silica nanoparticles and (b) schematic of charged stabilized silica nanoparticles.

commercial synthesis of silica nanoparticles in powder form. The other method (sol-gel) is a multi-step process where hydrolysis and condensation of metal alkoxides [$Si(OR)_4$] such as tetraethylorthosilicate [TEOS, $Si(OC2H5)_4$] or inorganic salts such as sodium silicate [Na_2SiO_3] is carried out in the presence of mineral acid (e.g. HCl) or base (e.g. NH_3) as catalyst. The hydrolysis of silicon compound (TEOS) molecules forms silanol groups. The condensation/polymerization between the silanol groups creates siloxane bridges (Si–O–Si) that form entire silica structure in colloidal form. A general flow chart summarizing the silica nanoparticle synthesis by sol-gel process using silicon alkoxides [$Si(OR)_4$] is shown in figure 1.4(a) [49]. In aqueous solution, the hydrogen ions from the surface of colloidal silica tend to dissociate, yielding an overall high negative charge [figure 1.4 (b)]. Because of the very small size, the surface charge density becomes high. The colloidal suspension is first stabilized by adjusting the pH of the solution and then concentrated, usually by evaporation. The maximum concentration obtainable depends on the particle size. 50 nm particles can be concentrated to greater than 50 wt% solids while 10 nm particles can only be concentrated to approximately 30 wt% solids before the suspension becomes too unstable.

1.3. Different types of macromolecules

The macromolecules are very large molecules of high molecular masses and the structure of which essentially comprises the multiple units derived from molecules of lower molecular masses. Different macromolecules (e.g. polymers, synthetic fibers, surfactant micelles, proteins, DNA, lipids) possess distinct structures and are characterized by unusual physical properties [50]. For example, individual pieces of DNA in a solution can be broken into two parts simply by using an ordinary straw which is not true for smaller molecules. Another common macromolecular property that is not characterized by smaller molecules is macromolecular

crowding in which the high concentrations of macromolecules in a solution can alter the rates and equilibrium constants of the reactions of other macromolecules. Such unusual properties of the macromolecules emerge due to their large size, specific shape and chemical structure. In general, the macromolecules provide structural integrity to the many natural and synthetic systems and perform several functions in our daily life. The macromolecules can broadly be classified in the following three types:

(i) Amphiphilic molecules: The amphiphilic molecules are made up of one hydrophilic moiety (referred to as head group) which is covalently bonded to another hydrophobic moiety (generally a single or double alkyl chain also called as tail). The hydrophobicity or hydrophilicity is decided by the non-polar or polar nature of the molecule, respectively [16, 51, 52]. The common examples of amphiphilic substances are detergents, cholesterol, surfactants etc. The coexistence of two opposite type of behavior (hydrophilic and hydrophobic) inside the same molecule is the origin of the local constraints which lead to the spontaneous aggregation of amphiphilic molecules. The process is known as micellization. The hydrophilic head remains in the contact with surrounding solvent, sequestering the hydrophobic tail regions in the micelle core. The micellization occurs after a critical concentration known as critical micellar concentration (cmc). Micelles are thermodynamically stable and entropically more favorable than the segregated amphiphilic molecules.

Surfactants are one of the most important and extensively used amphiphilic molecules [51]. These are surface active substances that are known to lower the surface tension (or interfacial tension) at air and water interface and can act as wetting agents, emulsifiers, foaming agents, stabilizing agents and dispersants. The surfactants have huge importance in the diverse fields of our day-to-day life including pharmacy, food industry and cosmetic, cleaning

applications and controlled synthesis of nanostructured materials. Surfactants are classified as anionic, non-ionic, cationic or zwitterionic according to the charge nature of their polar head group. The non-ionic surfactants (e.g. decyl glucoside, polyoxyethylene glycol alkyl ether) have no charge on the head groups. The hydrophilic head of anionic surfactants (e.g. sodium dodecyl sulfate, ammonium lauryl sulfate) carry a net negative charge while charge on cationic surfactants (e.g. benzalkonium chloride, cetyltrimethylammonium bromide) is positive. The zwitterionic surfactants (e.g. cocamidopropyl hydroxysultaine) consist of a head with two oppositely charged groups. Similar to other amphiphilic molecules, surfactants also have unprecedented capacity to form self-assembled structures. Based on molecular geometry of surfactant molecule as well as solution conditions these structures may acquire different shapes such as spherical and cylindrical micelles, bilayer and vesicles (figure 1.5).

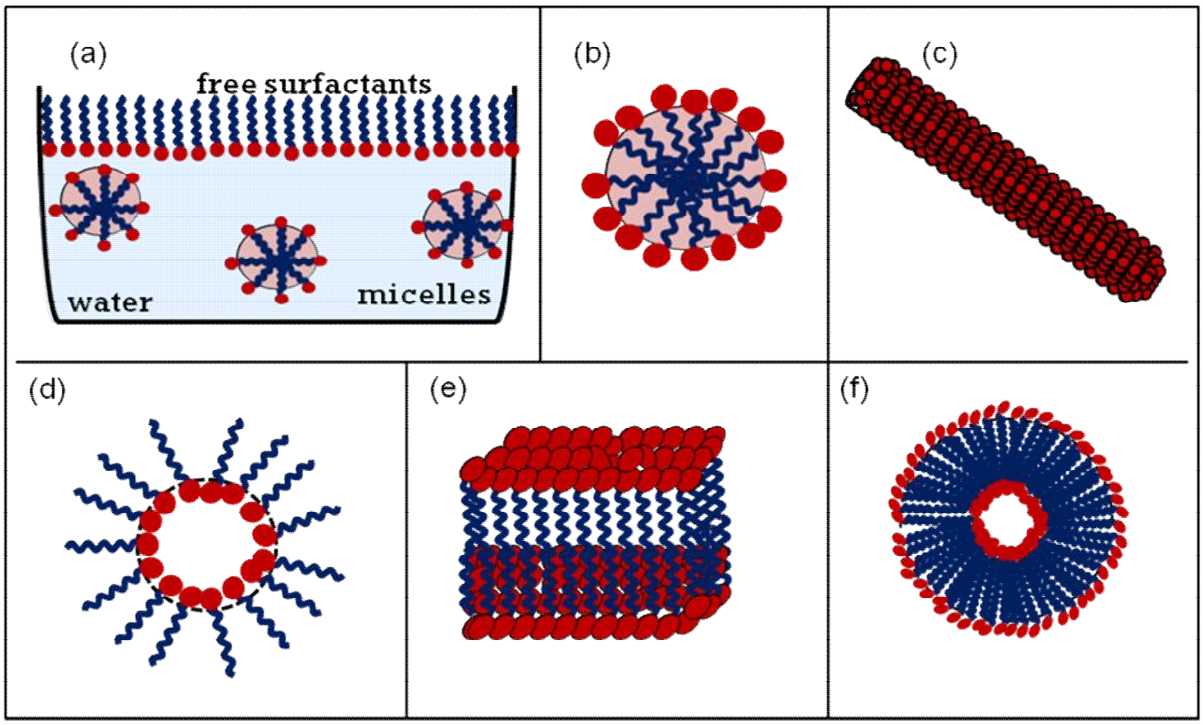

Figure 1.5. Different organized aggregates of surfactant (a) monolayer with micelles, (b) spherical micelle, (c) rod-like micelle, (d) reversed micelle, (e) bilayer and (f) vesicles.

(ii) Biomolecules: A biomolecule is defined as a molecule that is produced by a living organism and is involved in the maintenance and metabolism of living organisms [53-55]. The interactions of the biomolecules with each other constitute the molecular logic of life processes. The biomolecules are usually classified into four major groups, carbohydrates, proteins, nucleic acids and lipids. The carbohydrates are optically active polyhydroxy aldehydes or ketones or the compounds which produce such units on hydrolysis. The principle functions of carbohydrates include energy storage, cellular fuel, and structure formation. Proteins are made up of amino acids linked together by peptide bonds. Protein molecules can be found in every part of the body and constitute up to 75% of the dry weight of cells. The Nucleic acids are composed of nucleotides which function in the storage, utilization, and transmission of inherent genetic character. There are mainly two types of nucleic acids, deoxyribonucleic acid (DNA) and ribonucleic acid (RNA). Lipids are a diverse group of naturally occurring fatty or oily substances that are characterized by their insolubility in water and their solubility in nonpolar organic solvents. They form the major structural component of the plasma membrane and perform functions like cellular communication, signaling, storing energy etc.

Proteins are the most versatile biomolecule which underpin almost every aspect of biological activity and serve crucial role in essentially all biological processes [18, 53, 55]. Proteins perform several functions in living body such as catalytic activity, transportation, storage of other molecules, generating movement, transmitting nerve impulses and controlling growth. The function of a protein is decided by its three dimensional structure. Despite enormous functional diversity, all proteins are linear arrangement of twenty amino acid residues assembled together into a polypeptide chain. However, most proteins do not remain linear sequences of amino acids instead the polypeptide chain folds into a three dimensional characteristic shape

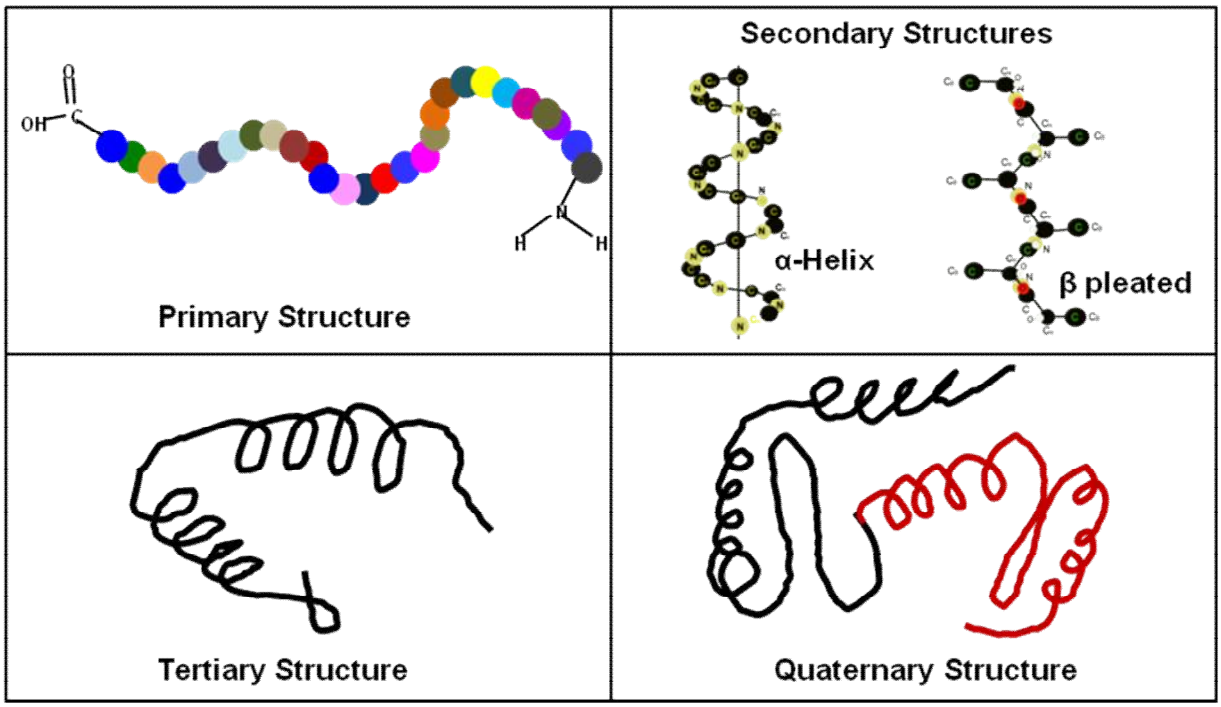

Figure 1.6. Different possible conformations of protein structures.

spontaneously and adopts configuration that is the most stable for its particular chemical structure and environment. The protein structure may be understood in terms of four distinct conformations namely primary, secondary, tertiary, and quaternary (figure 1.6). Primary structure represents sequence of different amino acids. The secondary structure of protein molecules refers to the formation of a regular pattern of twists or kinks of the primary structure of the protein molecule stabilized by hydrogen bonds. The two most common types of secondary structure are called the α helix and β pleated sheet. Atoms in an α helix, arrange themselves in a helical pattern whereas in case of β pleated sheet instead of peptide links arranging themselves via twists and turns, they can have bond with other sheets of the polypeptide in a sheet-like fashion. The folding of secondary structure elements in a compact unit is called the tertiary structure stabilized by non-local interactions like hydrophobic interaction, salt bridging,

hydrogen bonding, disulfide bonding etc. A protein containing more than one polypeptide chain exhibits the quaternary structure. This condition arises for proteins larger than 150 residues.

(iii) Polymers and block copolymers: A polymer molecule consists of the same repeating units (sub-units), called monomers, or different but resembling units [19, 56, 57]. Polymers play a very vital role in human life as there exists lot of polymers in our body. Apart from this, other naturally occurring polymers like wood, rubber, leather and silk are of high importance in human

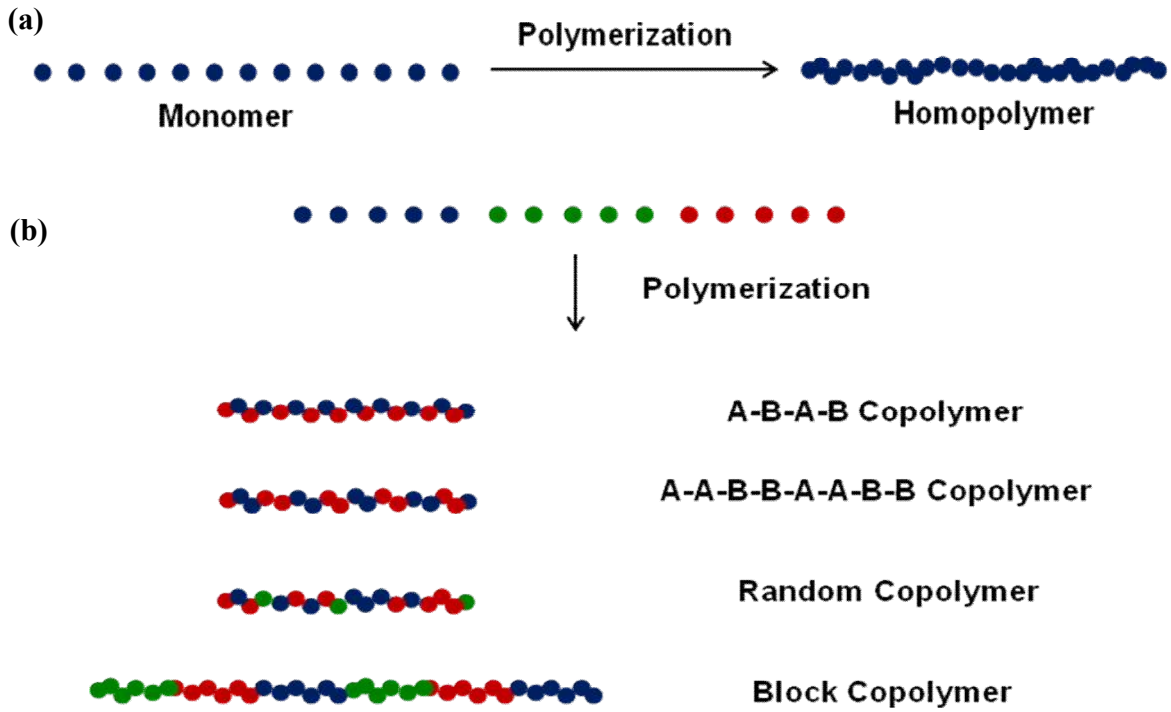

Figure 1.7. Schematic of polymerization in (a) homopolymer and (b) copolymer.

life. Modern scientific tools have revolutionized the processing of polymers thus now synthetic polymers like useful plastics, rubbers and fiber materials are also available. The physical arrangement of monomer residues along the backbone of the chain decides the microstructure of a polymer. Polymers containing only a single type of repeat unit are known as homopolymers, whereas polymers having a mixture of repeat units are known as copolymers [figure 1.7]. The

properties of polymers are related to their constituent structural elements, their arrangement and chain length.

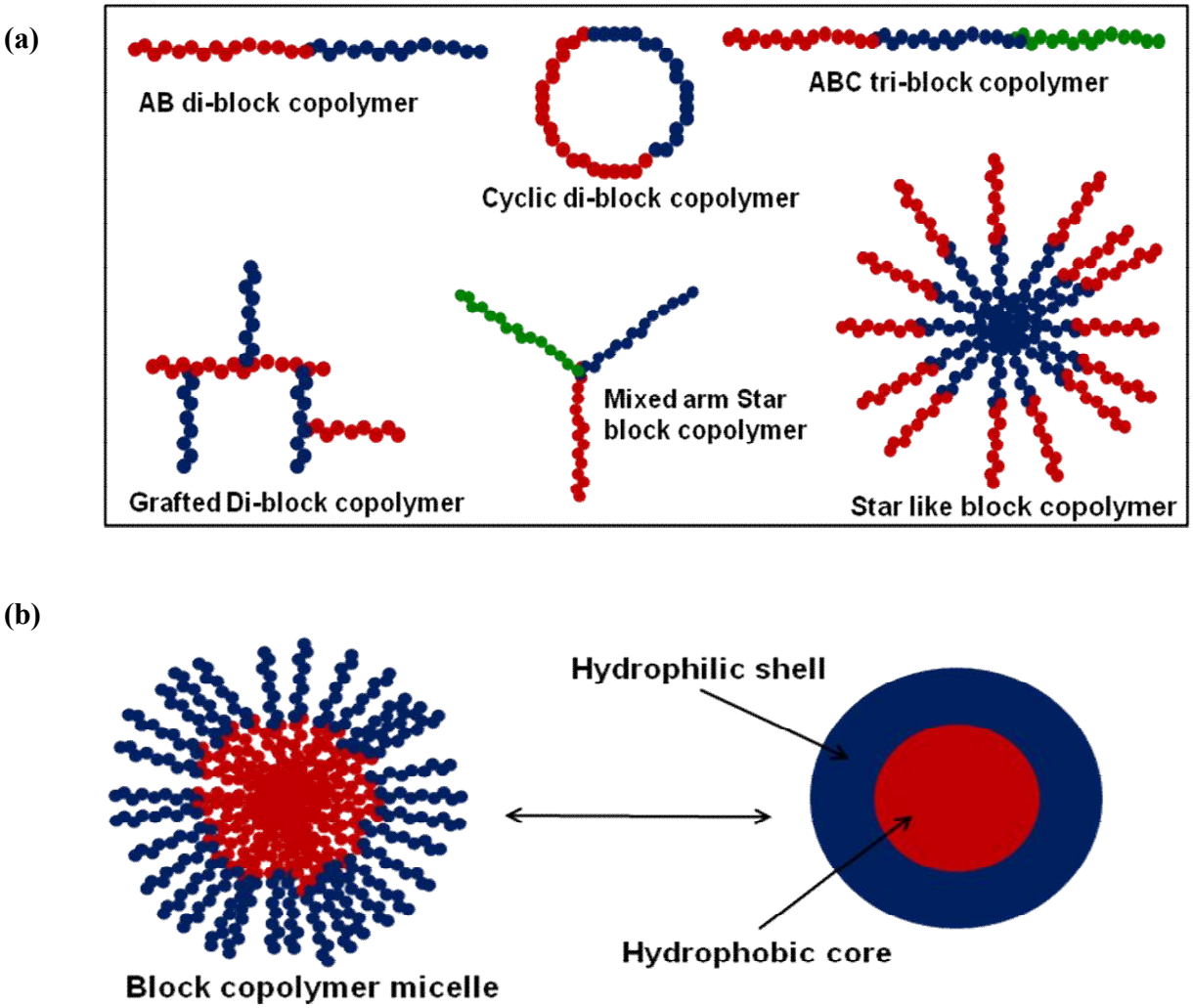

Figure 1.8. Examples of (a) different block copolymer architectures and (b) self-assembled amphiphilic block copolymers into supramolecular nanostructure (micelle) in solution.

Block copolymers are one of the types of copolymers composed of two or more chemically distinct polymer chains (blocks) linked together at one or more junction points usually through covalent bonds [58, 59]. In this way, they represent a sequence of different polymer blocks connected in series. These block copolymers can be classified based on the

number of blocks and their arrangements. For example, block copolymers consisting of two blocks are called diblock whereas those with three blocks are triblock and similarly that containing more than three are called multiblock copolymer. On the basis of arrangement, the block copolymers may be categorized as linear, star-like, mixed arm and grafted polymers [figure 1.8 (a)]. As a consequence of the distinct properties of different polymer segments, block copolymers are known to shown rich phase behavior. In solution, block copolymers will form micelles when the solvent is selective for one of the blocks. Amphiphilic block copolymers that contain hydrophilic (PEO) and hydrophobic (PPO) blocks, self-assemble in aqueous solution [figure 1.8 (b)] and are capable of generating a variety of micro domain morphologies with different physical and chemical properties. The micellization process for block copolymers is mainly governed by two parameters, critical micellization temperature (CMT) and critical micellization concentration (CMC). Self assembly will not occur if either of these is not reached to the critical value and the block copolymer will remain as unimers in the solution.

The interaction of silica nanoparticles with four different macromolecules (surfactant, protein, polymer and block copolymer) has been investigated in this thesis (figure 1.9). The three types of surfactants examined are, anionic sodium dodecyl sulphate (SDS), nonionic decaoxyethylene *n*-dodecylether ($C_{12}E_{10}$) and cationic dodecyltrimethyl ammonium bromide (DTAB). These surfactants comprise same tail length but differ in charge on their head group. A small globular protein lysozyme is used as a model protein. It has molecular weight about 14.7 kD and iso-electric point about 11.4. The interaction of nanoparticles is examined with polymer polyethylene glycol (PEG) having different molecular weights and tri-block copolymer P85 [$(EO)_{26}(PO)_{39}(EO)_{26}$]. The self-assembly of block copolymer is also used to tune the interaction of nanoparticle-block copolymer system.

(a) Surfactant

Anionic surfactant sodium dodecyl sulphate ($C_{12}H_{25}SO_4^-Na^+$)

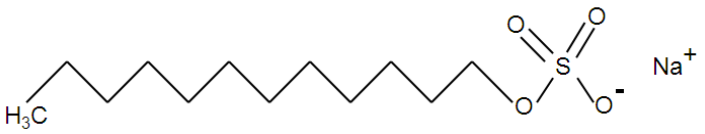

Cationic surfactant dodecyltrimethyl ammonium bromide [$C_{12}H_{25}N(CH_3)_3^+ Br^-$]

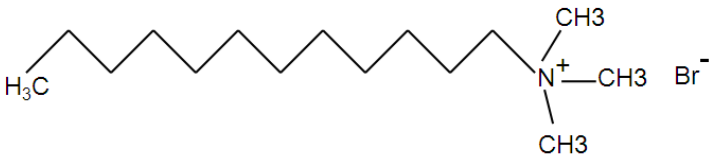

Non-ionic surfactant decaoxyethylene *n*-dodecylether [$CH_3(CH_2)11$ (CH2CH2O)10 OH]

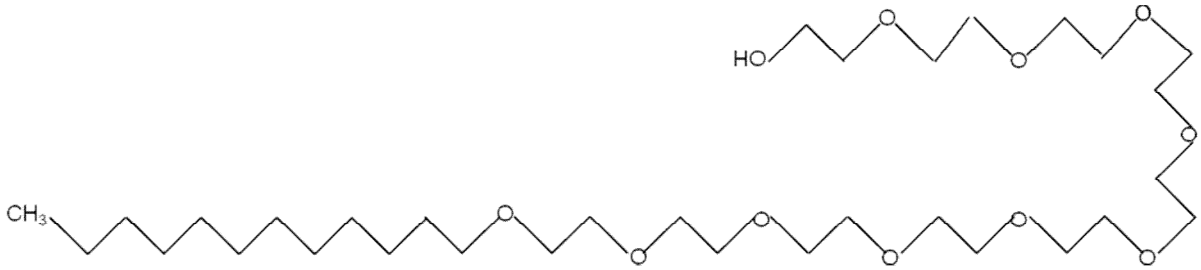

(b) Protein

Lysozyme

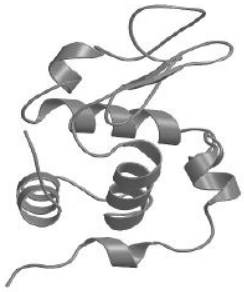

(c) Polymer

Polyethylene glycol
(H-(O-CH_2-CH_2)$_n$-OH)

(d) Block copolymer

P85 $[(EO)_{26}(PO)_{39}(EO)_{26}]$

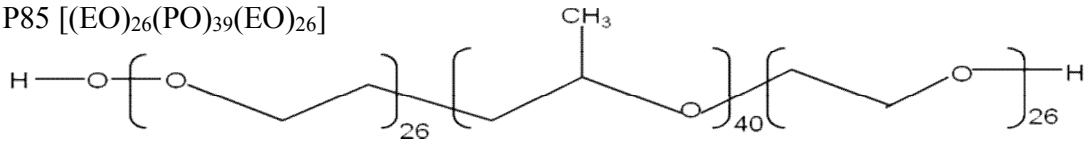

Figure 1.9. Chemical structures of different macromolecules used in this thesis (a) surfactants, (b) protein, (c) polymer and (d) block copolymer.

1.4. Important interactions in nanoparticle and macromolecule systems

The nanoparticles and macromolecules individually can interact through a number of forces depending on the solution conditions. These interactions not only govern the properties of nanoparticle and macromolecule but also dictate the phase behavior of their complex system. The control over interaction parameters essentially enables the integration of the two components, implementation of complex structures for desired functions and tuning of their properties. The commonly present interactions in nanoparticles and macromolecules are

(i) Electrostatic interaction: The electrostatic interaction determines the resultant force between charged particles. In the case, if the particles are suspended in water or any other suitable solvent, dissolved ions modify the nature of electrostatic interaction and hence instead of direct electrostatic (Coulomb force) interaction, one finds a screened Coulomb force between the charged objects [60-62]. For two spheres of radius R each having a charge Z (expressed in units of the elementary charge) separated by a center-to-center distance r in a fluid of dielectric constant ε containing a concentration n of monovalent ions, the screened Coulomb interaction is expressed as

$$\frac{V(r)}{k_B T} = Z^2 \lambda_B \left(\frac{\exp(\kappa R)}{1+\kappa R} \right)^2 \frac{\exp(-\kappa r)}{r} \tag{1.1}$$

where λ_B is the Bjerrum length and is given by $\lambda_B = \frac{e^2}{4\pi\varepsilon\varepsilon_0 k_B T}$ denoting the interparticle separation at which the electrostatic interaction between the particles is comparable to the magnitude of thermal energy $k_B T$. κ^{-1} is the Debye-Hückel screening length, which is expressed by $\kappa^2 = 4\pi\lambda_B n$. The strength of the force increases with the magnitude of the surface charge density or the electrical surface potential whereas range of the interaction is decided by the ionic strength of the solution [62].

The electrostatic forces are easily experienced in our daily life when hands are washed with soap, the skin becomes negatively charged by adsorption of soap molecules, and the slippery feeling is induced by the strongly repulsive screened Coulomb force. The electrostatic interaction between charged bodies (oppositely or similarly) is known to give rise to new types of versatile hybrid structures that have numerous advantages [22, 24, 63]. Many nonspecific associations especially relevant in biological systems (e.g. layer by layer self-assembly of nanoparticles and proteins in films, chromatin and protein complexes) are driven by electrostatic forces together with the other prominent processes such as formation of polyelectrolyte multilayer and coassembly of double hydrophilic block copolymers in the presence of oppositely charged species [22, 63-66].

The electrostatic forces are responsible for stability of charged colloids. According to DLVO theory the stability of a colloidal solution is determined by the sum of the van der Waals attractive (V_A) and screened Coulomb repulsive (V_R) interactions [62, 67, 68]. This theory proposes that there exists an energy barrier resulting from the repulsive force which prevents two particles approaching one another and adhering together. But if the particles collide with enough energy to overcome that barrier, the attractive force will pull them into contact where they adhere

strongly and irreversibly together. Therefore, for dispersion to resist against flocculation it is essentiality required to have sufficiently high repulsion, and the colloidal system then only will be stable. Figure 1.9 depicts the typical variation of the total interaction energy with particle separation according to DLVO theory.

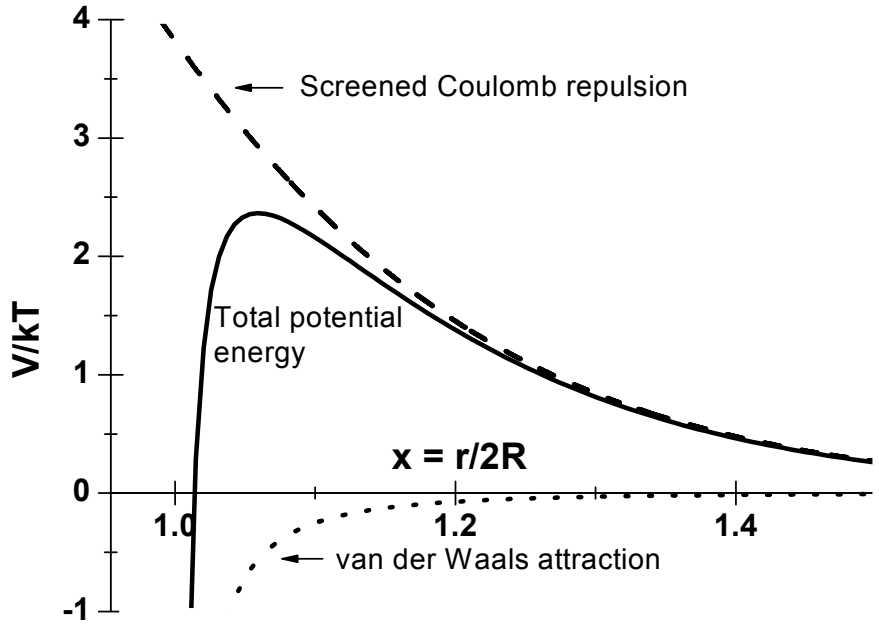

Figure 1.10. The variation of van der Waals attarctive, electrostatic repulsive interactions and total interaction energy in a charged colloidal solution.

(ii) Steric repulsion: The stability of colloidal particles can also be achieved by steric repulsion. The addition of macromolecules such as polymer, surfactant etc. on particle surface prevents the approach of the particle cores to a separation where their mutual van der Waals attraction would cause flocculation and the particles are said to be sterically stabilized. The origin of steric repulsion lie in both volume restriction and interpenetration effects, although it is unlikely that either effect would occur in isolation to provide a repulsive force [62, 69, 70]. The two polymer covered surfaces when approach (separation distance is less than R_g) each other

feels a repulsive interaction due to the overlap of the outer segments formed by polymer shells (figure 1.12). This repulsion results from the unfavorable entropy associated to the confinement of the polymer chains. The magnitude of the repulsion resulting from steric forces depends on the surface area of the particle occupied by the polymer and whether the polymer is reversibly or irreversibly attached to the particle's surface.

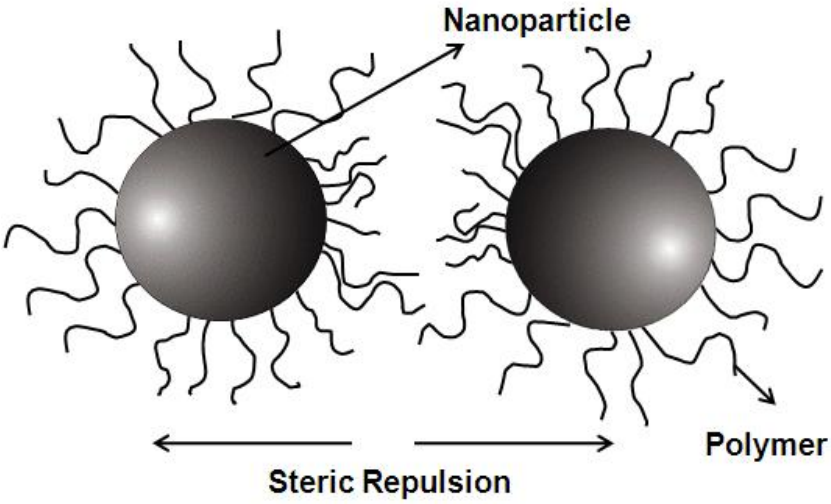

Figure 1.11. Two particles sterically repelling each other through adsorbed polymer layer.

Thermodynamically, steric effects are the manifestation of an entropic contribution to the overall free energy. These effects can dictate the reaction pathways and rates in chemical synthesis due the restricted configurations in which particles/molecules can collide and successfully react. Steric forces are of paramount importance in nanotechnology where nanostructures are stabilized by coating of macromolecules [71-73]. In many cases the adsorbed macromolecules not only stabilize the nanomaterials against aggregation but also perform functions those required for different applications. For example, polymers or biomolecules adsorbed on nanoparticles apart from stabilizing the particles also interact with cell membranes during targeted drug delivery. Moreover, the steric stabilization improves the particle

sustainability in the biological milieu thus allowing prolonged circulation in blood. The coating of polyethylene glycol (PEG) is known to improve the biocompatibility of the magnetic nanoparticles while utilized in sensing tumor [72, 73].

(iii) Depletion interaction: The polymers can either stabilize colloidal particles by adsorbing on them or can destabilize the particles by remaining free in the solution. The non-adsorbing nature of polymer usually induces depletion interaction between particles. The Depletion interaction is known to arise between large colloidal particles that are suspended in a solution of smaller entities such as polymers, when the latter experience an excluded volume interaction with the former [74, 75]. The first successful model to describe the depletion interaction between two hard spheres as induced by dilute non-adsorbing polymer was developed by Asakura and Oosawa [75]. According to their theory, the mechanism that is responsible for the attraction originates from the non-adsorbing nature of the smaller particles (depletants) giving rise to a depletion layer around colloidal particles. This depletion layer can be understood as a layer around the bigger particle where smaller particle can not be found (figure 1.13). The available volume for the smaller particles increases when the depletion layers overlap. It implies that the free energy of the smaller particles is minimized in the states for which the colloidal spheres are close together. The effect of this is just as if there were an attractive force between the spheres even while the direct colloid–colloid and colloid–polymer interactions may both be repulsive. The depletion interaction is purely entropic in nature and the manifestation of the second law of thermodynamics. The gain in translational entropy of the smaller particles, owing to the increased available volume, much greater than the loss of entropy from flocculation of the colloids results into an overall positive change in entropy.

Depletion interaction leads to a variety of phase transitions in multi-component systems. For example, interesting phase transitions like vesicle-to-micelle transition of block copolymers, colloidal aggregation through macromolecules, and re-entrant solidification in colloid-polymer systems are driven by depletion interaction [76-79]. The importance of depletion interaction in many biological systems and processes has been recognized. In presence of biological macromolecules like proteins or lipids, the effects of depletion force are observed in cell membrane interactions [80]. The depletion interaction is realized as one of the responsible forces in forming helical structure in biopolymers [81]. The casein micelles are found to be becoming attractive in presence of exocellular polysaccharides [82].

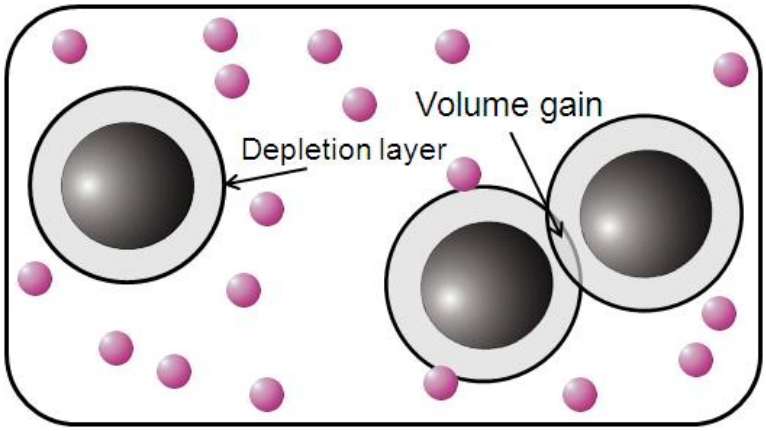

Figure 1.12. Schematic of origin of depletion interaction.

(iv) Hydrogen bonding: The hydrogen bonding is a weak type of dipole-dipole attraction which occurs when a hydrogen atom bonded to a strongly electronegative atom such as nitrogen, oxygen, fluorine etc. exists in the vicinity of another electronegative atom with a lone pair of electrons [62, 83]. The electronegative atom (bonded with hydrogen) attracts the electron cloud of the hydrogen atom and by decentralizing the cloud, leaves a partial positive charge on hydrogen atom while creates a small negative charge on itself. The resulting charge on hydrogen

atom, however only partial, represents a large charge density because of the small size of hydrogen relative to other atoms. A hydrogen bond arises when this strong positive charge attracts a lone pair of electrons on another electronegative atom. These hydrogen-bond attractions can occur between different molecules (intermolecular) or within different parts of a single molecule (intramolecular). The strength of the hydrogen bond is about 5 to 40 kJ/mole which makes them relatively stronger than a van der Waals interaction, but weaker than covalent or ionic bonds.

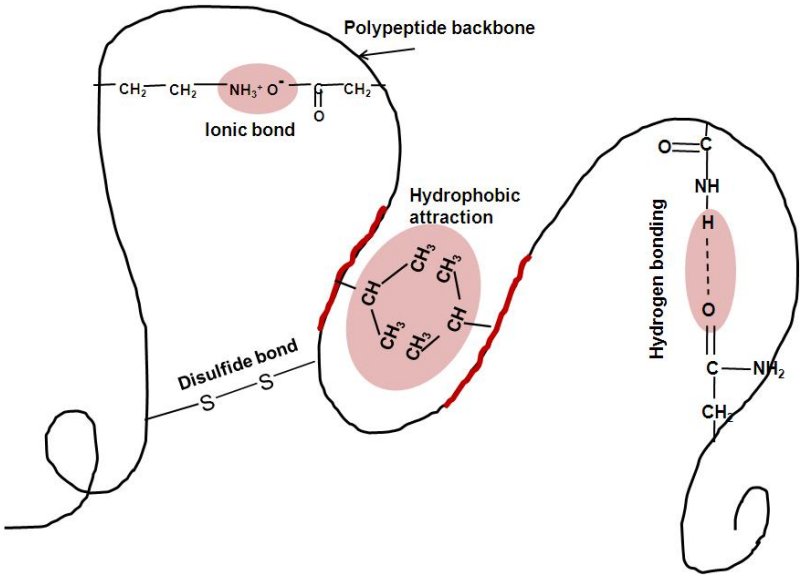

Figure 1.13. Representation of various interactions including hydrogen bonding and hydrophobic interaction.

The unique and novel characteristics of water arise because of its hydrogen bonded structure. Hydrogen bonding determines the secondary and tertiary structures as well as functions of many biological molecules like DNA, lipids and proteins including enzymes and antibodies [84]. The hydrogen bonding among others is responsible for the double helical structure of DNA where hydrogen bonding between base pairs join one complementary strand to

the other. The tertiary structure of protein molecules is attained by hydrogen bonding between the backbone oxygens and amide hydrogens of the secondary structure (figure 1.13). Many synthetic polymers such as nylon attain remarkable strength due to hydrogen bonded structure within them. The hydrogen bond enables polymers sensitivity towards humidity of the atmosphere because the diffusion of water molecules can disrupt the network.

(v) Hydrophobic interaction: Hydrophobic interactions describe the relations between water and non-polar molecules (hydrophobes) [62, 85, 86]. The water molecules have high inclination to form hydrogen bonds with each other and this tendency influences their interactions with non-polar molecules which are incapable of forming the hydrogen bonds. The presence of such a non-polar surface into water causes interruption in the hydrogen bonding network between water molecules. The hydrogen bonds thus reorients tangentially to such surface to minimize disruption of three dimensional network of water molecules leading to a structured water "cage" around the non-polar surface. As a result, the non-polar molecules experiences an effective attraction leading to their aggregation in order to reduce the surface area exposed to water to minimize their disruptive effect. The mixing of fat and water is a good example of this particular interaction. These forces are of supreme importance in understanding surface phenomena which dependent on the properties of the non-polar solute as well as solution conditions.

Hydrophobic interaction governs many processes occurring in macromolecules such as micelle formation, protein conformation and biological membrane structure [85, 86]. The amphiphilic molecules form self-assembled structures because of hydrophobic interaction. Along with hydrogen bonding, the hydrophobic forces also contribute in the formation of folded protein structure (figure 1.13). The hydrophobic patches of alkly chains in proteins form a core where the chains are buried from water. The protein molecules while interacting with nanoparticles are

reported to show the conformational changes possibly due to alteration in hydrophobic interactions. Similarly, other amphiphilic molecules have also been reported to show phase transitions in presence of nanoparticles. The lamellar phase formation in non-ionic surfactants has been shown to be controlled by presence of nanoparticles [87].

All or some of these forces may act in nanoparticle-macromolecule systems in a cumulative manner depending upon characteristics of nanoparticles and macromoelcules as well as solution conditions. In case of interaction of anionic silica nanoparticles with charge stabilized macromolecules (e.g. proteins, ionic micelles), the resultant interaction is pre-dominantly governed by electrostatic forces. In case if the macromolecule is uncharged, the resultant interaction is a combination of non-electrostatic forces. For examples, the changes in the hydrogen bonding or hydrophobic interaction present in the intermolecular structure of the macromolecule as induced by nanoparticles may lead to structural changes in the macromolecule. The adsorption of non-ionic surfactants (with groups like hydroxyl, phenolic, carboxylic) and polymers are known to driven through hydrogen bonding with variety of nanoparticles. The adsorbed macromolecules in general give rise to steric repulsion between nanoparticles. However, in many cases when macromolecules remain free, lead to depletion interaction driven phase transition in nanoparticle-macromolecule systems.

1.5. Techniques for the characterization of nanoparticle-macromolecule systems

In nanoparticle-macromolecule systems, the interest may lie in investigating the structural and interactional changes occurring in individual components as well as hybrid characteristics of their composites. For example, nanoparticle-surfactant system may either be examined for the stability of nanoparticles as influenced by surfactant or effect of nanoparticle on interfacial properties of surfactant or the resultant behavior of the complexes formed. Based

on the interest, the multi-components systems may be characterized by several techniques available in general for the characterization of materials, in one way or the other. The resulting information can be refined to yield images or spectra revealing the topographic, geometric, structural, chemical or physical details of the system. Different techniques providing complementary outcomes as per their sensitivity to the various physical parameters on different length scales are used. These techniques can be broadly classified into following four categories:

(i) Spectroscopic techniques: Optical spectroscopic techniques are means of studying the properties of the system by examining how the system emits and interacts with light. These techniques involve visible, ultraviolet and infrared light (alone or in combination) to extract the relevant information such as chemical compositions, bond strength and energy levels etc. The different techniques are usually based on absorption or emission of light by the material. Commonly used techniques include UV-visible spectroscopy, photoluminescence, infrared absorption and Raman scattering [20, 21, 24, 88]. While characterizing nanoparticle-macromolecule systems, the techniques generally look into the structural transitions and chemical bonding between the two components. For example, Raman and circular dichroism (CD) spectroscopy have been utilized to evaluate the extent of the protein deformation on interaction with nanoparticles [125]. Electron paramagnetic resonance (EPR) spectroscopy with spin–labeled proteins has been utilized to obtain insight into protein orientation on the nanoparticle surface [88]. Fluorescence spectroscopy has been adopted to investigate the self-assembly of the surfactants in adsorbed layers on particle surfaces and to obtain information on the polarity and viscosity of the interior of the layer as well as the aggregation number [20]. Electron spin resonance (ESR) spectroscopy and UV-Visible spectroscopy techniques have been used to calculate the adsorption isotherms of different macromolecules on nanoparticles [88].

(ii) Microscopic techniques: The microscopic techniques allow the direct visualization of the nanoparticle, macromolecules and their complex structures [89]. These techniques involves techniques like scanning electron microscopy (SEM), transmission electron microscopy (TEM), scanning tunneling microscopy (STM), and atomic force microscopy (AFM). The electron microscopic techniques involve interaction of electron beam with the specimen and the subsequent collection of transmitted or scattered electrons in order to create an image. This process may be carried out by scanning of a fine beam over the sample (e.g. scanning electron microscopy) or by wide-field irradiation of the sample (e.g. transmission electron microscopy). One major difference between SEM and TEM is that TEM detects transmitted electrons whereas SEM detects backscattered and/or secondary electrons. While both techniques can provide topological, morphological and compositional information about the sample, TEM can provide crystallographic information as well. On the other hand, scanning probe microscopy involves the interaction of a scanning probe with the surface of the object of interest. A common characteristic of these techniques is that an atom sharp tip scans across the specimen surface and images are formed by either measuring the current flowing through the tip or the force acting on the tip. These techniques are widely used to characterize nano-scale materials including nanoparticle-macromolecule complexes. The AFM has been used to characterize protein corona around nanoparticle-surface whereas nanoparticle-DNA has been investigated by TEM [90, 91]. The major disadvantage of these techniques is the requirement of dried or frozen samples where macromolecules in general lose their native structures.

(iii) Macroscopic techniques: These techniques are widely used to measure the abrupt variation of macroscopic properties which in turn indicates the changes in microscopic properties. The mostly used macroscopic techniques are zeta-potential measurements, rheology, conductivity

measurements etc. Such techniques explore the different bulk properties of the system and hence are useful for predicting overall behavior of the nanoparticle-macromolecule systems. For example, the zeta-potential measurements provide useful information about surface charge of the particles, nanoparticle stability as directed by macromolecules and iso-electric point of the mixed system [24, 88]. If macromolecule adsorb on nanoparticles, the extent of nanoparticle coverage can also be determined by zeta potential measurements [88]. On other hand, visco-elastic properties of the macromolecules as influenced by nanoparticles can be determined by rheology [24]. The transitions in phase behavior of amphiphilic molecules like block copolymers/surfactants in presence of nanoparticles have been observed by viscosity and conductivity measurements [93].

(iv) Scattering techniques: Scattering techniques constitute powerful probes for studying nanoparticle-macromolecule systems. These techniques measure the scattered intensity as a function of wave vector transfer [93-95]. Different techniques based on different radiations (light, X-ray and neutron) have been extensively used. The important techniques used are X-ray diffraction, light scattering (static light scattering and dynamic light scattering) and small-angle scattering (small-angle X-ray scattering and small-angle neutron scattering). In each of these techniques the radiation is scattered by a sample and the resulting scattering pattern is analyzed to provide information about the structure (shape and size), interaction, ordering in the sample etc. These techniques can be applied over a wide range of length scales from 1 to 1000 nm. The different techniques are often used as a complementary tool with each other, providing detailed information about the system. Dynamic light scattering has been utilized to measure the hydrodynamic properties of the complex system. Small-angle X-ray scattering (SAXS) is useful for studying nanoparticle-macromolecule interactions where in particular at least one of the

components has higher electron density (Z value). Small-angle neutron scattering (SANS) with its unique advantage of contrast variation has been used to study multi-component complex structures at various length scales [20, 23]. This technique has also been used to study the nanoparticle-macromolecule systems in the present thesis. The details of SANS technique are provided in chapter 2.

1.6. Applications of nanoparticle-macromolecule systems

The integration of nanoparticles (having unique electronic, optical, and chemical properties) with macromolecules (which display unique recognition, catalytic, and inhibition properties) gives rise to novel hybrid functional composites possessing synergetic properties and functions. The addition of nanoparticles and macromolecules not only allows alteration in physical properties of the individual components but also implement several new features. These new and novel characteristics of the composites have been utilized in a variety of industrial and technical fields covering from biotechnology to optics to electronics. Some of important applications of nanoparticle-macromolecule systems in different areas are:

(i) Medicine: Nanoparticles due to their size which can gain access to the cells have emerged as important players in modern medicine with clinical applications ranging from contrast agents in imaging to carriers for drug and gene delivery into tumors [96, 97]. Their application to the medicine mainly comprises two objectives, the detection of the diseases by nano-scale diagnostic devices and their cure through targeted delivery system (nanomedicine). Both of these objectives require interfacing of the nanoparticles with macromolecules to carry the drugs for targeted delivery and for utilizing their sensitivity (in case of biomolecules) towards living cells during diagnosis and cure [21]. It has been now well accepted that cellular responses to materials in a biological medium deals with the adsorbed biomolecule layer, instead of the material itself but it

is only nanoparticles which takes the drug or the sensing device to the target. A drug delivery system, named as nanocell, comprising a nuclear nanoparticle functionalized with PEGylated-lipid envelope has been shown to be successfully delivering the drug to the tumor site [97]. The magnetic iron oxide nanoparticles, interfaced with a chemotherapeutic agent and guided by external magnetic fields were used to complete tumor remission [98]. A silica nanoparticle-block copolymer composite is shown to be more useful for drug delivery system compare to pure polymeric micelles [99]. In case of diagnostic devices, several types of sensors based on nanoparticle-macromolecule complexes such as chemical sensor, optical sensors, magnetic sensors etc. have been realized. A chemical nose sensor composed of nanoparticle-polymer composites has been utilized for protein detection [100]. The silver nanoparticle based nanoscale optical biosensor has been developed in order to examine the interaction between antigens and antibodies [101]. Superparamagnetic iron oxide nanoparticles functionalized with different biomolecules were used for cancer detection as magnetic sensors [102].

(ii) Electronics: The current interests in the research field of nanometer scale electronics deals with three fundamental issues, the operation of small-scale devices, schemes leading to their realization and eventual integration into useful circuits [103]. The Studies on quantum dots as well as on other nanomaterials have confirmed an increasing role for charging effects as the device size diminishes [104]. However, the construction of nanoscale circuits remains problematic, largely due to the difficulties of achieving interelement wiring and electrical interfacing to macroscopic parts of the overall circuits. In this regard, nanoparticles functionalized with different macromolecules have become prominent candidates for nanoscale electronics as the attached macromolecule can drive electrical interfacing [105]. A nanometer sized silver wire attached with DNA skeleton has been used to connect the two gold electrodes

[103]. Also the nano-clusters composited with polymer chains have been utilized to control the electron transport between the electrodes [106]. Protein-mediated nanocrystal assembly has been demonstrated to be useful for flash memory fabrication [107]. In particular, the functionalized metal nanoparticles gathers additional attention in the electronics as they can display single-electron characteristics (e.g. quantized capacitance charging) and can be organized through external fields or through simple self-assembly methods. Nevertheless, in microelectronics and microsystems technology lithography, addition of nanosized ceramic fillers like SiO2 in to suitable photosensitive polymer based photo-resists improves the processing as well as resolution manifolds and enables the introduction of new electric properties [13].

(iii) Photonics: The surface geometry of nanoparticles (size, shape etc.) and the dielectric constant of the surrounding environment also play a crucial role in controlling the collective oscillations of the confined surface electrons (surface plasmon resonance) in metal nanoparticles [108, 109]. When a macromolecule interacts with these nanoparticles it alters the dielectric constant of the surroundings leading to the corresponding changes in the oscillation frequency of the electrons [13]. Consequently, optical properties of the nanoparticles (such as absorption and scattering) in presence of macromolecules show significant modifications which are being employed in various applications related to the photonics. For example, nanoparticles and polymer composites are shown to be useful for applications like solid state lighting, optical imaging and optical sensing. The large-area printings of optical gratings and 3dimensional photonic crystals have also been demonstrated using nanoparticle-polymer Composites [110]. Further, it has been shown that the infiltration of nanoparticle-macromolecule in planar photonic crystals offer the opportunity to tune the photonic band gap which can be utilized for developing tunable photonic crystal based devices and hybrid light emitting diodes [111]. The interaction of

bimolecular on the surface of nanoparticles has been exploited to develop optical biosensors, which operate based on optical properties such as localized surface plasmon resonance, surface-enhanced Raman scattering and surface-enhanced fluorescence [108].

(iv) Energy: Nanoparticle-macromolecule composites also find applications in the field of energy through the systems like solar cells and batteries [13]. The use of inorganic solar cells has been limited due to the high costs imposed by fabrication procedures and other technical parameters. On the other hand, as an alternative to low cost, the organic solar cells that use organic macromolecules mostly polymers suffer to the limitation of low efficiency due to the low intrinsic carrier mobilities or low charge transport. One way to overcome these limitations is to combine organic polymers with inorganic material [13]. The nanoparticles combined with with polymers provide one of the alternatives to improve the efficiency of the solar cells. It has been shown that composites of nanoparticles like SiO_2, Al_2O_3, or TiO_2 with solar cell conductive polymers like polyaniline (PANI) and polythiophene (PTP) not only improve the efficiency of the solar cells but also provide stability against photo degradation in contrast to the case of pure polymers [112, 113]. Further, the metal nanoparticles like Ag and Au incorporated with polymers are also used to ameliorate the light adsorption capacity of the polymer cells [114]. The electrical storage systems like primary and secondary batteries also represent one of the important subsections of the field energy which has gained a worldwide significance for portable electronic devices [115]. The progress in lithium batteries relies mostly on the improvements in the electrolyte. Solid polymer electrolytes in this regard offer best desirable properties such as solid-state construction, simplicity of manufacturing, a wide variety of shapes and sizes, a higher energy density and usually inflammable etc [13, 115].

(v) Food industry: The protective coatings and suitable packaging of the food items are of prime importance in food industry because of their potential for increasing the shelf life of many food products [116, 117]. The materials presently used for food packaging are non-degradable, therefore generating environment related problems. Now a day, several biopolymers being eco-friendly are exploited to develop food packaging material. However, the limitations of use of biopolymers are their poor mechanical and weak barrier properties. Addition of reinforcing compounds (fillers) into these polymer matrices improves their strength by forming composites, but most of these reinforced materials have poor matrix–filler interactions which tend to increase with decreasing filler dimensions. The use of Nanoparticles having proportionally larger surface provides one of the alternatives by favoring the filler–matrix interactions and improving the performance of the resulting material. Besides nano-reinforcements, nanoparticle-polymer composites can add multiple functions, such as antimicrobial activity, enzyme immobilization, biosensing, reduce the packaging waste, preservation of fresh foods, act as reservoirs for the controlled release functions of drugs or fungicides etc.

(vi) Miscellaneous: The nanoparticle-macromolecule composites have also numerous applications in other areas apart from the discussed above. The nanoparticle-surfactant complexes in particular are useful in the industry related with interfacial process such as oil recovery, emulsification, paints etc [20]. The nanoparticle-polymer systems have shown their usefulness in magnetic devices like magneto-switches, charge transport and shape memory devices [13]. The chemical reactivity and catalytic process can also be controlled by these complex structures [13]. Further, these composites can be designed to have anti-fungal and bacteriostatic properties creating large positive impact on our environment and show useful contribution in our environmental sustainability [116]. The composites also known to show varying mechanical, thermal and elastic properties such as strength, thermal expansion, transition

temperatures, elastic modulus etc. which can be of use as per requirements [13]. In all, the complexes of nanoparticle-macromolecule provide interesting systems to study them from the point of view of their wide range of fascinating applications.

1.7. Layout of the thesis

Many of the nanoparticle applications require their interfacing with macromolecules. The interfacing and resultant structure is decided by the various interactions such as electrostatic force, covalent, hydrogen bonding, non-polar and hydrophobic interactions in the system. The present thesis investigates evolution of interaction and structure of silica nanoparticles with different macromolecules (surfactant, protein, block copolymer and polymer) under varying solution conditions. These systems are characterized by small-angle neutron scattering (SANS), which is an ideal technique to study such multi-component systems. The thesis consists of seven chapters. In this chapter (chapter 1), a general introduction to nanoparticles and macromolecules, their possible interactions and applications have been presented. A brief discussion on different characterization techniques is also given in this chapter. The details of SANS technique and its usefulness are discussed in chapter 2. The Chapters 3 to 6 constitute results on the studies of silica nanoparticles interaction with different macromolecules namely surfactant, protein, block copolymer and polymer, respectively. The charged silica nanoparticles with varying size and different macromolecules with distinct properties are examined as model systems. The interaction and structure of nanoparticle with different charge state of surfactant is studied in chapter 3. Chapter 4 provides the study of protein adsorption on nanoparticles and their resultant structure. The depletion interaction between nanoparticles in presence of block copolymers is examined in chapter 5. Chapter 6 deals with the polymer dependent re-entrant phase behavior (one-phase to two-phase and back to one-phase) in nanoparticle-polymer system. The results of the thesis are summarized in chapter 7.

Chapter 2

SMALL-ANGLE NEUTRON SCATTERING (SANS) FOR CHARACTERIZATION OF MULTI-COMPONENT SYSTEMS

2.1. Introduction

The nanoparticles and macromolecules are known to be two important constituents of colloids. These systems are characterized by structures at mesoscopic length scales which are much larger than atomic or molecular scales [1, 2, 16, 50, 118]. Interestingly the properties of such systems at mesoscopic length scale govern the macroscopic behavior of individuals as well as their composite systems. There is a lot of recent interest to probe cause-and-effect relationship between inherent properties of individual components and their complexes. For this purpose, a reliable experimental technique providing detailed information about the system and a feedback data for system response towards external parameters is required. Most of the time a single technique is not sufficient and the outcomes from many techniques are required to be complemented in order to get a reasonable understanding of the system.

The nanoparticle-macromolecule systems are required to be investigated from the point of view of both research and applications. The objective could be investigation on effect of nanoparticles on macromolcues and/or effect of macromolecules on nanoparticles and/or properties of their complexes. The choice of technique for this purpose depends on research interest, application requirement, nature of the material, accessibility and ease of availability of

the method etc. As discussed in chapter 1, different techniques used to study these systems are broadly classified as macroscopic, spectroscopic, microscopic and scattering techniques. Macroscopic techniques provide information about the bulk properties of the system and hence are mostly useful to investigate the bulk behavior of one component as influenced by other. For examples, The interfacial properties of the surfactants or block copolymers as influenced by presence of nanoparticles have been examined by techniques like surface tension measurements, calorimetry etc [20, 119]. On the other hand, stability of nanoparticles as directed by macromolecules is studied by zeta potential measurements, turbidity measurements, sedimentation kinetics etc [88, 120]. The spectroscopic techniques mostly deal with structural transitions occurring in macromolecules due to the presence of nanoparticles and chemical bonding between macromolecule and nanoparticles. In case of nanoparticle-protein systems, techniques like circular dichroism (CD), nuclear magnetic resonance (NMR) and Raman spectroscopy are being utilized to observe the conformational changes occurred in the native protein structure as a result of their interaction with nanoparticle [88, 121]. The phase behavior of nanoparticle-macromolecule systems has been explored by various spectroscopic techniques like photon correlation spectroscopy, gel permeation chromatography etc. The Microscopic techniques such as transmission electron microscopy, scanning electron microscopy, atomic force microscopy etc. give the direct visualization of the morphology of the structures of nanoparticle-macromolecule complexes [89, 122]. The scattering techniques can provide details of evolution of interaction and resultant structures in these systems [20, 23, 120]. Each technique has its own advantages and disadvantages to get the required information under the given conditions.

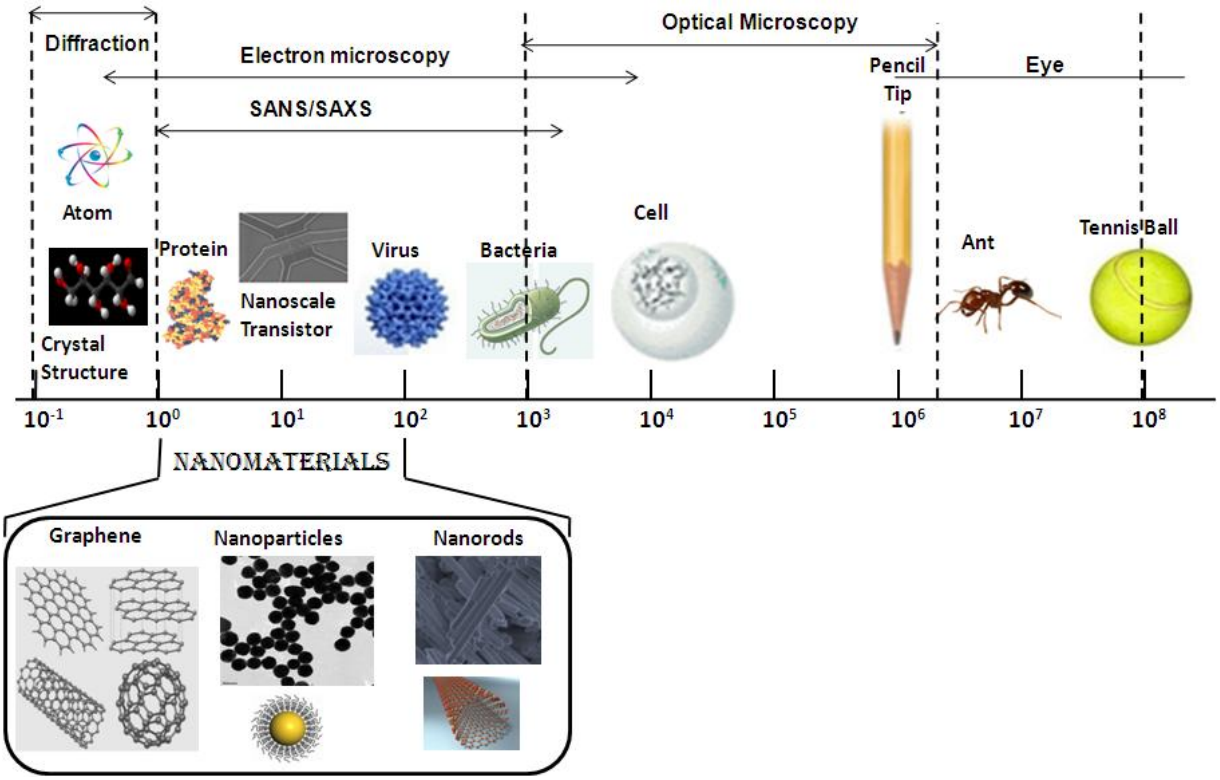

Figure 2.1. The various experimental techniques for microstructural characterization and the corresponding length scales.

Scattering techniques [e.g. light scattering (LS), small-angle x-ray scattering (SAXS) and small-angle neutron scattering (SANS)] are reliable for finding the particle size, shape, number density, interactions etc. In scattering techniques, intensity of scattered radiation due to interaction with the sample is measured as a function of angle [93-95, 123-125]. The probes in these techniques are light, x-rays or neutrons. Thermal neutrons used in neutron scattering are known to be useful probe for investigating the structure and dynamics of materials as they possess the wavelength compatible with interatomic spacings. In addition, the deeper penetration due to short-range nuclear interaction, isotope specific scattering and strong interaction with magnetic materials make them unique for condensed matter research. Neutron scattering consists of a whole family of techniques and SANS is one of the important techniques. This technique

can probe length scale those of nanoparticles and macromolecules (figure 2.1) with a unique advantage of contrast variation to make it more suitable for studying in particular their complexes. This chapter describes the details of SANS technique covering its theory, instrumentation and data analysis. The usefulness of SANS for characterizing nanoparticles and macromolecules in comparison with other complementary techniques such as SAXS, LS and TEM are also highlighted in this chapter.

2.2. Theory of SANS

Neutrons being quantum particles, show wave particle duality. This implies that neutrons may be diffracted by the structural arrangements of nuclei within the sample and this fact constitutes the basis for the neutron scattering. We consider incident neutron by a plane wave $\exp(i\mathbf{k}_i.\mathbf{r})$ travelling in the direction of $\mathbf{k}_i$. The scattered wave may be represented by a spherical wave as $-[f(\theta)/r]\exp(i\mathbf{k}_s.\mathbf{r})$, where $\mathbf{k}_i$ and $\mathbf{k}_s$ are incident and scattered wave-vectors, respectively (figure 2.2). The parameter f gives the scattering amplitude where ff^* describes the probability that an initial plan wave with amplitude unity will be scattered in a given direction. To calculate this probability, the following Schrodinger equation is solved:

$$\left(\frac{-\hbar^2}{2m}\nabla^2 + V(r)\right)\psi(\mathbf{r}) = E\psi(\mathbf{r}) \tag{2.1}$$

where $V(r)$ is Fermi pseudo-potential representing the interaction between neutron and nucleus and is expressed by

$$V(\mathbf{r}) = -\frac{2\pi\hbar^2}{m} b\delta(\mathbf{r}) \tag{2.2}$$

where b is scattering length representing the strength of nucleus neutron interaction and can be positive or negative. The neutron-nucleus interaction is isotropic in nature due to the small range

of nuclear potential compared to the wavelength of the neutron and varies somewhat randomly throughout the periodic table.

Using the first Born approximation, the following solution is obtained [124]

$$\psi(\mathbf{r}) = exp(i\mathbf{k}_i.\mathbf{r}) + \frac{exp(i\mathbf{k}_s.\mathbf{r})}{r}\frac{m}{2\pi\hbar^2}\int exp(-i\mathbf{k}_s.\mathbf{r}_1)V(\mathbf{r}_1)exp(i\mathbf{k}_i.\mathbf{r}_1)d\mathbf{r}_1 \quad (2.3)$$

where first and second terms correspond to the incident and scattered neutron beams, respectively. The comparison with the outgoing spherical wave reveals

$$f = \frac{m}{2\pi\hbar^2}\int exp(-i\mathbf{Q}.\mathbf{r}_1)V(\mathbf{r}_1)d\mathbf{r}_1 \quad (2.4)$$

where $\mathbf{Q} = \mathbf{k}_i - \mathbf{k}_s$ is wave vector transferred in the scattering. For elastic scattering, the incoming and outgoing wave vectors are related as $k = |\mathbf{k}_i| = |\mathbf{k}_s|$. The magnitude of wave-vector transferred in the scattering thus is given by

$$Q = |\mathbf{Q}| = |\mathbf{k}_i - \mathbf{k}_s| = (4\pi\sin\theta)/\lambda, \quad (2.5)$$

where λ is the wavelength of the probing radiation and 2θ is the scattering angle. The wave vector transfer Q and real space dimension d is reciprocal to each other. This implies that determination of structure at larger length scales require scattering intensity measurement at smaller Q or smaller θ values

The scattering amplitude using Fermi pseudo potential in equation 2.4 is given by

$$f = -b \quad (2.6)$$

The differential scattering cross section or the probability of the neutron being scattered in the solid angle dΩ can be defined as [124]

$$\frac{d\sigma}{d\Omega} = \frac{No.\ of\ neutrons\ scattered\ per\ unit\ time\ per\ unit\ solid\ angle}{Incident\ flux} = b^2 \quad (2.7)$$

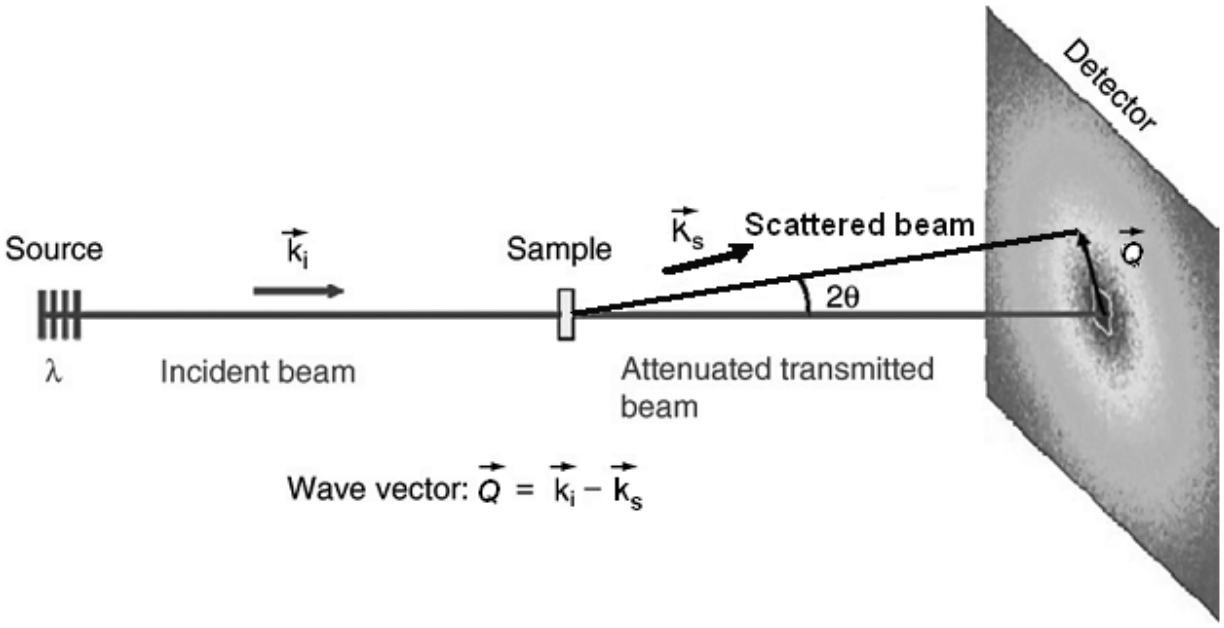

Figure 2.2. Schematic of a neutron scattering experiment.

The integral scattering cross-section for a nucleus is thus given by $\sigma = 4\pi b^2$and it can be looked as an effective area presented by the nucleus (scatterer) to the incident radiation.

For a single scatterer in a sample differential scattering cross-section is given by [124, 126]

$$\frac{d\sigma}{d\Omega}(Q) = \left| b \exp(-i\mathbf{Q}.\mathbf{r}) \right|^2 \tag{2.8}$$

However, for an assembly of scatterers in a macroscopic sample, microscopic differential scattering cross section can be obtained by summing over all the scattering centres

$$\frac{d\sigma}{d\Omega}(Q) = \left\langle \left| \sum b_j \exp(-i\mathbf{Q}.\mathbf{r}_j) \right|^2 \right\rangle \tag{2.9}$$

where $\mathbf{r}_j$ is the position vector of the j^{th} scatterer in the sample and the bracket represents an average over all the possible orientations. In SANS, one studies large scale heterogeneities

rather than locating the individual scattering centers, the individual scattering length b_j therefore can be replaced by locally averaged scattering length density $\rho(r)$ so that

$$\frac{d\sigma}{d\Omega}(Q) = \left\langle \left| \int \rho(\mathbf{r}) \exp(-i\mathbf{Q}.\mathbf{r})\, d\mathbf{r} \right|^2 \right\rangle \tag{2.10}$$

where $\rho(\mathbf{r})$ is defined as $\rho(\mathbf{r}) = \frac{1}{V(\mathbf{r})} \sum_j b_j$ and the summation is carried over all the scatterers in volume element $V(\mathbf{r})$ around $\mathbf{r}$.

If the inhomogeneities and the matrix are considered to have homogeneous composition with scattering length densities denoted by ρ_p and ρ_m, respectively, then the equation 2.10 can be written as

$$\frac{d\sigma}{d\Omega}(Q) = \left\langle \left| \rho_p \int_{V_{ptot}} \exp(-i\mathbf{Q}.\mathbf{r}) d\mathbf{r} + \rho_m \int_{V_{mtot}} \exp(-i\mathbf{Q}.\mathbf{r}) d\mathbf{r} \right|^2 \right\rangle \tag{2.11}$$

where the integration in the first term is over the volume V_{ptot} occupied by all particles and that in the second term is over the volume V_{mtot} occupied by the matrix. The equation can be rewritten as

$$\frac{d\sigma}{d\Omega}(Q) = \left\langle \left| (\rho_p - \rho_m) \int_{V_{ptot}} \exp(-i\mathbf{Q}.\mathbf{r}) d\mathbf{r} + \rho_m \left[\int_{V_{mtot}} \exp(-i\mathbf{Q}.\mathbf{r}) d\mathbf{r} + \int_{V_{ptot}} \exp(-i\mathbf{Q}.\mathbf{r}) d\mathbf{r} \right] \right|^2 \right\rangle \tag{2.12}$$

The uniform integration in the second term of the above equation behaves like a delta function and only contributes for Q value of the order of (sample dimensions)$^{-1}$and may be neglected for $Q \neq 0$ for all practical purposes. After neglecting the second term, the above equation becomes

$$\frac{d\sigma}{d\Omega}(Q) = (\rho_p - \rho_m)^2 \left\langle \left| \int_{V_{ptot}} \exp(-i\mathbf{Q}.\mathbf{r}) d\mathbf{r} \right|^2 \right\rangle \tag{2.13}$$

The macroscopic differential scattering cross section ($d\Sigma/d\Omega$) can be obtained by normalizing to the irradiated sample volume (V_{sample}) and hence

$$\frac{d\Sigma}{d\Omega}(Q) = \frac{(\Delta\rho)^2}{V_{sample}} \left\langle \left| \int_{V_{ptot}} \exp(-i\mathbf{Q}.\mathbf{r}) d\mathbf{r} \right|^2 \right\rangle \tag{2.14}$$

If N_p is the number of inhomogeneities and V_p is the average volume of a single particle then $V_{ptot} = N_p V_p$ provided all the inhomogeneities are identical. Here $(\Delta\rho)^2 = (\rho_p - \rho_m)^2$ is called the scattering length density contrast or simply contrast factor and it is one of the most important sample parameters in SANS studies. It is evident that with a good contrast value, the inhomogeneities are perceived clearly by the probing radiation while at low value of this factor the inhomogeneities appear to be smeared. The equation 2.14 can be rewritten as

$$\frac{d\Sigma}{d\Omega}(Q) = \frac{(\rho_p - \rho_m)^2}{V_{sample}} V_p^{\,2} \left\langle \left| \sum_k F_k(\mathbf{Q}) \exp(-i\mathbf{Q}.\mathbf{r}_k) \right|^2 \right\rangle \tag{2.15}$$

where, $\mathbf{r}_k$ is the position vector of the center of the k_{th} inhomogeneity and $F_k(\mathbf{Q})$ is the form factor associated with that particle. From the above equation $F(\mathbf{Q})$ can be expressed as

$$F(\mathbf{Q}) = \frac{1}{V_p} \int_{V_p} \exp(-i\mathbf{Q}.\mathbf{r}) d\mathbf{r} \tag{2.16}$$

and is normalized so that $|F(0)|^2 = 1$

For a mono-dispersed system, i.e., when all the particles posses identical shape as well as size, equation 2.15 can be expressed as

$$\frac{d\Sigma}{d\Omega}(Q) = \frac{N_p(\rho_p - \rho_m)^2 V_p^{\,2}}{V_{sample}} \left\langle |F(\mathbf{Q})|^2 \right\rangle . \frac{1}{N_p} \left\langle \left| \sum_k \exp(-i\mathbf{Q}.\mathbf{r}_k) \right|^2 \right\rangle \tag{2.17}$$

$$\frac{d\Sigma}{d\Omega}(Q) = \frac{N_p(\rho_p - \rho_m)^2 V_p^{\,2}}{V_{sample}} P(Q)\, S(Q) \tag{2.18}$$

where

$$P(Q) = \left\langle \left| F(\boldsymbol{Q}) \right|^2 \right\rangle \tag{2.19}$$

and

$$S(Q) = \frac{1}{N_p} \left\langle \left| \sum_k \exp(-i\boldsymbol{Q}.\mathbf{r}_k) \right|^2 \right\rangle = 1 + \frac{1}{N_p} \left\langle \sum_k \sum_{k'} \exp(i\boldsymbol{Q}.(\mathbf{r}_k - \mathbf{r}_{k'})) \right\rangle \tag{2.20}$$

$P(Q)$ is known as intraparticle structure factor while $S(Q)$ is called interparticle structure factor. It is evident from the expressions that $P(Q)$ depends on the shape and size of the inhomogeneities while the form of $S(Q)$ is determined by the interparticle correlation. In terms of the volume fraction ($n = N_p V_p / V_{sample}$) of the inhomogeneities, this equation becomes [123-126]

$$\frac{d\Sigma}{d\Omega}(Q) = n\ (\rho_p - \rho_s)^2 V_p P(Q) S(Q) \tag{2.21}$$

The typical functionality of $P(Q)$, $S(Q)$ and $d\Sigma/d\Omega$ as a function of Q are plotted in figure 2.3

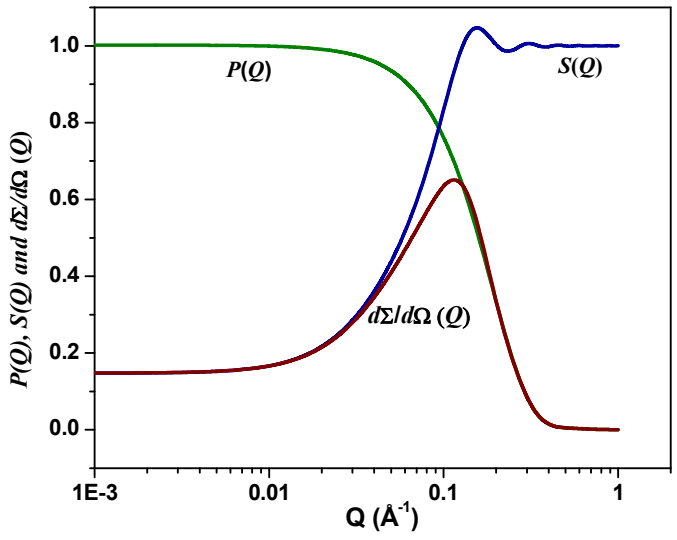

Figure 2.3. Typical plots of $P(Q)$, $S(Q)$ and $d\Sigma/d\Omega$ (Q).

Uptill now, the assumption has been that the system is monodispersed i.e. the shape as well as size of the inhomogeneities in the system under consideration are identical. However, in reality, the inhomogeneities in most cases are not strictly monodispersed in size and/or shape but polydispersed in nature. Size polydispersity can be expressed in terms of a distribution function $f(R)$. In case of a polydisperse system, the $d\Sigma/d\Omega$ can be expressed as [173]

$$\frac{d\Sigma}{d\Omega}(Q) = \int \frac{d\Sigma}{d\Omega}(Q,R)\, f(R)\, dR + B \tag{2.22}$$

The size distributions commonly used are Gaussian distribution, Schultz distribution and log-normal distribution [127-129].

The Gaussian distribution $f(R)$, a symmetric continuous probability function, for particles having radius R is given by

$$f(R) = \frac{1}{\sigma\sqrt{2\pi}} exp\left[-\frac{(R - R_m)^2}{2\sigma^2} \right] \tag{2.23}$$

where R_m and σ are mean radius and standard deviation, respectively.

The Schultz distribution function for polydispersity of particle with radius R is accounted by distribution function given by

$$f(R) = \left(\frac{Z+1}{R_m} \right)^{Z+1} R^Z \; exp\left[-\left(\frac{Z+1}{R_m} \right) R \right] \frac{1}{\Gamma(Z+1)} \tag{2.24}$$

where R_m is the mean value of distribution and Z is the width distribution. The polydispersity of this distribution is given by $\Delta R / R_m = 1/\sqrt{Z+1}$.

In case of log-normal size distribution, f(R) is given by [26]

$$f(R) = \frac{1}{R\sigma\sqrt{2\pi}} \exp\left[-\frac{\left(\ln R/R_{med} \right)^2}{2\sigma^2} \right] \tag{2.18}$$

where R_{med} and σ are the median radius and standard deviation respectively. The mean and median values are related as $R_m = R_{med} \exp(\sigma^2/2)$.

The Schultz and log-normal distributions possess a long tail in the higher R region and hence more suitable for practical purposes.

2.2.2. Determination of intraparticle structure factor

For some of the regular shapes, having an axis of symmetry, the analytical expressions for $P(Q)$ are available in literatures [124, 127]. It is assumed that the particles are randomly oriented in the sample so that the theoretical form factors for anisotropic particles have to be averaged over all orientations. $P(Q)$ expressions for some standard shapes are given below:

Spherical particle: For spherical particle of radius R and having uniform scattering length density the $P(Q)$ is given as

$$P(Q) = \left[\frac{3(\sin QR - QR\cos QR)}{(QR)^3} \right]^2 \tag{2.26}$$

Figure 2.4 shows the functional form of $P(Q)$ for spherical particles of radii 25, 50 and 100 Å. The width of distribution gets narrowed as the size of the particle increases. The oscillations in the high Q region (observed when plotted on log-log scale) are the form factor oscillations whose maxima are analogous to the bright fringes in interference pattern.

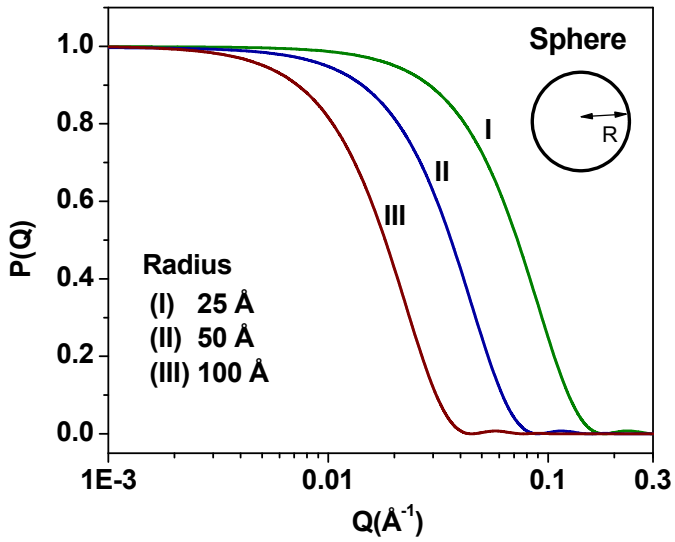

Figure 2.4. $P(Q)$ plots of a spherical particle with varying radius.

Ellipsoidal particle: The expression for $P(Q)$ of prolate ellipsoidal particle with semi-major axis a and semi-minor axis $b = c$ is given by

$$P(Q) = \int_0^1 F\left(Q,\mu\right)^2 d\mu \tag{2.27}$$

where $F(Q,\, x) = \dfrac{3(sin\, x - x\cos x)}{x^3}$ in this $x = Q\left[a^2\mu^2 + b^2\left(1-\mu^2\right)\right]^{\frac{1}{2}}$ and μ is the cosine of the angle between the direction of major axis a and wave vector transfer Q. For oblate ellipsoid (b=c>a), a and b can be interchanged in above equations.

Figure 2.5 shows dependence of $P(Q)$ for ellipsoidal particles of semi-major axes 25, 50, and 100 Å while the semi-minor axis is being fixed at 25 Å. The width of distribution gets narrowed as the size of the semi-major axis increases and also the distributions tend to overlap at higher Q values which are decided by the semi-minor axis.

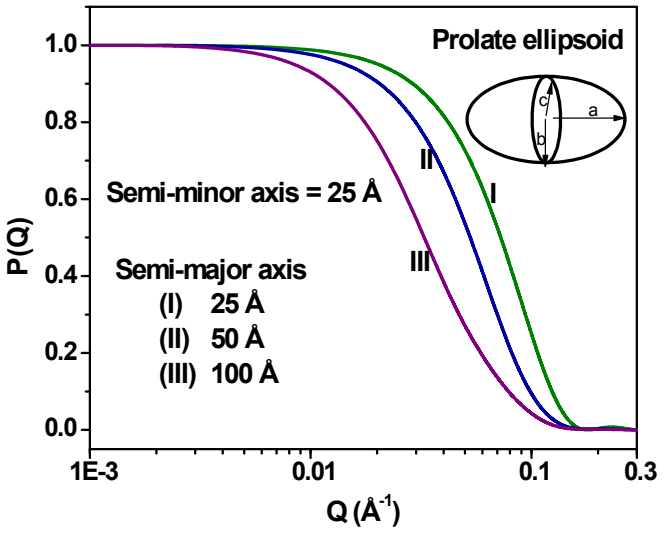

Figure 2.5. $P(Q)$ dependence of prolate ellipsoidal particles as the semi-major axis is varied.

Spherical shell (core-shell particle): The $P(Q)$ for spherical shell with inner radius R_1 and outer radius $R_2 = R_1+t$, where t is shell thickness obtained by subtracting the empty core of radius R_1 from sphere of radius R_2 with proper weighting by the volumes. Therefore, $P(Q)$ for spherical shell is written as

$$P(Q) = [(\rho_{core} - \rho_{shell})V_1 \frac{3j_1(QR_1)}{QR_1} + (\rho_{shell} - \rho_m)V_2 \frac{3j_1(QR_2)}{QR_2}]^2 \qquad (2.28)$$

where ρ_{core}, ρ_{shell} and ρ_m are the scattering length densities of core, shell and solvent, respectively, j_1 is first order Bessel function.

Figure 2.6 shows functional form of $P(Q)$ for spherical shell with inner radius 25 Å and thickness 5 Å. The distribution for shell is compared with those with spherical particles of radii 25 and 30 Å. The shell has the lowest width and also shows the oscillations of much higher magnitude than those for spherical particles.

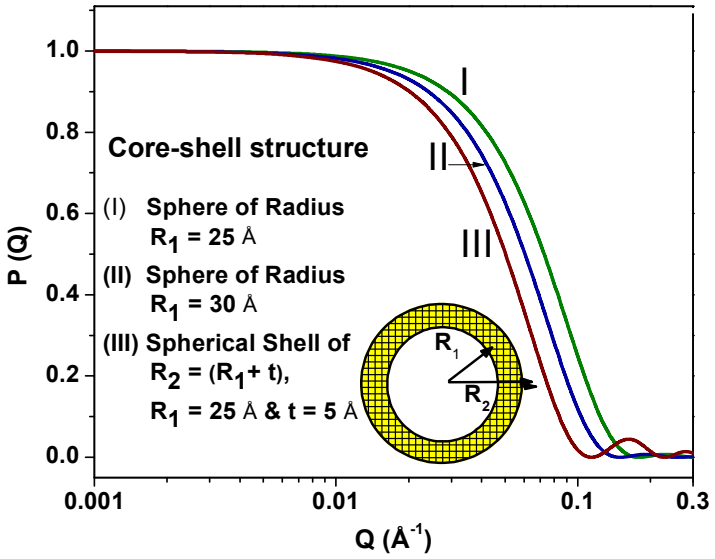

Figure 2.6. *P*(*Q*) plots for a spherical shell as compared with the spherical particle.

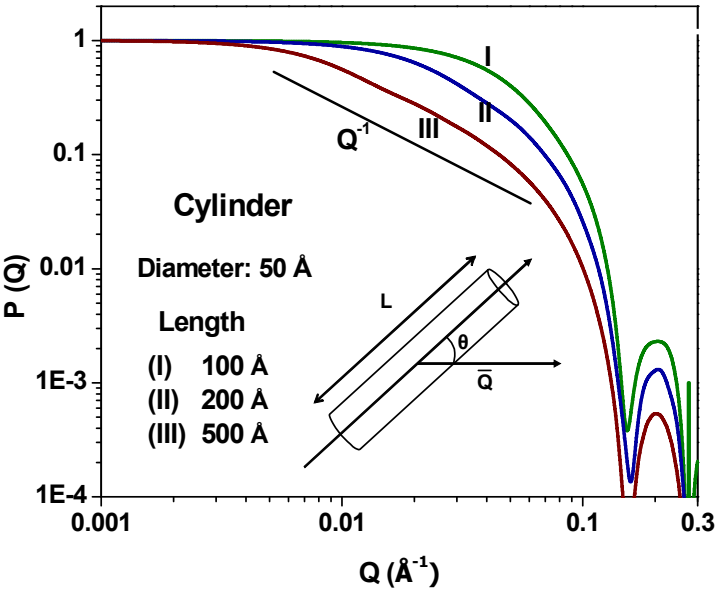

Figure 2.7. *P*(*Q*) plots for cylinders of different lengths and fixed radius.

Cylindrical particle: The $P(Q)$ of randomly oriented cylindrical particles with the radius R and length L (=2l) is given by

$$P(Q) = \int_0^{\pi/2} \frac{4 j_1^2(QR\sin\theta)}{Q^2R^2\sin^2\theta} \frac{\sin^2(Ql\cos\theta)}{Q^2l^2\cos^2\theta} \sin\theta d\theta \tag{2.29}$$

where j_1 (x) is first order Bessel function and θ is the angle subtended by the principal axis of the cylinder with Q.

Figure 2.7 shows the $P(Q)$ variation for cylindrical particles of different lengths and a fixed radius 25 Å. As the length of the particle increases $P(Q)$ on log-log scale shows a linear region in the intermediate Q range $1/l < Q < 1/R$. The slope of the linear region is -1.

Disc-like particle: The small-angle scattering technique can differentiate between cylindrical (rod-like) particles and disc-like particles. The form factor for a disc is given by the same equation as that for a rod (equation 2.29) with the diameter having much larger than the thickness. Unlike for a rod-like particle, $P(Q)$ for a disc-like particle has a slope of -2 in the intermediate Q range. Figure 2.8 depicts the form factor for disc-like particles of a constant thickness but varying diameter.

Figure 2.9 compares $P(Q)$s of spherical, rod-like and disc-like particles. The slope of the curves in a particular Q range depends on the shape of the particle and this method is commonly used to get the information on the shape of the particle.

Gaussian coil: The form factor of Gaussian chain coils with the radius of gyration R_g is given by

$$P(Q) = 2\frac{\exp(-Q^2R_g^2) + Q^2R_g^2 - 1}{(Q^2R_g^2)^2} \tag{2.30}$$

The form factor of Gaussian chains is usually used model the polymer molecules. $P(Q)$ for Gaussian chains show a slope of -2 at higher Q values. The form factos for different R_g are shown in figure 2.10. The cutoff of $1/Q^2$ dependence in the low Q region shifts towards low Q value with increasing R_g.

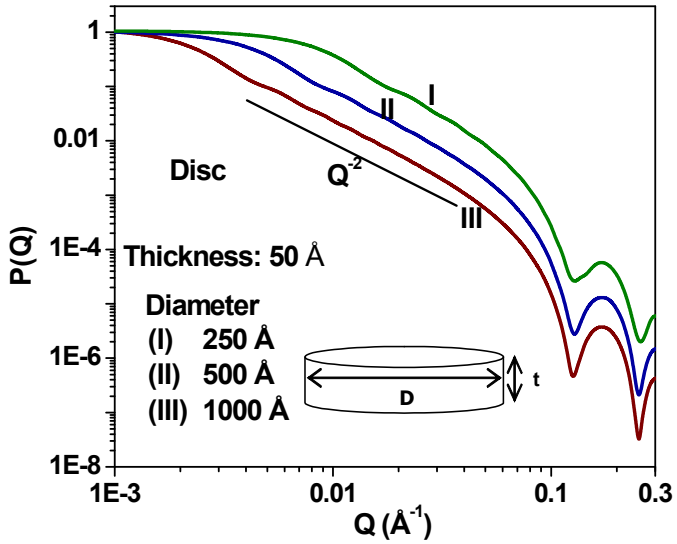

Figure 2.8. $P(Q)$ for disc-like particles of different diameters and fixed thickness.

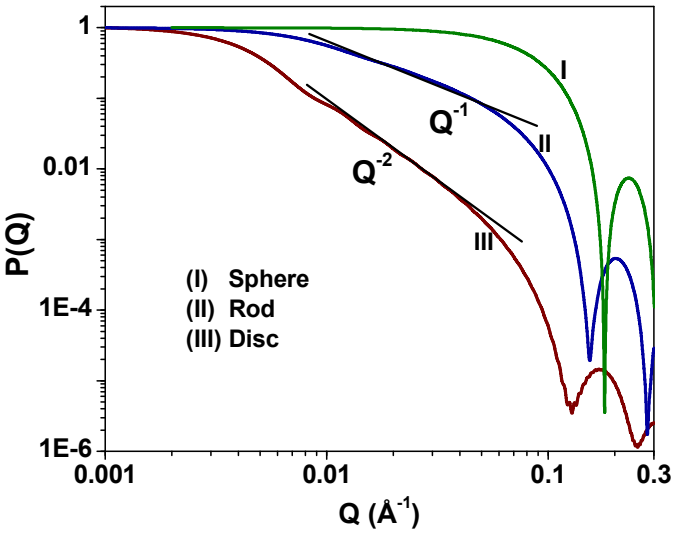

Figure 2.9. Comparison of $P(Q)$ plots for different shapes of the particles.

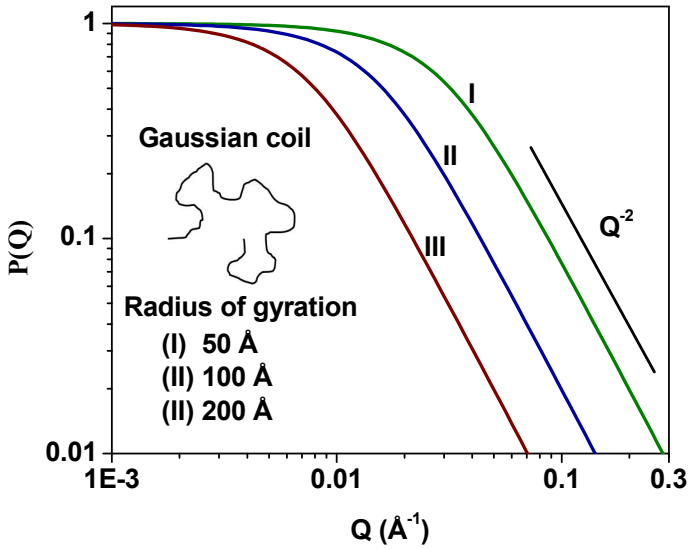

Figure 2.10. $P(Q)$ for Gaussian coil model of different radii of gyration.

Irrespective of the shape of the particles, $P(Q)$ can be written in simple forms for limited Q range. The most important of these simple forms are the Guinier approximation and the Porod law.

Guinier approximation: For a system of randomly oriented inhomogeneities of any arbitrary shape, $P(Q)$ can be approximated for small enough Q ($QR_g < 1$) as a form of Gaussian function such $P(Q)$ decreases exponentially with Q^2 [130]. This is known as Guinier approximation

$$P(Q) = \exp(-\frac{Q^2 R_g^{\ 2}}{3}) \tag{2.31}$$

where R_g is the radius of gyration of the inhomogeneity and gives an intuitive measure for the spatial extension of the particle. R_g can be found out from the slope of the log [$P(Q)$] v/s. Q^2 plot. It is defined as the mean square distance from the center of the gravity where the scattering length plays role of mass i.e.

$$R_g^{\ 2} = \frac{\int \rho(r) r^2 dr}{\rho(r) dr} \tag{2.32}$$

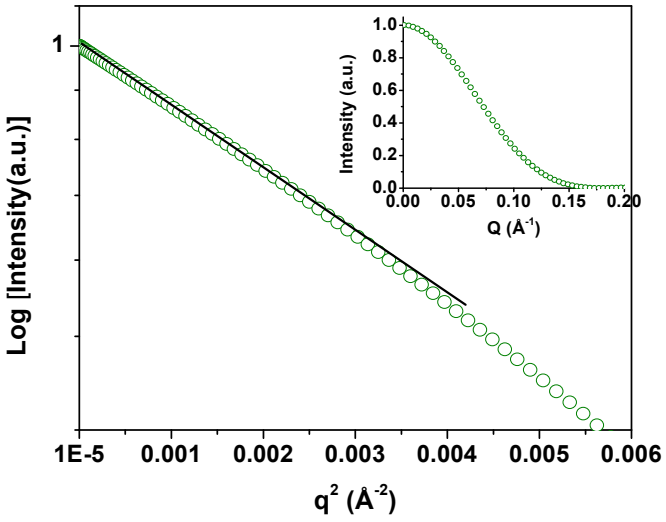

Figure 2.11. Guinier plot for a dilute system of spherical particle. Inset shows $P(Q)$ of the spherical particle.

For spherical homogeneity of radius R, the radius of gyration

$$R_g^{\,2} = \frac{3}{5}R^2 \tag{2.33}$$

Figure 2.11 shows a Guinier plot for a dilute system having spherical particles of radius 25 Å. The plot of logarithm of the scattering intensity versus Q^2 shows a straight line in low Q region and the slope gives the radius of gyration of the particle. The Guinier approximation offers the simplest, most straightforward and fairly reliable approximation to SANS for small enough Q values.

Porod law: Porod law states that for inhomogeneies with sharp boundary and uniform scattering length density, at large value of Q, $P(Q)$ can be approximated as [131]

$$P(Q) \sim \frac{2\pi S}{V}\frac{1}{Q^4} \tag{2.34}$$

where S is the surface area of the inhomogeneity. The differential cross section becomes (figure 2.12)

$$\frac{d\Sigma}{d\Omega}(Q) = \frac{2\pi N_p}{V_{sample}}(\rho_p - \rho_m)^2 S \frac{1}{Q^4} \tag{2.35}$$

Hence the total surface area of the inhomogeneities bathed in the beam can be extracted from the slope. However this is possible only when the scattering intensity $I(Q)$ is expressed in absolute scale.

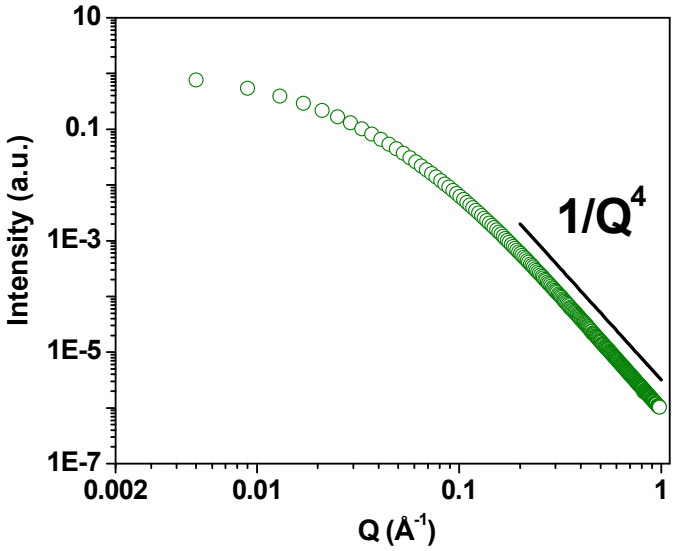

Figure 2.12. Scattering intensity at large Q values (QR > 5) for particles obeying Porod law.

2.2.2. Determination of interparticle structure factor

$S(Q)$ depends on the correlation of the particles and hence interaction between the particles. In general, $S(Q)$ shows several maxima and minima of decreasing amplitude. The first peak in $S(Q)$ occurs at $Q_{max} \sim 2\pi/d$, where d is the average distance between the particles. For an isotropic system, $S(Q)$ can be written as [127, 132]

$$S(Q) = 1 + 4\pi n \int [g(r) - 1] \frac{\sin Qr}{Qr} r^2 dr \tag{2.36}$$

where $g(r)$ is the radial distribution function. It is the probability of finding another particle at a distance r from a reference particle centered at the origin. The details of $g(r)$ depend on the interaction potential $U(r)$ between the particles. Thus, one has to have the knowledge of $U(r)$ for calculating $S(Q)$. This in turn implies that the measured $S(Q)$ can be used to obtain information about the interaction potential $U(r)$.

The statistical description of colloidal solutions treats the solutions in terms of a single component model. The major accountables of the model are the particles and the effect of solvent (with or without ions) introduced via an effective interaction potential $U(r)$.

$U(r)$ could consist of several terms such as (i) hard sphere term $U_{hs}(r)$, (ii) van der Waals attractive term $U_{vw}(r)$, (iii) solvent mediated term $U_s(r)$ and (iv) Coulomb repulsion term $U_c(r)$. It is thus possible to calculate $g(r)$ or $S(Q)$ for these solutions using methods which have been developed for liquids. The $g(r)$ is related to the total correlation $h(r)$ between the two particles separated by distance r as

$$g(r) = 1 + h(r) \tag{2.37}$$

The radial distribution function for a pair of scattering particles with no internal structure separated by a distance r is called $g(r)$. The $g(r)$ is related to the interparticle interaction potential $U(r)$ as follows:

$$g(r) = \exp(-U(r)/k_B T) \tag{2.38}$$

where k_B is the Boltzmann constant and T is temperature.

Since the potential of mean-force $U(r)$ contains contributions from many-body interactions, it is expanded in terms of binary (w_{ij}), ternary (w_{ijk}), and higher order interactions as

$$U(r) = \sum_{i,j} w_{ij}(r) + \sum_{i,j,k} w_{ijk}(r) + ... \tag{2.39}$$

Note that $g(r)$ is zero for very short distances since two particles cannot occupy the same space and is equal to one for large distances since at far enough distance, a particle can be located with certainty. Direct interactions between the pair of interacting particles are represented by the direct correlation function $c(r)$ whereas interactions through other particles are represented by the total correlation function $h(r) = g(r) - 1$.

The Ornstein-Zernike integral equation denotes a relation between the direct correlation function $c(r)$ and the total correlation function $h(r)$ [133]:

$$h(\boldsymbol{r}) = c(\boldsymbol{r}) + n\int c\left(\boldsymbol{r}'\right) h\left(\left|\boldsymbol{r} - \boldsymbol{r}'\right|\right) d^3\boldsymbol{r}' \tag{2.40}$$

where n (N/V) is particle number density.

The Ornstein-Zernike equation contains two unknowns [$h(r)$ and $c(r)$]. It can be solved only if another (so called closure) relation is added. Many of these closure relations have been introduced (Percus-Yevick approximation, mean spherical approximation, hypernetted chains approximation etc). Using one such closure relation, numerical solutions of the Ornstein-Zernike equation yield realistic interparticle structure factors. Some frequently used closure relations are as follows:

The Percus-Yevick approximation: The Percus-Yevick approximation (PYA) uses the following closure relation in order to solve the Ornstein-Zernike integral equation [134]

$$c(r) = g(r)\left[1 - \exp\left(-\frac{U(r)}{k_B T}\right)\right] \tag{2.41}$$

The mean spherical approximation: The mean spherical approximation (MSA) closure relation to the Ornstein-Zernike equation is given by [135]

$$\begin{aligned} c(r) &= -\frac{U(r)}{k_B T} \qquad r > \sigma \\ h(r) &= -1 \qquad\qquad r \le \sigma \end{aligned} \tag{2.42}$$

The hypernated chain approximation: The hypernated chain approximation (HNCA) closure relation to the Ornstein-Zernike equation is given by [136]

$$c(r) = -\frac{U(r)}{k_B T} + h(r) - \ln\left[h(r)+1\right] \tag{2.43}$$

The interparticle structure factors $S(Q)$ for some of the most commonly used potentials are described below:

***S*(*Q*) for hard sphere potential:** This is the simplest potential which may be defined as

$$\begin{aligned} U(r) &= \infty \quad r \le 2R_{HS} \\ &= 0 \quad r > 2R_{HS} \end{aligned} \tag{2.44}$$

where $2R_{HS}$ is the hard sphere diameter. In this case following analytic solution for the structure factor using Percus-Yevick approximation is obtained [137]:

$$S(Q) = \frac{1}{1 + 24\eta f(R_{HS}Q)/(R_{HS}Q)} \tag{2.45}$$

In this equation, $f(x)$ is further defined as follows:

$$\begin{aligned} f(x) &= \alpha(\sin x - x\cos x)/x^2 \\ &+ \beta[2x\sin x + (2-x^2)\cos x - 2]/x^3 \\ &+ \gamma[-x^4\cos x + 4\{(3x^2-6)\cos x + (x^3-6x)\sin x + 6)\}]/x^5 \end{aligned} \tag{2.46}$$

and

$$\alpha = (1+2\eta)^2/(1-\eta)^4$$
$$\beta = -6\eta(1+\eta/2)^2/(1-\eta)^2 \qquad (2.47)$$
$$\gamma = \eta\alpha/2$$

where η is particle volume fraction.

Figure 2.13 shows the variation of $S(Q)$ calculated for hard sphere potential in Percus-Yevick approximation as a function of particle volume fraction. The peak positions shift to larger Q values with the increase in the concentration as the average distance between the particles decreases.

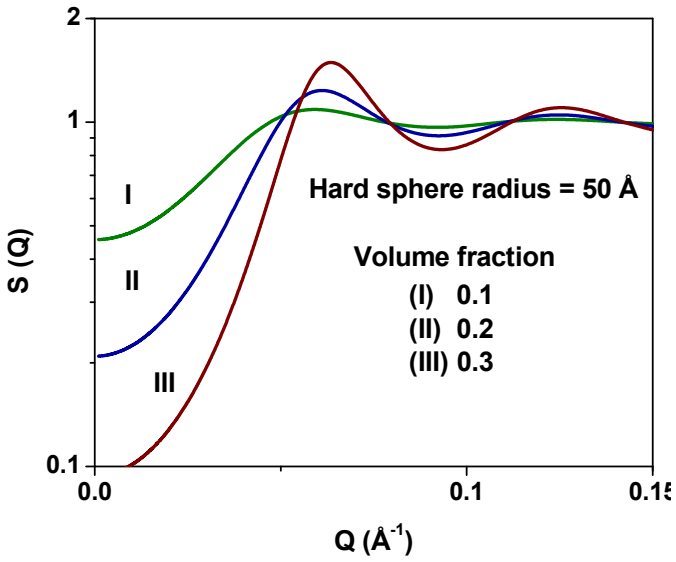

Figure 2.13. S(Q) dependence for particle interaction with hard sphere interaction. The peak positions shift to larger Q values with the increase in the volume fraction.

***S*(*Q*) for Baxter's sticky hard sphere potential:** If there exists a short-range attractive interaction among the particles then the simplest potential one can use is the Baxter's sticky hard sphere potential [138]. This potential assumes hard sphere repulsion along with the short-range attraction (represented by a thin attractive well). The sticky hard sphere interaction of particles of diameter $\sigma(2R)$ interacting via a thin attractive potential of width Δ is given by

$$\begin{aligned} \frac{U(r)}{kT} &= \infty && (0 < r < \sigma) \\ &= \ln\frac{12\ \tau\ \Delta}{\Delta+\sigma} && (\sigma \le r \le \Delta+\sigma) \\ &= 0 && (r > \Delta+\sigma) \end{aligned} \tag{2.48}$$

The expression for $S(Q)$ for particles with volume fraction η is expressed as

$$S(Q) = \frac{1}{A^2(Q) + B^2(Q)} \tag{2.49}$$

$$A(Q) = 1 + 12\ \eta\ \left(\alpha\ \frac{sin(k) - k\ cos(k)}{k^3} + \beta\ \frac{1 - cos(k)}{k^2} - \frac{\lambda}{12}\frac{sin(k)}{k} \right)$$

$$B(Q) = 12\ \eta\ \left(\alpha\left[\frac{1}{2k} - \frac{sin(k)}{k^2} + \frac{1 - cos(k)}{k^3} \right] + \beta\left[\frac{1}{k} - \frac{sin(k)}{k^2} \right] - \frac{\lambda}{12}\frac{1 - cos(k)}{k} \right) \tag{2.50}$$

where

$$\alpha = \frac{1 + 2\eta - \mu'}{(1-\eta)^2} \quad , \quad \beta = \frac{-3\eta + \mu'}{2(1-\eta)^2} \quad , \quad \mu' = \lambda'\eta(1-\eta)$$

$$\lambda' = \frac{6}{\eta}\left[\delta - \left(\delta^2 - \nu\right)^{1/2} \right], \quad \delta = \tau + \frac{\eta}{1-\eta} \quad , \quad \nu = \eta\frac{1 + \eta/2}{3(1-\eta)^2}$$

and k = Q(σ+Δ). The parameter stickiness (τ^{-1}) provides the information about the strength of adhesion and is given as

$$\tau = \frac{\sigma + \Delta}{12\Delta} exp\left(\frac{V}{kT} \right) \tag{2.51}$$

The variation of $S(Q)$ with stickiness (τ^{-1}) is depicted in figure 2.14. The value of $S(Q=0)$ increases with increase in stickiness (τ^{-1}) indicating the enhancement in attraction.

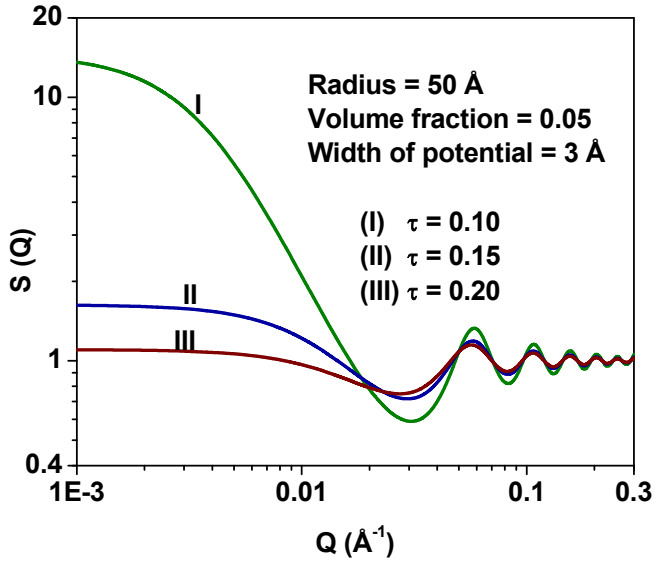

Figure 2.14. S(Q) dependence on stickiness (τ^{-1}). The value of $S(Q)$ at low Q increases with increase in τ^{-1}.

***S*(*Q*) for screened Coulomb repulsive potential:** $S(Q)$ has been calculated for particles interacting through screened Coulomb potential using mean spherical approximation as developed by Hayter and Penfold and is given by [132, 135]

$$U(r) = U_0 \sigma \frac{\exp[-\kappa(r-\sigma)]}{r} \quad (r > \sigma) \tag{2.52}$$

where κ is the Debye-Huckel inverse screening length and is calculated by

$$\kappa = \left[\frac{8\pi N_A e^2 I}{10^3 \varepsilon k_B T} \right]^{1/2} \tag{2.53}$$

N_A is the Avogadro number and I correspond to the ionic strength. The contact potential U_0 is given by

$$u_0 = \frac{Z^2 e^2}{\pi \varepsilon \varepsilon_0 \sigma (2 + \kappa\sigma)^2} \tag{2.54}$$

where ε is the dielectric constant of the solvent medium, ε_0 is the permittivity of free space and e is the electronic charge. Figure 2.15 shows the effect of charge on the interparticle structure factor. It has been observed that peaks in $S(Q)$ become more sharper with increase in the particle charge.

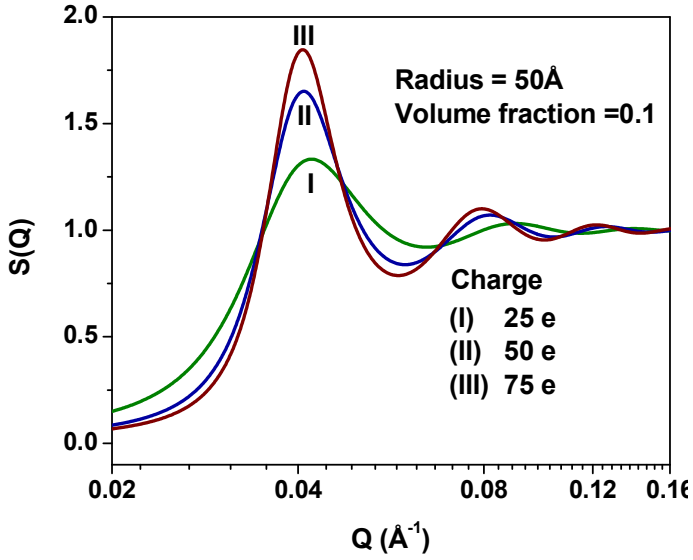

Figure 2.15. S(Q) dependence on the charge (in electronic unit e) of the particle. The correlation peak becomes pronounced with increase in charge.

The profile of $S(Q)$ for attractive, hard sphere and repulsive potentials are given in figure 2.16. All the $S(Q)$ curves converge to unity in high Q region whereas the distinct behavior in low Q region in particular approaching $Q = 0$ arise because of the differences in isothermal compressibilities of the corresponding systems. Therefore, $S(Q)$ diverges in the low Q region on interaction changing from repulsive to attractive.

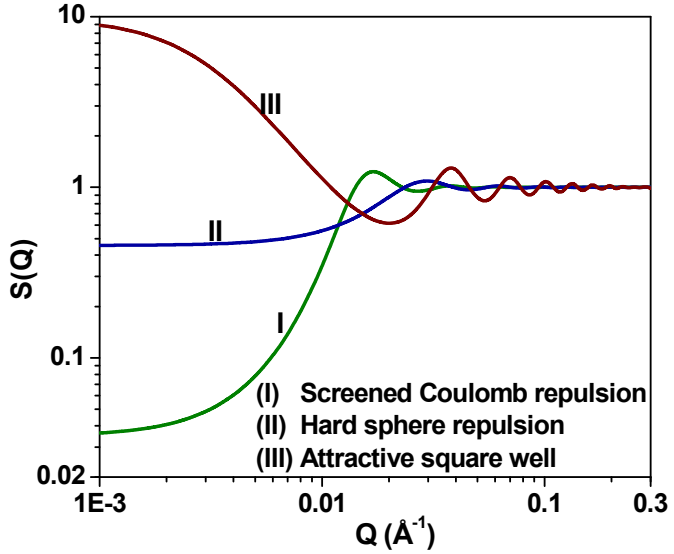

Figure 2.16. Comparison of $S(Q)$ curves for repulsive, hard sphere and attractive potentials.

***S*(*Q*) for a fractal structure:** Some objects or some processes exhibit a self-similarity over a wide length scale and possess a characteristic fractional dimension and are called fractal objects [139-142]. The self similarity of these objects means they appear same when examined on different scale of magnification. The properties of the fractal systems can be described by quantities, which are proportional to a power of another quantity. This relation is frequently called a power law.

These structures may be mass fractals where mass distribution shows self similar behavior throughout the volume, or can be surface fractals where self similarity exists only on the surfaces. For mass fractals, the mass $M(r)$ inside a spherical surface with radius r inscribing the structure is given by $M(r) \alpha r^d$, $d \leq 3$ and $S(Q)$ for such fractal structure can be expressed as

$$S_{mf}(Q) = 1 + \frac{1}{(QR_b)^{D_m}} \frac{D_m \Gamma(D_m - 1)}{[1 + (Q\xi)^{-2}]^{[(D_m-1)/2]}} \times \sin[(D_m - 1)\tan^{-1}(Q\xi)] \qquad (2.55)$$

where $\Gamma(x)$ is the gamma function of argument x. R_b is the building-block size forming the fractal structure. D_m and ξ are the fractal dimension and the correlation length of the fractal network, respectively.

The expression of $S(Q)$ for surface fractal structure is given by

$$S_{sf}(Q) = Q^{-1}\Gamma(5-D_s)\xi^{5-D_s}\left[1+(Q\xi)^2\right]^{\left(D_s-5/2\right)} sin\left[(D_s-1)tan^{-1}(Q\xi)\right] \qquad (2.56)$$

It may be mentioned that the scattering intensity from both kind of fractal structures is governed by power law behavior in a definite Q range.

$$\frac{d\Sigma}{d\Omega}(Q) \sim Q^{-D_m} \qquad \frac{1}{\xi} < Q < \frac{1}{R_b} \text{ for mass fractals} \qquad (2.57)$$

$$\frac{d\Sigma}{d\Omega}(Q) \sim Q^{-(6-D_s)} \qquad \frac{1}{\xi} < Q \text{ for surface fractals} \qquad (2.58)$$

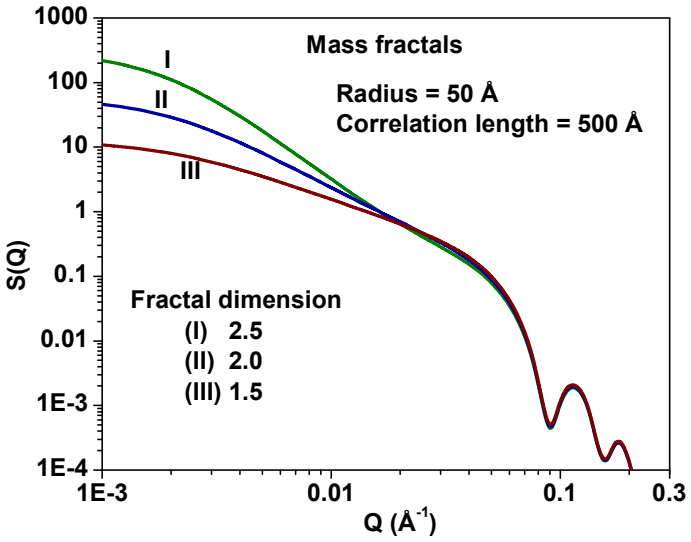

Figure 2.17. The typical $S(Q)$ for mass fractal systems with varying fractal dimension.

For mass fractals, scattering intensity show a linearity [$I(Q) \sim Q^{-\alpha}$] in profile in the intermediate Q values ($1/\xi < Q < 1/R_b$). Figure 2.17 shows the scattering intensity from mass

fractal structure. On the other hand, for surface fractals since the scattering is governed by surfaces, intensity show a Porod law kind of behavior where linearity (~ $Q^{-\alpha}$) appears at high Q values ($1/\xi < Q$) (figure 2.12). The value of exponent α varies between 1 and 3 for mass fractals while in between 3 to 4 for surface fractals.

2.2.3. Concept of contrast in SANS

The fundamental difference between neutrons and electromagnetic radiation is the mechanism by which they interact with matter. The x-rays are scattered by electrons surrounding atomic nuclei, but neutrons are scattered by the nuclei. As one moves across the periodic table, the neutron scattering lengths vary in a random way, whereas the x-ray scattering lengths increase with the atomic number of the atom (figure 2.18). For neutrons, isotopes of the same element can have significantly different scattering lengths. For example the scattering length of hydrogen is negative (- 0.3741×10^{-12}cm) and that deuterium is positive (0.6674×10^{-12}cm).

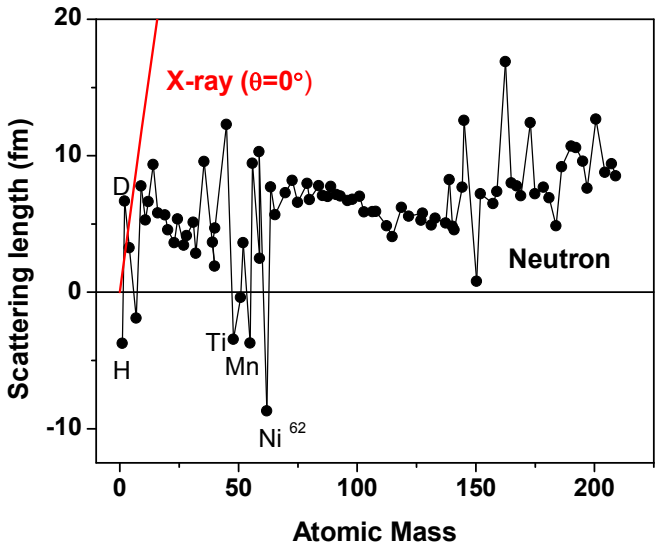

Figure 2.18. Scattering length variation for neutrons and X-rays.

Due to the difference in the scattering lengths of H and D, it is possible to have very good

contrast between the hydrogenous particle and the solvent by deuterating either the particle or the solvent. Scattered neutron intensity in a SANS experiment depends on $(\rho_p - \rho_s)^2$ - the square of the difference between the average scattering length densities of the particle and solvent (equation 2.21). The term $(\rho_p - \rho_s)^2$ is referred as the contrast factor. The contrast term depends on the radiation used. The values of ρ_p and ρ_s also depend on the chemical composition of the particle and the solvent. The contrast between the particle and the solvent can be varied continuously by using mixed hydrogenated and deuterated solvents. Various possibilities of contrast variation by using D_2O and/or H_2O as solvent are shown in figure 2.19.

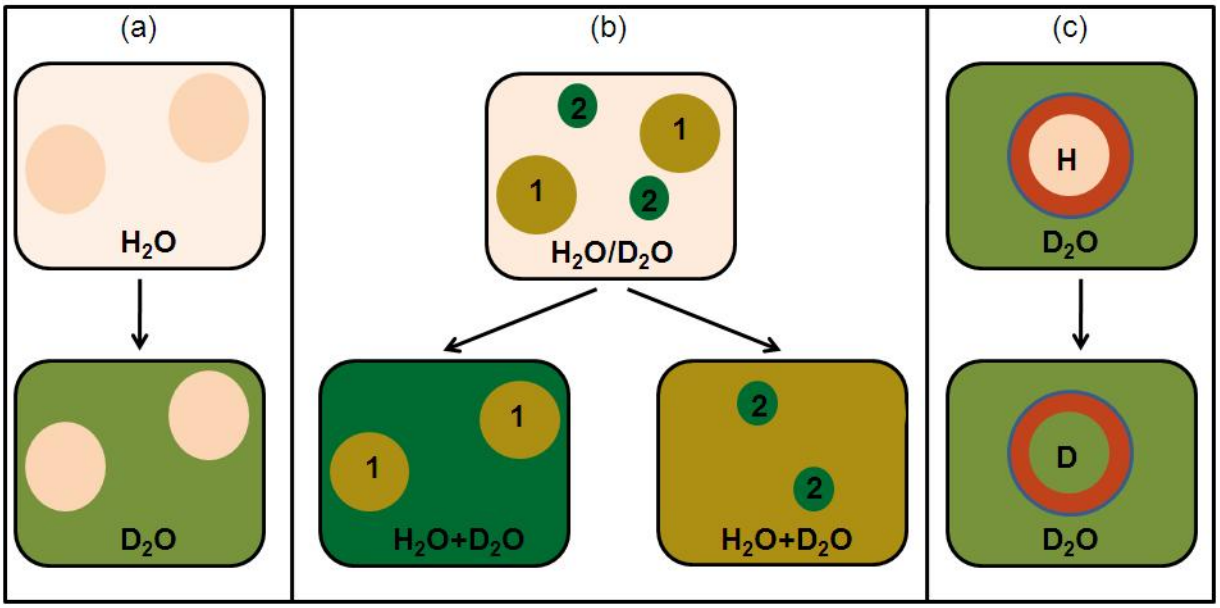

Figure 2.19. Various possibilities of contrast variations in SANS experiment (a) solvent replacement, (b) use of combination of H_2O- D_2O as a solvent and (c) isotope labeling where the core is deuterated.

Figure 2.19 (a) shows a hydrogenous spherical particle suspended in H_2O. Let the scattering length densities be ρ_p of the particle and ρ_H of the solvent. In this case $\rho_p \sim \rho_H$ and thus

the particle is not visible for neutrons. However, the solvent can be replaced with D_2O, so the scattering length density of D_2O is ρ_D which is quite different from ρ_p. In this way, SANS distribution is determined from the particle. Figure 2.19 (b) shows a two-component system suspended in H_2O or D_2O. Let ρ_1 and ρ_2 be the scattering length densities of the components 1 and 2, respectively. The solvent has a scattering length density ρ_s, which can be varied by varying the relative amounts of H_2O and D_2O in the solvent. Thus ρ_s can be either matched with ρ_1 so that the SANS distribution is determined by the component 2 alone or ρ_s with ρ_2 so that the SANS intensity is governed by component 1 alone. This method is called as external contrast variation. Deuterium labeling is another way of contrast matching [figure 2.19 (c)]. Considering a spherical core-shell particle is placed in D_2O solvent. The constituents of the inner core are different from those of the outer shell of the particle. By deuterating the core of the particle, scattering length densities of the core (ρ_{core}) and D_2O (ρ_D) can be matched, thus only the shell is visible. In a similar way, the scattering signal only from the core can be obtained by deuterating the shell (ρ_{shell}). This method is known as internal contrast variation.

Figure 2.20 shows the SANS data of silica nanoparticles dispersed in H_2O/D_2O mixed solvent of varying composition. In the mixed solvent, as the scattering length density of the solvent (ρ_s) approaches to that of the particle (ρ_p), the scattering intensity tends to zero. The linear plot of the square root of scattering intensity [$\{I(Q)\}^{0.5} \alpha (\rho_p-\rho_s)$] with solvent composition gives the contrast-matched point corresponding to zero scattering intensity as shown in figure 2.20(b) [143, 144]. The silica nanoparticles are found to be contrast-matched for 37 vol% of H_2O in the H_2O/D_2O mixed solvent.

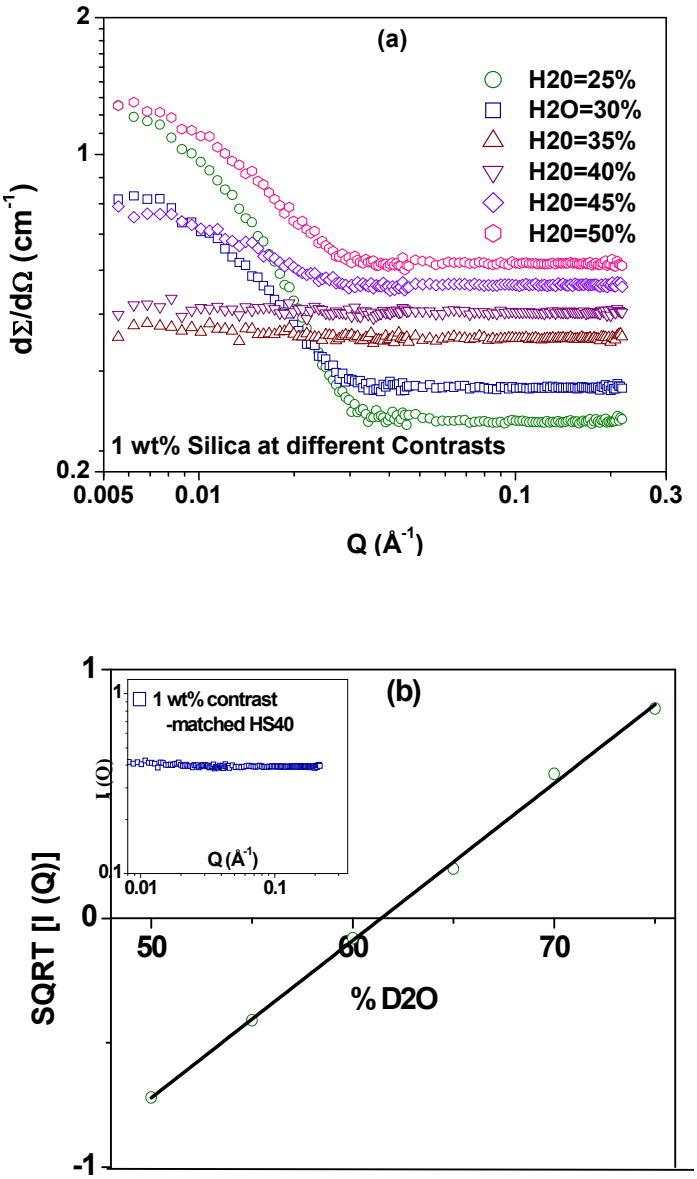

Figure 2.20. (a) SANS data of 1 wt% silica nanoparticles in different solvent with varying H_2O/D_2O ratio. (b) Square root of the scattering intensity for 1 wt% silica nanoparticle system as a function of composition of mixed solvent of H_2O/D_2O. Inset shows scattering intensity from 1 wt% HS40 nanoparticles in contrast-matched solvent (63 vol% D_2O).

2.3. Instrumentation in SANS

SANS experiments involve the scattering of monochromatic neutron beam from the sample and measuring the scattered neutron intensity as a function of scattering angle at small angles. The design of a SANS instrument therefore needs a suitable neutron source of white beam of neutrons, a monochromator for selecting desired wavelength of neutrons, a collimator for collimating the beam to achieve scattering signal at small angles and a high efficiency detector to detect the scattered neutrons [123-126].

The two main sources of neutrons are steady-state reactors and spallation sources. The energy and intensity of the neutrons in the beam and the time structure of the flux – continuous or pulsed – determines the design of neutron instruments. These characteristics are determined both by the type of source, and by the environment through which the neutrons pass immediately after production. Reactor source is based on fission reaction in which the radioactive nucleus such as ^{235}U is bombarded with neutrons. The produced neutrons are the fast neutrons which further pass through moderator (often D_2O or H_2O) to obtain thermal neutron beam useful for condensed matter research. Unlike the disintegration process involved in reactor sources, high energy protons splinter neutrons from heavy nuclei in spallation sources. The methods of acceleration of protons tend to produce short intense bursts of high energy protons, and hence pulses of neutrons.

After moderation, the neutrons are to be carried to respective instruments. Since the neutron flux per square centimeter decrease as the square of the distance from the source, it is obviously advantageous to construct the instruments close to the source. However, this imposes the constraint on the number of instruments which can be built around the given source. This problem is solved by use of neutron guides. These are the rectangular pipes coated internally

with suitable reflecting material so that the travelling neutron will undergo total external reflection. This not only ensures to minimize the loss of neutrons during transportation but also allows constructing the instruments far from the source where the background radiation is low. Most of the SANS instruments have been installed in these guides.

The neutrons coming from the reactor constitute a white beam of neutrons. However, every scattering experiment requires a monochromatic beam of incident particles having a desired wavelength. For the reactor source this process is essential for defining the parameters **Q** and ΔE in the neutron instruments. Pulsed sources give the option of using the whole of this white beam and measuring the wavelength distribution carefully. There are basically only two ways of choosing a given wavelength. The first uses the wave nature of neutrons via Bragg diffraction from a suitable crystal. In the second the particle nature and mechanical velocity selector to select narrow velocity range are used.

In scattering experiment, the change in wavevector has to be measured with good precision. Thus, both the wavelength (λ) and the scattering angle (θ), have to be well defined. The process of defining λ is performed in monochromation. The process of defining neutron beam so that θ can be measured is called collimation. There are two ways for collimating the beam (i) point collimation and (ii) slit collimation. The point collimation instruments have pinholes that shape the neutron beam to a small circular or elliptical spot illuminating the sample. Owing to the small illuminated sample volume and the wastefulness of the collimation process, the measurement time is usually large in case of very weak scatterers. In slit collimation, spacing of the set of diaphragms is carefully designed. The choice of the collimation distance is a compromise between the size of the direct beam and the flux. Usually, a collimation distance matching the sample-to-detector distance is used. However, for strong scatterer and/or short

sample-to-detector distance, larger collimation distances can be used to reduce the flux and the scattering to avoid detector saturation and damage.

The neutrons after scattering from the samples are detected at the detector. Neutron detection involves a process of absorption by a suitable nucleus followed by the detection of charged particles produced. These reactions involve the light nuclei ^{3}He, ^{6}Li, ^{10}B etc. and make use of nuclear reactions such as

$$^{3}He + {}^{1}n \longrightarrow {}^{3}H + {}^{1}H + 0.77\ MeV \quad (2.59)$$

$$^{6}Li + {}^{1}n \longrightarrow {}^{4}He + {}^{3}He + 4.79\ MeV \quad (2.60)$$

$$^{10}B + {}^{1}n \longrightarrow 7Li + 4He + 2.79\ MeV \quad (2.61)$$

These fast ions produced are used in actual detection process. In gas detectors, they produce a trail of secondary ionization which travels towards an electrode and is detected as an electronic pulse.

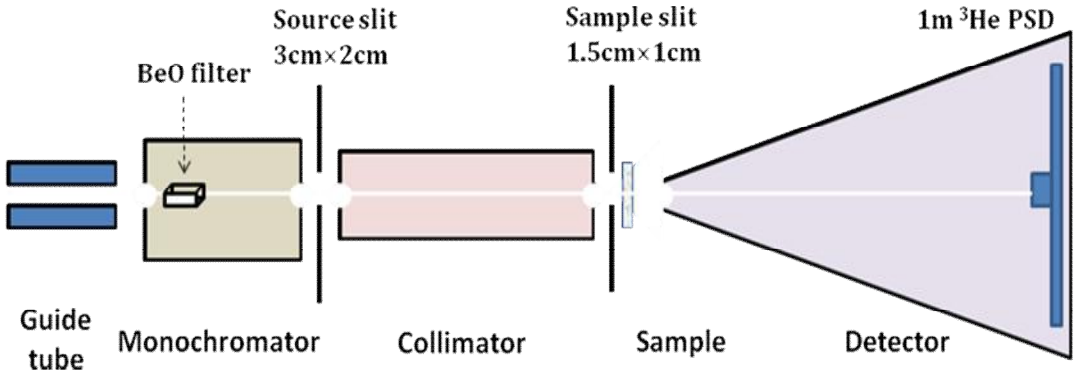

Figure 2.21. Schematic of SANS instrument at Dhruva reactor, BARC, India.

Figure 2.21 shows the schematic of small-angle neutron scattering facility installed at the guide tube laboratory of Dhruva reactor, BARC, India [145]. The neutron beam from the guide is monochromated by passing through a 15 cm long polycrystalline block of beryllium oxide (BeO)

filter. Neutrons of wavelength larger than 4.7 Å pass through the BeO filter and those having wavelengths smaller than 4.7 Å are Bragg scattered. The mean wavelength of the monochromated beam is 5.2 Å and has a spread of $\Delta\lambda/\lambda \sim 15\%$. This beam passes through two slits S_1 (2 cm × 3 cm) and S_2 (1 cm × 1.5 cm) before it is incident on the sample. Distance between S_1 and S_2 is 2 m and this gives an angular divergence of $\pm 0.5^{o}$. The angular distribution of neutrons scattered by the sample is recorded using a one-dimensional position sensitive detector. This is a fixed geometry instrument with sample to detector distance equal to 1.85 m. The *Q* range of the diffractometer is 0.017-0.35 $Å^{-1}$ and it is suitable for the study of particles in a size range of 20-200 Å.

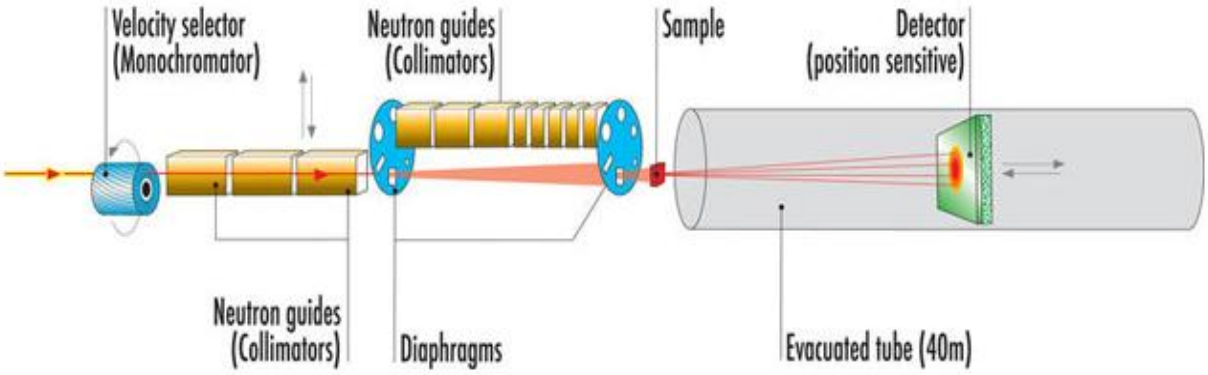

Figure 2.22. Schematic of a typical state-of-art SANS facility.

The schematic of a state-of-art instrument is shown in figure 2.22. These instruments (e.g. SANS I, PSI, Switzerland or D22, ILL, France or SANS facility at HANARO, Republic of Korea) are quite long (about 40 m) instruments [146-148]. Such facilities make use of velocity selector with pinhole collimation where the average wavelength and wavelength spread can be

varied. The collimator allows for the adjustment of the collimation length, i.e. the distance between the two pinholes at the guide exit and at the specimen position, in discrete steps which then matches the Q-resolution chosen by the sample-detector distance. Mechanically, this flexibility is achieved by a system of different collimator segments mounted in sequence. A ^{3}He multiwire detector with a large area (1×1 m^2) is used. The sample to detector distance can be varied to cover a wide Q range 0.001 to 1 Å^{-1} in a single instrument.

2.4. Data reduction and normalization

Data from the position sensitive detector are stored in a multichannel analyzer as intensity v/s channel number/pixel. There is a one to one correspondence between the channel number/pixel and the distance a between the point of neutron detection and the centre of the incident beam at the detector. The scattering angle is given by $2\theta = \tan^{-1}\left(a / L_2\right)$ where L_2 is sample to detector distance. Thus, each channel/pixel is related to the corresponding Q value.

In a SANS measurement from a sample (e.g. protein solution) requires evaluation of the scattered intensity contributions from the solvent I_{so} and the ambient background I_B. The transmissions of the sample and the solvent should also be determined to correct for the attenuation of neutrons in traversing them. The transmission of the sample T_s should be kept high to minimize multiple scattering effects. The sample cells are usually flat quartz cells with path lengths of 1 to 10 mm. The measured intensity from the sample I_S is corrected for the above various contributions. The background is determined by blocking the beam using a cadmium sheet. The measured intensity $I_B(Q)$ consists of the two contributions, namely the room background [$BKG(Q)$] and the fast neutrons [$I_F(Q)$] because cadmium does not block the fast neutrons.

$$I_B(Q) = BKG(Q) + I_F(Q) \tag{2.62}$$

The measured intensity with solvent I_{SO} consists of three terms: first from the fast neutrons [$I_F(Q)$], second from the room background [$BKG(Q)$] and the third is unscattered transmitted intensity from the solvent $I_O T_{SO}$, where T_{SO} is the transmission of the solvent and I_O is the intensity of thermal neutrons in the beam.

$$I_{SO}(Q) = I_O T_{SO} + BKG(Q) + I_F(Q) \tag{2.63}$$

When the scattered intensity (I_S) with the sample is measured, we get

$$I_S(Q) = I_O T_S + BKG(Q) + I_F(Q) + I_c(Q) \tag{2.64}$$

where T_S is the transmission of the sample, $I_O T_S$ is the unscattered transmission intensity from the sample and $I_c(Q)$ is the scattered intensity of interest from the sample. The counting time for the experiment is controlled using the monitor detector, which is installed in the incident beam. Solving equations 2.62-2.64 for $I_c(Q)$, we get

$$I_c(Q) = \left[\frac{I_S(Q) - I_B(Q)}{T_S} - \frac{I_{SO}(Q) - I_B(Q)}{T_{SO}} \right] T_S \tag{2.65}$$

In a SANS experiments, the sample is usually taken in a cell, so that it has uniform thickness over the beam area. If $d\Sigma/d\Omega(Q)$ is the differential scattering cross-section per unit volume of the sample, the measured scattered neutron intensity is given by

$$I_c(Q) = K T_S t \frac{d\Sigma}{d\Omega}(Q) \tag{2.66}$$

where t is the sample thickness, K is a constant, which depends on instrumental parameters such as incident neutron flux, detector efficiency, solid angle subtended by detector element at sample position etc.

By combining equations 2.65 and 2.66, we get the following expression for the differential scattering cross-section of the sample [94, 123-126]

$$\frac{d\Sigma}{d\Omega}(Q) = \frac{1}{Kt}\left[\frac{I_S(Q) - I_B(Q)}{T_S} - \frac{I_{SO}(Q) - I_B(Q)}{T_{SO}}\right] \tag{2.67}$$

The instrumental constant K is determined by recording the data from a standard sample like H_2O, Vanadium, etc. the measurement thus provides $d\Sigma/d\Omega$ (Q) in absolute units (cm^{-1}).

In SANS experiments, the measured SANS distribution is a convolution of the theoretical ($d\Sigma/d\Omega$)(Q) and the resolution function of the instrument. Thus one needs to take account of these resolution effects while comparing the calculated and the measured distributions. There are three components to the resolution function for the diffractometer. These contributions arise from the finite collimation, the wavelength distribution and the spatial resolution of the detector. The Q resolution from the first two factors (uncertainties in θ and λ) is given by

$$\frac{\Delta Q}{Q} = \left[\left(\frac{\Delta\theta}{\theta}\right)^2 + \left(\frac{\Delta\lambda}{\lambda}\right)^2\right]^{1/2} \tag{2.68}$$

When a diffractometer is set to detect neutrons with wave vector transfer Q, neutrons with wave vector transfers Q' in the neighbourhood of Q also contribute to the scattering due to the finite instrument resolution. If we describe the resolution function of the diffractometer by $R(Q, Q')$ at the wave vector transfer Q, the measured intensity $I(Q)$ is related to the scattering cross-section ($d\Sigma/d\Omega$) (Q) by the integral

$$I(Q) = \int R(Q, Q')\frac{d\Sigma}{d\Omega}(Q')dQ' \tag{2.69}$$

The resolution function from the collimation and the detector are independent of Q but to wavelength it depends linearly on Q. Thus the resolution function is decided by the beam collimation at low Q values whereas by wavelength resolution at high Q values.

2.5. SANS data analysis

The extraction of structural information from the SANS data usually faces the problem of lack of ordering in the samples under investigation. As a result, only some general structural characteristics such as radius of gyration and specific surface area based on invariants can be evaluated directly from the intensity curves. In order to obtain detailed information more sophisticated methods of data analysis are required. The goal of these methods is to obtain real space information from SANS data representing the system in Fourier space. The data are usually analyzed by following two methods [127, 143]:

Model independent analysis: This data analysis approach consists of Fourier transformation of the experimental scattering curve which provides real space information in terms of pair distance distribution function $p(r)$ describing the set of all paired-distances within a structure. This distance distribution function or correlation function [$p(r) = r^2 g(r)$] and scattered intensity are related with following Fourier transformation.

$$p(r) = \frac{r^2}{2\pi^2} \int_0^\infty Q^2 I(Q) \frac{\sin Qr}{Qr} dr \tag{2.70}$$

The Direct Fourier transformation of the experimental data to obtain $p(r)$ using above equation 2.70 is not easy, as the exact intensity $I(Q)$ in the full required range (0, ∞)is not available rather the experimental intensity consists of finite number of data points in a limited Q window (Q_{min}, Q_{max}). Moreover, the experimental data contain smearing effects due to finite

beam size, divergence and/or polychromaticity etc. which cause deviations from ideal scattering curves. All these points make practically impossible to obtain information through direct Fourier transformation. The Fourier transformation is therefore done utilizing the indirect Fourier transformation (IFT) method [149]. This method contains several advantages over the direct Fourier transformation as it allows corrections for instrumental smearing and can be applied to all systems having finite correlations. In this method, $p(r)$ is expressed as a linear combination of orthogonal functions in the range $(0, D_{max})$ where the coefficient of expansion are obtained by fitting the experimental data. In principle, the scattering intensity $I(Q)$ and distance distribution function $p(r)$ contains same information, though difficult to obtain but the real space representation in terms of $p(r)$ may be easy to understand, more intuitive and informative. The particle shape and size of some simple geometric bodies can often be deduced by straightforward visual inspection of $p(r)$ [143].

Model dependent analysis: For obtaining structural information about the more complex systems, model dependent data analysis methods are normally used. In this approach, a suitable model for the system is assumed based on the system understanding, physical constraints and information obtained through different techniques. Accordingly intraparticle structure factor $P(Q)$ and interparticle structure factor $S(Q)$ are chosen to calculate theoretical $d\Sigma/d\Omega(Q)$. The calculated $d\Sigma/d\Omega(Q)$ is convoluted with resolution function and compared with experimental data for a given set of parameters [127, 143, 150]. The values of parameters are optimized using non-linear least square fitting method. This method involves determination of a quantity known as reduced chi square. The origin of the chi-square is statistic and is typically employed to imply goodness of fit for iterative fitting of data. The expression for reduced chi-square is given by

$$\chi^2 = \sum_{i=1}^{N} \left\{ \frac{1}{\sigma_i^{\,2}} \left[y_i - f(x_i) \right]^2 \right\} \tag{2.71}$$

where N is the number of data points.

σ_i^2 is the variance related to the measurement error in y_i.

f is the assumed relationship between x and y.

y_i is the experimental mean.

$f(x_i)$ is the predicted theoretical mean.

The basis for the rule of thumb states that a best fit is achieved with a reduced chi-square value of about 1. If the models are chosen poorly then the reduced-chi square value will be high suggesting re-assessment for the models. This approach is very useful for structure as well as interaction determination through the proper modeling of $P(Q)$ and $S(Q)$.

2.6. Usefulness of small-angle neutron scattering for studying multi-components systems

SANS is used for characterization of particles having sizes in a length scale (1 to 100 nm) where most of the colloidal particles such as micelles, nanoparticle and proteins exist. In particular, this technique is one of the most suitable techniques to study multi-components systems constituted of these colloids. SANS can probe both interactions and structures in these systems. Usefulness of SANS in investigating multi-component system is multifold and some of the important advantages are:

(i) The different components forming the multi-component systems may interact with each other by different forces (e.g. electrostatic interaction, steric repulsion, depletion forces, hydrophobic force and hydrogen bonding) whose delicate balance in turn determines the complex structures formed. For example, in nanoparticle-surfactant systems, the type of surfactant governs the interaction between the two components leading to variety of structures. Similarly, in surfactant-

protein complexes, degree of protein unfolding depends on how the two components are interacting. SANS can be used to examine the role of these interactions in determining the system behavior. The measured scattering intensity in SANS is the product of the intraparticle structure factor $P(Q)$ and interparticle structure factor $S(Q)$, where the $P(Q)$ provides information on the structure (shape and size) of particles and $S(Q)$ depends on the interaction between particles. Thus, SANS provides information on both interactions and structure of the system [20, 23, 120, 151].

(ii) The unique advantage of SANS to study multi-components systems is easy possibility of contrast-variation in this technique. The scattering due to internal variation of scattering length density could be separately determined if the solvent scattering density is changed isomorphously. The scattering intensity depends on $(\rho_p - \rho_s)^2$, which is square of the difference of scattering length densities of the particle and solvent. Due to large difference between neutron scattering amplitudes of hydrogen and deuterium, SANS is of considerable importance for mulit-component systems unlike the complementary SAXS and light scattering techniques. In the case of SAXS and light scattering, the choice of hydrogen or deuterium isotope does not matter. The constituents of these multi-component systems usually have neutron scattering densities that are between those of H_2O and D_2O. These systems are selectively simplified by matching the scattering density of one of the components with the solvent [23, 144, 152].

(iii) SANS measures the scattering intensity in the absolute scale and this fact can be used to obtain different levels of information such as particle concentration, internal structure of particle, formation of aggregates. For example, in case of macromolecules mediated nanoparticle aggregation, the magnitudes of data of different Q ranges depend on their number densities and hence the population of each component in the aggregates can be determined. Any change in the

internal structure of the particle is expected to change the particle contrast with respect to solvent, which can be directly measured by the change in the scattering intensity in the absolute scale [120, 143].

(iv) The possibility of performing measurements in solution conditions has enhanced the advantage of SANS in many systems. SANS also allows in-situ studies of these systems. For example, SANS provides useful information on interaction of protein molecules in the system which were difficult to crystallize. Furthermore, the structures of protein molecules in solution and crystal state may be different due to conditions of crystallization and packing in the crystal. This relationship between protein structure in solution and crystal form has been studied extensively. The structures of such systems are also investigated by other techniques such as TEM or SEM. Even though these techniques provide a direct image of the system, they have disadvantage of requiring a frozen or dried sample. The actual structure in such case could be different from those in native solution conditions [143, 144, 151].

In this thesis, SANS has been used to probe interaction of nanoparticles with different macromolecules and their resultant structures. The possibility of contrast-variation has extensively utilized in order to simplify the system either by matching the nanoparticles or macromolecules to the solvent. The interaction of nanoparticle with different surfactants is investigated in chapter 3 under three different contrast conditions (i) both the components are visible, (ii) nanoparticles are contrast-matched and (iii) surfactants are contrast-matched. Similarly, the complexes of nanoparticles with proteins under these different contrast conditions are studied in chapter 4. The evolution of interaction and structure of nanoparticles in presence of block copolymer (chapter 5) and polymer (chapter 6) are investigated where block copolymer/polymer are contrast-matched.

Chapter 3

TUNING OF NANOPARTICLE-SURFACTANT INTERACTIONS AND RESULTANT STRUCTURES

3. 1. Introduction

Surfactants are known for their specialty of playing with interfacial properties. The presence of nanoparticles in surfactant solutions causes structural transitions in surfactants, which modify their key properties governing the interfacial processes such as hydrophobicity, surface charge etc [20, 153-155]. Also the presence of nanoparticles in the solution may force micelles to undergo some structural transformation. As a result, the interaction of surfactants with nanoparticles is utilized extensively for applications associated with colloidal stability, enhanced oil recovery, dispersion, detergency and design of nanostructured functional interfaces.

The interaction of nanoparticle and surfactant strongly depends on the characteristics of both the nanoparticle (e.g. size, stability, surface roughness, polydispersity and charge) and surfactant (e.g. type, charge, shape and solution conditions). Depending on the system conditions, the different interactions between two components can lead to various hybrid structures of multiple functionalities. The degree of interaction between nanoparticle and surfactant, and thus their resultant structure can be simply varied by the charge state of the surfactant [20, 153-161]. In the case two components are of similar charge nature (anionic or cationic) strong electrostatic repulsion prevents them from direct adsorption. However, the non-adsorbing nature of smaller component in such cases can give rise to attractive depletion force in

these systems. The role of size ratio of the particle and surfactant micelle becomes important as it influences the available volume for smaller macromolecule and hence the effective depletion potential [74, 75, 162]. When two components are oppositely charged, nanoparticles may destabilize and undergo surfactant-mediated aggregation where the controlled electrostatic complexion gives rise to the aggregates of different shapes, patterns and utilization [22, 63, 156, 163, 164]. If one or both components are non-ionic, they interact through relatively weak interactions such as hydrogen bonding or hydrophobic forces. For instance, the adsorption of a variety of non-ionic surfactant on nanoparticles such as ethoxylated alcohol, polyoxy ethylene glycol, sugar-based alkyl glucoside and other containing hydroxyl, phenolic, carboxylic and amine group are known to involve hydrogen bonding [20]. There are two models discussed in the literature for the adsorption of nonionic surfactants through the bilayer formation or individual micelles decorating nanoparticles [165]. It is interesting to investigate the formation of different structures from nanoparticle interaction with different ionic and non-ionic surfactants. The surfactants in the presence of nanoparticles can form micelles of different shapes and sizes, leading to a variety of possibilities.

In this chapter, contrast variation small-angle neutron scattering (SANS) has been used to examine the interaction and structure of anionic silica nanoparticles with three types of surfactants (anionic, cationic and non-ionic) [166-170]. The surfactants used comprise same hydrophobic tail but differing in the charge on their head groups are anionic sodium dodecyl sulphate (SDS), nonionic decaoxyethylene *n*-dodecylether ($C_{12}E_{10}$) and cationic dodecyltrimethyl ammonium bromide (DTAB). The silica nanoparticles used are of three different sizes (8, 16 and 26 nm). The nanoparticle size controls the surface-to-volume ratio and surface curvature for nanoparticle interaction with surfactant. The interaction is expected to

enhance with the increase in the surface-to-volume ratio, whereas decrease with increase the surface curvature, and thereby the resultant structure can be tuned by the competition of these two effects [20, 33, 121].

3.2. Experimental section

Electrostatically stabilized colloidal suspensions of different sized Ludox silica nanoparticles (SM30, HS40 and TM40) and surfactants (SDS, DTAB and $C_{12}E_{10}$) were purchased from Sigma-Aldrich. Ludox SM30, HS40 and TM40 systems consist of 30, 40 and 40 wt% nanoparticle concentrations in H_2O. In neutron scattering experiments, use of H_2O and D_2O as solvent provides different contrast for the particles because of very different neutron scattering lengths for H and D [144, 145]. Samples were prepared by dissolving weighted amount of nanoparticle suspensions and surfactants in mixed H_2O/D_2O solvent according to the three contrast requirements: (i) no component contrast-matched, (ii) silica nanoparticles are contrast-matched and (iii) surfactants are contrast-matched. The contrast conditions (ratio of H_2O/D_2O) for different components are listed in table 3.1. Small-angle neutron scattering experiments were performed using SANS facilities at the Dhruva reactor, Bhabha Atomic Research Centre, Mumbai [145] and the Swiss Spallation Neutron Source SINQ, Paul Scherrer Institut, Switzerland [146]. These two facilities together provide the data collection in a wide Q range to probe different length scales of the system. All the measurements were carried out for fixed concentration (1 wt%) of silica nanoparticles and surfactants. The temperature was kept constant at 30 ^{o}C during the measurements. The data were corrected and normalized to absolute scale using standard procedure.

Table 3.1. The calculated scattering length densities and contrast of different components of silica nanoparticles and surfactants.

Component	Scattering length density (cm^{-2})	Contrast-match point (% vol D_2O)
Silica	3.81×10^{10}	63
SDS	0.31×10^{10}	13
DTAB	-0.42×10^{10}	2
$C_{12}E_{10}$	0.30×10^{10}	13
D_2O	6.38×10^{10}	100
H_2O	-0.56×10^{10}	0

3.3. SANS analysis

In SANS experiments, one measures the coherent differential scattering cross-section per unit volume ($d\Sigma/d\Omega$) as a function of Q. For particles dispersed in a medium, it can be written as [124, 127, 171]

$$\frac{d\Sigma}{d\Omega}(Q) = nV^2\left(\rho_p - \rho_s\right)^2 P(Q)S(Q) + B \tag{3.1}$$

where n is the number density and V is particle volume. ρ_p and ρ_s are scattering length densities of particles and solvent, respectively. $P(Q)$ is intraparticle structure factor (square of form factor) and $S(Q)$ is interparticle structure factor. B is a constant term denoting incoherent background. The expressions of different form factors and interparticle structure factors used are described in chapter 2.

The scattering from the system composed of two non-interacting components (nanoparticle and micelle) can be modeled by summing up the two contributions from individual components as given by [166]

$$\left(\frac{d\Sigma}{d\Omega}\right)(Q)=\left(\frac{d\Sigma}{d\Omega}\right)_n(Q)+\left(\frac{d\Sigma}{d\Omega}\right)_m(Q) \tag{3.2}$$

where the subscripts *n* and *m* correspond to nanoparticles and micelles, respectively.

In the case of weak interaction leading to the direct adsorption of micelles on nanoparticles, the scattering cross-section comprise four terms: two terms corresponding to the scattering from nanoparticle and micelles, third term is cross-term between the adsorbed micelles and the nanoparticle and the last term represents the cross-term between the different micelles adsorbed on the same nanoparticle [172].

$$\left(\frac{d\Sigma}{d\Omega}\right)(Q)=\left(\frac{d\Sigma}{d\Omega}\right)_n(Q)+\left(\frac{d\Sigma}{d\Omega}\right)_m(Q)+\left(\frac{d\Sigma}{d\Omega}\right)_{nm}+\left(\frac{d\Sigma}{d\Omega}\right)_{mm} \tag{3.3}$$

where the subscripts *n*, *m*, *nm* and *mm* denote nanoparticles, micelles, nanoparticle-micelles interference and micelle-micelle interference terms, respectively. Equation 3.3 can be simplified to two terms (that from micelles and micelle-micelle interference) by contrast matching silica nanoparticles. Therefore, scattering for a dilute system is given by the following expression

$$\left(\frac{d\Sigma}{d\Omega}\right)(Q)=n_{fr}V_m(\rho_m-\rho_s)^2P_m(Q)S_{fr}(Q)+n_{ads}V_m(\rho_m-\rho_s)^2P_m(Q)S_{mm}(Q)+B \tag{3.4}$$

where n_{fr} and n_{ads} are the number densities of free and adsorbed micelles, respectively. $P_m(Q)$ is the intraparticle structure factor of the micelles. $S_{fr}(Q)$ is the interparticle structure factor of free micelles. S_{mm} is the interparticle structure factor of micelle-micelle interaction of the adsorbed micelles and is numerically calculated using following relation [23, 165]

$$S_{mm}(Q) = 1 + \frac{1}{N}\sum_{j=1}^{N}\sum_{k>j}^{N}\frac{\sin\{Q(r_j - r_k)\}}{Q(r_j - r_k)} \tag{3.5}$$

where $(r_j - r_k)$ is the distance between the centers of two micelles adsorbed on the same nanoparticle. N is the number of micelles adsorbed on the nanoparticle.

The strong attraction between oppositely charged nanoparticles and micelles is known to result in aggregation of nanoparticles. The scattering cross-section in this case may be given by [139, 140]

$$\frac{d\Sigma}{d\Omega}(Q) = n_a V^2 \left(\rho_p - \rho_s\right)^2 P_b(Q) S_f(Q) + B \tag{3.6}$$

where n_a is the number density of the individual scatter in the aggregates. $P_b(Q)$ is the intraparticle structure factor of the building block in aggregated structures and $S_f(Q)$ is the structure factor for mass fractal structures, the expression for which is described in chapter 2 (equation 2.55).

The data have been analyzed by comparing the scattering from above different models to the experimental data. Throughout the data analysis corrections were also made for instrumental smearing. The modeled scattering profiles were smeared by the appropriate resolution function to compare with the measured data. The fitted parameters in the analysis were optimized by means of nonlinear least-square fitting program [127, 150].

3. 4. Results and discussion

3.4.1. Characterization of individual nanoparticle and surfactant systems

The SANS data from 1wt% of all the pure components (nanoparticles and surfactants solutions) prepared in D_2O for which both the nanoparticles and surfactants have good contrast with low incoherent scattering background are shown in figure 3.1. All the three silica nanoparticles

systems (SM30, HS40 and TM40) show a monotonically decreasing scattering cross-section as a function of *Q*. This is because the scattering is governed by intraparticle structure factor *P(Q)* at 1 wt% (~ 0.4 vol%) concentration of silica nanoparticles, where the interparticle structure factor *S*(*Q*) contribution can be neglected [173]. The width and the position of oscillations are determined by reciprocal of the size. The overall scattering intensity also increases with the size

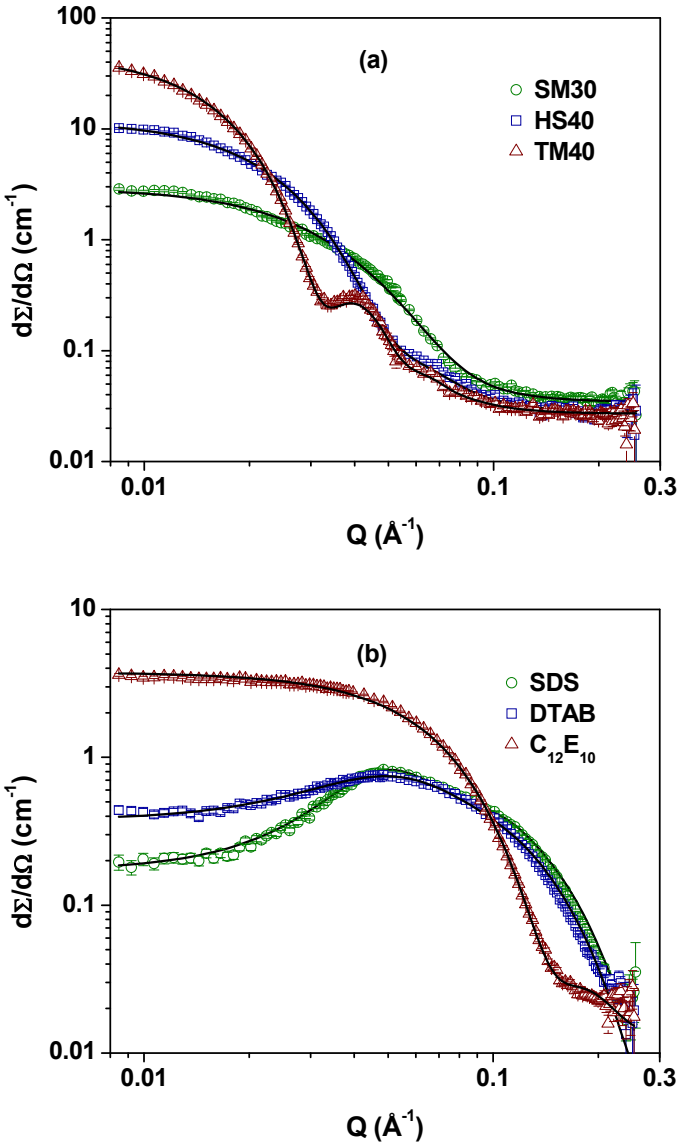

Figure 3.1. SANS data from 1 wt% (a) silica nanoparticle systems (SM30, HS40 and TM40) and (b) micellar systems (SDS, DTAB and $C_{12}E_{10}$).

Table 3.2. Structural parameters of 1 wt% silica nanoparticle and micellar systems.

(a) Silica nanoparticle systems

Nanoparticle system	Mean radius R_m(nm)	Polydispersity σ
SM30	4.1 ± 0.2	0.30 ± 0.05
HS40	8.0 ± 0.3	0.20 ± 0.04
TM40	13.0 ± 0.4	0.15 ± 0.03

(b) Micellar systems

Surfactant system	Semi-major axis a (nm)	Semi-minor axis b=c (nm)	Fractional charge α (*e.u.*)	Aggregation number N	Equivalent radius $(ab^2)^{1/3}$(nm)	Polydispersity σ
SDS	2.6 ± 0.1	1.5 ± 0.1	0.31 ± 0.03	61	1.8 ± 0.1	0.15 ± 0.03
$C_{12}E_{10}$[a]	1.7 ± 0.1	1.7 ± 0.1	-	60	1.7 ± 0.1	0.15 ± 0.03
DTAB	3.0 ± 2.0	1.5 ± 0.1	0.22 ± 0.02	63	1.9 ± 0.1	0.15 ± 0.03

[a] Radius of gyration of hydrophilic chain for nonionic micelles is calculated to be 1.2 nm.

proportional to the particle volume at constant volume fraction of particles. It is observed that the scattering cross-section increases in the order SM30 < HS40 < TM40, whereas width variation opposite to this order, indicating the order of increasing particle sizes for these systems. The nanoparticles have been modeled using a form factor of spheres with log-normal size distribution (chapter 2). The silica nanoparticles SM30, HS40 and TM40 are found to have the particle sizes (mean diameter) 8.2, 16.0 and 26.0 nm with polydispersity 0.3, 0.2 and 0.15, respectively. Ionic surfactants (SDS and DTAB) unlike silica nanoparticles show correlation peaks in the SANS data, which is as a result of observance of inter-micellar correlation among the charged micelles.

Usually, this peak occurs at $Q \sim 2\pi/d$, where d is the distance between the particles [174-176]. The fact that micelle size is expected to be much smaller than nanoparticles used, the higher number density of micelles (thus low value of d) gives rise a correlation peak within the Q range of measurements. The ionic micelles are fitted with the $P(Q)$ of prolate ellipsoidal shape and $S(Q)$ as calculated by Hayter and Penfold analysis under Mean Spherical Approximation for charged macroions (chapter 2). The scattering profile of $C_{12}E_{10}$ is similar to that of non-interacting particles ($S(Q) \sim 1$) and $P(Q)$ has been calculated for micelles consisting of a spherical core attached with Gaussian chain model [172]. The fitted structural parameters of silica nanoparticles and micelles are given in table 1. The micelles are found to be almost similar size and aggregation number for different surfactants used.

3.4.2. Interaction of nanoparticles with different types of surfactants

The SANS data of 1 wt% HS40 silica nanoparticles ($2R_m \sim 16$ nm) mixed with 1 wt% different surfactants (SDS, $C_{12}E_{10}$ and DTAB) in D_2O are shown in figure 3.2. For comparison, the data of respective pure components are also shown. It is observed that the data of silica nanoparticles with micelles are quite different than that of the pure components. The scattering profile of anionic nanoparticles with anionic surfactant SDS seems to be additive as if these two components do not interact directly. This is confirmed in the inset of figure 3.2 (a), where the data of silica nanoparticles with SDS is similar to that of the calculated addition of data of the two components. Unlike anionic SDS, the data of cationic DTAB and nonionic $C_{12}E_{10}$ surfactants with silica nanoparticles are different from the addition of constituent components [insets of figures 3.2 (b) and (c)]. This suggests the direct interaction of DTAB and $C_{12}E_{10}$

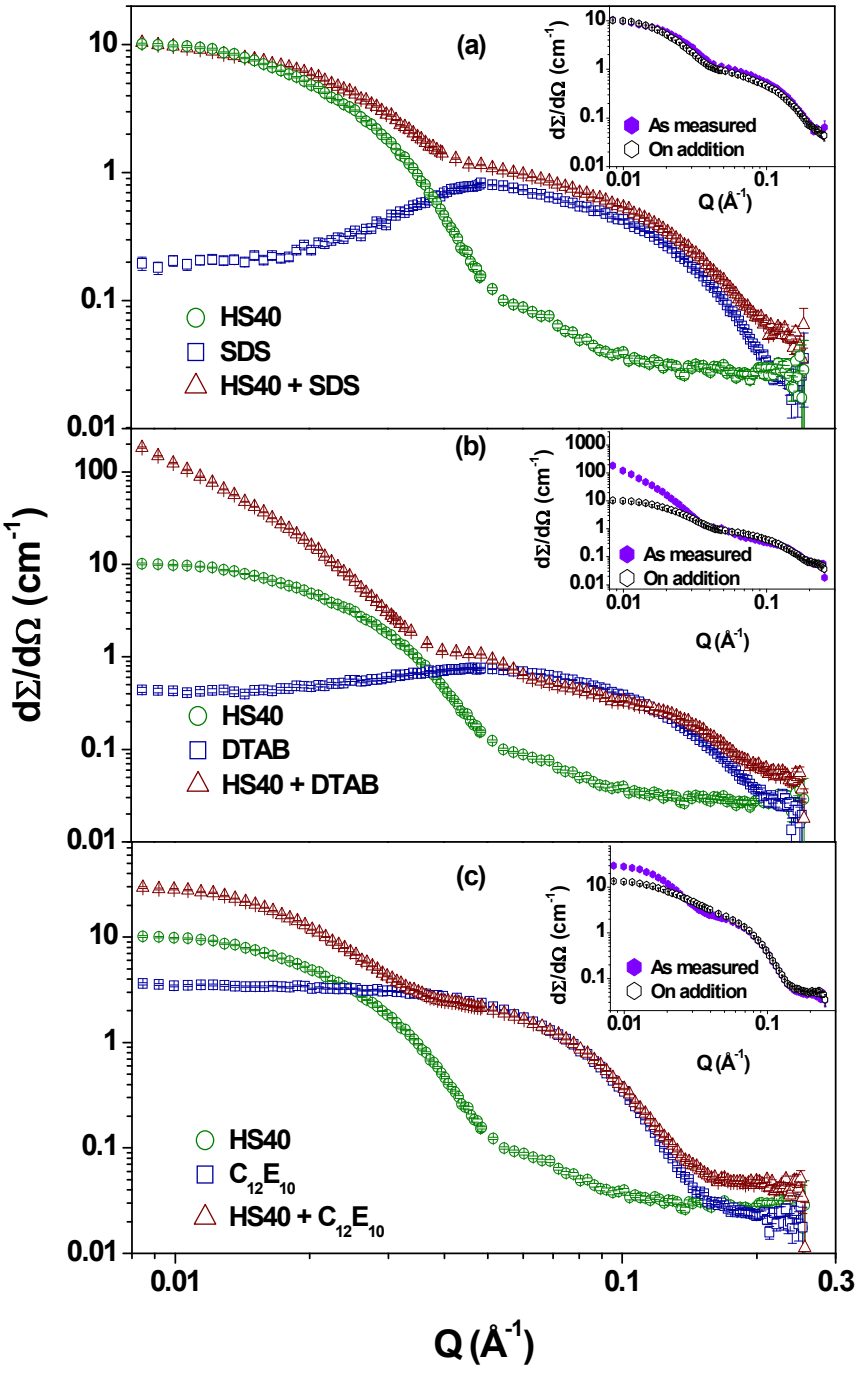

Figure 3.2. SANS data of 1 wt% HS40 nanoparticles with 1 wt% surfactants (a) SDS (b) DTAB and (c) $C_{12}E_{10}$. Insets show the comparison of measured data of nanoparticle-surfactant system with the calculated addition of data of respective pure components.

micelles with the silica nanoparticles [156, 165-167]. The scattering in low *Q* region is found to be higher than the addition of the scatterings from the individual components indicating the formation of larger structures than those of the individual ones in these systems. The turbid nature of the samples is observed in the case of DTAB which could be because of strong attraction between nanoparticles and micelles leading to the micelle-mediated aggregation of nanoparticles [168, 177, 178]. On the other hand, nanoparticle systems with $C_{12}E_{10}$ remain clear and the interaction of two components is believed to be governed by either micelles decorating the nanoparticles or through bilayer formation on nanoparticles [27, 165-167]. These structures have been systematically probed by the contrast matching individual components.

Figure 3.3 shows SANS data of 1 wt% HS40 mixed with 1 wt% SDS when (a) nanoparticles and (b) micelles are contrast-matched to the solvent. It is observed that SANS data of nanoparticle-SDS system for nanoparticle contrast-matched (63 vol% of D_2O in H_2O/D_2O) to the solvent are exactly similar to that of pure surfactant in the same solvent [figure 3.3 (a)]. Also the SANS data of nanoparticle-SDS system for surfactant contrast-matched to the solvent (87 vol% of D_2O in H_2O/D_2O) are identical to that of pure nanoparticle system in the solvent [figure 3 (b)]. These observations confirm no physical interaction of the nanoparticles with SDS as well as no changes in the micellar structure observed in presence of nanoparticles. These results can be used to examine if the presence of micelles cause attractive depletion forces between nanoparticles which is usually known to arise in the non-interacting mixtures of colloidal particles with smaller entities similar to the present case [74, 179]. The fact that the scattering from silica nanoparticles without and with surfactant is almost identical in surfactant contrast-matched solvent suggests no significant depletion force induced between nanoparticles by the presence of charged surfactant micelles.

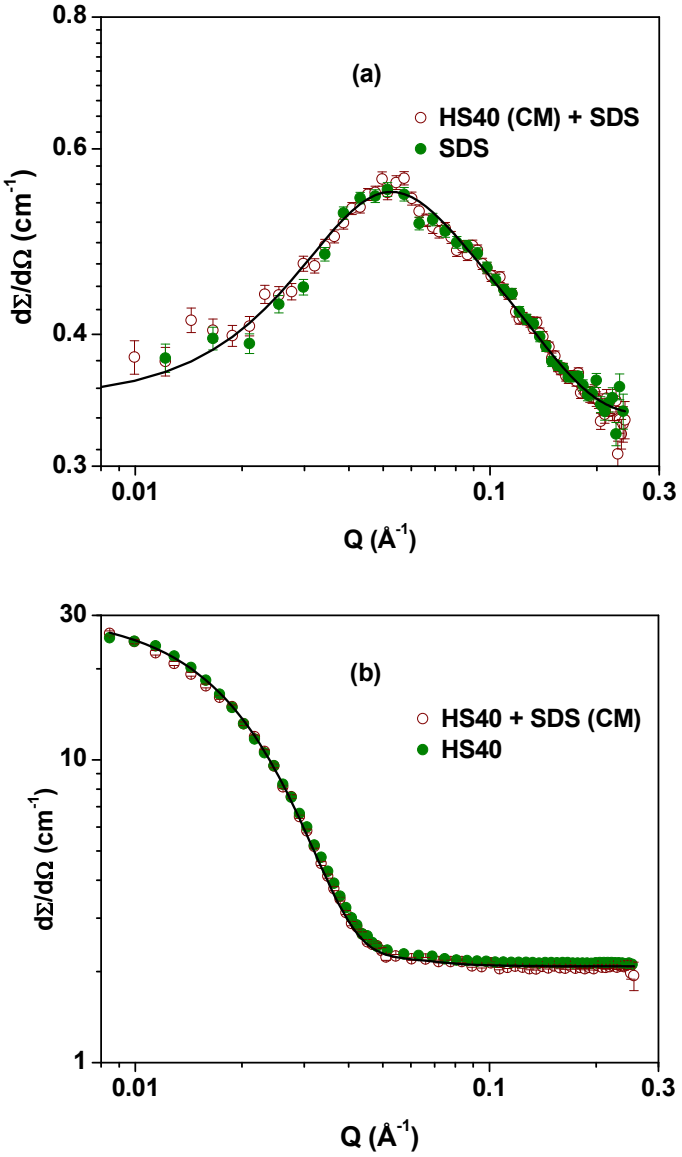

Figure 3.3. SANS data of 1 wt% HS40 with 1 wt% SDS (a) nanoparticles are contrast-matched along with data from pure surfactant system under the same contrast condition and (b) micelles are contrast-matched along with data from pure nanoparticle system under the same contrast condition.

Similar to figure 3.3, the SANS data of 1 wt% HS40 mixed with 1 wt% DTAB when (a) micelles (98 vol% of D_2O in H_2O/D_2O) and (b) nanoparticles are contrast-matched to the solvent are shown in figure 3.4. In contrast to nanoparticle-SDS system, the data for nanoparticle-DTAB

system in both the solvent conditions show high scattering build up in the low Q region. The data of surfactant contrast-matched to the solvent when compared with that of corresponding pure nanoparticle system under the same solvent condition have clearly different features. In particular, the linear dependence of scattering in the low Q region on log-log scale suggests the formation of large aggregates which can be characterized by fractal structure [140, 180-181]. The aggregation of nanoparticles is also evident by the observed turbid nature of the sample and believed to be mediated by micelle adsorption on nanoparticles due to strong attraction between two components [156, 170]. The redistribution of micelles leading to nanoparticle aggregation in nanoparticle-DTAB system is brought in figure 3.4 (b) (nanoparticles are contrast-matched to the solvent), which shows a very large increase in the scattering in the low Q region compared to that from pure surfactant solution. The large scattering in the low Q region can be expected by the formation of shell of micelles around the nanoparticles. The distribution of these shells of micelles will follow the same fractal structure that of nanoparticles. These fractal aggregates are characterized by two sizes as the building block size and the overall size of the aggregates. These two sizes are represented in scattering profiles as upper and lower cut offs, respectively and reflected in $S(Q)$ equation 2.55 [139, 140]. The data have been fitted for mass fractal structure of aggregates consisting of building block corresponding to the core-shell structure of DTAB micelles as a shell adsorbed on the nanoparticle core. The fractal dimension has a value of about 2.3. We have not observed any features corresponding to the overall size of the aggregates (lower Q cut-off) within Q range of present measurements. However, a fixed overall size greater than $2\pi/Q_{min}$ has been used in the analysis [140].

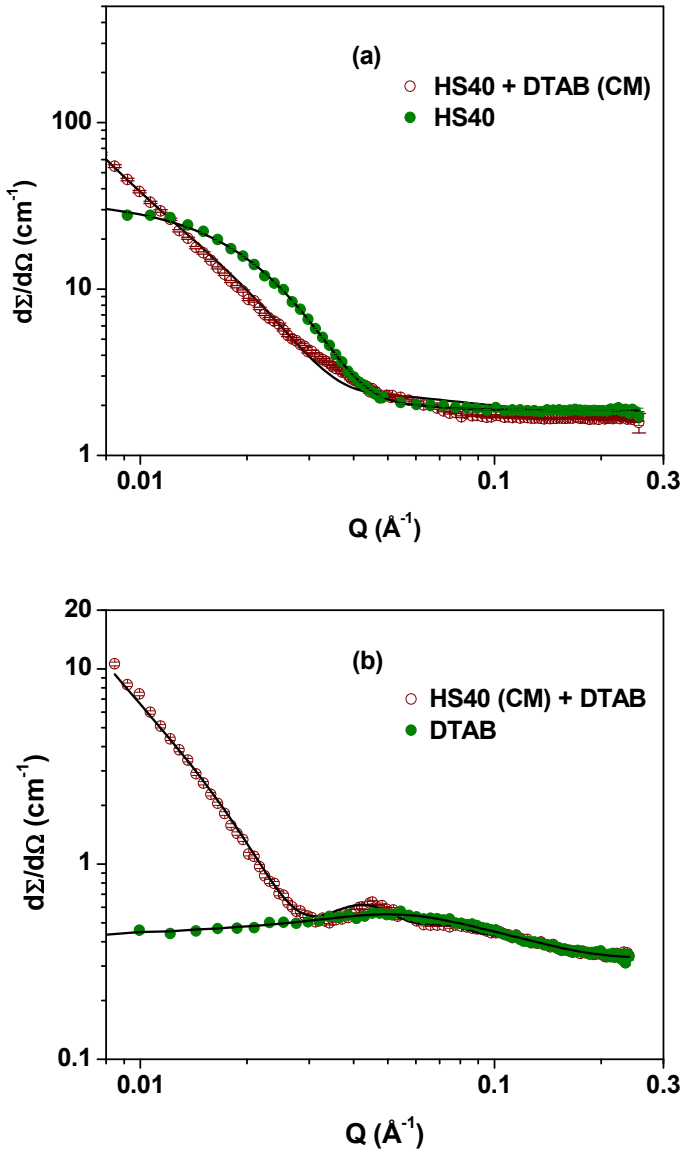

Figure 3.4. SANS data of 1 wt% HS40 with 1 wt% DTAB (a) micelles are contrast-matched along with data from pure nanoparticle system under the same contrast condition and (b) nanoparticles are contrast-matched along with data from pure surfactant system under the same contrast condition.

Figure 3.5 shows SANS data of 1 wt% HS40 with 1 wt% $C_{12}E_{10}$ (nonionic surfactant) under solution conditions of nanoparticles and micelles contrast-matched (87 vol% of H_2O in H_2O/D_2O) separately. The scattering profile of nanoparticle-$C_{12}E_{10}$ system changes dramatically from that of pure $C_{12}E_{10}$ system when the nanoparticles are contrast matched, suggesting the

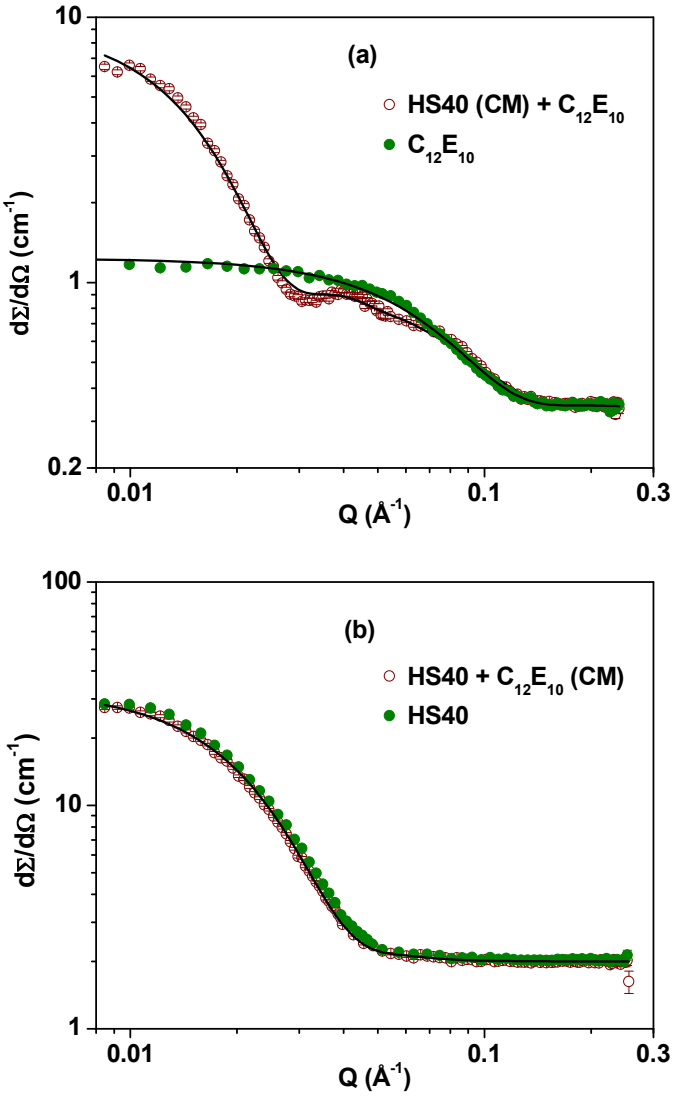

Figure 3.5. SANS data of 1 wt% HS40 with 1 wt% $C_{12}E_{10}$ (a) nanoparticles are contrast-matched along with data from pure surfactant system under the same contrast condition and (b) micelles are contrast-matched along with data from pure nanoparticle system under the same contrast condition

redistribution of micelles on their interaction with nanoparticles. There are two models known in the literature for the interaction (i) surfactant bilayer formation on the nanoparticle surface or (ii) direct adsorption of micelles on the nanoparticles [23, 27, 165, 182]. At 1 wt% concentration of nanoparticles and surfactant, the surfactant amount used is not enough to form bilayers on all the nanoparticles. It will require about 4 wt% of surfactant to able to form bilayer on all the

nanoparticles for 1wt% concentration which rules out the model of bilayer formation on the nanoparticle [166]. These adsorbed micelles form a shell around the nanoparticle which then has a larger scattering volume and thus results to the larger scattering in the low *Q* region. It may be mentioned that increase in the low Q data can also arise by considering the micelle generated attractive depletion interaction between nanoparticles. Similar to the SDS case, this has been examined in figure 3.5(b) where data of nanoparticle-$C_{12}E_{10}$ system with micelles contrast-matched match to that of pure nanoparticles suggesting that the buildup of scattering in the low *Q* region [figure 3.5(a)] cannot be because of the attractive depletion force [167]. It may also be mentioned that no aggregation of silica nanoparticles due to bridging through $C_{12}E_{10}$ has been observed even at higher concentration of $C_{12}E_{10}$. This is because of electrostatic repulsion of charge stabilized nanoparticles prevent them to approach each other to aggregate. The fitting of adsorption of micelles is simplified when the nanoparticles are contrast matched and therefore, the scattering is given by two terms that from adsorbed individual micelles and by interference of scattering from adsorbed micelles [167, 168]. The analysis gives that there are 40 micelles adsorbed per particle. It has also been found that there is a significant population of free micelles (46 %) in this system. Dynamic light scattering (DLS) from these systems show that the hydrodynamic size of nanoparticles increases significantly (17.0 to 30.6 nm) on addition of surfactant and is consistent with that of adsorption of their micelles at the nanoparticle surface (figure 3.6). A schematic of the microstructures formed as a result of interaction of silica nanoparticles with different surfactants is shown in figure 3.7.

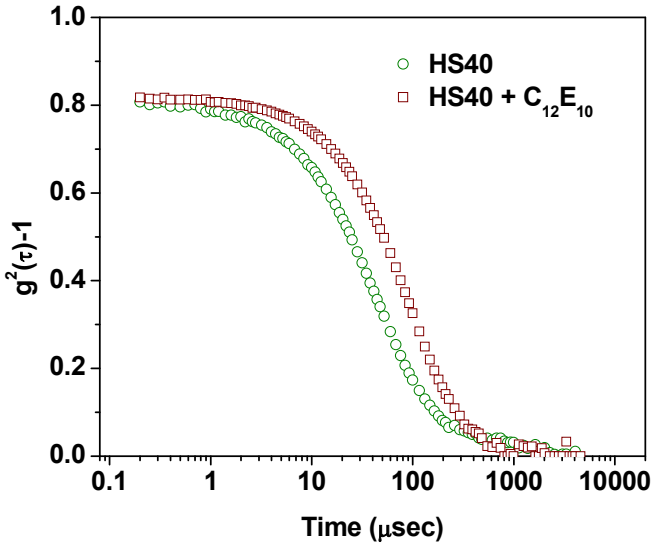

Figure 3.6. Autocorrelation functions of 1 wt% HS40 nanoparticles without and with 1 wt% $C_{12}E_{10}$ micelles as measured by dynamic light scattering.

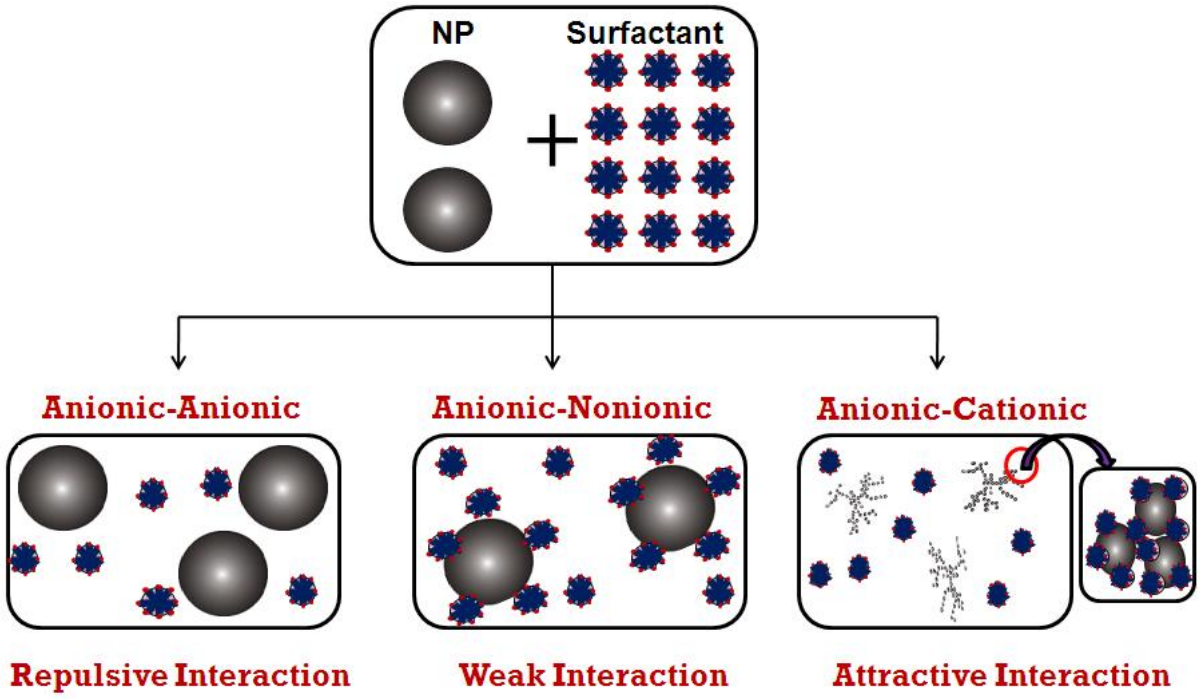

Figure 3.7. Schematic of the microstructures formed as a result of interaction of anionic silica nanoparticles with different charged surfactants.

3.4.3. Role of nanoparticle size on nanoparticle-surfactant interaction

The nanoparticles are known to show size dependent properties. Their interaction with surfactants is dictated by the combined effect of surface-to-volume ratio and surface curvature. Nanoparticle size can play a major role in case of interaction with anionic SDS surfactant where due to non-adsorbing nature of surfactants, the depletion interaction is expected to arise. The strength and range of the depletion interaction is known to be governed by size ratio of the components as well as their number density [25]. SANS data of SDS micelles mixed with varying sized nanoparticle systems SM30, HS40 and TM40 are given in figure 3.8 for each component (nanoparticle and surfactant) contrast-matched separately. Figure 3.8(a) show data of surfactant being contrast-matched whereas figure 3.8(b) nanoparticles contrast-matched to the solvent. All the data in figure 3.8(a) superimpose to curves of pure nanoparticle solutions indicating no consequence of depletion forces on particles and interaction in all the three systems because of the resultant interaction between particles is still dominated by the electrostatic repulsion [166, 167]. In this regards, the role of presence of salt to suppress electrostatic repulsion between colloidal particles and increasing surfactant concentration to enhance depletion could be interesting to examine. The data in figure 3.8(b) of silica nanoparticles (contrast-matched) with SDS exactly match to that of pure surfactant suggest that there is no physical interaction of nanoparticles with SDS as well as no changes in the micellar structure irrespective of the size of nanoparticles. The data in two contrast conditions are analyzed by considering the scattering only from nanoparticles (when micelles are contrast-matched) and from micelles (when nanoparticles are contrast-matched). The fitted parameters obtained are listed in table 3.3 and are in good agreement with that found for pure components.

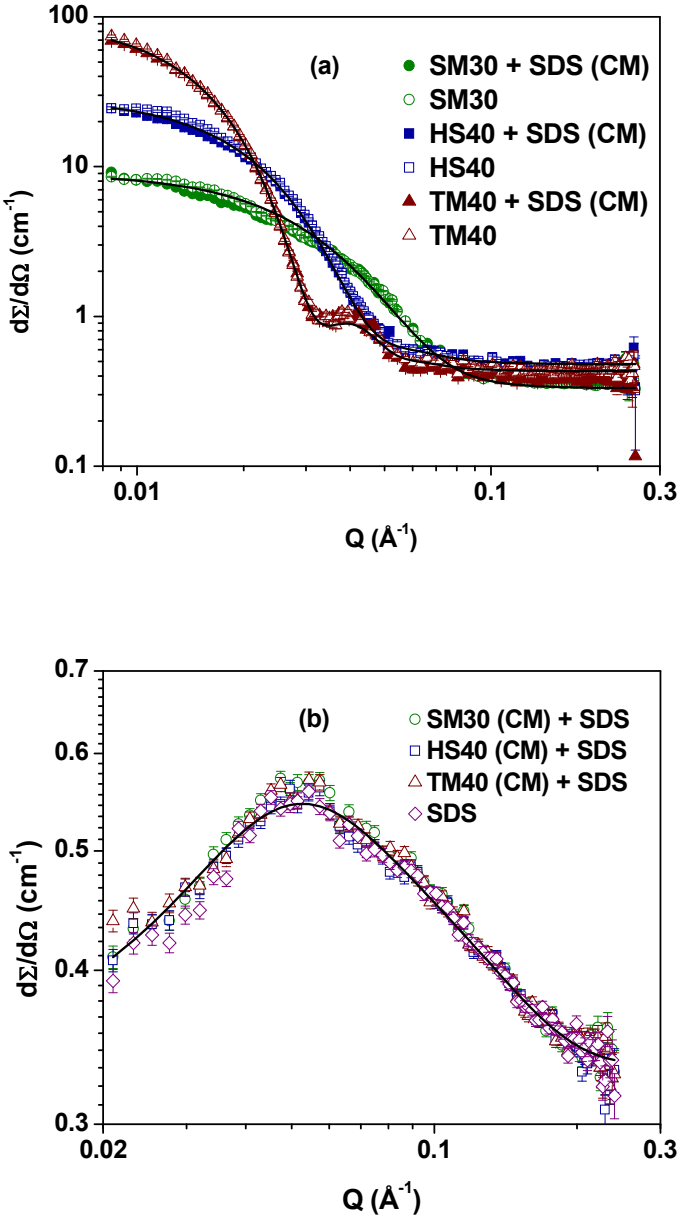

Figure 3.8. SANS data of 1 wt% SDS surfactant with 1 wt% silica nanoparticle systems (a) micelles are contrast-matched along with data from pure nanoparticle system under the same contrast condition and (b) nanoparticles are contrast-matched along with data from pure surfactant system under the same contrast condition.

Table 3.3. Fitted parameters of interaction of silica nanoparticle with SDS micelles.

(a) Structural parameters of SDS micelles as obtained by contrast matching nanoparticles.

Nanoparticle system	Semi-major axis a (nm)	Semi-minor axis b=c (nm)	Fractional charge α (*e.u.*)	Aggregation number N	Polydispersity σ
SM30	2.6 ± 0.2	1.5 ± 0.1	0.31 ± 0.03	61	0.15 ± 0.03
HS40	2.7 ± 0.2	1.5 ± 0.1	0.31 ± 0.04	61	0.15 ± 0.02
TM40	2.6 ± 0.2	1.5 ± 0.1	0.30 ± 0.04	61	0.15 0.03

(b) Structural parameters of nanoparticles when SDS micelles are contrast-matched.

Nanoparticle system	Mean radius R_m (nm)	Polydispersity σ
SM30	4.1 ± 0.2	0.3 ± 0.05
HS40	8.0 ± 0.4	0.2 ± 0.04
TM40	13.0 ± 0.5	0.15 ± 0.03

SANS data of 1 wt% different sized silica nanoparticle systems with 1 wt% DTAB micelles in 3 different contrast conditions [(a) no components (solvent is D_2O), (b) micelles and (c) nanoparticles are contrast-matched] are shown in figure 3.9. All these data can be divided in three Q regions as (i) low Q data where the scattering is governed by the fractal aggregates, (ii) the scattering from the building block of the aggregate structure in the intermediate Q range and (iii) scattering from individual micelles at high Q values. In figure 3.9 (a) with no components contrast-matched, the SANS data for each of the three sized nanoparticles mixed with DTAB

show similar features at low and high Q regions, whereas differ mainly in intermediate Q region. This can be explained if the individual micelles (adsorbed or free) as well as overall aggregates of nanoparticles in the resultant structure are similar irrespective of the size of nanoparticles [183]. The similar structure of overall aggregate of nanoparticles means that they can be forming the similar fractal dimension and size. The data of micelles contrast-matched [figure 3.9 (b)] show high scattering in the low Q region for the larger size of the particles because of the larger volume fraction of particles in the aggregate structure as the adsorbed micelle volume fraction is expected to decrease with the increase in the nanoparticle size. This decrease of adsorbed micelle volume fraction is directly observed for the scattering data of particles contrast-matched [figure 3.9 (c)]. It may be added that even though micelles are not seen in figure 3.9 (b), the data at large Q are found similar because of high incoherent background from the solvent of micelles contrast-matched. The significant differences in all the data of figures 3.9 (a) – (c) in the intermediate Q range is observed because the intensity in this Q range is mainly governed by different sized building blocks. The data have been analyzed using equation (3.6) making use of different contrast conditions for different information. In the case of micelles contrast-matched [figure 3.9 (b)], the values of fractal dimension, particle size and building block size are obtained from the analysis [table 3.4 (a)]. It is interesting to note that irrespective of the particle size the fractal dimension of particle aggregates is same about 2.3. The building block size is found approximately by sum of the sizes of particle and micelle. The fitted parameters of SANS data of no components contrast-matched [figure 3.9 (a)] are given in table 3.4 (b). These data provide additional information on the volume fraction of free micelles in these systems. The volume fraction of free micelles as expected increases with the particle size as overall surface

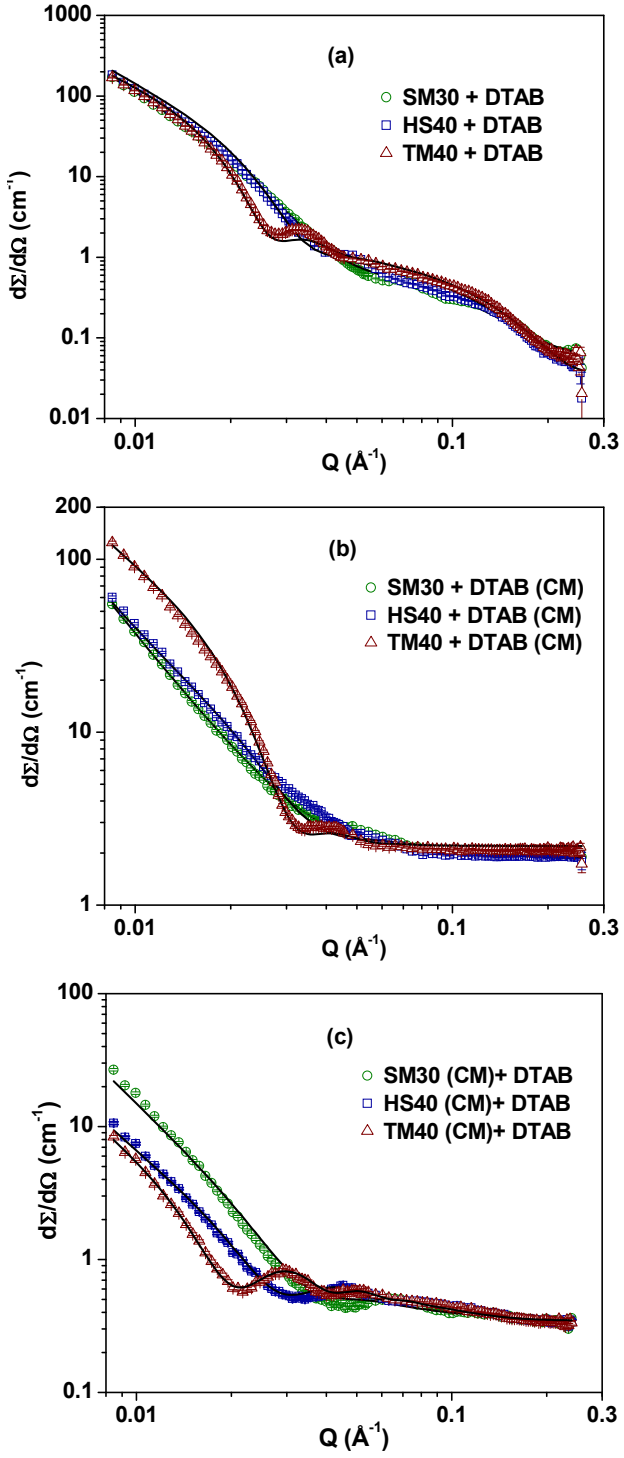

Figure 3.9. SANS data of 1 wt% DTAB surfactant with 1 wt% silica nanoparticle systems (a) no component is contrast-matched, (b) DTAB micelles are contrast-matched and (c) nanoparticles are contrast-matched to the solvent.

Table 3.4. Structural parameters of interaction of silica nanoparticle with DTAB micelles.

(a) Micelles are contrast-matched.

Nanoparticle system	Particle radius Rp (nm)	Building block radius R_b (nm)	Fractal dimension D_m
SM30	4.0 ± 1.0	5.8 ± 0.2	2.2 ± 0.2
HS40	8.0 ± 0.3	10.2 ± 0.4	2.3 ± 0.2
TM40	13.0 ± 0.5	14.8 ± 0.5	2.3 ± 0.2

(b) Both components (nanoparticles and micelles) are visible.

Nanoparticle system	Particle radius Rp (nm)	Building block radius R_b (nm)	Fractal dimension D_m	% Vol of free micelles
SM30	4.0 ± 1.0	5.8 ± 0.2	2.2 ± 0.2	56
HS40	8.0 ± 0.3	10.2 ± 0.4	2.3 ± 0.2	70
TM40	13.0 ± 0.5	14.8 ± 0.5	2.3 ± 0.2	77

(c) Nanoparticles are contrast-matched.

Nanoparticle system	Particle radius Rp (nm)	Building block radius R_b (nm)	Fractal dimension D_m	Number of adsorbed micelles per particle	Surface number density (10^{-2}/nm^2)
SM30	4.0 ± 1.0	5.8 ± 0.2	2.2 ± 0.2	7	3.3
HS40	8.0 ± 0.3	10.2 ± 0.4	2.3 ± 0.2	42	5.2
TM40	13.0 ± 0.5	14.8 ± 0.5	2.3 ± 0.2	150	7.0

available for micelle adsorption decreases for fixed concentration of particles. The fitting of nanoparticles contrast-matched data provide direct observation of adsorption of micelles on the nanoparticle. The number of adsorbed micelles per unit surface area of the nanoparticles is also found to increase with increasing particle size [table 3.4 (c)]. This suggests that the smaller curvature supports to higher surface number density as for micelles to contact with nanoparticle become easier [20, 167]. However, the resultant adsorption of micelles on the nanoparticle surface is decided by the competitive effects of curvature and surface effect. The measured number of adsorbed micelles in all three nanoparticle systems is found to be significantly less than the theoretical limit of number of adsorbed micelles based on maximum surface availability of nanoparticle to micelles. The theoretical limit was calculated considering adsorption of micelles on nanoparticle surface in the ordered packing. However, in actual this may not be the case because of randomness of available sites for hydrogen bonding.

The SANS data of interaction of 1 wt% of different sized nanoparticles with 1 wt% $C_{12}E_{10}$ in the two contrast conditions (a) nanoparticles are contrast-matched and (b) micelles are contrast-matched are shown in figure 3.10. These data are for the solution condition when nanoparticles are contrast-matched to the solvent which simplify the analysis by minimizing the number of fitting parameters. When the components, nanoparticles and micelles are visible for the solvent (prepared in D_2O) the scattering from such systems is much more complex than with nanoparticles contrast-matched. The scattering therefore in figure 3.10 (a) is only from that of the adsorbed and free (if any) micelles [166-168]. The data of nanoparticle-$C_{12}E_{10}$ systems are also compared with that from $C_{12}E_{10}$ micelles alone. All the data match at higher Q region corresponding to number of micelles (adsorbed + free) whereas there is build up in the scattering

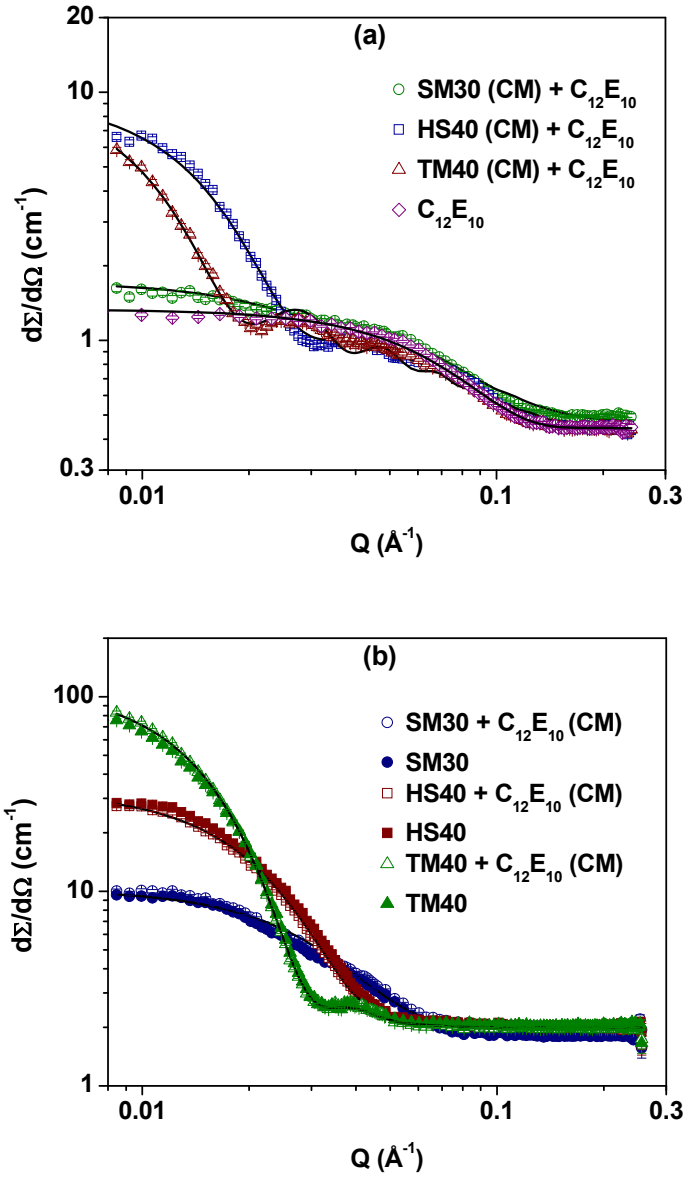

Figure 3.10. SANS data of 1 wt% $C_{12}E_{10}$ surfactant with 1 wt% silica nanoparticle systems (a) nanoparticles are contrast-matched along with data from pure surfactant system under the same contrast condition and (b) micelles are contrast-matched along with data from pure nanoparticle systems under the same contrast condition.

data in the low *Q* region decided by the adsorbed micelles. The width of the scattering buildup in the low *Q* region depends inversely on the particle size. The fitted parameters of particle size dependent micelle adsorption are given in table 3.5. It is found that the number of

adsorbed micelles per particle increases drastically with the size of the particle. However, the fraction of adsorbed micelles decreases and can be expected as the surface available to micelle adsorption decreases with the increase in the nanoparticle size. There are also no significant changes observed in the interaction of nanoparticles irrespective of its size where all systems [figure 3.9 (b)] follow same features of that of pure nanoparticles [figure 3.1 (a)]. The increase in number of adsorbed micelles per unit surface area in this case of nonionic surfactant show a different variation than that of cationic surfactant, indicating both curvature of particle and type of micelle are important to decide the resultant adsorption of micelle on nanoparticle [167].

Table 3.5. Structural parameters of interaction of silica nanoparticle systems with $C_{12}E_{10}$ micelles when nanoparticles are contrast-matched.

Nanoparticle system	Adsorbed number of micelles	Fraction of free micelles (%)	Fraction of adsorbed micelles (%)	Surface number density (10^{-2}/nm^2)
SM30	3	30	70	1.4
HS40	40	46	54	4.9
TM40	105	77	23	4.9

3.5. Conclusions

The interaction of anionic silica nanoparticles with three different types of surfactants (anionic, cationic and non-ionic) has been examined. It is found that the interaction of anionic silica nanoparticles with anionic, cationic and nonionic surfactants is very different and each case leads different microstructures. Further, these microstructures can be tuned by varying the particle size. The dominant repulsion in the case of silica nanoparticles with anionic SDS

micelles prevents any physical interaction of the two components irrespective of particle size. There are neither any significant changes seen in the structure of micelle nor any depletion force arising between particles by micelles. The strong attractive interaction of nanoparticles with cationic DTAB micelles leads to the aggregation of particles and is characterized by a fractal structure. The fractal dimension is found to be same about 2.3 for all the sizes of particles and indicates a DLA (diffusion limited aggregation) type of fractal morphology of the aggregates. In the case of nonionic surfactant $C_{12}E_{10}$, surfactant molecules adsorb on the individual silica nanoparticles through hydrogen bonding of ether oxygen of the ethylene oxide group and the surface OH group. The interaction is examined using two models: first one that considers the surfactant layer coating on silica nanoparticles and the second one where the surface of nanoparticles is decorated by the micelles. The present results confirm the uniform decoration of non-ionic micelles on the nanoparticles. The number of adsorbed micelles per particle increases drastically but the overall percentage of adsorbed micelles decreases with the increase in the particle size.

Chapter 4

PROTEIN ADSORPTION ON NANOPARTICLES AND THEIR COMPLEX STRUCTURES

4.1. Introduction

The use of nanoparticles in biotechnology is of high scientific interest due to the amazing potential displayed by complex systems combining the properties of nanoparticles and the specific architectures and functions of the biological molecules. The nanoparticle-biomolecule complexes in particular are useful in the emerging field of nanobiotechnology (nanomedicine, drug delivery and biosensors) as the nanoparticles having sizes comparable to that of living cells as well as can access and operate within the cell [184-186]. The biomolecules adjoined to nanoparticles enable them to probe biological processes that are critical for diagnostics and the modulation of cell functions [187-189]. The understanding of nanoparticle interaction with different biomolecules like DNA, phospholipid and protein is prerequisite for such applications.

The interaction of nanoparticle with protein represents a model system to understand the behavior of nanoparticle-biomolecule complexes. Proteins are charged molecules and their function depends on the native folded structure [55, 190]. In physiological environment, proteins are known to cover nanoparticles immediately and therefore their structure and functionality may be disturbed [184]. A number of studies have been carried out to examine the adsorption of proteins on nanoparticles and its effect on the protein structure and activity using different techniques such as ellipsometry, reflectometry, circular dichroism (CD), nuclear magnetic resonance (NMR), Raman spectroscopy, infrared spectroscopy etc [88, 191-195]. The presence

of protein is also known to cause interactional changes of the nanoparticle systems. The tuning of interaction between nanoparticles through the adsorption of different macromolecules has been of recent great interest as nanoparticle-protein system can lead from enhancement in stabilization to the aggregation of particles [120, 196]. Dependence of particle-mediated adhesion energies on their adsorption curves has also been reported [197]. While there are many studies focusing on the effect of nanoparticles on protein structures, it is not clear how protein adsorption affects the interaction between nanoparticles.

The lysozyme protein and silica nanoparticles are one of the most studied model systems, where both components individually are charge stabilized colloids interacting via a short-range attractive potential combined with long-range repulsion [88, 120, 121, 192, 198]. The interaction in their complexes between nanoparticles and protein is predominantly governed by the resultant electrostatic interactions which are known to lead many nonspecific associations especially relevant in biological systems and having several important applications [199-201]. The competition of attraction between two components and repulsion between individual components in oppositely charged nanoparticles and protein systems plays important role in determining the protein adsorption as well as resultant structure of their complexes. In this regard, charge on the two components as governed by solution properties (e.g. pH) can play important role to control their interaction and resultant structure in these systems. The formation of different nanostructures from randomly branched complexes to single-strand nanorods have been reported in oppositely charged nanoparticle and polyelectrolyte systems by tuning of electrostatic interactions whereas growth of 3D networks of silica nanoparticles of different geometry demonstrated in nanoparticle-DNA system [202-204]. There is interest to know such evolution of structures in nanoparticle-protein systems with the systematic variation of their charge states.

In this chapter, the interaction and resultant structure of lysozyme protein with different sized silica nanoparticle at varying pH have been examined [205-209]. UV-visible spectroscopy is carried out to measure the adsorption curves of protein on nanoparticles. SANS measurements provide resultant structures of nanoparticles at different protein concentrations of the adsorption curves.

4.2. Experimental section

Electrostatically stabilized colloidal suspension of silica nanoparticles (Ludox SM30, LS30 and TM50) and hen egg protein lysozyme were purchased from Sigma-Aldrich and Fluka, respectively. The adsorption curves of protein interaction with silica nanoparticles in aqueous solution were studied using a nanodrop spectrophotometer ND 1000. The instrument is based on surface retention technology utilizing the surface tension to hold the sample. A pulsed Xenon flash lamp is used as a source to cover the spectrum range from 220 to 750 nm and the light coming through the sample is analyzed by CCD arrays. Absorbance spectra of protein solutions of different concentrations (wt%) prepared in H_2O at three pH (5, 7 and 9) values were recorded as a function of wavelength. Three buffer solutions (20 mM) from acetate buffer for pH 5, phosphate buffer for pH 7 and Borax buffer for pH 9 were used for maintaining the pH. D_2O was used as solvent in samples for SANS experiments as it provides better contrast for hydrogenous samples and low incoherent background. Small-angle neutron scattering experiments were performed using SANS spectrometer at the Dhruva reactor, Bhabha Atomic Research Centre, Mumbai [145] and D22 facility at the Institut Laue Langevin, France [147], to cover a data in a wide Q range (0.003 to 0.35 $Å^{-1}$). All the measurements were carried out for fixed concentration (1 wt%) of silica nanoparticles and varying the concentration of protein in the range 0 to 10 wt%.

The temperature was kept constant at 30 ^{o}C during all the measurements. The data were corrected and normalized to absolute scale using standard procedure.

4.3. SANS analysis

In SANS experiments, one measures the coherent differential scattering cross-section per unit volume ($d\Sigma/d\Omega$) as a function of Q. For particles dispersed in a medium, it can be written as [124, 127]

$$\frac{d\Sigma}{d\Omega}(Q) = n(\rho_p - \rho_s)^2 V_p{}^2 P(Q) S(Q) + B \tag{4.1}$$

where n denotes number density and V_p is the volume of the nanoparticle. ρ_p and ρ_s are the scattering length densities of nanoparticle and solvent, respectively. $P(Q)$ is intraparticle structure factor, $S(Q)$ is interparticle structure factor and B is a constant term representing incoherent background.

Different models are used for the calculation of $P(Q)$ for the nanoparticles and proteins. The structures which involve protein adsorption onto the nanoparticles are modeled by core-shell structure. The details and the expressions for different $P(Q)$ are discussed in chapter 2. The particle aggregation is characterized by mass fractal and surface fractal structures. The expressions for $S(Q)$ accounting these structures are as described in chapter 2.

The corrections were made during the data analysis for the instrumental smearing where calculated scattering profiles are smeared by the appropriate resolution function to compare with the measured data. The parameters in the analysis were optimized by means of nonlinear least-square fitting program [127, 150].

4.4. Results and discussion

4.4.1. Protein adsorption and aggregation of nanoparticles

The lysozyme protein adsorption curve on LS30 silica nanoparticles ($2R_m$ ~ 16 nm) expressed as amount of protein adsorbed (wt%) vs. total protein obtained using UV-Visible spectroscopy is depicted in figure 4.1. The samples for these experiments were prepared by mixing the fixed concentration of 1 wt% silica nanoparticles and varying concentrations of lysozyme protein in aqueous solution. These samples are filled in cuvettes and centrifuged to separate free protein if any from that of the protein adsorbed on the nanoparticles. After the first run, the supernatants were carefully removed and kept in fresh cuvettes. The same procedure is repeated couple of times to improve the separation process. The UV-visible spectrum of the

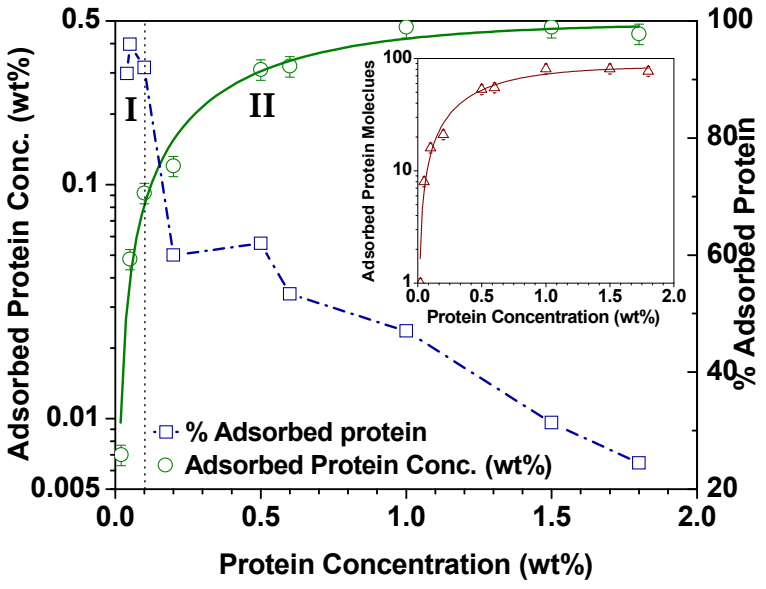

Figure 4.1. Lysozyme protein adsorption curve in 1 wt% LS30 silica nanoparticle solution. The variations of adsorbed protein concentration (in wt%) as well as fraction (in %) of adsorbed protein (protein adsorbed×100/total protein) are plotted on left and right Y-axis, respectively. Inset shows the protein concentration dependent adsorption of protein molecules per nanoparticle.

lysozyme shows a peak at about 280 nm due to the absorption of the incident light by protein [210]. The concentration of the free protein in the sample is calculated by measuring the ratio of this absorbance of the supernatants to the corresponding pure protein solution. It is seen in figure 4.1 that at low protein concentrations the amount of the adsorbed protein increases with the increase in concentration and saturates at high protein concentrations. These data are fitted with an exponential rise of the adsorbed protein (A) as a function of protein concentration (C) as given by $A=A_0[1- \exp^{-kC}]$, where A_0 is the saturation value and k is the adsorption coefficient [205, 206]. The values of A_0 and k are found to be 0.50 wt% protein and 2.0 per wt% protein, respectively. Based on these data, the concentration dependent propensity (A/C) of protein adsorption on nanoparticles has also been calculated (figure 4.1). The results show while the adsorption of protein is very high at low protein concentrations (e.g. 95 % at 0.05 wt%), it significantly decreases at higher protein concentrations (e.g. 20 % at 2 wt%).[26] The inset of figure 4.1 shows the variation of calculated number of adsorbed protein molecules (proportional to the adsorbed protein concentration) on individual nanoparticle with protein concentration.

The strong electrostatic attraction between nanoparticle and protein leads to protein-mediated aggregation of nanoparticles [120, 205]. SANS has been used to examine the structures of the aggregates formed. Figure 4.2 shows the SANS data of 1 wt% silica nanoparticles with varying concentration of lysozyme. The data are divided into two sets (i) low protein concentration in figure 4.2(a) and (ii) high protein concentration in figure 4.2(b) regimes. The first data set is considered in the protein concentration range from 0 to 0.1 wt% which shows the rise in scattering towards linearity on log-log scale in the low Q region and no significant change at high Q region on addition of protein. On the other hand, all the data in the second set (protein concentration > 0.2 wt%) show the linearity on log-log scale with no significant change in the

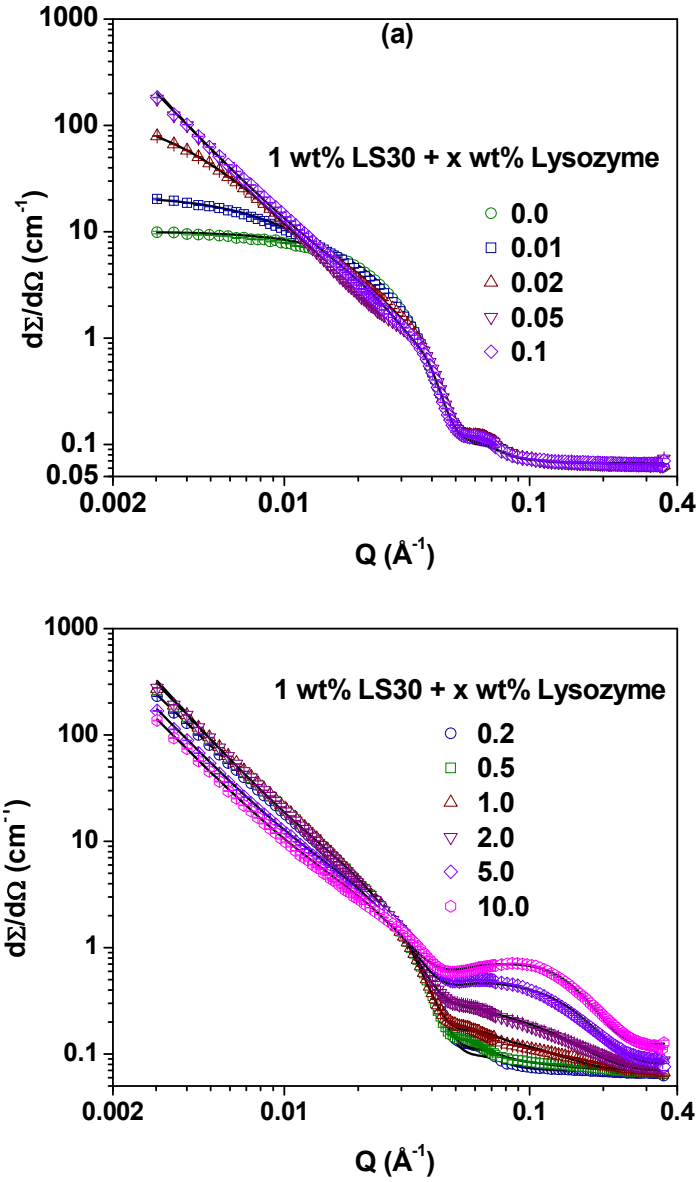

Figure 4.2. SANS data of 1 wt% LS30 silica nanoparticle system with (a) lower protein concentration (0.0 to 0.1 wt%) and (b) higher protein concentration (0.2 to 10 wt%) at pH 7.

low *Q* region on further addition of protein. Moreover, in second data set there is distinct buildup in scattering profile at higher *Q* region with increasing protein concentration [figure 4.2 (b)]. The large rise in the scattering intensity in the low *Q* region in figure 4.2 (a) can not be explained just based on the adsorption of protein on individual nanoparticles (core-shell structure) because

of the low scattering from proteins being smaller molecule with low contrast. However, these data can be explained by the aggregation of the particles arising as a result of neutralization of charge on the nanoparticle by the adsorption of protein. The aggregates are fitted with the fractal structure as indicated by linearity in the low Q region on log-log scale [140, 205]. The analysis shows that in the first data set protein concentration is not enough to aggregate all the particles and therefore particle aggregates coexist with the free particles. The fitting involves the resultant scattering cross-section governed by sum of two contributions from fractal aggregates and non-aggregated nanoparticles. The fitted parameters are given in table 4.1. It is believed that beyond this concentration charge neutralization by protein adsorption approaches to the value that all particles can aggregate. To confirm this, the iso-electric point (point of zero charge) for the mixture of silica nanoparticles and lysozyme has also been measured [205]. For 1 wt% LS30 silica nanoparticles at pH=7, the isoelectric point is obtained at 0.25 wt% lysozyme. This is typically the value before which all the nanoparticles have been found to be aggregated in SANS study. It is expected that protein molecules can still adsorbed on the nanoparticles beyond this concentration (0.25 wt%) up to the value of their saturation. The aggregates are found to have fractal structure having fractal dimension about 2.4 and the number fraction of aggregated particles increases with increasing protein concentration (table 4.1). It is also found that all the nanoparticles get aggregated for protein concentration at 0.1 wt% and beyond this concentration. The data of second set consists of all particles aggregates as there is no significant change in the data in the low Q region. The buildup observed at high Q region is because of increasing protein concentration. In this case, the data are analyzed by combining the contributions from free proteins and nanoparticle aggregates, respectively. The fractal dimension is found to be 2.4 and building block radius of about 9.2 nm. The building block size of the fractal structure (~ 18.4

nm) is larger than the size of the silica nanoparticle (16.0 nm).This increase is expected as the attraction of nanoparticles is mediated by the presence of oppositely charged protein molecules between them. The difference in the size of the building block and the nanoparticle (2.4 nm) is significantly less than that of the folded size of the protein molecule (equivalent diameter ~ 3.2 nm which could be as a result of disruption in the folded structure of protein on interaction with

Table 4.1. Fitted parameters of interaction of 1 wt% LS30 silica nanoparticle system with varying lysozyme protein concentration.

(a) Low protein concentration regime.

Concentration C (wt%)	Particle radius R_m (nm)	Building block radius R_b (nm)	Fractal dimension D	Fraction of aggregated nanoparticles ϕ_{anp} (%)
0.0	8.0 ± 0.2	-	-	0
0.01	8.0 ± 0.2	9.0 ± 0.2	2.5 ± 0.1	24
0.02	8.1 ± 0.2	9.0 ± 0.2	2.5 ± 0.1	43
0.05	8.0 ± 0.2	9.1 ± 0.2	2.4 ± 0.1	80
0.1	8.0 ± 0.2	9.2 ± 0.2	2.5 ± 0.1	100

(b) High protein concentration regime.

Concentration C (wt%)	Particle radius R_m (nm)	Building block radius R_b (nm)	Fractal dimension D	Fraction of free protein ϕ_{fp} (%)
0.2	8.1 ± 0.2	9.3 ± 0.2	2.5 ± 0.1	24
0.5	8.0 ± 0.2	9.2 ± 0.2	2.5 ± 0.1	48
1.0	8.0 ± 0.2	9.3 ± 0.2	2.4 ± 0.1	60
2.0	8.1 ± 0.2	9.4 ± 0.2	2.5 ± 0.1	69
5.0	8.0 ± 0.2	9.3 ± 0.2	2.3 ± 0.1	75
10.0	8.1 ± 0.2	9.4 ± 0.2	2.4 ± 0.1	82

silica nanoparticle [121, 192]. Further any features corresponding to the overall size of the aggregates (low Q cut-off) are not observed within Q range of our measurements. A fractal dimension 2.4 in three dimension Euclidean space indicates a diffusion limited aggregate (DLA) type of fractal morphology of the aggregates [211, 212]. These fractal structures are highly branched and usually formed when the density of particles is quite low and the repulsive forces are relatively weak as is the case of present system. It may be mentioned that the results of SANS are consistent to that of UV-Visible spectroscopy where first and second SANS data sets correspond to the region I and II in figure 4.1, respectively. The first SANS data set and region I corroborate to the high protein adsorption whereas second SANS data set and region II in figure 4.1 confirms the existence of free protein in the system. Such coexistence of aggregated nanoparticle and un-aggregated nanoparticles has also been observed in case of addition of Al_{13} polycations to silica nanoparticles [213]. A schematic of evolution of nanoparticle-protein complex structures corresponding to two protein concentration regimes is shown in figure 4.3.

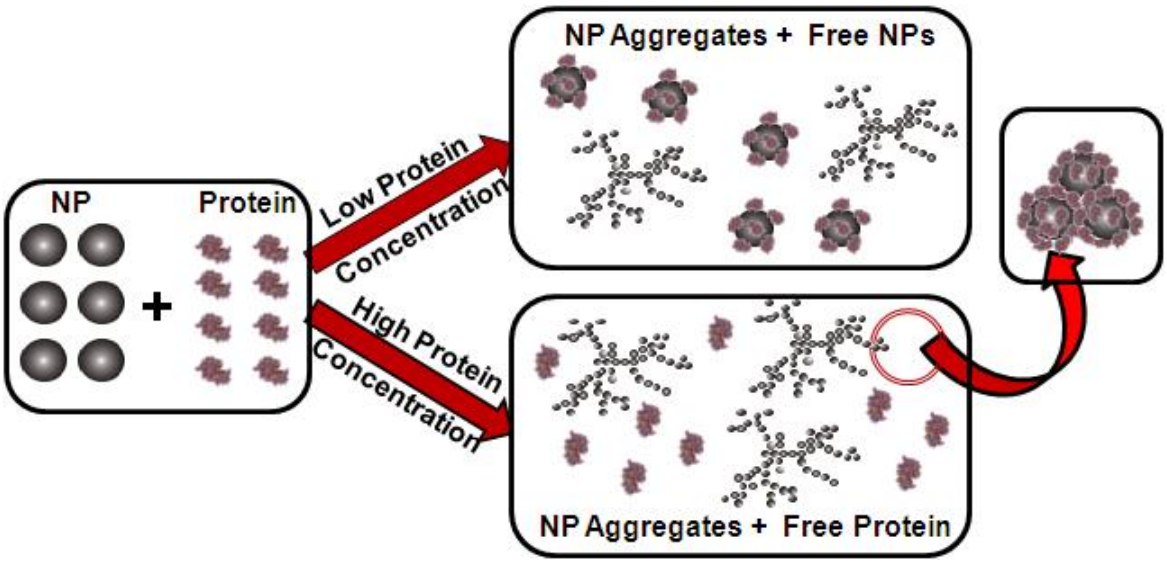

Figure 4.3. Schematic of aggregation of silica nanoparticles in presence of lysozyme protein.

4.4.2. pH dependent nanoparticle-protein interaction

Firstly, the effect of pH on pure components has been examined in figure 4.4, where the SANS data of 1 wt% concentration of pure silica nanoparticles (LS30) and lysozyme protein at three pH values (5, 7 and 9) are shown. Irrespective of the pH value, there is no change observed in the silica nanoparticle systems. However, protein solution shows change in scattering behavior with the change in pH. The SANS data of 1 wt% concentration of silica nanoparticles indicates that the system may be treated as dilute at all the three pH values. The SANS data of lysozyme protein also show scattering governed by form factor $P(Q)$ at pH 7 and 9 whereas contribution from $S(Q)$ is observed in the data at pH 5. This is as a result of interparticle interaction in protein solutions changing with pH. The iso-electric point of lysozyme is about 11.4 and as one goes away from this value the charge on protein is known to increase [120, 214]. The increase in charge along with higher number density of protein molecules results in the $S(Q)$ observed at pH 5. In fact as the concentration of protein is increased, the contribution of $S(Q)$ is observed at all

Table 4.2. Fitted parameters of SANS data from 5 wt% lysozyme protein solutions at three pH values (5, 7 and 9).

pH	Semi-major axis a (nm)	Semi-minor axis (b=c) (nm)	Equivalent radius R_e (nm)	Charge Z (e.u.)
5	2.4 ± 0.1	1.4 ± 0. 1	1.7 ± 0.1	10.0 ± 0.8
7	2.4 ± 0.1	1.4 ± 0.1	1.7 ± 0.1	7.0 ± 0.5
9	2.4 ± 0.1	1.4 ± 0.1	1.7 ± 0.1	5.8 ± 0.3

the pH values [inset of figure 4.4(b)]. The SANS data of lysozyme protein are fitted using form factor $P(Q)$ for prolate ellipsoidal shape and structure factor $S(Q)$ using Hayter and Penfold

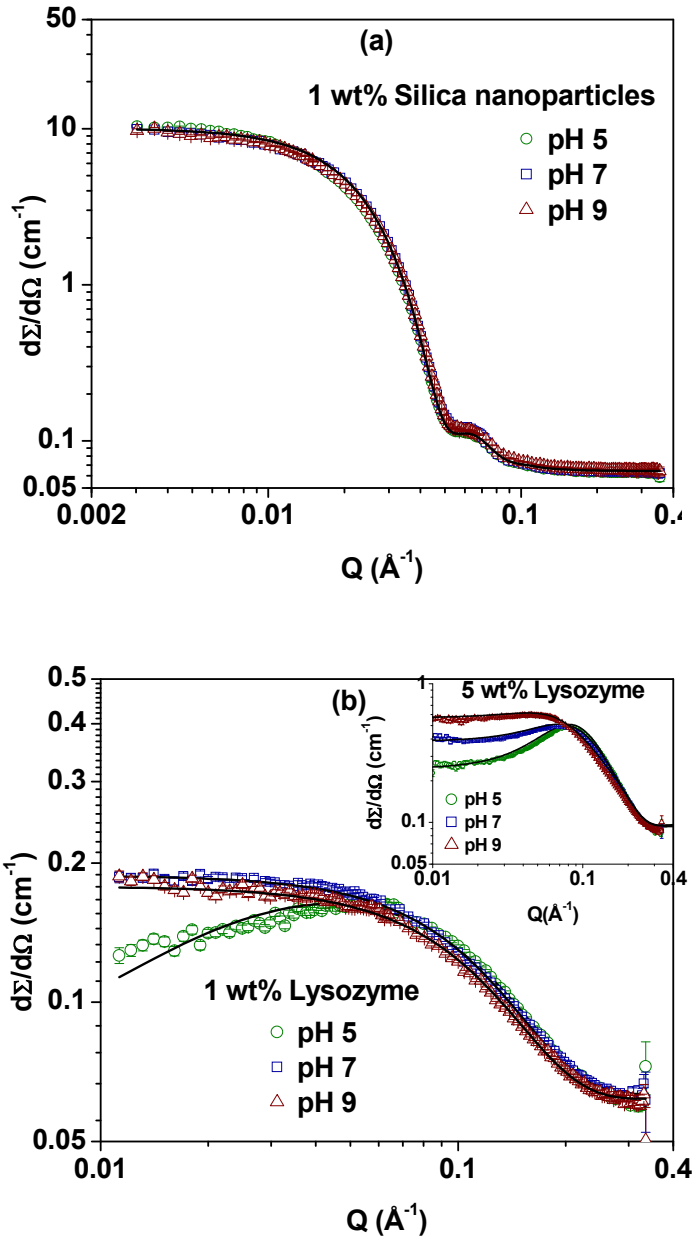

Figure 4.4. SANS data of 1 wt% concentration of (a) LS30 silica nanoparticles and (b) lysozyme protein solutions at three pH values (5, 7 and 9). Inset of figure 4.4(b) shows SANS data of 5 wt% protein solutions.

analysis under Rescaled Mean Spherical Approximation for charged macroions as discussed in chapter 2 [215]. The pH dependent fitted parameters for lysozyme protein are given in table 4.2

and found to have similar values to those reported earlier. These results suggest that the structure of silica nanoparticles and lysozyme protein remain same but degree of interaction between them changes with the pH.

The protein adsorption depends on the interparticle interactions present in the nanoparticle-protein system which are tuned by varying pH. The adsorption curves for protein adsorption on silica nanoparticles (LS30) at three pH values (5, 7 and 9) is compared in figure 4.5. Regardless of the pH, the adsorption curves are found to show an exponential behavior as found in figure 4.1. The calculated values of saturation value (A_0) and adsorption coefficient (k) for different pH are given in table 4.3.

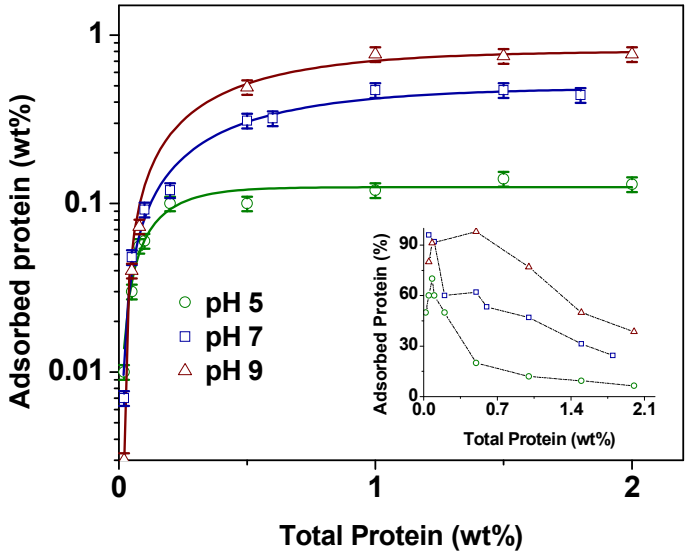

Figure 4.5. Lysozyme protein adsorption curve on LS30 silica nanoparticles (1 wt%) expressed as adsorbed protein vs. total protein (in wt%) at three pH values (5, 7 and 9). Inset shows the calculated variation of % adsorbed protein on nanoparticles in these systems.

The saturation value (A_0) of the protein adsorption is interestingly found to be increasing with increase in pH of the solution. The saturation value is believed to be governed by the cumulative effect of two factors (i) the attraction between silica nanoparticles and protein (ii) mutual repulsion between protein molecules [121, 192, 206]. Surface charge density of the silica

particles increases whereas charge on protein molecules decreases with increasing pH. Therefore the strength of attraction between the silica particles and lysozyme decreases but at the same time the repulsion between lysozyme also decrease causing more protein to adsorb on the nanoparticles. On the contrary, adsorption coefficient (k) decreases with the pH of the solution. Adsorption coefficient is decided by the strength of attraction between nanoparticles and protein, which therefore increases with decrease in pH (increase of the protein charge). The value of A/C (% protein adsorbed) is found strongly depending on pH as well as protein concentration. Further, it shows that the decrease in % protein adsorption on nanoparticle is similar to that of an exponential decay behavior where the amount of protein adsorption at high protein concentration is expected to be small but finite [206].

Table 4.3. Fitted parameters for adsorption curves of lysozyme protein on silica nanoparticles.

pH	A_0 (wt %)	k (1/wt %)
5	0.12 ± 0.02	6.8 ± 0.9
7	0.49 ± 0.03	2.1 ± 0.3
9	0.80 ± 0.04	1.9 ± 0.3

In order to examine the pH dependence of protein-mediated nanoparticle aggregates, SANS measurements have been carried out at different pH values. Figure 4.6 shows the SANS data of 1 wt% LS30 silica nanoparticles with varying protein concentration at pH 5. Unlike the case of pH 7, based on the features of the scattering profiles SANS data are divided into three protein concentration regimes (i) low protein concentration [figure 4.6(a)], (ii) intermediate concentration [figure 4.6(b)] and (iii) high protein concentration [figure 4.6(c)]. Similar to figure 4.2 (a), in the first data set (0 to 0.02 wt% protein concentration) there is a strong buildup of scattering intensity in the low Q region with relatively small changes in the intermediate and

high Q region. The second data set (0.05 to 1.0 wt%) show evolution of a Bragg peak like behavior at intermediate Q values which interestingly disappears with increasing protein concentration. On the other hand, data in the third set (2 to 10 wt%) show systematic scattering build up at high Q values while almost no change in scattering intensity at low and intermediate Q values. As explained earlier, in the first data set, the nanoparticle aggregates coexist with the un-aggregated nanoparticles [205, 206]. The scattering buildup in the low Q region is enhanced as the fraction of aggregated nanoparticles increases with protein concentration. The presence of Bragg peak in figure 4.6 (b) arises as a result of ordering of nanoparticles in the aggregates [206]. Only 0.02 wt% protein is required to aggregate all the nanoparticles. In this set, all nanoparticles have been aggregated where order of aggregate structures changes with the protein concentration. These aggregates have been characterized by surface fractals [$Q^{-(6-Ds)}$] having fractal dimension (D_s) about 2.7 [141, 142, 206]. The order aggregates coexists with free protein in second data set. The ordering of particles within the aggregates as reflected in the Bragg peak has been fitted using hard sphere interaction between the nanoparticles under PYA (equation 2.46). The surface fractal dimension and volume fraction of particles within aggregates decrease with increase in protein concentration. Further addition of protein molecules (third data set) suppress the protein-mediated attraction between nanoparticles through increase in protein–protein repulsion, which results in the transformation of order aggregates of second data set into fractal structure. Such morphological transition in aggregated structure is also suggested in other reports [120, 196]. The third data set fit to the mass fractal [Q^{-Dm}] morphology of the aggregates along with free proteins similar to that at pH 7 [figure 4.2(b)]. The fractal aggregates remain unchanged and the fraction of free protein increases with the increase in protein concentration.

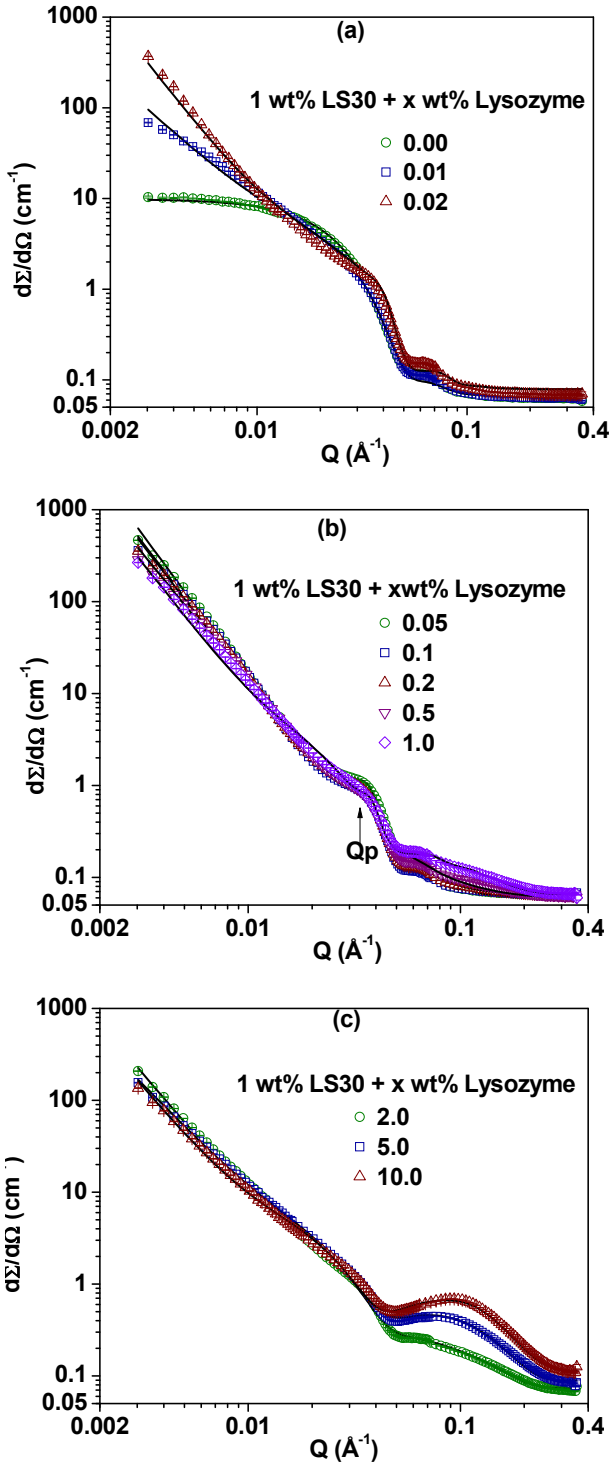

Figure 4.6. SANS data of 1 wt% LS30 silica nanoparticle system at pH 5 with (a) lower protein concentration (0.0 to 0.1 wt%), (b) intermediate protein concentration (0.05 to 1.0 wt%) and (c) higher protein concentration (2 to 10 wt%).

Table 4.4. Fitted parameters of interaction of 1 wt% LS30 silica nanoparticle system with varying lysozyme protein concentration at pH 5.

(a) Low protein concentration regime

Concentration C (wt%)	Hard sphere radius R_{hs} (nm)	Surface fractal dimension D_s	Volume fraction η	Aggregated nanoparticles ϕ_{np} (%)
0.0	8.1 ± 0.2	-	-	0
0.01	9.0 ± 0.2	2.7 ± 0.1	0.05 ± 0.02	68
0.02	8.9 ± 0.2	2.7 ± 0.1	0.27 ± 0.02	100

(b) Intermediate protein concentration regime

Concentration C (wt%)	Hard sphere radius R_{hs} (nm)	Surface fractal dimension D_s	Volume fraction η	Fraction of free protein ϕ_p (%)
0.05	9.0 ± 0.2	2.9 ± 0.1	0.36 ± 0.02	-
0.1	9.0 ± 0.2	2.8 ± 0.1	0.34 ± 0.02	-
0.2	9.1 ± 0.2	2.8 ± 0.1	0.33 ± 0.03	30
0.5	9.1 ± 0.2	2.7 ± 0.1	0.28 ± 0.02	52
1.0	9.0 ± 0.2	2.7 ± 0.1	0.20 ± 0.03	80

(c) High Protein concentration regime

Concentration C (wt%)	Building block radius R_b (nm)	Mass fractal dimension D_m	Fraction of free protein ϕ_p (%)
2.0	9.2 ± 0.2	2.6 ± 0.2	87
5.0	9.0 ± 0.2	2.5 ± 0.1	90
10.0	9.2 ± 0.2	2.5 ± 0.1	92

The role of pH on nanoparticle-protein interaction at different protein concentrations has been examined in figure 4.7. SANS data of 1 wt% silica nanoparticles with lysozyme over four

order of concentrations (0.01, 0.1, 1.0 and 10.0 wt%) at three pH values (5, 7 and 9) are compared in figure 4.7. The scattering data show significant differences with pH variation at all the four protein concentrations. At lowest protein concentration (0.01 wt%), the SANS data show a buildup of scattering in low Q values which is maximum for pH 5. There exists nanoparticle aggregates with un-aggregated nanoparticles at this protein concentration for all three pH values [213, 206]. The data show that the protein-mediated nanoparticle aggregation is most prominent at pH 5 when the electrostatic attraction between nanoparticle and protein is stronger. At protein concentration 0.1 wt%, the scattering data at pH 5 show a Bragg peak which is absent for the data of pH 7 and 9. This supports to the fact that nanoparticle aggregation morphology depends on interaction between two components where aggregates change from surface fractal to mass fractal with increasing pH (e.g. 5 to 7). It is found that at pH 9 much higher protein (0.2 wt%) amount is required to aggregate all the nanoparticles as compared to that at pH 5 (0.02 wt%). Further the protein adsorption significantly increases with increasing pH (figure 2) whereas the protein-mediated aggregation of nanoparticles is suppressed. This can be understood by the fact that with increasing pH, charge on protein decreases and surface charge density of the nanoparticle increases, which means more amount of protein will be required to mediate nanoparticles aggregation. For 1 wt% protein, nanoparticles aggregates coexist with excess free protein in the case of all the three pH values. The aggregates formed at pH 5 are surface fractal whereas mass fractal at pH 7 and 9. The structures are also found different at pH 7 and 9 having mass fractal dimensions 2.5 and 2.1, respectively. It may be mentioned that higher fractal dimension corroborate to the denser packing of the particles within the aggregates. The fractal dimension at pH 9 (~ 2.1) corresponds to a reaction limited aggregate (RLA) kind of mass fractal morphology unlike to that observed at pH 7 (DLA kind of morphology) [212, 216, 217]. The

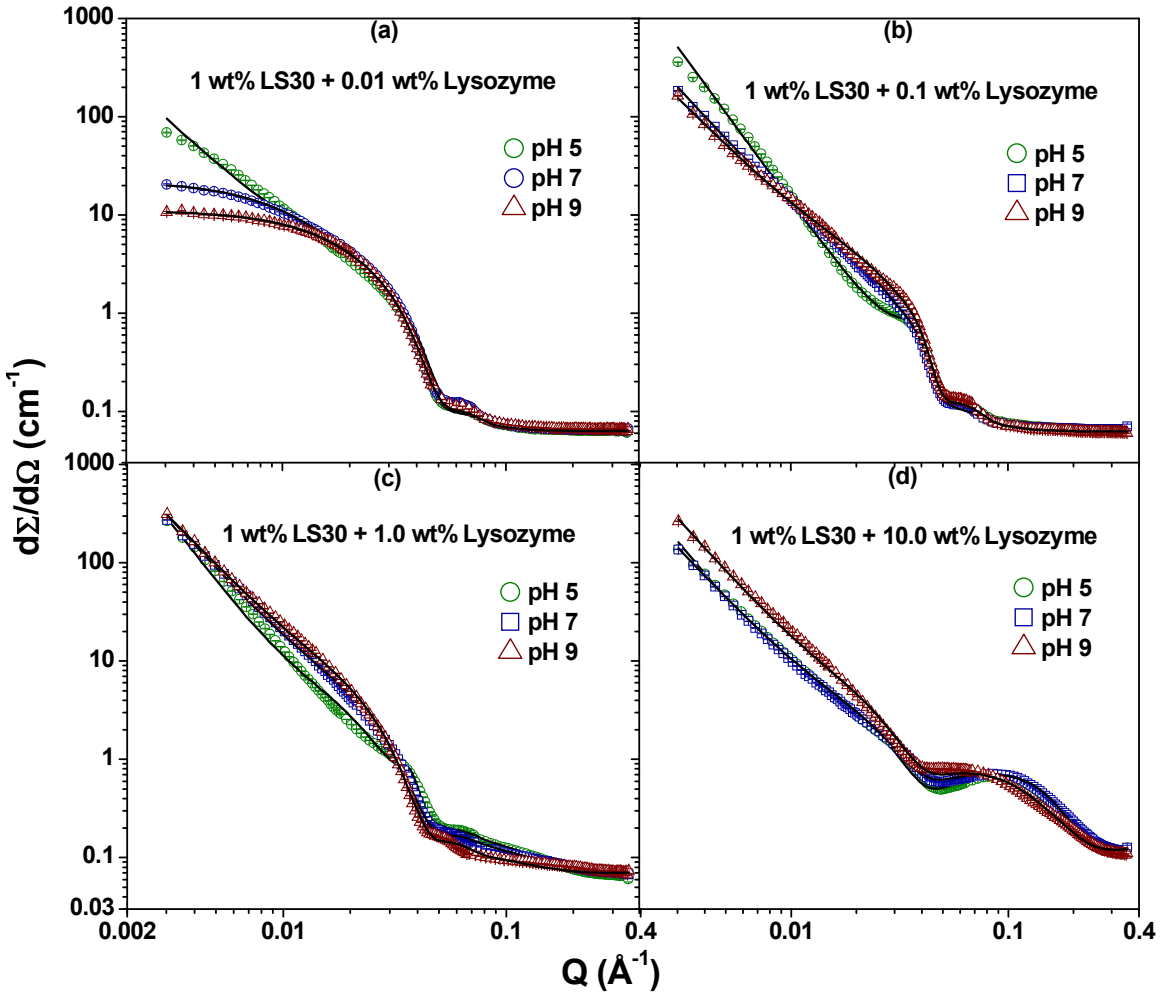

Figure 4.7. Comparison of SANS data of 1 wt% LS30 silica nanoparticle system with (a) 0.01 wt%, (b) 0.1 wt%, (c) 1.0 wt% and (d) 10.0 wt% concentration of protein at three pH values (5, 7 and 9).

Bragg peak at pH 5 which is observed up to 1 wt% protein concentration disappears at 10 wt% concentration. At this protein concentration (10 wt%), all the nanoparticle aggregates are mass fractal irrespective of the pH. The mass fractal dimension (2.1) of aggregates at pH 9 remains unchanged as in the case of 1 wt% protein concentration whereas it slightly decreases for pH 7 (~2.3). The fact that surface fractals are formed at pH 5 and mass fractals at pH 7 and 9 up to 1 wt% protein concentration, therefore the data are found to be different for pH 5 than that at pH 7

and 9. The surface fractals at pH 5 convert to mass fractals with increase in protein concentration (10 wt%) resulting in similar behavior to that of pH 7 and 9. However, the difference seen in SANS data between pH 9 with pH 5 and 7 could be because of different sizes of aggregates in these systems. Overall, the results show that the amount of protein adsorption on nanoparticles plays an important role in deciding the aggregate morphology [120, 206, 208]. It is governed by the competition of protein-mediated attraction between nanoparticles and adsorbed protein-protein repulsion. Figure 4.8 shows the schematic of the structures of the nanoparticle protein complexes at different pH.

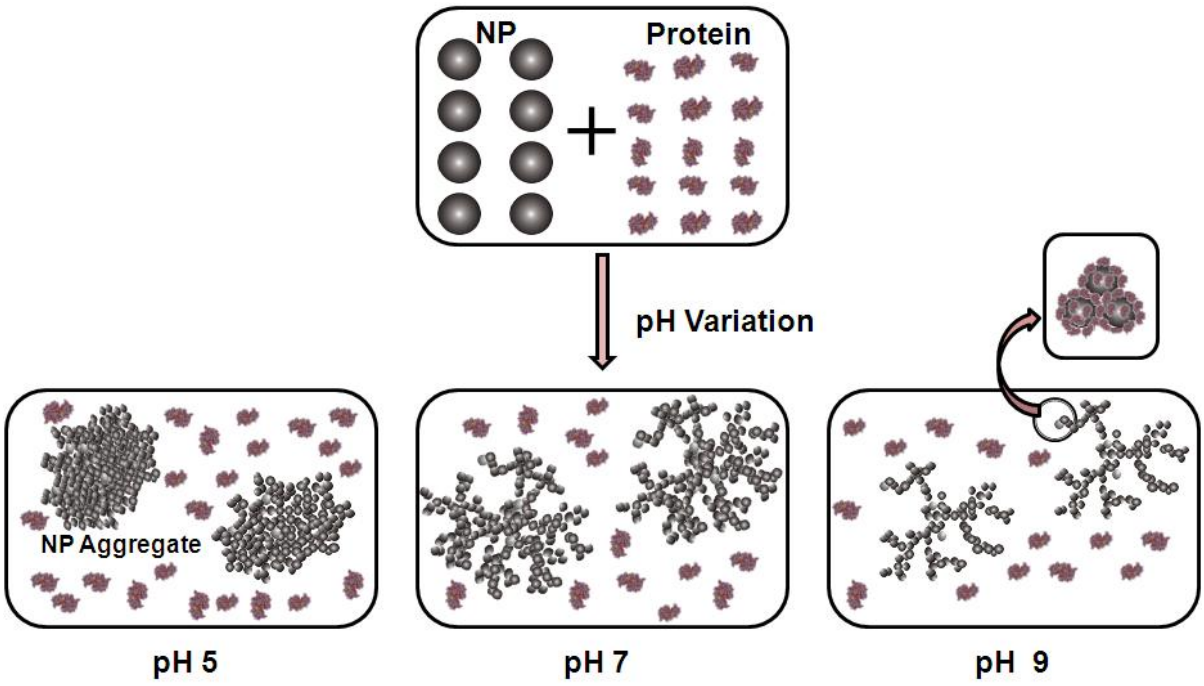

Figure 4.8. Schematic of structures of nanoparticle-protein aggregates at different pH.

4.4.3. Effect of nanoparticle size on protein adsorption and resultant structures

The nanoparticle-protein interaction can be tuned by varying the size of the nanoparticles. We have examined pH dependent interaction of protein with three different sized nanoparticles (SM30, LS30 and TM40) [206]. The nanoparticles SM30 and TM40 have sizes about 8 nm and

26 nm with polydispersity 0.3 and 0.15, respectively (table 3.2). Figure 4.9 shows adsorption curves of lysozyme protein on SM30 and TM40 nanoparticles measured at three pH values (5, 7 and 9). The behavior of the adsorption curves is found to be similar to that seen for LS30 nanoparticles as shown in figure 4.5. All the curves for protein adsorption on nanoparticles

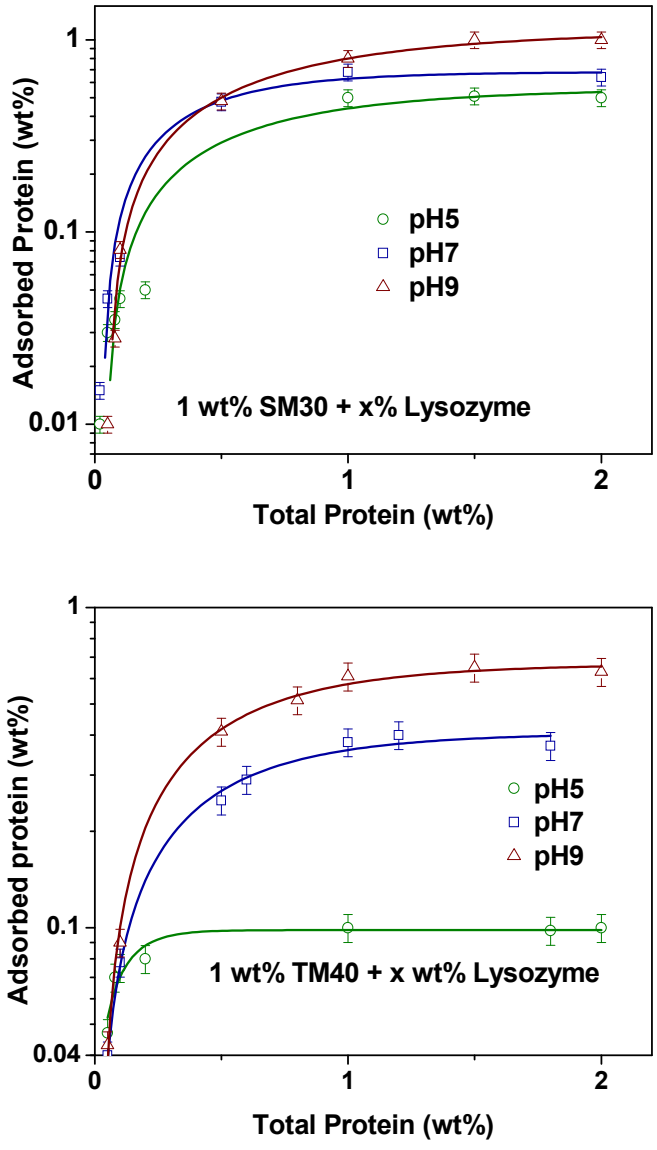

Figure 4.9. Lysozyme protein adsorption curve on 1 wt% (a) SM30 (b) TM40 silica nanoparticles at three pH values (5, 7 and 9).

follow an exponential behavior [206]. The fitted parameters are given in table 4.5. The saturation value is found to be increasing whereas adsorption coefficient decreasing with increase in the pH of the solution. In case of SM30 adsorption coefficient decreases for pH from 7 to 9, could be because of additional effect of low curvature as it is known that adsorption is also governed by curvature [121, 206]. For LS30 and TM40 nanoparticles, adsorption coefficient does not change much from pH 7 to 9. The comparison for different sized nanoparticle suggests protein adsorption per nanoparticle increases with the increase in the nanoparticle size. However, the overall saturation value at fixed particle concentration decreases with increase in particle size because of the decrease in overall surface area.

Table 4.5. Fitted parameters for adsorption curves of lysozyme protein on 1 wt% different sized silica nanoparticles at three pH values (5, 7 and 9).

Nanoparticle system	Particle radius R_m(nm)	pH 5		pH 7		pH 9	
		A_0 (wt%)	k (1/wt%)	A_0 (wt%)	k (1/wt%)	A_0 (wt%)	k (1/wt%)
SM30	4.2 ± 0.1	0.55 ± 0.07	1.6 ± 0.5	0.70 ± 0.05	2.6 ± 0.7	1.10 ± 0.08	1.3 ± 0.2
LS30	8.0 ± 0.2	0.12 ± 0.02	6.8 ± 1.0	0.49 ± 0.03	2.1 ± 0.3	0.80 ± 0.04	1.9 ± 0.3
TM40	13.0 ± 0.5	0.09 ± 0.01	9.9 ± 1.5	0.40 ± 0.02	2.2 ± 0.3	0.65 ± 0.02	2.3 ± 0.2

The comparison of the SANS data of protein (1 wt%) with three different sized silica nanoparticles (1 wt% each) at three different pH values is shown in figure 4.10. The data can be divided in three distinct Q regions (i) low Q data where the scattering is governed by the fractal aggregates of nanoparticles (ii) the intermediate Q range where scattering is decided by the building block (nanoparticle with adsorbed protein) of the aggregate and (iii) the high Q region determined by scattering from protein. SANS data on varying nanoparticle size at a given pH

show different features in the low and intermediate *Q* regions but remain almost same at high Q values. This shows the change in structure of the aggregates (overall size and/or fractal dimension) with the nanoparticle size [206]. It is observed that the aggregates formed are mass fractal nature at all three pH values for smallest nanoparticle system (SM30) whereas other two nanoparticle systems (LS30 and TM40) show surface fractal morphology of the aggregates at pH 5 which convert to mass fractal at pH 7 and 9. The fitted structural parameters are given in table 4.6. The morphology of aggregate structure is believed to be decided by the adsorption of protein on the nanoparticles [120, 206]. The smaller surface number density of adsorbed protein molecules for larger particle size (TM40) at lowest pH (pH 5) leads their higher propensity to form clusters (surface fractal) than mass fractal. The overall protein adsorption however depends on the total surface area of nanoparticles, which decrease with the increase in the size of the nanoparticle when compared at fixed concentration.

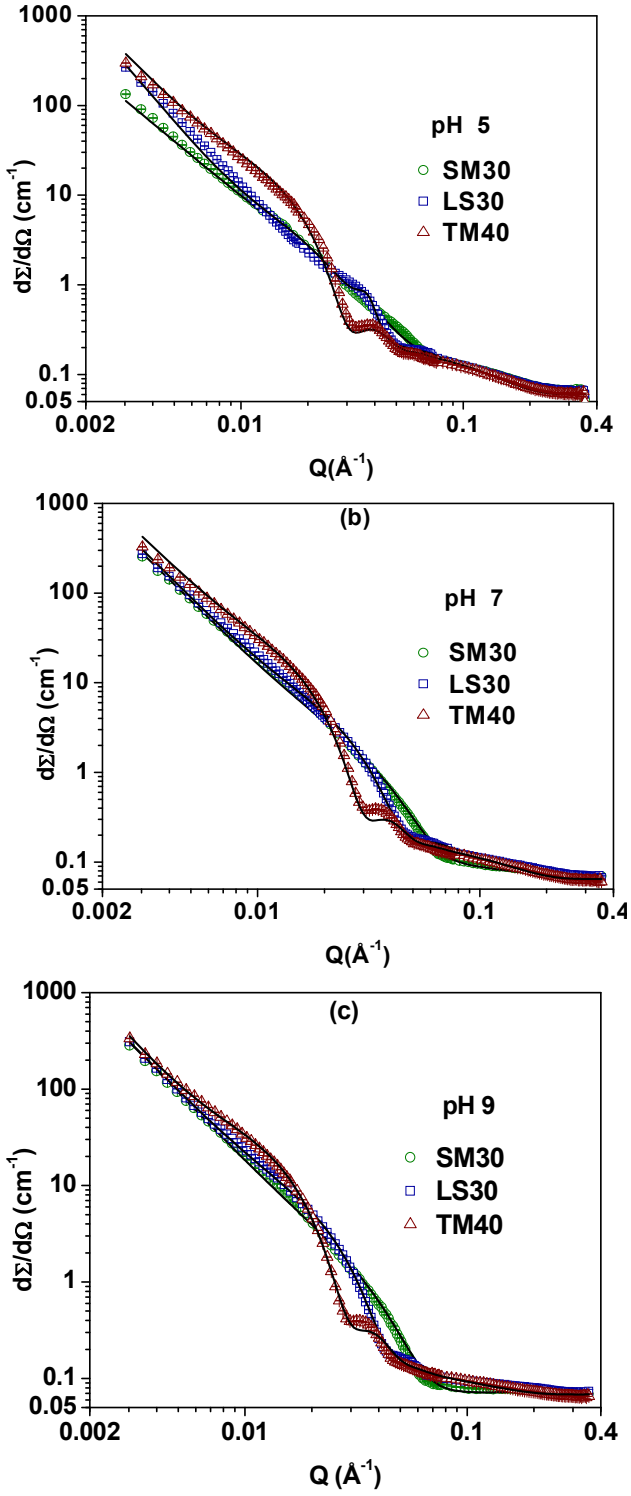

Figure 4.10. SANS data of 1 wt% protein with 1 wt% SM30, LS30 and TM40 silica nanoparticles each at three pH values (a) pH 5, (b) pH 7 and (c) pH 9.

Table 4.6. Fitted structural parameters of complexes of 1 wt% lysozyme protein with 1 wt% different sized silica nanoparticles (SM30, LS30 and TM40) at three pH values (5, 7 and 9).

Nanoparticle system	Particle radius R_m (nm)	Fractal morphology	Building block radius R_b (nm)	Fractal dimension D_s/D_m	Adsorbed protein molecules/particle	Fraction of free protein ϕ_p
			pH 5			
SM30	4.1 ± 0.2	Mass	5.8 ± 0.2	2.3 ± 0.1	15	52
LS30	8.1 ± 0.2	Surface	9.0 ± 0.2	2.7 ± 0.1	36	80
TM40	13.0 ± 4.2	Surface	15.3 ± 0.5	2.7± 0.1	77	90
			pH 7			
SM30	4.1 ± 0.2	Mass	5.7 ± 0.2	2.3 ± 0.1	20	35
LS30	8.0 ± 0.2	Mass	9.2 ± 0.2	2.4 ± 0.1	76	58
TM40	13.0 ± 0.5	Mass	150.3 ± 4.0	2.4 ± 0.1	294	62
			pH 9			
SM30	4.1 ± 0.2	Mass	5.9 ± 0.2	2.2 ± 0.1	26	20
LS30	8.1 ± 0.2	Mass	9.2 ± 0.2	2.1 ± 0.1	151	28
TM40	13.0 ± 0.5	Mass	15.0 ± 0.5	2.3 ± 0.1	464	40

5.5. Conclusions

The interaction and resultant structure of oppositely charged silica nanoparticles and lysozyme protein by varying pH and size of the nanoparticles have been studied. Adsorption curves as determined by UV-Vis spectroscopy show an exponential behavior for all pH (5, 7 and 9) and nanoparticle sizes (8, 16 and 26 nm) examined. The adsorption coefficient decreases but the saturation amount increases with increase in pH, whereas opposite of this behavior is observed with the increase in the size of the nanoparticles. The strong electrostatic attraction between nanoparticle and protein leads to the protein-mediated aggregation of nanoparticles. There exist two different concentration regimes of interaction of nanoparticles with protein (i) un-aggregated nanoparticles coexisting with aggregated nanoparticles at low protein concentrations and (ii) free protein coexisting with aggregated nanoparticles at higher protein concentrations. These concentration regimes are found to be strongly depending on both pH and nanoparticle size. The nanoparticle aggregates are found to have ordered structures (clusters) having surface fractal morphology at low pH 5 which changes into mass fractals (branched) at higher pH (pH 7 and 9). The similar behavior of fractal morphology transition is also observed with decreasing nanoparticle size for lower pH 5. These studies thus show that pH and nanoparticle size play important role in tuning the interaction of nanoparticle with protein and their resultant structures.

Chapter 5

BLOCK COPOLYMER INDUCED DEPLETION INTERACTION AND CLUSTERING OF NANOPARTICLES

5.1. Introduction

The nanoparticle-block copolymer systems are known to show rich phase behavior and hence find numerous applications in biotechnology, catalysis, magnetic sealing, optics, photonics and electronics [13, 218-221]. The tuning of the self-assembly of block copolymers simply by using supramolecular chemistry based on the solution conditions (concentration, temperature, ionic strength etc.) allows the formation of different phases as well as hybrid structures in these systems depending on the interparticle interactions involved [222]. In many cases, the evolution of phase behavior can be explained using well known DLVO theory, considering the competition between short-range van der Waals attraction and long-range electrostatic repulsion among the particles. However, there are numerous examples where DLVO theory fails and non-DLVO contributions (e.g. hydration and depletion interactions etc.) are required to explain the system behavior [78, 223-226]. The resultant interaction in these systems can be a combination of short-range attraction, long-range attraction and long-range repulsion.

The block copolymers may either adsorb on the nanoparticles to stabilize them or remain free in the solution leading to depletion driven flocculation [25, 227, 228]. In multi-components system, the depletion interaction is known to play an important role in deciding the phase behavior of these systems. The depletion interaction governs various interesting kinematic phase transitions (e.g. from individual steel rods to self assembled polymer-like structures or from

vesicles to hybrid core–shell micelles) in different colloidal systems [229, 230]. The depletion interaction has been mostly considered as short-range attraction and found applicable to the systems which are sterically stabilized as hard sphere potential as repulsive part [25, 74]. There have been numerous cases recently where long-range attraction has been observed in charged colloidal systems leading to their aggregation [223, 231-235].

In this chapter, small-angle neutron scattering (SANS) experiments have been carried out to examine if depletion force can be of long-range nature [236]. The clustering of charged nanoparticles in the presence of block copolymer is observed, which can be obtained when the depletion interaction caused by block copolymer can overcome long-range repulsion between charged nanoparticles. Block copolymer is used as their self-assembly can be varied simply by temperature and thereby tuning depletion interaction through excluded volume effect [59]. Data are modeled using a combination of two Yukawa potentials accounting for both depletion attraction and electrostatic repulsion. The choice of Yukawa potentials can establish range and strength of the individual parts of the total potential without any pre-defined assumption [237].

5.2. Experimental section

Electrostatically stabilized 30% (by weight) colloidal suspensions of silica nanoparticles (Ludox LS30 and SM30) and Pluronic P85 block copolymer were obtained from Sigma Aldrich and BASF, respectively. Samples were prepared by dissolving weighted amount of silica and block coplymer in 15 vol% D_2O in the mixed D_2O/H_2O solvent where the block copolymers are contrast-matched. All the measurements were carried out in the presence of 0.1 M NaCl in order to reduce electrostatic repulsion to be comparable with depletion attraction where the particle clustering can be observed. Also In presence of electrolyte, the counterion binding suppresses any adsorption of the PEO block through hydrogen bonding on the nanoparticles. Distilled

deionized water from Milipore MilliQ unit and 99.9 % pure D_2O were used for sample preparation. SANS measurements were carried out using SANS facilities at the Dhruva reactor, Bhabha Atomic Research Centre, Mumbai [145] and at the HANARO at the Korea Atomic Energy Research Institute (KAERI), Republic of Korea [196]. The measurements were taken at three temperatures 20, 30 and 40 ^{o}C. Data were corrected for background and empty cell contributions and normalized to absolute cross-sectional unit using standard procedure.

5.3. SANS analysis

In SANS experiments, the coherent differential scattering cross-section per unit volume ($d\Sigma/d\Omega$) is given by [127]

$$\frac{d\Sigma}{d\Omega}(Q) = nV^2\left(\rho_p - \rho_s\right)^2 P(Q)S(Q) + B \tag{5.1}$$

where n is the particle number density and V is particle volume. ρ_p and ρ_s are scattering length densities of particles and solvent, respectively. B is a constant term representing the incoherent background.

The expressions for intraparticle structure factor $P(Q)$ for different shapes and sizes are discussed in chapter 2. The interaction for calculation of inter-particle structure factor $S(Q)$ between particles may be attractive or repulsive or combination of both and hence can be calculated from double Yukawa potential accounting for both attraction and repulsion as given by [237]

$$\begin{aligned} U(r) &= \infty \ \ for\ 0 < r < \sigma \\ &= -K_1 \frac{exp\left\{-\alpha_1\left(r/\sigma - 1\right)\right\}}{r/\sigma} + K_2 \frac{exp\left\{-\alpha_2\left(r/\sigma - 1\right)\right\}}{r/\sigma} \ for\ r > \sigma \end{aligned} \tag{5.2}$$

where K (in units of k_BT; k_B is Boltzmann constant and T is temperature) is proportional to magnitude of the potential while $1/\alpha$ is proportional to the range of the potential. $S(Q)$ from interaction potential $U(r)$ is obtained by solving Ornstein-Zernike (OZ) equation under a suitable closure relation.

The data have been analyzed by comparing the scattering from different models to the experimental data. Throughout the data analysis corrections were also made for instrumental smearing. The modeled scattering profiles were smeared by the appropriate resolution function to compare with the measured data. The fitted parameters in the analysis were optimized by means of nonlinear least-square fitting program [150].

5.4. Results and discussion

5.4.1. Modeling of depletion interaction

Figure 5.1 shows the SANS data from 1wt% of LS30 silica nanoparticles ($2R_m \sim 16.0$ nm) with varying concentration of block copolymer (P85). It is observed that there is build up of scattering data in the low Q region whereas data overlap at high Q region with increase in block copolymer concentration. There are two possible cases of block copolymer behavior in this system either they are adsorbed on nanoparticles or non-adsorption of block copolymer is providing depletion force to the nanoparticles. The fact that block copolymer are contrast-matched to the mixed H_2O/D_2O solvent (15% D_2O), their simple adsorption is expected to show no changes in the scattering pattern. The scattering changes may occur if polymer adsorbs on multiple nanoparticles thereby initiating nanoparticle aggregation (bridging aggregation). However, this is not possible in the present case because of the relatively small radius of gyration (R_g~2.2 nm) of P85 block copolymer to nanoparticle radius (8 nm).

This suggests that the changes seen in the scattering pattern (figure 5.1) arise because of interactional changes in the system (depletion interaction) as a result of non-adsorption behavior of block copolymer. Also, the systematic buildup of scattering in the low Q region indicates increase in the depletion attraction with increasing

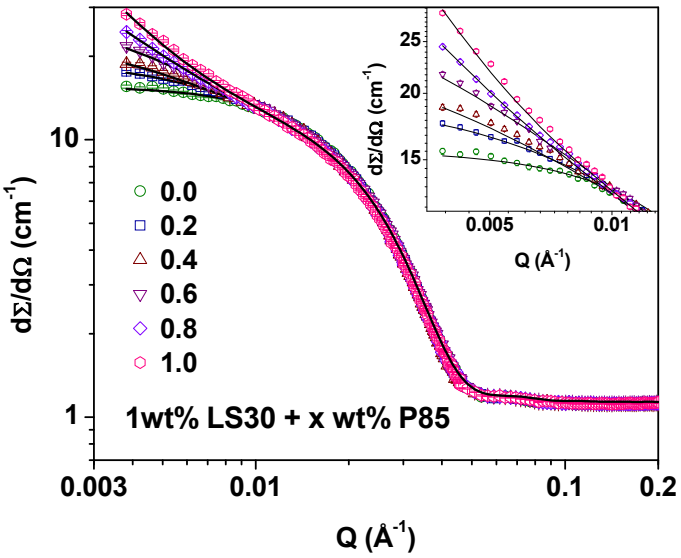

Figure 5.1. SANS data of 1 wt% LS30 silica nanoparticles with varying concentration of P85 block copolymer at 20 ^{o}C. Inset highlights the variation in low Q data.

block copolymer concentration [236, 237, 241]. This evolution of attraction has been examined by calculating the structure factor $S(Q)$ by dividing the corresponding data with that of pure nanoparticles and is shown in figure 5.2 (a). The structure factor has been fitted considering a two-Yukawa potential (equation 5.2) taking into account of both attractive (depletion) and repulsive (electrostatic) forces in the system in the system. There are four unknown parameters K_1, K_2, α_1 and α_2 in equation (5.2). The parameters K_1 and α_1 represent magnitude and range ($1/\alpha_1$) of the interaction, respectively. On the other hand, parameters K_2 and α_2 represent effective charge (strength) and the Debye length (ionic strength) of electrostatic repulsion [239, 243]. The parameters K_2 and α_2 are kept fixed as are not expected to change with block

copolymer concentration. These parameters have been calculated from the data of concentrated nanoparticle solution. The fitted parameters (K_1 and α_1) are given in table 5.1 and corresponding potentials are shown in figure 5.2 (b). The calculated values of K_1 and α_1 for van der Waals interaction (short-range attraction) are around 5 and 30, respectively. The significantly lower

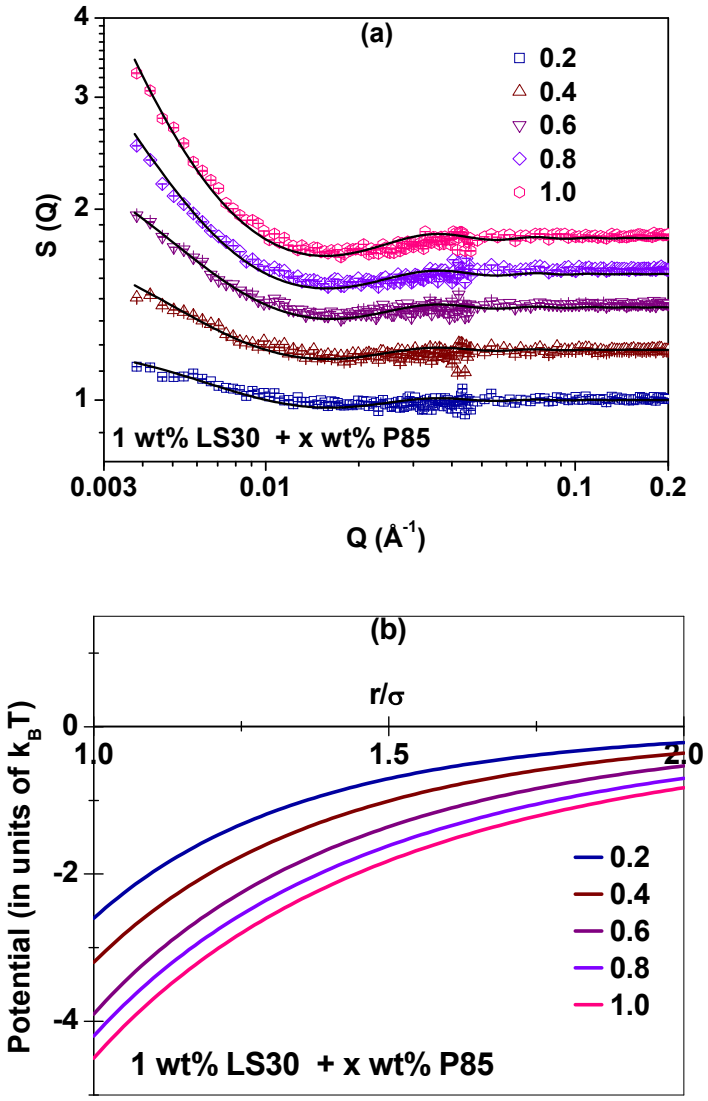

Figure 5.2. The variation of (a) structure factor $S(Q)$ and (b) total interaction potential for 1 wt% LS30 silica nanoparticles with varying concentration of P85 block copolymer. The data of structure factor are shifted vertically for clarity.

value of α_1 in table 5.1 as compared to that for van der Waals suggests relatively long-range nature of the depletion interaction observed in this system [244, 247]. It may be mentioned that long-range attraction has also been observed in several charged systems such as charged proteins, confined charged colloids and solutions of supramolecular polymers [151, 242-244]. In the system of charged proteins, long-range attraction is induced by the partial ion clouding around protein molecules whereas redistribution of electric double layers of ions and counterions are found to be responsible for long-range attraction in confined colloids [151]. In the case of supramolecular polymers, long-range attraction is achieved through depletion interaction by associating small molecules. The natural process like ligand binding to the protein molecules is also observed driven through long-range attraction [231]. It is generally believed that the long-range attraction in these systems arises due to manifestation of multi-body interactions [223].

Table 5.1. The calculated parameters of attractive depletion interaction in 1 wt% LS30 nanoparticles as a function of block copolymer concentration. The parameters of repulsive interaction (K_2 = 3.0, α_2 = 9) are fixed.

P85 Concentration (wt%)	K_1 (k_BT)	α_1
0.0	-	-
0.2	2.6 ± 0.2	1.8 ± 0.1
0.4	3.2 ± 0.2	1.5 ± 0.1
0.6	3.9 ± 0.3	1.3 ± 0.1
0.8	4.2 ± 0.3	1.1 ± 0.1
1.0	4.5 ± 0.3	1.0 ± 0.1

In the above measurements the silica nanoparticle concentration was 1 wt% where the system may be considered dilute for the repulsive interaction. SANS measurements were also carried out at much higher concentration of silica nanoparticles (10 wt%) to examine the competition of attractive depletion with repulsive electrostatic interactions in these systems. Figure 5.3 shows comparison of SANS data of 1 and 10 wt% pure silica nanoparticles. The scaling of two data by concentration factor shows significant differences in these data sets in the low Q region. The fall of scattering in the low Q region at higher particle concentration is observed because of repulsive interaction between the nanoparticles. The data are fitted with a repulsive Yukawa potential in order to obtain the parameters K_2 and α_2.

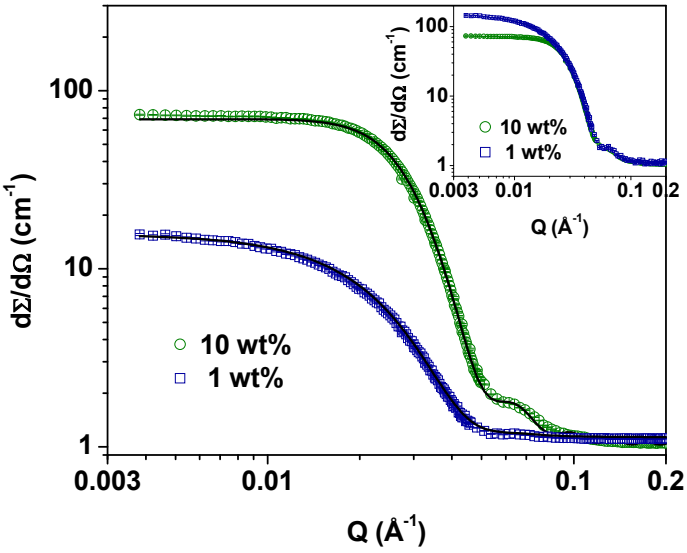

Figure 5.3 SANS data of pure 1 and 10 wt% of LS30 nanoparticles systems. Inset shows data after scaling.

The data of 10 wt% silica nanoparticles in the presence of block copolymers are shown in figure 5.4. These data suggest attractive depletion competing with repulsive electrostatic where former interaction dominating with increasing block copolymer concentration. The fitted parameters are given in table 5.2. The magnitude and range increase with increasing block

copolymer concentration. The variation in calculated structure factor and total interaction potential for 10 wt% nanoparticles in presence of increasing block copolymer concentration at 20 ^{o}C are plotted in figure 5.5. The signature of resultant potential can be observed from low Q

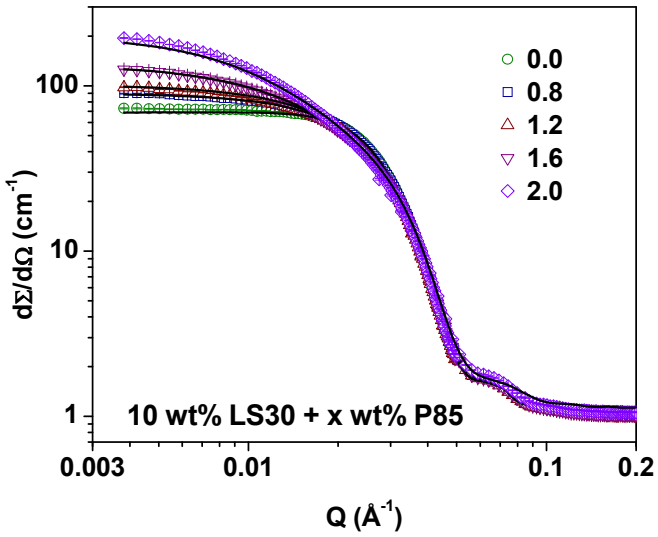

Figure 5.4. SANS data of 10 wt% LS30 silica nanoparticles with varying concentration of P85 block copolymer at 20 ^{o}C.

behavior of structure factor, in particular, through $S(Q=0)$ decided by the isothermal compressibility [124, 127]. The variation of structure factor thus show repulsive nanoparticle system becoming attractive with increase in block copolymer concentration. The correlation peak shifting towards the higher Q value with increasing block copolymer concentration indicates the reduction in the interparticle separation with increasing depletion attraction [124, 135]. The fitted total interaction potentials corresponding to structure factors [figure 5.5 (a)] are plotted in figure 5.5(b). The depletion interaction becomes less effective on increasing particle concentration. It is found that up to 1.2 wt% of block copolymer concentration the total potential is dominated by repulsive component whereas prominence of depletion interaction is experienced at higher block copolymer concentration (>1.6 wt%).

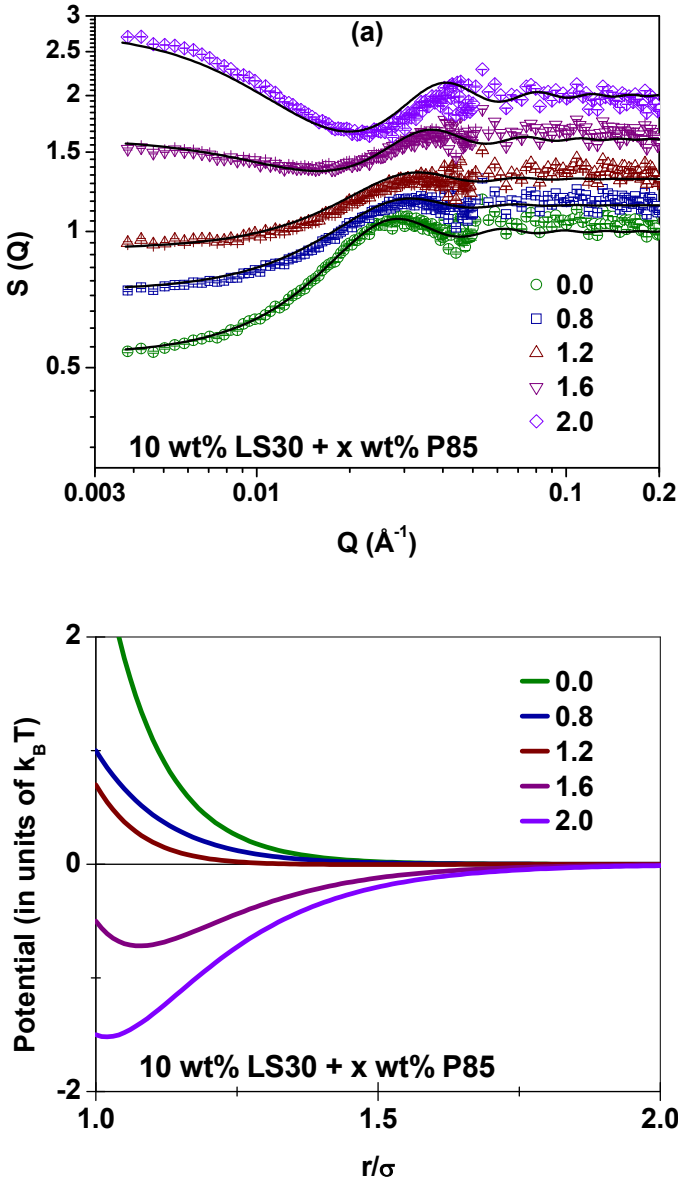

Figure 5.5. The variation of (a) structure factor and (b) total interaction potential for 10 wt% LS30 silica nanoparticles with varying concentration of P85 block copolymer. The data of structure factor are shifted vertically for clarity.

Table 5.2. The calculated parameters of total interaction potential of 10 wt% LS30 nanoparticles as a function of block copolymer concentration. The parameters of repulsive interaction ($K_2 = 3.0$, $\alpha_2 = 9$) are fixed.

P85 Concentration (wt %)	K_1 (k_BT)	α_1
0.0	-	-
0.8	2.0 ± 0.1	7.0 ± 0.5
1.2	2.4 ± 0.2	6.5 ± 0.5
1.6	3.5 ± 0.2	5.6 ± 0.5
2.0	4.5 ± 0.3	5.2 ± 0.4

5.4.2. Temperature (self-assembly) dependence of depletion interaction

The measurements discussed so far were taken at 20 ^oC where block copolymers are expected to be unimers. Block copolymers at low temperatures [below critical micelle temperature (CMT)] when both PEO and PPO blocks are hydrophilic remain as unimers [58, 245]. The PPO block becomes hydrophobic with increase in temperature leading to micellization. There exists a temperature range above CMT where spherical micelles coexist with unimers. At higher temperatures spherical micelles convert to rod-like micelles prior to clouding (phase separation). The effect of self-assembly of block copolymer as induced by temperature on depletion interaction of nanoparticles (figure 5.6) is examined by increasing the solution temperature (30 ^oC) significantly above the CMT (25 ^oC) of the block copolymer [39]. It is observed that the behavior of scattering curves is dramatically altered at higher temperature with increase in block copolymer concentration. There is strong buildup of scattering in the low

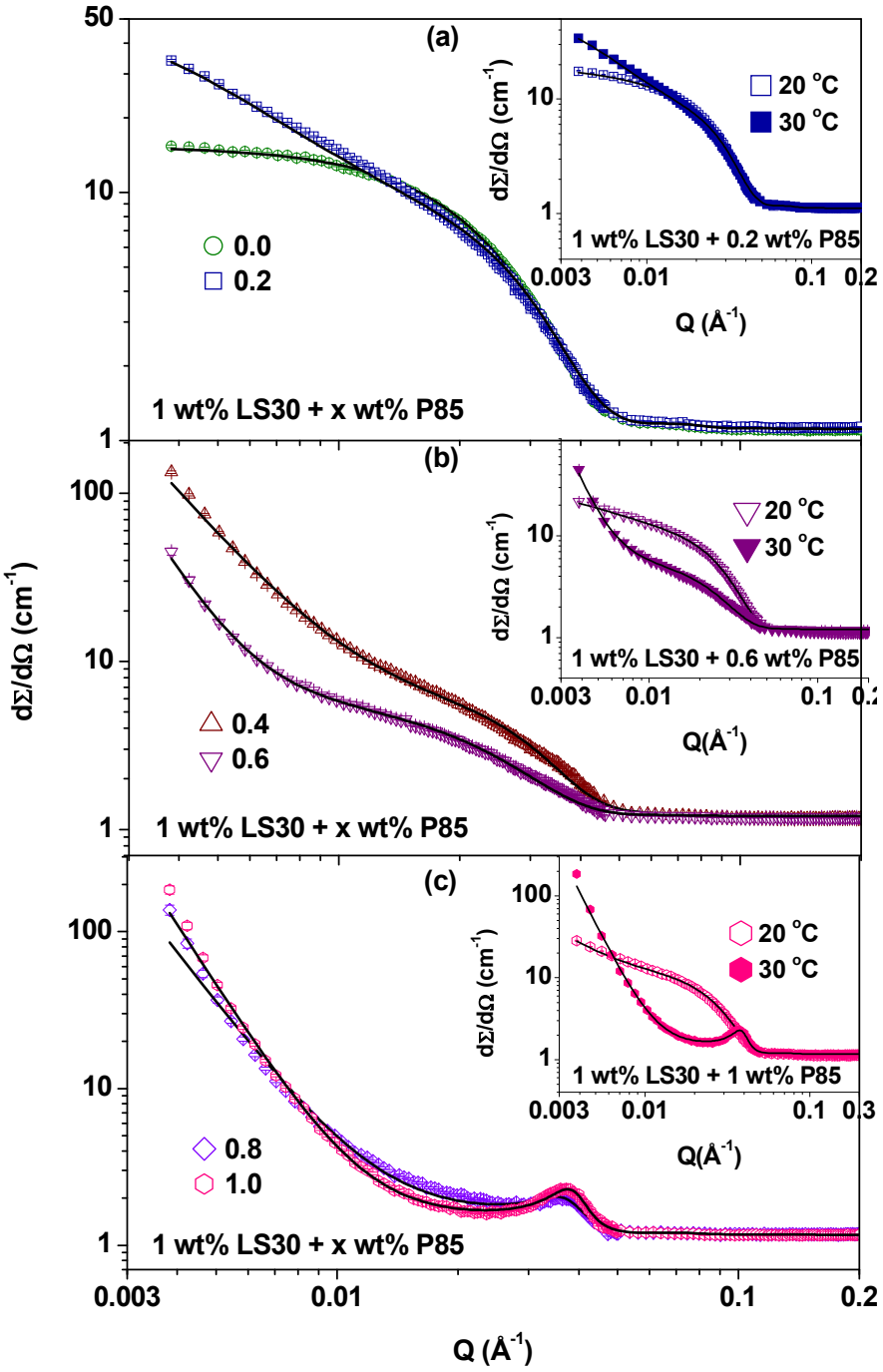

Figure 5.6. SANS data of 1 wt% LS30 silica nanoparticles with varying concentration of P85 block copolymer at 30 °C. The data are divided into three distinct regions [(a) to (c)] of block copolymer concentrations. Inset shows comparison of data of 30 °C with 20 °C for one block copolymer concentration in each region.

Q region (< 0.01 $Å^{-1}$) followed by Bragg peak around Q = 0.035 $Å^{-1}$. This is as a result of enhanced attraction leading to nanoparticle aggregation where the scattering in the low Q region arise from the aggregates (clusters) and Bragg peak from the repeat distance of particles within the aggregates. The data in figure 5.6 are divided in three regions: (i) interacting nanoparticles exist in monomeric form, (ii) coexistence of aggregated with un-aggregated (monomeric) nanoparticles and (iii) all nanoparticles have been aggregated. In region (i), even though the concentration of block copolymer is quite low, its effect on depletion interaction with increase in temperature is significantly enhanced (insets figure 5.6). It is expected that micellization increases the excluded volume whereas the corresponding decrease in number density of micelles will decrease it. The net change in the excluded volume interaction would be cumulative effect of both of these contributions. Our observations suggest that the increase in excluded volume by the micellization dominates the corresponding decrease in number density of micelles and enhances the depletion force [236]. In this region, the attractive potential is expected to be less than average thermal kinetic energy (1.5 k_BT) at an average distance of the particle which prevents them from any aggregation [62]. The second region corresponds to block copolymer concentrations when the attractive potential becomes significantly larger than average thermal kinetic energy and the particle aggregation can take place. These data have three different Q dependent regimes. The low Q regime governed by the aggregates of particles, intermediate Q regime suggesting aggregates coexisting with un-aggregated nanoparticles and high Q regime dominated by the incoherent background. The decrease in the scattering intensity in particular in the intermediate Q range indicates the decrease in number density of un-aggregated particles (increase in number density of aggregated particles). In region (iii) of block copolymer concentration, the increase in depletion with increase in block copolymer

Table 5.3. The calculated parameters of depletion interaction and resultant structures for 1 wt% silica nanoparticles as a function of block copolymer concentration at 30 ^{o}C.

(a) System is characterized by individual nanoparticles undergoing depletion interaction.

P85 Concentration (wt%)	K_1 (k_BT)	α_1
0.2	10.0 ± 0.8	1.7 ± 0.1

(b) System consists of nanoparticle aggregates coexisting with individual nanoparticles.

P85 Concentration (wt%)	Surface fractal dimension D_s	Fraction of non-aggregated particles (%)
0.4	2.9 ± 0.1	78
0.6	2.8 ± 0.1	60

(c) System consists of nanoparticle aggregates.

P85 Concentration (wt%)	Surface fractal dimension D_s	Particle-particle distance d (nm)	Volume fraction within the aggregates φ
0.8	2.5 ± 0.1	17.0 ± 0.5	0.4 ± 0.05
1.0	2.0 ± 0.1	17.0 ± 0.5	0.4 ± 0.05

concentration gives rise to ordered aggregates reflected in the Bragg peak observed around Q = 0.04 Å^{-1}. The corresponding average distance between the particles ($d \sim 2\pi/Q$) having values similar to the particle size suggests simple cubic type packing of the particles within the aggregates. The scattering from aggregates is fitted by the sum of power law behavior of fractal aggregates and contribution from particles within the aggregates [206, 236]. The fitted

parameters are given in table 5.3. The magnitude of depletion interaction is enhanced on self-assembly (micellization) of block copolymer at higher temperature. The particle aggregation induced by depletion interaction is characterized by surface fractal [$\sim Q^{-(6-D_s)}$] as the slope of the intensity in log-log scale has a value more than 3 [142]. The fractal dimension D_s is found to be decreasing with increase in block copolymer concentration. The higher propensity to aggregate at higher block copolymer concentration is expected to lead smooth surfaces and hence lower smaller fractal dimension. The Bragg peak is fitted through $S(Q)$ by employing hard sphere potential in the Percus-Yevick approximation [137].

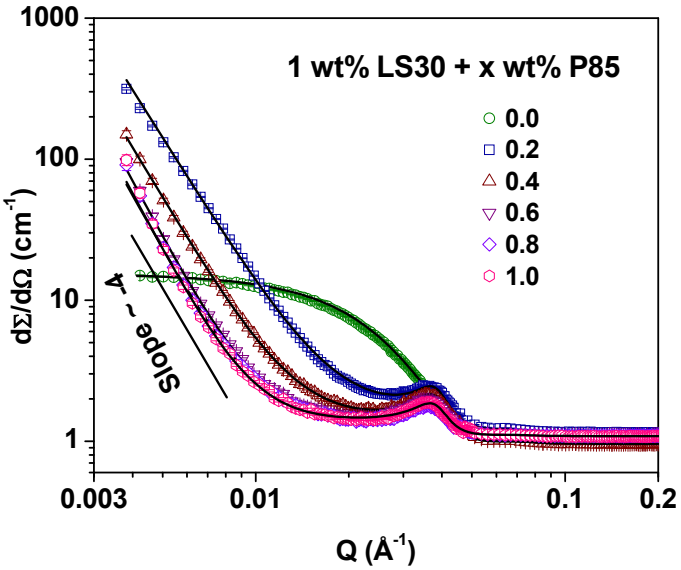

Figure 5.7. SANS data of 1 wt% LS30 silica nanoparticles with varying concentration of P85 block copolymer at 40 ^{o}C.

Figure 5.7 shows SANS data of results of depletion interaction at 40 ^{o}C. The subsequent increase in the size of the micelles at this temperature results in the increase in excluded volume effect causing increase in depletion attraction. This increase in attraction leads to the nanoparticle aggregation at 40 ^{o}C even at lowest block copolymer concentration unlike the case of 30 ^{o}C. All SANS data at 40 ^{o}C show a Bragg peak whose position remain independent ($Q \sim 0.04$ Å^{-1}) of the

block copolymer concentration whereas scattering profile becoming narrower in the low Q region with increase in block copolymer concentration. This can be understood in terms of increase in the size of the aggregates whereas maintaining its ordered structure. The fitted parameters of aggregates of nanoparticles are given in table 5.4. The surface fractal dimension of aggregates in accordance with increase in size of aggregate decreases as expected with increase in block copolymer concentration. The volume fraction of the particles within the aggregates has a value around 0.4 which is significantly less than for ordered simple cubic structure (0.54) and can be expected for deviations from perfect ordering of particles (i.e. short range ordered structures). The combined effect of temperature and concentration has been examined in figure 5.8 where SANS data of 1 wt% and 10 wt% nanoparticles with 1 wt% block copolymer are compared at different temperatures. It is clearly seen that there is suppression in attractive interaction followed by suppressed aggregation at higher temperature in the case of higher nanoparticle concentration.

The strong temperature dependence of depletion interaction in present system arises as a result of enhanced micellization of block copolymer with increase in temperature which has been examined in figure 5.9. The data of pure block copolymer solution (prepared in D_2O) show increase in scattering intensity (proportional to the scattering volume) with temperature indicating increasing size of block copolymer self-assembly. These block copolymer micelles can be modeled as consisting of hydrophobic core with Gaussian chains (hydrophilic part) attached to it [168]. The dependence of calculated micellar parameters on temperature are given in table 5.5 which clearly shows increase in micellization (volume fraction and size) with temperature.

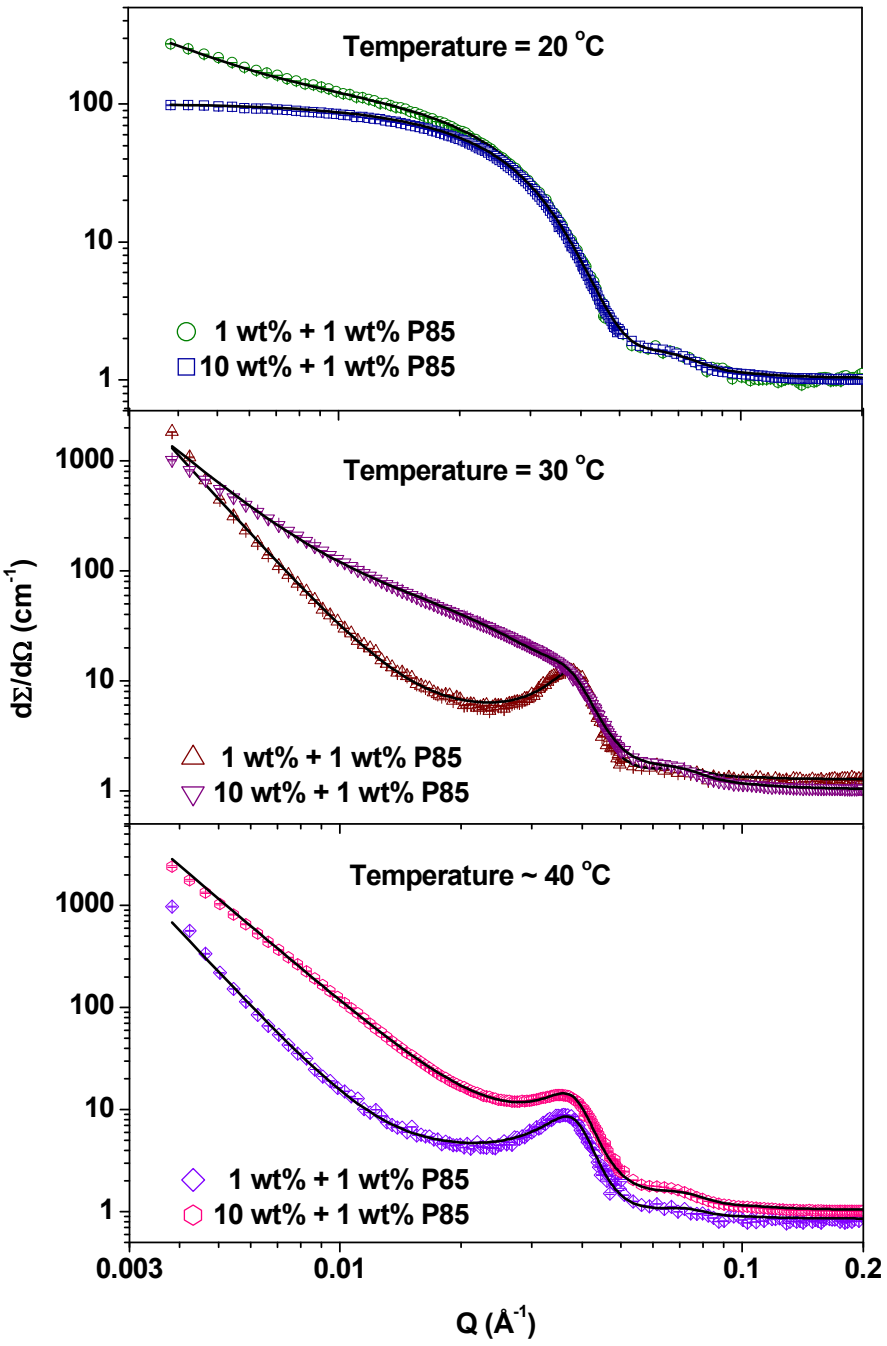

Figure 5.8. Comparison of SANS data of 1 and 10 wt% nanoparticles with 1 wt% block copolymer at different temperatures.

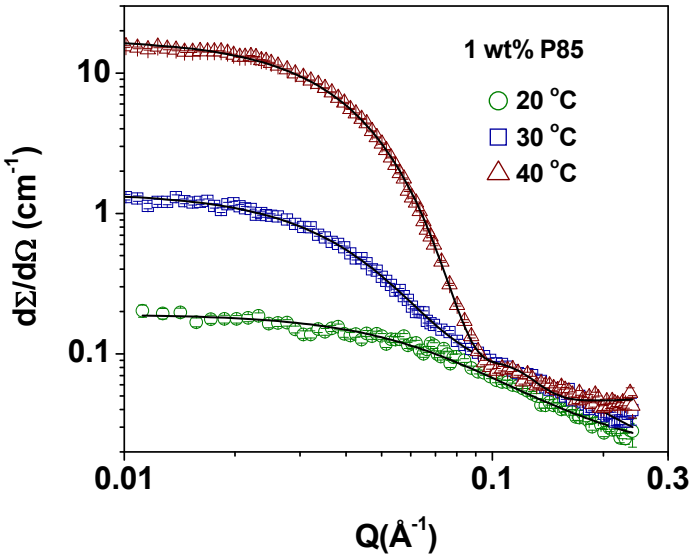

Figure 5.9. SANS data of 1 wt% P85 block copolymer system with increasing temperature.

Table 5.4. The structural parameters of nanoparticle aggregates as induced by block copolymer at 40 °C.

P85 concentration (wt%)	Surface fractal dimension D_s	Particle-particle distance d (nm)	Volume fraction within the aggregates φ
0.0	-	-	-
0.2	2.5 ± 0.1	17.0 ± 0.5	0.37 ± 0.02
0.4	2.3 ± 0.1	17.0 ± 0.5	0.38 ± 0.02
0.6	2.0 ± 0.1	17.0 ± 0.5	0.40 ± 0.03
0.8	2.0 ± 0.1	17.0 ± 0.5	0.40 ± 0.03
1.0	2.0 ± 0.1	17.0 ± 0.5	0.40 ± 0.03

Table 5.5. The parameters of micellar structure of 1 wt% P85 block copolymer at different temperatures. The calculated value of radius of gyration of unimer is 2.2 ± 0.2 nm.

Temperature (^oC)	Micellar fraction ϕ (%)	Core radius R_c (nm)	Aggregation number N	Radius of gyration of PEO chain R_{gc} (nm)
15	0	-	-	-
30	15	3.6 ± 0.2	52	1.5 ± 0.2
45	100	3.8 ± 0.2	63	1.5 ± 0.2

5.4.3. Role of nanoparticle size in tuning of depletion interaction

The depletion force depends on excluded volume, which can be varied by different ways depending on the components and solution conditions. We have already seen that increase in excluded volume on micellization of block copolymer with increasing temperature enhances depletion interaction. The excluded volume can also be tuned by the size of nanoparticles and therefore it is expected to play important role in determining the depletion force. The SANS data of smaller sized Ludox SM30 nanoparticles ($2R_m$ ~ 8 nm) with varying block copolymer concentration are shown in figure 5.10. It is observed unlike the case of larger sized nanoparticles (figure 5.1), the data in figure 5.10 do not show any significant change even up to very large concentration (5 wt%) of block copolymer. There is in fact no depletion interaction observed for the smaller sized nanoparticles. The calculated structure factor (inset of figure 5.10) more or less remains same with increasing block copolymer concentration. The absence of depletion interaction may be understood in terms of decrease in excluded volume effect with decrease in the size of nanoparticles [74].

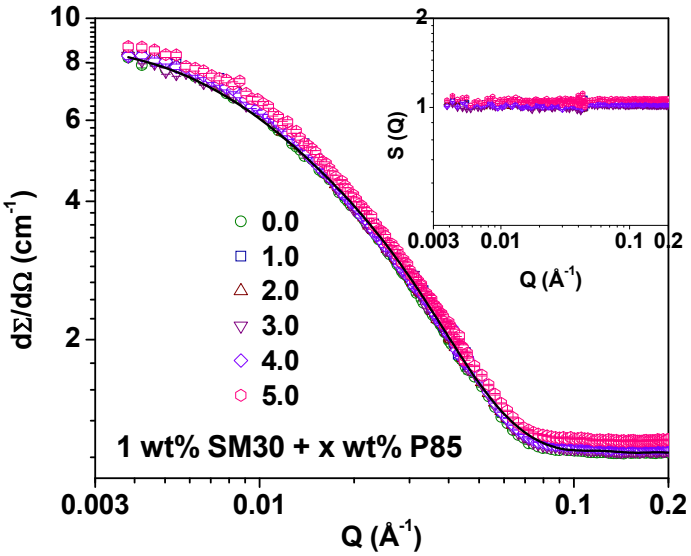

Figure 5.10. SANS data of 1 wt% SM30 silica nanoparticles with varying concentration of P85 block copolymer at 20 ^{o}C. Inset shows corresponding structure factors.

5.5. Conclusions

The evolution of structure and interaction in aqueous solution of charged silica nanoparticles and amphiphilic block copolymer has been studied. The presence of amphiphilc block copolymer induces depletion interaction between charged silica nanoparticles leading to particle clustering. The depletion interaction has been modeled using an attractive Yukawa potential whose range has been found to be much larger than van der Waals attraction. The aggregation of charged nanoparticles is observed as a consequence of dominance of depletion interaction over long-range electrostatic repulsion. The magnitude and range of depletion interaction can be tuned by the size of the nanoparticles and concentration of block copolymer as well as by the self-assembly of block copolymer through solution temperature. The particles under depletion interaction form large-sized ordered clusters and characterized by the surface fractal structure.

Chapter 6

POLYMER-DEPENDENT RE-ENTRANT PHASE BEHAVIOR OF CHARGED NANOPARTICLE SOLUTION

6.1. Introduction

Polymers may either adsorb on the nanoparticles or may remain free in solution depending on the system conditions [246-248]. The non-adsorbing nature of polymer molecules is known to give rise to depletion interaction between nanoparticles [25, 74, 162, 236]. Depletion interactions are at the core of many important properties of the nanoparticle-polymer composites, including the conditions of colloid stability and critical points of phase separations in different nanoparticle-polymer-solvent mixtures. The understanding of depletion interaction is typically based on pseudo-one-component description where reduction in polymer density between the particles creates an imbalance in osmotic pressure resulting in a net particle attraction of entropic origin [75, 249, 250]. At sufficient polymer concentration, when the attraction is large enough, phase separation occurs in the colloid-polymer mixture as observed in the case of nanoparticle-block copolymer system (chapter 5).

The well established models for depletion interaction predict monotonic growth in the strength of depletion attraction with increasing polymer concentration [74, 75, 162, 251]. However, a colloidal dispersion which is destabilized at low polymer concentrations due to depletion attraction may re-stabilize at high concentrations due to so called depletion

stabilization [74, 252-254]. The evolution of depletion attraction is reasonably understood, but the formalism of stabilization effect is still a subject of debate. One understanding is that the stability arises due to the presence of repulsive maxima in the free energy curve of interaction between the particles at high polymer concentrations [254]. Presence of other forces such as electrostatic repulsion and/or polymer-polymer repulsion (non-ideality of the polymer molecules) is also found to results in a positive potential barrier in combination with an attractive well in the depletion interaction [255-259]. As the polymer concentration increases towards the semi dilute or overlap concentration, and/or the radius of gyration (R_g) is not much less than particle radius (R_p), the polymer–polymer interaction becomes important leading to an oscillatory form of interaction potential [250]. On the contrary, there are some studies assuming that depletion interactions are purely attractive, and the depletion re-stabilization at higher concentrations is solely due to the decrease of the depletion layer thickness leading to weaker depletion attraction [75, 251, 260]. For understanding nanoparticle-polymer phase behavior, it is therefore of interest to look into the evolution of depletion interaction between nanoparticles in presence of wide range of polymer concentration.

In this chapter, a re-entrant phase behavior in nanoparticle-polymer system has been observed where one-phase charge stabilized silica nanoparticles undergo two-phase system (nanoparticle aggregation) and back to one-phase as a function of polymer (polyethylene glycol) concentration [261, 262]. Small-angle neutron scattering (SANS) studies have been carried out to examine the role of various interactions during this re-entrant phase behavior responsible for the nanoparticle attraction, aggregation and stabilization at low, intermediate and high polymer concentrations, respectively. The polymer is contrast-matched for directly studying the interaction between nanoparticles. The interaction between the nanoparticles has been modeled

using a two-Yukawa potential accounting for electrostatic repulsion between charged nanoparticles along with varying polymer dependent depletion interaction [236, 237].

6.2. Experimental section

Electrostatically stabilized colloidal suspensions of 30 wt% of silica nanoparticles (Ludox LS30) in water and polyethylene glycol (PEG) polymers having molecular weights 4, 6 and 20 K (kg/mol) were purchased from Sigma Aldrich. Samples for pure nanoparticles and polymer systems were prepared by dissolving weighted amount of silica and polymer in D_2O. For nanoparticle-polymer systems, samples were prepared in a mixed H_2O/D_2O solvent for which polymer is contrast-matched to the solvent. All the measurements were carried out for fixed concentration (1 wt%) of silica nanoparticles with varying polymer concentration (0 to 5 wt%). Measurements were carried out in the presence of 0.2 M NaCl in order to reduce electrostatic repulsion between nanoparticles, so that it can be comparable with the depletion attraction to observe particle clustering. Some measurements were also carried out to examine the role of varying salt concentration (0.1 to 0.3 M NaCl). Small-angle neutron scattering measurements were carried out using SANS facilities at the Dhruva reactor, Bhabha Atomic Research Centre, Mumbai [145] and the Swiss Spallation Neutron Source SINQ, Paul Scherrer Institut, Switzerland [146]. The temperature was kept fixed at 30 ^{o}C during the measurements. Data were corrected for background and empty cell contributions and normalized to absolute cross-sectional unit using standard procedure.

6.3. SANS analysis

The coherent differential scattering cross-section per unit volume ($d\Sigma/d\Omega$) in SANS experiments is expressed by [127, 143]

$$\frac{d\Sigma}{d\Omega}(Q) = nV^2\left(\rho_p - \rho_s\right)^2 P(Q)S(Q) + B \tag{6.1}$$

where n is the number density and V is particle volume. ρ_p and ρ_s are scattering length densities of particles and solvent, respectively. $P(Q)$ is intraparticle structure factor and $S(Q)$ is interparticle structure factor. B is a constant term denoting incoherent background mostly arising from the hydrogen present in the system.

The data analysis has been carried out for $P(Q)$ and $S(Q)$ using the same methodology as discussed in chapter 5. The fitted parameters are obtained by comparing the experimental scattering data with different theoretical models. Corrections for instrumental smearing were taken into account throughout the data analysis. The modeled scattering profiles were smeared by the appropriate resolution function to compare with the measured data [150].

6.4. Results and discussion

6.4.1. Observation of re-entrant phase behavior

An insight into the microscopic understanding of the effective polymer-induced interaction between nanoparticles can be obtained by studying the phase behavior of nanoparticles macroscopically as a function of polymer concentration. Figure 6.1 shows the phase behavior of 1 wt% LS30 silica nanoparticles with varying concentration of PEG-6 K in presence of 0.2 M salt (NaCl) in H_2O. The figure depicts the variation of the transmission of light through silica nanoparticle system as a function of polymer concentration. It is observed that the value of transmission decreases dramatically from a clear solution (one-phase) after a critical concentration (~ 0.004 wt%) of polymer. The optical appearance of the system also shows turbidity (two-phase) which increases with increasing polymer concentration. On further addition of polymer (>0.5 wt%), an increase in the transmitted light intensity is observed and the

system regains its original behavior (one-phase). This variation of transmission of light may be related to the evolution of the structure in the system where the formation of larger structures will scatter more light and hence, the decrease in the transmission [263]. Based on this fact the phase behavior may be divided into three regimes of polymer concentration (figure 6.1). The system converts from charge stabilized one-phase nanoparticle system to two-phase (nanoparticle aggregation) system in the regime I, remains throughout in two-phase system in regime II and returns back to one-phase in regime III. Such re-entrant phase behavior has stimulated interest in ascertaining the details of the responsible interactions.

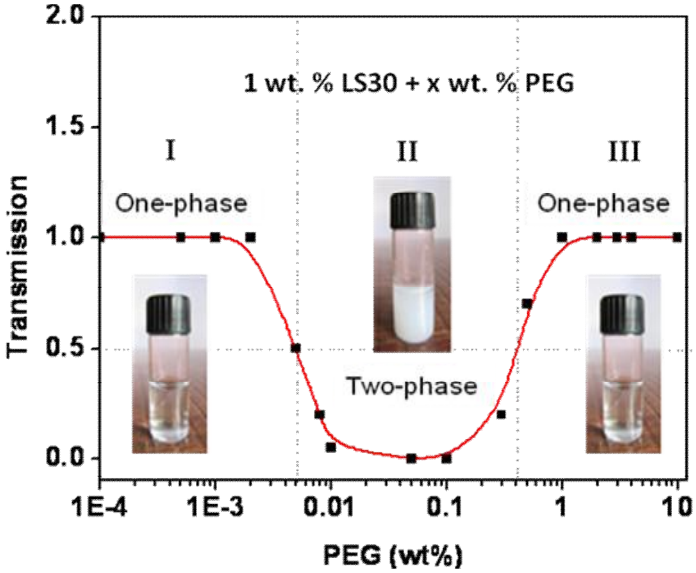

Figure 6.1. Phase behavior of 1 wt% LS30 silica nanoparticles with varying PEG concentration in presence of 0.2 M NaCl in H_2O. The figure depicts the transmission of light through the nanoparticle-polymer system with varying concentration of polymer. The insets show the physical state of the samples in different regimes of phase behavior.

The interplay of different interactions (electrostatic repulsion vs. depletion attraction) and resultant structures in deciding the above phase behavior has been examined by SANS. Figure 6.2 shows the SANS data of 1 wt% silica nanoparticles in presence of varying concentration of PEG-6 K in a H_2O/D_2O solvent for which PEG molecules are contrast-matched. The SANS data

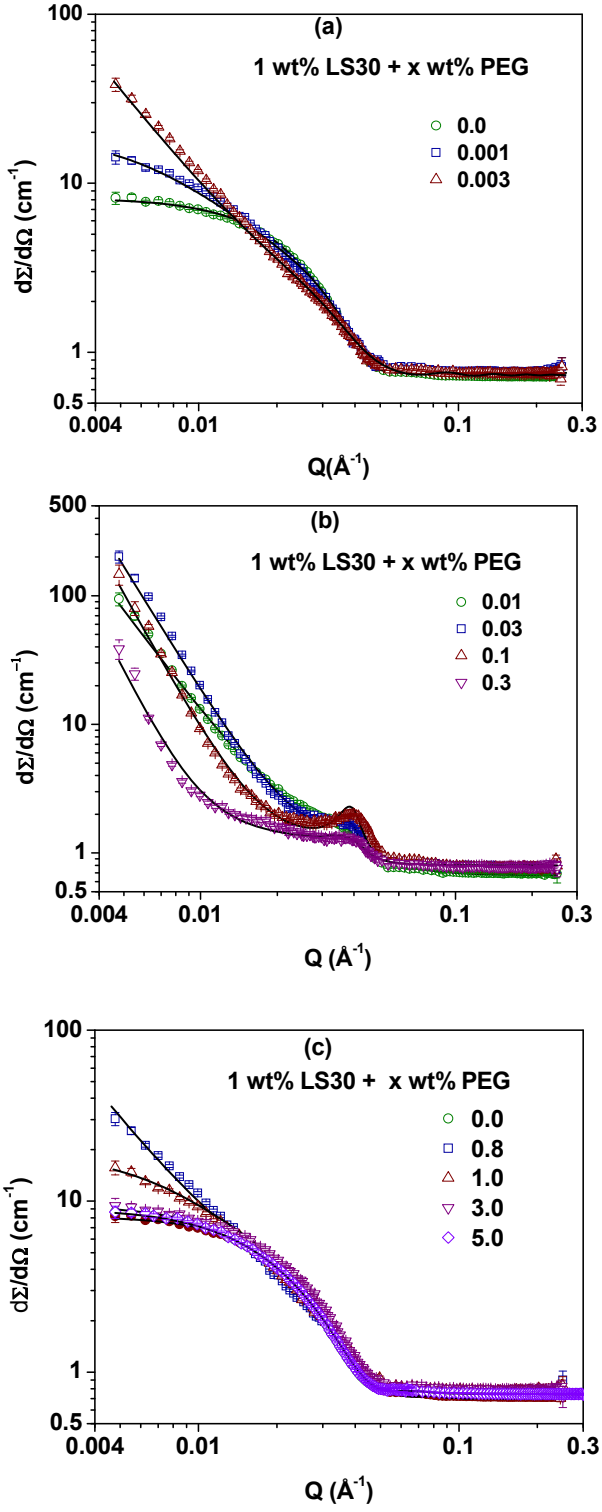

Figure 6.2. SANS data of 1 wt% silica nanoparticles with varying PEG-6 K polymer concentration (0 to 5.0 wt%) corresponding to three regions of phase behavior in figure 6.1.

are divided into three sets corresponding to three different polymer regimes of phase behavior in figure 6.2. The features of scattering data are observed to be significantly different for the three data sets. In the first data set [figure 6.2(a)] where nanoparticle-polymer system converting from one-phase to two-phase system, there is a systematic buildup of scattering in the low Q region with data remaining almost similar in the intermediate and high Q values. The second data set [figure 6.2(b)] for two-phase system shows a very large scattering intensity buildup in the low Q region followed by a Bragg peak at intermediate Q value. In the third set [figure 6.2(c)], the features of SANS data are quite similar to that of the first set. However, the buildup of scattering in third set (unlike first set) suppresses with the increase in the polymer concentration as the two-phase system returns back to one-phase system. Finally, the scattering profile at higher polymer concentration (5 wt%) is found to be almost overlapping with that of the pure nanoparticle system [261].

The buildup of scattering in the low Q region at low polymer concentrations [figure 6.2 (a)] arises because of attractive interaction induced in the system. The corresponding $S(Q)$ plots as calculated by dividing the data with that of nanoparticles without polymer are shown in figure 6.3 (a). The diverging nature of $S(Q)$ in the low Q region and in particular increase in the value of $S(Q=0)$ clearly suggests enhancement in the attractive interaction with the increasing polymer concentration [236, 259]. The $S(Q)$ in this concentration regime has been calculated using a two-Yukawa potential [eqn. 5.2] accounting for both attractive (depletion) as well as repulsive (electrostatic) forces in the system. The fact that no features of $S(Q)$ in 1 wt% nanoparticle solution (without polymer) were observed in the Q range of measurement, therefore the parameters of repulsive interaction (K_2 and α_2) were determined from the concentrated nanoparticle solutions. The values of K_2 and α_2 are found to be $2.0\,k_BT$ and 12.5,

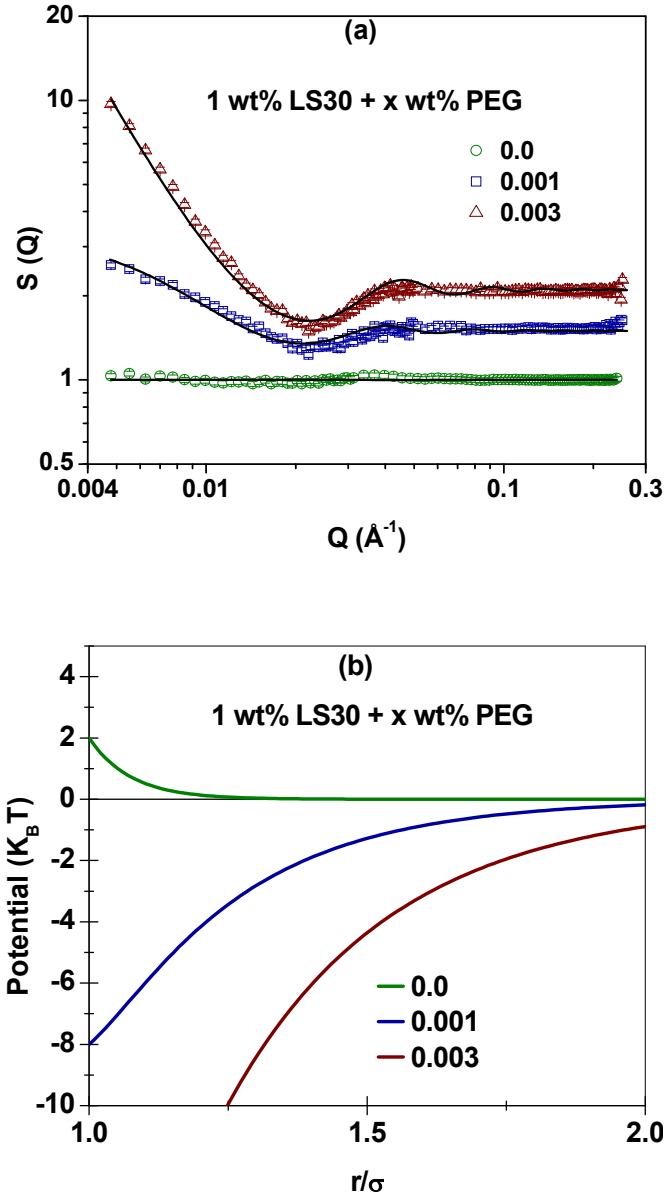

Figure 6.3. Variation of (a) structure factor and (b) total interaction potential for 1 wt% LS30 silica nanoparticles with varying PEG concentration (0 to 0.003 wt%). The data of the structure factor are shifted vertically for clarity.

respectively in presence of 0.2 M NaCl. These parameters were kept fixed during the analysis as the electrostatic part of the interaction on addition of polymer is expected to remain unchanged. Thus only parameters K_1 and α_1 corresponding to depletion interaction were used as fitting

parameters in $S(Q)$. The calculated resultant interaction potentials are plotted in figure 6.3 (b). Both the magnitude of attraction (K_1) and the range ($1/\alpha_1$) (table 6.1) are found to be much larger than that of repulsion. The strength of the attraction increases whereas range remains almost same with the increase in the polymer concentration. It is also found that the value of interaction potential at an average distance has a value around 1.5 k_BT (average thermal kinetic energy) for 0.003 wt% of polymer, which is thereafter (higher polymer concentration) responsible for one-phase system converting to two-phase system as shown in figure 6.1 [261].

The SANS data [figure 6.2(b)] corresponding to two-phase system (nanoparticle aggregation) show linearity in the low Q region indicating the fractal nature of nanoparticle clusters, whereas Bragg peak around Q_p = 0.04 $Å^{1}$ represents the ordered packing of nanoparticles within the aggregates [206, 236]. The slopes of all the data in figure 6.2(b) in low Q region have a value greater than 3, implies the scattering resulting from surface fractal structure of the aggregates [142, 143]. The average distance ($d \sim 2\pi/Q_p$) between the particles as calculated from Bragg peak position is similar to the particle size suggesting the simple cubic type packing of the particles within the clusters [264, 265]. Therefore, the data have been fitted by the sum of power law behavior for surface fractal and contribution from ordered particles within the clusters. The Bragg peak emerging as a result of interaction between the particles within the clusters is fitted through $S(Q)$ calculated from the analytical solution of Ornstein-Zernike equation in the Percus-Yevick approximation (PYA) employing a hard sphere potential between the particles [137]. These two calculated contributions for a typical data (polymer concentration of 0.03 wt%) are shown in figure 6.4. The fractal dimension (D_s = 6-m, where m is slope of the data) decreases with the increase in the polymer concentration [figure 6.2 (b)], which may be explained on the basis of the polymer concentration dependent size of nanoparticle

aggregates. The large size of aggregates means smoother surfaces, and hence lower surface fractal dimension. There is suppression of scattering (polymer concentration 0.3 wt%) in the intermediate Q range and probably indicate the loosening of aggregates (signature of re-entrant phase behavior) with increase in polymer concentration.

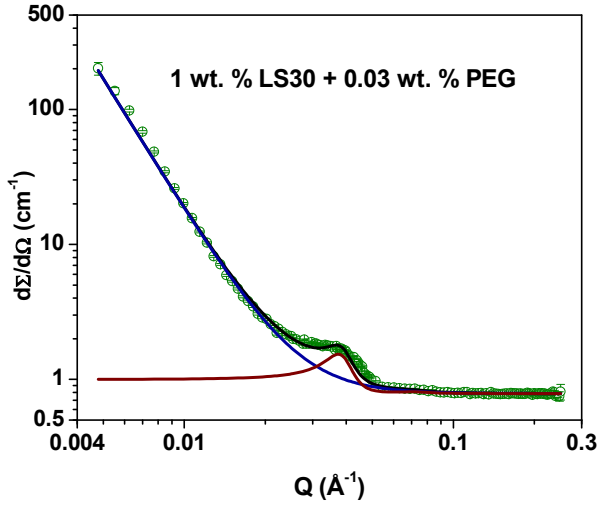

Figure 6.4. The fitted data of 1 wt% LS30 + 0.03 wt% PEG-6 K along with calculated contributions arising from nanoparticle aggregates (power law) and nanoparticles within aggregate (Bragg peak).

The SANS data approaching to re-entrant phase behavior [figure 6.2 (c)] have also been analyzed using two-Yukawa potential. The systematic decrease in the low Q data suggests that the attractive interaction between nanoparticles is now decreasing with increasing polymer concentration. The structure factors and calculated potentials corresponding to the data in figure 6.2(c) are shown in figure 6.5. The fitted parameters of attractive potential are given table 6.1 (c). It is clear that the strength of the attractive part decreases dramatically with increasing polymer concentration. The range of the attractive potential is also found to be decreasing at higher polymer concentrations. These results thus demonstrate that the change in depletion interaction dictates the re-entrant phase behavior. Usually, the phase behavior in such systems is governed by the interplay of following interactions present in the system (i) anoparticle-nanoparticle

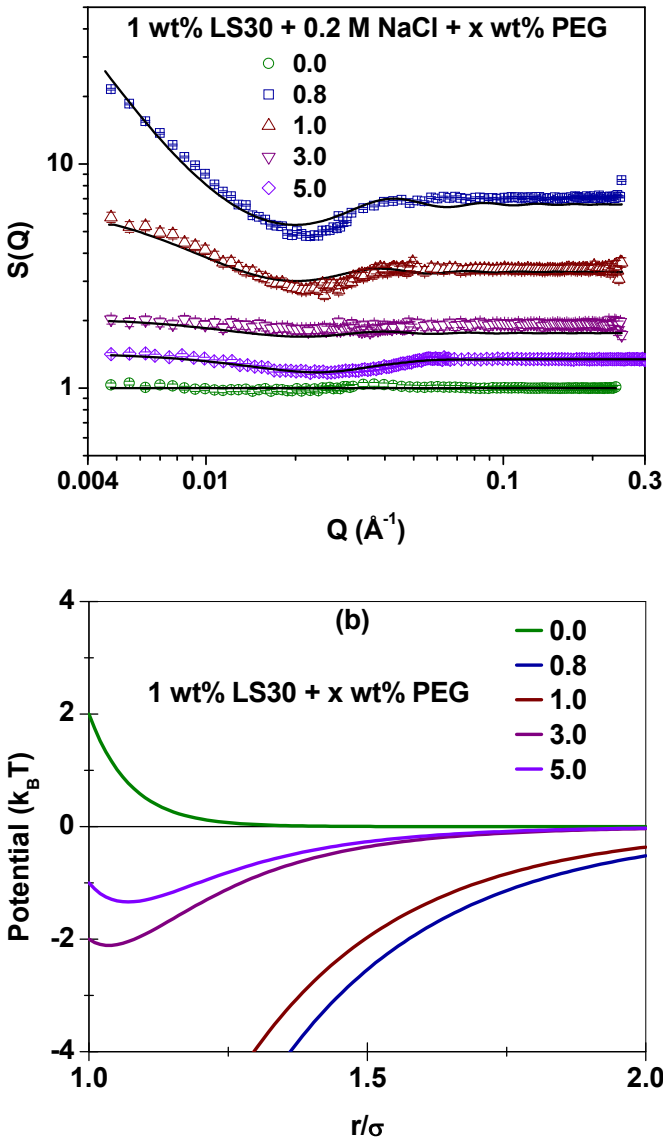

Figure 6.5. Variation of (a) structure factor and (b) total interaction potential for 1 wt% LS30 silica nanoparticles with varying PEG concentration (0.8 to 5.0 wt%). The data of the structure factor are shifted vertically for clarity.

electrostatic interaction, (ii) polymer-induced depletion interaction between nanoparticles and (iii) polymer-polymer interaction. The electrostatic repulsion between nanoparticles is not expected to change much with increasing polymer concentration. However, at low polymer concentrations, the electrostatic repulsion dominates over the depletion attraction. The increase

Table 6.1. Fitted parameters of interaction and structure for 1 wt% silica nanoparticles as a function of polymer (PEG) concentration.

(a) The evolution of depletion interaction in the regime of low polymer concentration. The parameters of repulsive interaction (K_2 = 2.0, α_2 = 12.5) are fixed.

Polymer concentration (wt%)	K_1 (k_BT)	α_1
0.0	-	-
0.001	10.0 ± 0.9	3.0 ± 0.3
0.003	24.0 ± 2.0	2.6 ± 0.3

(b) The structure of nanoparticle aggregates in the intermediate polymer concentration.

Polymer concentration (wt%)	Surface fractal dimension D_s	Particle-particle distance d (nm)	Volume fraction ϕ
0.01	2.9 ± 0.1	-	0.33 ± 0.03
0.03	2.5 ± 0.1	17.0 ± 0.8	0.41 ± 0.03
0.1	2.3 ± 0.1	16.0 ± 0.8	0.43 ± 0.03
0.3	2.1 ± 0.1	17.5 ± 0.9	0.27 ± 0.03

(c) The evolution of depletion interaction in the regime of high polymer concentration. The parameters of repulsive interaction (K_2 = 2.0, α_2 = 12.5) are fixed.

Polymer concentration (wt%)	K_1 (k_BT)	α_1
0.8	14.0 ± 0.9	2.6 ± 0.2
1.0	12.0 ± 0.9	2.8 ± 0.3
3.0	4.0 ± 0.3	3.0 ± 0.3
5.0	1.0 ± 0.1	4.0 ± 0.4

in polymer concentration enhances depletion attraction to give rise to the nanoparticle aggregation in two-phase system. The re-entrant to one-phase system arises because of increase in polymer-polymer repulsion at high polymer concentrations [257, 259, 266, 267]. This polymer-polymer interaction effectively tends to suppress the depletion attraction by forcing the system to do more work for expelling the polymer molecules from the depletion zones. Moreover, at high polymer concentrations, the polymer chains between the particles are required to be transported against a very steep osmotic pressure gradient between depletion region and the bulk causing a stabilization effect [74, 254]. It may be noted that the strength of the depletion attraction is not monotonically increasing with increasing polymer concentration. However, its nature remains attractive [figure 6.5].

6.4.2. Tuning of electrostatic interaction in deciding the phase behavior

The degree of attractive and repulsive forces acting in the system decides the phase behavior [figure 6.1]. In the experiments discussed so far we have only tuned the attractive component of the interaction. The effect of varying electrostatic repulsion and hence the total potential on the evolution of structure and interaction of nanoparticles has also been examined by varying the ionic strength of the solution. Figure 6.6 shows the SANS data of 1 wt% nanoparticles with 1 wt% PEG and varying salt concentration (0.1 to 0.3 M NaCl). The SANS data show significantly different features as the salt concentration is increased suggesting that the interaction and structure in the system is modifying with the increasing salt concentration. The buildup of scattering in the low Q region for salt concentration for 0.1 M to 0.2 M is because of total potential becomes more attractive on screening of the repulsion part. However, increase in overall attractive potential for salt concentration 0.3M and beyond leads to nanoparticle

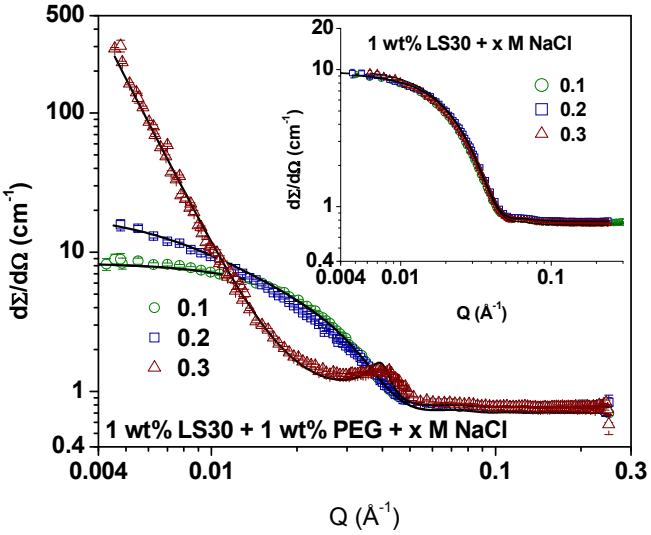

Figure 6.6. SANS data of 1 wt% silica nanoparticles with 1 wt% PEG-6 K polymer in presence of varying salt (NaCl) concentration. Inset shows the SANS data of the nanoparticle system without any polymer in presence of salt.

Table 6.2. Fitted parameters of the interaction and structure in nanoparticle-polymer (1 wt% LS30 + 1 wt% PEG-6 K) system with varying salt concentration.

(a) The calculated parameters of two-Yukawa potential prior to formation of two-phase system.

Salt concentration (M)	K_1 (k_BT)	α_1	K_2 (k_BT)	α_2
0.1	12.0 ± 0.9	3.0 ± 0.3	3.0 ± 0.3	9.0 ± 0.9
0.2	12.0 ±0.9	2.8 ± 0.3	2.0 ± 0.3	12.5 ± 0.9

(b) The structure of nanoparticle aggregates at high salt concentration.

Salt concentration (M)	Surface fractal dimension D_s	Particle-particle distance d (nm)	Volume fraction ϕ
0.30	2.2 ± 0.1	16.8 ± 0.8	0.45 ± 0.02

aggregation (table 6.2). Charged colloids are known to undergo attractive interaction when the ionic strength of the solution is increased, but no significant changes are observed in the data of nanoparticles with salt alone in absence of any polymer [inset of figure 6.4], as the system may still be repulsive [268]. The LS30 silica nanoparticle system shows salt-induced aggregation for NaCl concentration of greater than 1 M. The structure of these salt-induced aggregates has the same morphology as found with the polymers. However, the system with increasing salt concentration does not show any re-entrant phase behavior as obtained in the case of increasing polymer concentration.

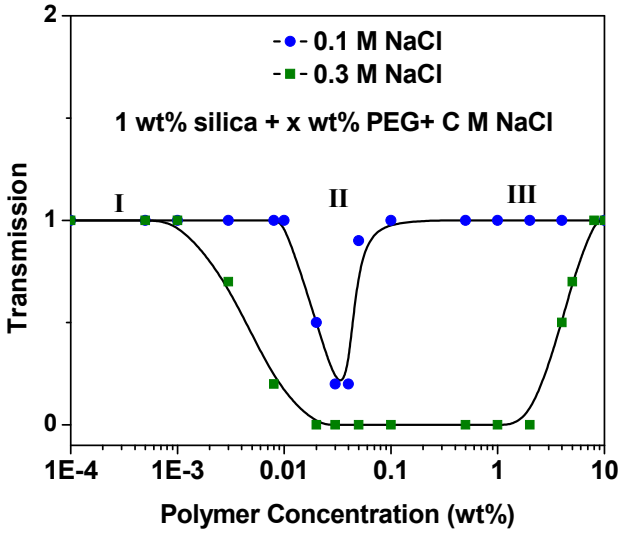

Figure 6.7. The phase behavior of 1 wt% silica nanoparticles in presence of 0.1 M and 0.3 M NaCl with varying PEG concentration.

Figure 6.7 shows the phase behavior of 1 wt% LS30 silica nanoparticles with varying concentration of PEG-6 K in presence of 0.1 M and 0.3 M salt (NaCl) in H_2O. Figure 6.7 shows the variation of the transmission of light through silica nanoparticle system as a function of polymer concentration. The transmission follows the similar trends as seen in figure 6.1 with three regions of polymer concentration. The values of transmission decrease dramatically after

critical polymer concentrations in both the cases (0.1 and 0.3 M salt) where the systems convert from one-phase to two-phase system [261]. On further addition of polymer, both the systems show re-entrant phase behavior from two-phase system (region II) to one-phase (region III) system. Interestingly, the region II of phase behavior corresponding to two-phase system is observed to be quite extended in 0.3 M in comparison to that for 0.1 M salt concentration. This implies that the transformation from one-phase to two-phase system occurs at lower polymer concentration while re-entrant from two-phase to one-phase system takes place at higher polymer concentration with increasing salt concentration. In order to understand these features SANS studies have been performed on silica nanoparticles-PEG systems in presence of 0.1 M and 0.3 M salt concentrations also.

The SANS data of 1 wt% silica nanoparticles at different PEG concentrations (0.01, 0.1, 1.0 and 10.0 wt%) with three salt concentrations (0.1, 0.2 and 0.3 M) are compared in figure 6.8. The scattering data show significant differences with salt variation at all four PEG concentrations. At lowest PEG concentration (0.001 wt%), the SANS data show a buildup of scattering in low Q values which increases with increasing salt concentration. The nanoparticles experience an effective enhancement in attractive force due to suppression of electrostatic repulsion. At polymer concentration 0.01 wt%, SANS data in presence of 0.2 and 0.3 M NaCl show signatures of particle aggregation whereas attraction is still evolving at 0.1 M salt. For polymer concentration 0.1 wt%, the SANS data are governed by nanoparticle aggregates with ordered packing of particles for salt concentrations 0.2 and 0.3 M NaCl. On the other hand, system with 0.1 M NaCl shows the re-entrant of one-phase. This may be explained by considering the fact that higher electrostatic repulsion combined with even smaller polymer-polymer interaction (low salt and low polymer concentrations) may cause sufficient decrease in

the attraction leading to the re-entrant of the one phase. Finally at quite high concentration (10 wt%) of PEG, the system undergo re-entrant phase behavior for all three salt concentrations. These results clearly show that the phase behavior of nanoparticle-polymer system may be varied by tuning ionic strength and polymer concentration.

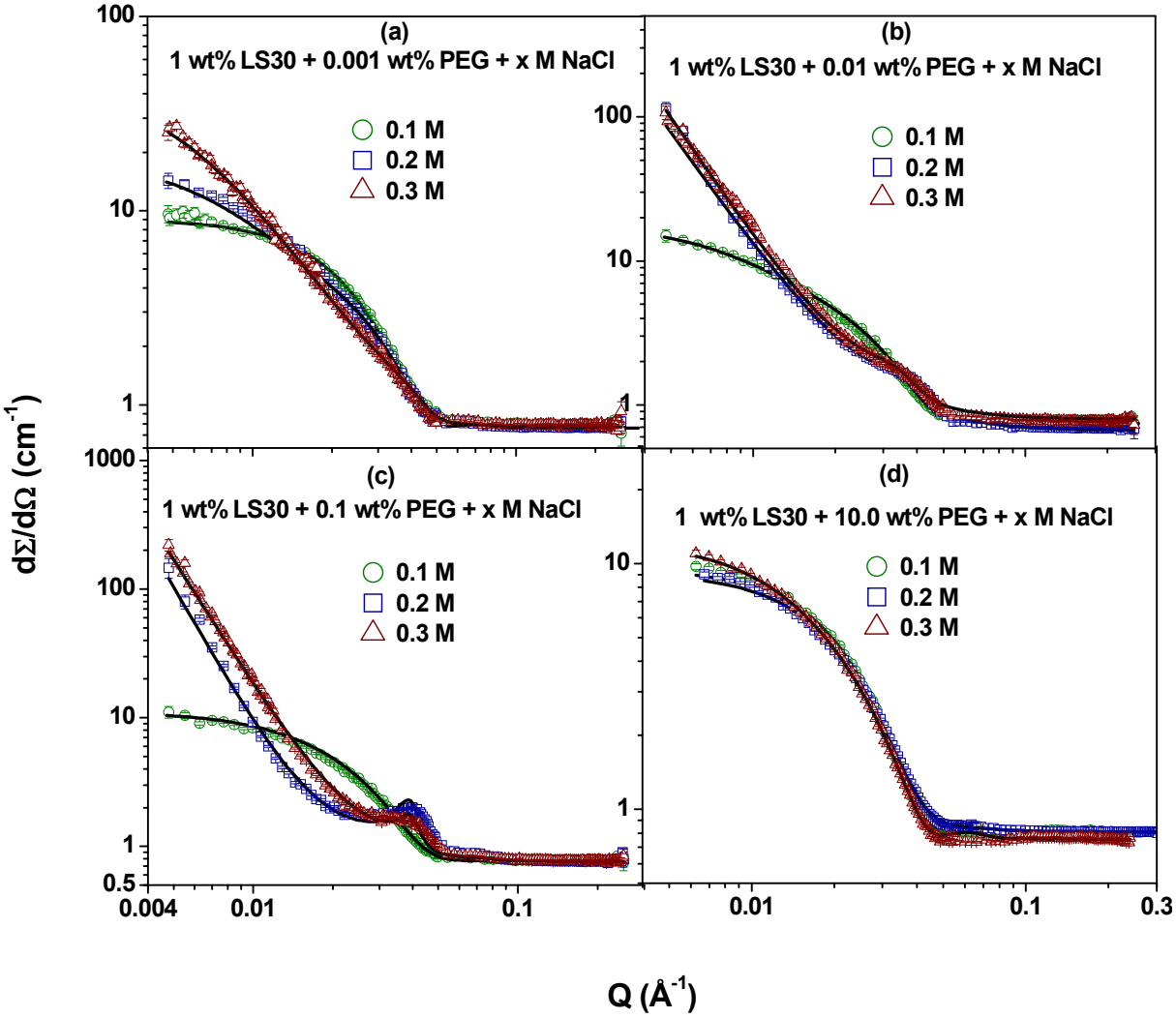

Figure 6.8. SANS data of 1 wt% LS30 nanoparticles with varying (a) 0.001 wt% (b) 0.01 wt% (c) 0.1 wt% (d) 10 wt% PEG in the presence of three salt concentrations.

6.4.3. Role of polymer molecular weight in re-entrant phase behavior

Figure 6.9 shows the SANS data of pure 1 wt% polymers having different molecular weights (M_W = 4K, 6K and 20 K) in presence of 0.2 M NaCl in D_2O. The SANS data of polymer systems show typical features of the form factor $P(Q)$ that governed scattering with $1/Q^2$ dependence at high Q values. The $1/Q^2$ cutoff (reciprocal of R_g) dependence of polymer scattering, as expected shifts to lower Q values with the increase in the molecular weight. The polymers have been modelled using Gaussian coil model. The calculated radii of gyration are 2.2 nm, 2.8 nm and 5.5 nm for PEG-4 K, PEG-6 K and PEG-20 K polymers, respectively (table 6.3). It may be mentioned that the variation of radius of gyration with molecular weight follows the relation R_g α $(M_W)^{\gamma}$, where γ=0.61 is found to be quite near to the Flory exponent for real chains in good solvent [19, 269]. The choice of sizes ($R_g < R_p/3$) of the polymers with respect to nanoparticles in present study is varied within the range following colloidal limit of the polymer-induced depletion interaction between nanoparticles [74].

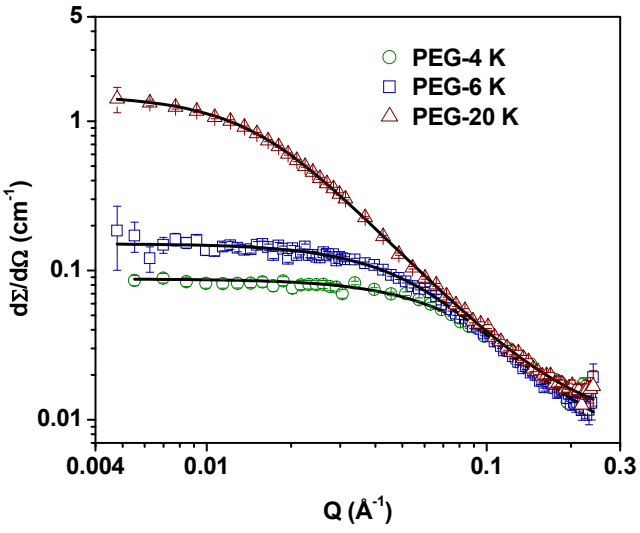

Figure 6.9. SANS data of 1 wt% PEG of different molecular weights (M_W= 4K, 6K and 20 K) in presence of 0.2 M NaCl in D_2O.

Table 6.3. Fitted structural parameters of 1 wt% of different molecular weight polymers.

Molecular weight M_W (kg/mol)	Radius of gyration R_g (nm)
4 K	2.2 ± 0.2
6 K	2.8 ± 0.2
20 K	5.5 ± 0.4

The molecular weight of polymer is known to be one of the strong parameters in tuning the polymer-induced depletion interaction. The excluded volume effect is enhanced with increasing polymer size and hence depletion interaction [25]. Figure 6.10 shows SANS data of 1 wt% nanoparticles with three different molecular weight (4 K, 6 K and 20 K) polymers in one-phase system for polymer concentrations (a) prior and (b) after the region of two-phase system in phase behavior. The analysis (table 6.4) shows that conversion from one-phase to two-phase system (increase in attractive depletion) is favored with the increase in the molecular weight of the polymer. However, same is not the case in achieving the re-entrant phase behavior. This is possibly because the polymer-polymer interaction is suppressed with increasing molecular weight (decrease in number density of polymer reducing the interparticle distance between polymer molecules). Both the magnitude and range of depletion interaction are found to be increasing with the molecular weight of polymer. These results thus show that the total interaction and resultant structure in nanoparticle-polymer system can also be tuned by varying molecular weight of polymer [261].

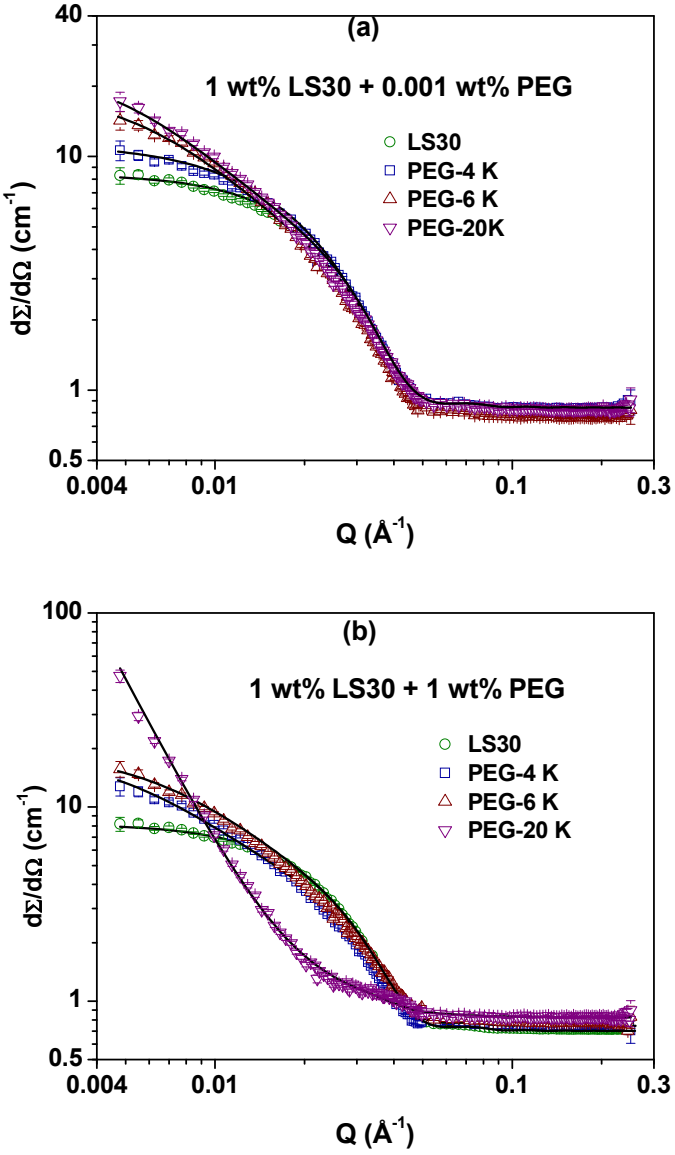

Figure 6.10. SANS data of 1 wt% silica nanoparticles with different molecular weight polymers (M_W= 4 K, 6 K and 20 K) at (a) 0.001 and (b) 1.0 wt% concentrations of polymers.

Table 6.4. Fitted parameters of 1 wt% silica nanoparticles with different molecular weight polymers (M_W = 4 K, 6 K and 20 K) at (a) 0.001 and (b) 1.0 wt% concentrations of polymers.

(a) The comparison of depletion interaction for different polymers at 0.001 wt% concentration. The parameters of repulsive interaction (K_2 = 2.0, α_2 = 12.5) are fixed.

Polymer molecular weight M_W (kg/mol)	K_1 (k_BT)	α_1
4 K	8.0 ± 0.6	3.5 ± 0.4
6 K	10.0 ± 0.9	3.0 ± 0.4
20 K	12.5 ± 0.9	2.3 ± 0.3

(b) The comparison of depletion interaction for different polymers at 1.0 wt % concentration. The parameters of repulsive interaction (K_2 = 2.0, α_2 = 12.5) are fixed. In the case of PEG-20 K, the re-entrant phase is suppressed and the system is characterized by nanoparticle aggregates (Ds = 2.2 ± 0.1).

Polymer molecular weight M_W (kg/mol)	K_1 (k_BT)	α_1
4 K	9.0 ± 0.9	3.4 ± 0.5
6 K	10.0 ± 0.9	3.0 ± 0.4

6.5. Conclusions

The charge stabilized silica nanoparticles in presence of PEG polymer show a re-entrant phase behavior where nanoparticles undergo from one-phase to two-phase system and back to one-phase system as a function of polymer concentration. The evolution of interaction and structure responsible for this phase behavior has been studied by SANS by contrast matching the polymer. The phase behavior is found to be governed by the interplay of different interactions (i) electrostatic repulsion between nanoparticles, (ii) polymer-induced attractive depletion between nanoparticles and (iii) repulsive polymer-polymer interaction present in the system. At low polymer concentrations, the stability of this one-phase system is dictated by the dominance of electrostatic repulsion over the depletion attraction. On further addition of polymer, depletion attraction between nanoparticles sufficiently increases to give rise to the clustering of nanoparticles in two-phase system. Further, the re-entrant phase is driven by the reduction in depletion attraction as a result of polymer-polymer repulsion at higher polymer concentrations. The interaction between nanoparticles has been modelled by a two-Yukawa potential accounting for depletion as well as electrostatic interaction. The depletion interaction increase in going from one-phase to two-phase system, whereas decrease back in the re-entrant of one-phase system. The two-phase system is characterized by the nanoparticle clusters having surface fractal morphology. The role of varying electrostatic repulsion by ionic strength and depletion attraction by molecular weight of polymer has also been studied. The combination of these parameters (ionic strength and molecular weight of polymer) with polymer concentration decides the interaction and structure, which can be used to tune the re-entrant phase behavior in nanoparticle-polymer systems.

Chapter 7

SUMMARY

Complex structures formed by nanoparticle-macromolecule interactions strive to meet the promises of enhanced and often unique properties combining the features of nanoscale dimension and chemistry of macromolecules [11-15, 20, 152-154, 187-189, 218-221, 270]. The present thesis provides an understanding of nanoparticle interaction with different macromolecules and resultant structure of their composites. The model nanoparticles used are anionic silica nanoparticles whose interaction with four macromolecules (surfactant, protein, block copolymer and polymer) has been explored. The complex systems have been investigated under the varying solution conditions such as concentration, temperature, ionic strength, pH etc.

The interaction of nanoparticle with macromolecule in general is a combined effect of a number of forces such as electrostatic force, covalent bonding, hydrogen bonding, depletion interaction, hydrophobic interaction etc. These interactions can lead to a variety of structures depending upon the characteristics of the two components and solution conditions. Small-angle neutron scattering (SANS) has been used to investigate such complex structures as well as the responsible interactions. SANS with the easy possibility to vary contrast is an ideal technique to study such multi-component systems.

The thesis consists of seven chapters including this chapter on summary of thesis. Chapter 1 provides an introduction to characteristics of nanoparticles and macromolecules, their possible interactions as well as applications. The layout of the thesis is provided in chapter 1. Chapter 2 gives details of the SANS technique and its usefulness for characterizing such multi-

component systems. The results of the investigations of silica nanoparticle interaction with four different macromolecules (surfactant, protein, block copolymer and polymer) are described in chapters 3 to 6. The tuning of nanoparticle-surfactant interactions by varying surfactant type has been studied in chapter 3. Chapter 4 provides the study of protein adsorption and protein-mediated aggregation of nanoparticles. The nanoparticle aggregation as driven by block copolymer induced depletion interaction has been studied in chapter 5 while the re-entrant of individual particle phase from particle aggregation as directed by polymer has been examined in chapter 6.

Chapter 1 is devoted to a general introduction to nanoparticles and different macromolecules, their possible interactions and applications as well as an overview of important experimental techniques which can be used to investigate these systems. The silica nanoparticles are used as a model system because of their easy commercial availability, less expensive, high stability, biocompatibility and ability to be functionalized with a range of macromolecules [47, 48]. The macromolecules used are surfactant, protein, block copolymer and polymers belonging to different class of macromolecules with distinct properties. Surfactants are amphiphilic molecules which form micelle of different shapes and sizes [271] whereas proteins are biological molecules having a native folded structure [18]. Block copolymers are special type of non-ionic macromolecules consisting of blocks of two dissimilar moieties (e.g. hydrophilic PEO block and hydrophobic PPO block) [58]. In a suitable environment or solution conditions, these molecules can self-assemble to form micelles. Unlike block copolymers, simple polymers usually do not form self-assembled structures [19]. The complexes of nanoparticles with these macromolecules have tremendous applications in the areas ranging from electronics to nanomedicine to optics. There is need to understand the interaction of two components from the point of view of both the

scientific and application. Many of these applications require understanding of the interaction of two components which further depends on the characteristics of individual ones. A number of experimental techniques can be used to probe these systems. A brief description of these techniques broadly classified as macroscopic, microscopic, spectroscopic and scattering techniques is provided.

Chapter 2 gives the details of SANS technique. In SANS, similar to diffraction experiments, one measures the intensity of scattered neutron as a function of the wavevector transfer Q (= $4\pi\sin\theta/\lambda$, where λ is the incident neutron wavelength and 2θ is the scattering angle) [123-127]. The expression for scattering intensity [$I(Q) \sim (\rho_p - \rho_s)^2 \times P(Q) \times S(Q)$] contains two Q dependent terms: the intra-particle structure factor $P(Q)$ and the inter-particle structure factor $S(Q)$. $P(Q)$ is decided by the shape and size of the particle whereas $S(Q)$ depends on the spatial arrangement of particles and is thereby provide information of interparticle interactions. The analytical expressions of $P(Q)$ for different shapes and $S(Q)$ for different interactions are discussed. The term $(\rho_p-\rho_m)^2$ is known as contrast factor which is the square of the difference between the average scattering length densities of the particle (ρ_p) and the medium (ρ_m). The opposite sign of scattering lengths of hydrogen (-0.372×10^{-12} cm) and deuterium (0.667×10^{-12} cm) makes SANS ideally suited for studying the structural aspects in multi-component systems through the isotope substitution. The scattering intensity from one of the components can be suppressed by preparing a mixed H_2O/D_2O solvent having scattering length density equal to that component. In this way, the complex structures of multi-component systems can be simplified. This property of SANS is efficiently utilized in the characterization of nanoparticle-macromolecule system in this thesis.

The main results of the thesis are:

The tuning of nanoparticle-surfactant interaction and resultant structure of their complexes have been studied in chapter 3 [166, 167]. Surfactants are amphiphilic molecules and are known to form micelles in aqueous solution. The interaction of nanoparticle with surfactant may lead to either structural transition in micelles or interactional changes in nanoparticles or both. The results of interaction of different sized anionic silica nanoparticles with three types of surfactants (anionic, cationic and nonionic) are reported. The surfactants used are anionic sodium dodecyl sulphate (SDS), nonionic decaoxyethylene *n*-dodecylether ($C_{12}E_{10}$) and cationic dodecyltrimethyl ammonium bromide (DTAB). The interaction of nanoparticles with three surfactants is found to be significantly different and in each case resulting into different microstructures. In case of anionic SDS micelles, the interaction is dominated by electrostatic repulsion which does not allow any direct contact between nanoparticles and micelles. There are neither any observable structural changes in micelles nor any depletion force observed between nanoparticles because of non-adsorbing nature of micelles [167]. On the contrary, the strong electrostatic attraction between oppositely charged nanoparticles and DTAB micelles results in micelle-mediated aggregation of nanoparticles. The aggregated complexes are characterized by mass fractal structure where the fractal dimension is found constant (D~2.3) irrespective of the size of the nanoparticle and consistent with diffusion limited aggregation type fractal morphology in these systems. For nonionic surfactant ($C_{12}E_{10}$), the resultant interaction is governed by hydrogen bonding between hydrophilic chain of surfactant and surface group of nanoparticle. The structure of the complexes thus formed is analyzed using two models: one that considers the redistribution of micelles to form a bilayer around the nanoparticles and other where micelles decorate the nanoparticle surface [166]. The contrast variation SANS

experiments confirms the uniform adsorption of micelles on nanoparticles. The role of nanoparticle size in each of these cases (anionic, cationic and non-ionic surfactants) has also been examined. The nanoparticle size governs the surface-to-volume ratio and surface curvature for its interaction with surfactant. The interaction of the two components enhances with the increase in the surface-to-volume ratio but decrease in the surface curvature. The resultant structure is found to be decided by the competition of these two opposing effects [167].

The protein due to their labile nature forms a dynamic layer (protein corona) around nanoparticle surface when they come into contact with biological fluids. This corona has remarkable recognition properties that have vital importance in nanobiotechnology [184-188]. The investigations on charge driven protein adsorption on nanoparticles and modeling of the resultant structure of the complexes have been reported in chapter 4 [205, 206]. The interaction of silica nanoparticles with a globular protein lysozyme (iso-electric point ~ 11.4) is examined as a model system at three solution pH (5, 7 and 9). The two components (nanoparticles and protein) both being oppositely charged interact predominantly by the electrostatic interactions. The interplay of attraction between the two components and repulsion between individual components dictate the resultant system behavior. The protein adsorption on nanoparticles is shown to obey an exponential behavior as a function of protein concentration where adsorption initially increases and then saturates [206]. The enhanced electrostatic attraction with decrease in the pH increases the adsorption coefficient but decreases the overall amount protein of adsorption on nanoparticles, whereas opposite of this behavior is observed with increase in nanoparticle size. The adsorption of protein leads to the protein-mediated aggregation of nanoparticles. Two concentration regimes of protein for their interaction with nanoparticles have been observed: (i) low protein concentration regime where unaggregated nanoparticles

coexisting with aggregated nanoparticles and (ii) high protein concentration regime where free protein coexisting with aggregated nanoparticles [205]. These concentration regimes as well as morphology of the aggregates are found to be strongly dependent on pH and nanoparticle size. These aggregates are characterized by surface fractals at the lowest pH and change to mass fractals with increasing pH and decreasing nanoparticle size.

Depending upon the interaction involved, in the case of non-adsorbing macromolecules may induce depletion interaction between nanoparticles. Depletion interactions are known to lead interesting kinematic phase transitions governing the conditions of colloid stability and critical points of phase separations in different nanoparticle-polymer systems. The block copolymer P85 [$(EO)_{26}(PO)_{39}(EO)_{26}$] induced depletion attraction and resulting clustering in charged silica nanoparticles has been studied in chapter 5 [236]. The effective interaction of silica nanoparticles is modeled by a combination of two Yukawa potentials accounting for attractive depletion and repulsive electrostatic forces. The temperature dependent self-assembly of block copolymer has been used to further enhance the depletion interaction. The aggregation of charged nanoparticles is observed as a consequence of the dominance of the depletion interaction over long-range electrostatic repulsion. The particles in depletion interaction form large clusters and are characterized by the surface fractals with simple cubic type packing of particles within the clusters. The depletion interaction can also be tuned by the change in the size of the nanoparticles, where the excluded-volume effect increases with the increase in the size of nanoparticles [236].

The understanding of depletion interaction suggests monotonic increase in the strength of depletion attraction with increasing polymer concentration [74, 74]. At sufficient polymer concentration, the attraction becomes large enough to cause phase separation in the colloid-

polymer mixture. However, in some cases a colloidal dispersion which is destabilized due to depletion attraction is observed to re-stabilize at higher polymer concentrations. The evolution of depletion attraction is reasonably understood, but the formalism of such stabilization effect is still a subject of study [252-255]. Both of these effects (depletion attraction and stabilization) have been examined by studying the silica nanoparticles in presence of polyethylene glycol (PEG) polymer system over a wide range of polymer concentration in chapter 6 [261]. The nanoparticle-polymer solution interestingly shows a re-entrant phase behavior where the one-phase charge stabilized nanoparticles undergo two-phase system (nanoparticle aggregation) and back to one-phase as a function of polymer concentration. The phase behavior is explained in terms of the interplay of different interactions (i) electrostatic repulsion between nanoparticles, (ii) polymer-induced attractive depletion interaction between nanoparticles and (iii) repulsive polymer-polymer interaction present in the system. At low polymer concentrations, the stability of the nanoparticles in one-phase is due to the dominance of electrostatic repulsion over the depletion attraction. On further addition of polymer, depletion attraction increases sufficiently to give rise nanoparticles clustering in two-phase system. The re-entrant phase arises due to the reduction in depletion attraction as a result of polymer-polymer repulsion at higher polymer concentrations. The total interaction potential of nanoparticles has been modeled by a two-Yukawa potential accounting for both attractive as well as repulsive parts. The depletion interaction increases in going from one-phase to two-phase system, whereas during the re-entrant of one-phase system, both the magnitude and range of interaction decrease. The clusters in two-phase system are characterized by surface fractal structure. The repulsive and the attractive parts of the total interaction potential are tuned by varying the ionic strength and polymer molecular weight, respectively. These parameters (ionic strength, molecular weight of polymer and

polymer concentration) together are found to control the re-entrant phase behavior in nanoparticle-polymer systems [261].

To conclude, the present thesis has investigated the evolution of interaction and resultant structure in a number of different nanoparticle-macromolecule systems. The responsible interaction leading to different phases and microstructures in these systems is shown to be a combination of short/long-range attractive/repulsive forces. It has been demonstrated that the overall behavior of nanoparticle-macromolecule complexes can be tailored by the choice of the macromolecule (surfactant, protein, block copolymer or polymer) as well as by varying solution conditions (ionic strength, temperature, pH etc.). This thesis provides useful results which can be utilized for nanoparticle applications in targeted drug delivery, biosensors, phase colloidal stability and designing of functional materials. Future work involves examining of the phase behavior of three-component systems (e.g. nanoparticle-polymer-surfactant) in terms of results of two-component systems (nanoparticle-polymer, nanoparticle-surfactant and polymer-surfactant) as presented in this thesis.

REFERENCES

1. G. Cao and Y. Wang, Nanostructures and Nanomaterials: Synthesis, Properties and Applications; World Scientific: Singapore (2011).
2. E. Roduner, Nanoscopic Materials: Size Dependent Phenomena; RSC Publishing: Cambridge (2006).
3. P. Moriarty, Rep. Prog. Phys., **64**, 297 (2001).
4. A. P. Alivisatos, Science, **271**, 933 (1996).
5. M.-C. Daniel and D. Astruc, Chem. Rev. **104**, 293 (2004).
6. D. A. Giljohann, D. S. Seferos, W. L. Daniel, M. D. Massich, P. C. Patel and C. A. Mirkin, Angew. Chem. Int. Ed., **49**, 3280 (2010).
7. S. Chakraverty, M. Bandyopadhyay, S. Chatterjee, S. Dattagupta, A. Frydman, S. Sengupta, and P. A. Sreeram, Phys. Rev. B, **71**, 054401 (2005).
8. J. Tang, J. Liu, N. L. Torad , T. Kimura and Y. Yamauchi, Nano Today, **9**, 305 (2014).
9. R. A. Sperling, P. R. Gil, F. Zhang, M. Zanella and W. J. Parak, Chem. Soc. Rev., **37**, 1896 (2008).
10. O. V. Salata, J. Nanobiotechnol., **2**, 3 (2004).
11. W. H. Suh, Y. H. Suh and G. D. Stucky, Nano Today, **4**, 27 (2009).
12. D. I. Gittins, D. Bethell, D. J. Schiffrin and R. J. Nichols, Nature, **408**, 67 (2000).
13. T. Hanemann and D. V. Szabó, Materials, **3**, 3468 (2010).
14. L. Zhang, W.-F. Dong and H.-B. Sun, Nanoscale, **5**, 7664 (2013).
15. A. G. Tkachenko , H. Xie , D. Coleman , W. Glomm , J. Ryan , M. F. Anderson , S. Franzen and D. L. Feldheim, *J. Am. Chem. Soc.,* **125,** 4700 (2003).
16. M. Daoud and C. Williams, Soft Matter Physics; Springer-Verlag: Germany (1999).
17. E. J. W. Verwey and J. Th. G. Overbeck, Theory of the Stability of Lyophobic Colloids; Elsevier: Amsterdam (1948).
18. A. V. Finkelstein and O. Ptitsyn, Protein Physics: A Course of Lectures; Academic Press: Amsterdam (2002).
19. I. Teraoka, Polymer Solutions: An Introduction to Physical Properties; A John Wiley & Sons Inc.: New York (2002).
20. R. Zhang and P. Somasundaran, Adv. Colloid Interface Sci., **123-126**, 213 (2006).
21. J. Klein, Proc. Natl. Acad. Sci. U.S.A., **104**, 2029 (2007).

22. J.-F. Berret, Adv. Colloid Interface Sci., **167**, 33 (2011).
23. D. Lugo, J. Oberdisse, M. Karg, R. Schweins and G. H. Findenegg, Soft Matter, **5**, 2928 (2009).
24. K. Rezwan, L. P. Meier and L. J. Gauckler, Biomaterials, **26**, 4351 (2005).
25. C. N. Likos, Phys. Rep., **348**, 267 (2001).
26. K. Park, H. Koerner, and R. A. Vaia, Nano Lett., **10**, 1433 (2010).
27. K. P. Sharma, V. K. Aswal and G. Kumaraswamy, *J. Phys. Chem. B*, **114**, 10986 (2010).
28. D. L. Feldhim and C. A. Foss, Metal Nanoparticles: Synthesis, Characterization, and Applications; Marcel Dekker Inc: New York (2002).
29. B. Viswanathan, Nanomaterials; Narosa Publishing House: Kolkata (2013).
30. C. W. Shong, S. C. Haur and A. T. Wee, Science at the Nanoscale; Pan Stanford Publishing: Singapore (2010).
31. J. Y. Ying, Nanostructured Materials; Academic Press: California (2001).
32. C. N. R. Rao, A. Müller and A. K. Cheetham, The Chemistry of Nanomaterials: Synthesis, Properties and Applications; Wiley-VCH Verlag GmbH & Co. KGaA: Weinheim (2004).
33. R. Rigler and H. Vogel, Eds. Single Molecules and Nanotechnology; Springer: Berlin (2008).
34. D. Vanmaekelbergh, Nat. Nanotech., **4**, 475 (2009).
35. J. Z. Zhang, Optical Properties and Spectroscopy of Nanomaterials; World Scientific Publishing: Singapore (2009).
36. W. L. Barnes, A. Dereux and T. W. Ebbesen, Nature, **424**, 824 (2003).
37. R. H. Kodama, J. Magn. Magn. Mater., **200**, 359 (1999).
38. A.-H. Lu, E. L. Salabas and F. Schüth, Angew. Chem. Int. Ed., **46**, 1222 (2007).
39. N. A. Frey, S. Peng, K. Cheng and S. Sun, Chem. Soc. Rev., **38**, 2532 (2009).
40. M. A. Garcia, J. M. Merino, E. F. Pinel, A. Quesada, J. de la Venta, M. L. R. González, G. R. Castro, P. Crespo, J. Llopis, J. M. González.-Calbet, and A. Hernando, Nano Lett., **7**, 1490, (2007).
41. J. N. Coleman, U. Khan, W. J. Blau, Y. K. Gun'ko, Carbon, **44**, 1624 (2006).
42. C.-W. Chou, S.-H. Hsu, H. Chang, S.-M. Tseng, H.-Ru Lin, Polym Degrad Stab, **91**, 1017, (2006).
43. T. L. Hill, Nano Lett., **1**, 111, (2001).
44. V. H. Grassian, J. Phys. Chem. C, **112**, 18303 (2008).

45. W. Jiang, B. Y. S. Kim, J. T. Rutka and W. C. W. Chan, Nature Nanotechnol., **3**, 145 (2008).
46. A. Verma and F. Stellacci, Small, **6**, 12, (2010).
47. R. K. Iler, The Chemistry of Silica; Wiley: New York (1979).
48. W. O. Roberts and H. E. Bergna, Colloidal Silica: Fundamentals and Applications- Surfactant Science Series, Vol. **131**; Taylor and Francis: US (2006).
49. I. A. Rahman and V. Padavettan, J. Nanomater., **2012**, 132424 (2012).
50. S. F. Sun, Physical Chemistry of Macromolecules; John Wiley & Sons, Inc: New Jersey (2004).
51. Dynamics of Surfactant Self-Assemblies: Micelles, Microemulsions, Vesicles and Lyotropic Phases- Surfactant Science Series, **125**; Taylor & Francis: London (2005).
52. J.-M. Lehn, Science, **295**, 2400 (2002).
53. A. L. Lehninger, Principles of Biochemistry 5th edition, edited by D.L. Nelson and M.M. Cox; W. H. Freeman & Co.: New York (2009).
54. Sergei M Mirkin, DNA topology: fundamentals Encyclopedia of Life Sciences (ELS); John Wiley & Sons, Ltd: Chichester, West Sussex, UK (2001).
55. D. Whitford, Proteins: Structure and Function; John Wiley & Sons. Ltd.: Chichester (UK) (2005).
56. U. W. Gedde, Polymer Physics; Kluwer Academic Publishers: Netherlands (1995).
57. D. I. Bower, An Introduction to Polymer Physics; University Press: Cambridge (2002).
58. P. Alexandridis and B. Lindman, Amphiphilic Block Copolymers: Self-Assembly and Applications; Elsevier: Amsterdam (2000).
59. I. W. Hamley, Block Copolymers in Solution: Fundamentals and Applications; Wiley: New York (2005).
60. A. A. Kumar and T. B. V. Rao, Complex Fluids and Fluid Microstructures; VCH: New York (1996).
61. P. Attard, Adv. Chem. Phys., **92**, 1(159) (1996).
62. J. N. Israelachvili, Intermolecular and Surface Forces, 3rd edition; Academic Press: London (1994).
63. L. Qi, A. Sehgal, J.-C. Castaing, J.-P. Chapel, J. Fresnais, J.-F. Berret and F. Cousin, ACS Nano, **2**, 879 (2008).
64. F. Caruso, H. Lichtenfeld, M. Giersig and H. Möhwald, J. Am. Chem. Soc. **120**, 8523 (1998).

65. N. Korolev, O. V. Vorontsova and L. Nordenskiöld, Prog. Biophys. Mol. Biol., **95**, 23 (2007).
66. P. He, N. Hu and J. F. Rusling, Langmuir, **20**, 722 (2004).
67. B. V. Derjaguin and L. Landau, Acta Physiochim (USSR), **14**, 633 (1941).
68. J. P. Hansen and I. R. McDonald, Theory of Simple Liquids, 3rd edition; Academic Press: Amsterdam (2006).
69. D. H. Napper, J. Colloid Interface Sci., **58**, 390 (1977).
70. K. van Gruijthuijsen, M. Obiols-Rabasa, M. Heinen, G. Nägele, and A. Stradner, Langmuir, **29**, 11199 (2013)
71. V. Singh, V. Srinivas, M. Ranot, S. Angappane and Je-Geun Park, Phys. Rev. B, **82**, 054417 (2010)
72. H. Otsuka, Y. Nagasaki and K. Kataoka, Adv. Drug. Deliv. Rev., **54**, 403 (2003).
73. A. K. Guptaa and M. Gupta, Biomaterials, **26**, 3995 (2005).
74. H. N. W. Lekkerkerker and R. Tuinier, Colloids and the Depletion Interaction; Springer: Heidelberg (2011).
75. S. Asakura and F. Oosawa, J. Chem. Phys. **22**, 1255 (1954).
76. W. Agut, D. Taton, A. Brûlet, O. Sandre, and S. Lecommandoux, Soft Matter, **7**, 9744 (2011).
77. Daan Frenkel, Physica A, **263**, 26 (1999).
78. V. J. Anderson and H. N. W. Lekkerkerker, Nature, **416**, 811 (2012).
79. L. Feng, B. Laderman, S. Sacanna and P. Chaikin, Nature Materials, (2014) doi:10.1038/nmat4109
80. R. Roth, B. Götzelmann and S. Dietrich, Phys. Rev. Lett. **83**, 448 (1999).
81. Y. Snir and R. D. Kamien, Science, **307**, 1067 (2005).
82. R. Tuinier, E. ten Grotenhuis, C. Holt, P. A. Timmins and C. G. de Kruif, Phys. Rev. E, **60**, 848 (1999).
83. E. Arunan, G. R. Desiraju, R. A. Klein, J. Sadlej, S. Scheiner, I. Alkorta, D. C. Clary, R. H. Crabtree, J. J. Dannenberg, P. Hobza, H. G. Kjaergaard, A. C. Legon, B. Mennucci, and D. J. Nesbitt, Pure Appl. Chem., **83**, 1637 (2011).
84. C. L. Perrin and J. B. Nielson, Annu. Rev. Phys. Chem., **48**, 511 (1997).
85. C. Tanford, The Hydrophobic Effect; Wiley: New York (1980).

86. J. N. Israelachvili, Acc. Chem. Res., **20**, 415 (1987).
87. E. Venugopal, V. K. Aswal, and G. Kumaraswamy, Langmuir, 29, 9643 (2013).
88. F. Turci, E. Ghibaudi, M. Colonna, B. Boscolo, I. Fenoglio and B. Fubini, Langmuir, **26**, 8336 (2010).
89. Y. Leng, Materials Characterization: Introduction to Microscopic and Spectroscopic Methods; John Wiley & Sons: Singapore (2008).
90. S. R. Saptarshi, A. Duschl and A. L. Lopata, J. Nanobiotechnol., **11**, 26 (2013).
91. E. Katz and I. Willner, Angew. Chem. Int. Ed., **43**, 6042 (2004).
92. P. Esmaeilzadeha, A. Bahramianb and Z. Fakhroueian, Physics Procedia., **22** ,63 (2011).
93. R. Borsali and R. Pecora, Soft Matter Characterization; Springer: New York (2008).
94. S.W. Lovesey, Theory of neutron scattering from condensed matter; Oxford University Press: New York (2003).
95. W. Schärtl, Light Scattering from Polymer Solutions and Nanoparticle Dispersions; Springer: Mainz (2007).
96. S. K. Murthy, International Journal of Nanomedicine, **2**, 129 (2007).
97. S. Sengupta, D. Eavarone, I. Capila, G. Zhao, N. Watson, T. Kiziltepe and R. Sasisekharan, Nature, **436**, 568 (2005).
98. R. Jurgons, C. Seliger, A. Hilpert, L. Trahms, S. Odenbach and C. Alexiou, J. Phys.: Condens. Matter, **18**, S2894 (2006).
99. Q. Huo, J. Liu, L.-Q. Wang, Y. Jiang, T. N. Lambert and E. Fang, J. Am. Chem. Soc., **128**, 6447 (2006).
100. C. C. You, O. R. Miranda, B. Gider, P. S. Ghosh, I. B. Kim, B. Erdogan, S. A. Krovi, U. H. F. Bunz and V. M. Rotello, Nature Nanotechnol., **2**, 318 (2007).
101. A. J. Haes, L. Chang, W. L. Klein and R. P. Van Duyne, J. AM. Chem. Soc., **127**, 2264 (2005).
102. Y.-M. Huh, Y.-W. Jun, H.-T. Song, S. Kim, J.-S. Choi, J.-H. Lee, S. Yoon, K.-S. Kim, J.-S. Shin, J.-S. Suh and J. Cheon, J. Am. Chem. Soc., **127**, 12387, (2005)
103. E. Braun, Y. Eichen, U. Sivan, G. Ben-Yoseph, Nature, **391**, 775, (1998)
104. L. Langer, V. Bayot, E. Grivei, J.-P. Issi, J. P. Heremans, C. H. Olk, L. Stockman, C. Van Haesendonck, Y. Bruynseraede, Phys. Rev. Lett., **76**, 479 (1996).
105. I. Willner and B. Willner, Nano Lett., **10**, 3805, (2010).

106. D. I. Gittins, D. Bethell, D. J. Schiffrin and R. J. Nichols, Nature, **408**, 67, (2000).
107. S. Tang, C. Mao, Y. Liu, D. Q. Kelly, and S. K. Banerjee, IEEE Trans. Electron Devices, **54**, 433 (2007).
108. Z. YuJuan, H. Rao, Z. XianFang, W. LianZhou and W. ChenXu, Chin. Sci. Bull., **57**, 238 (2012).
109. R. Mezzenga and J. Ruokolainen, Nature, **8**, 927, (2009).
110. M. R. Beaulieu , N. R. Hendricks and J. J. Watkins, ACS Photonics, **1**, 799 (2014).
111. S. Tay, J. Thomas, B. Momeni, M. Askari, A. Adibi, P. J. Hotchkiss, S. C. Jones, S. R. Marder, R. A. Norwood and N. Peyghambarian, Appl. Phys. Lett., **91**, 221109, (2007).
112. N. Ballav and M. Biswas, Polym. Int., **52**, 179 (2003).
113. B. D. Yang, K. H. Yoon and K. W. Chung, Synth. Met., **143**, 25 (2004).
114. L. Lu, Z. Luo, T. Xu, and L. Yu, Nano Lett., **13**, 59 (2013)
115. A. S. Arico, P. Bruce, B. Scrosati, J.-M. Tarascon and W. V. Schalkwijk, Nature Materials, **4**, 366 (2005)
116. H. M. C. de Azeredo, Food Res. Int., **42**, 1240 (2009).
117. N. Sozer and J. L. Kokini, Trends Biotechnol., **27**, 82 (2009).
118. R. J. Hunter, Foundations of Colloidal Science; Oxford University Press: New York (2001).
119. Z. Király, R. H. K. Börner and G. H. Findenegg, Langmuir, **13,** 3308 (1997).
120. B. Bharti, J. Meissner, and G. H. Findenegg, Langmuir, **27**, 9823 (2011).
121. M. Lundqvist, I. Sethson and B. -H. Jonsson, Langmuir, **20**, 10639 (2004).
122. J. J. Bozzola and L. D. Russell, Electron Microscopy: Principles and Techniques for Biologists; Jones and Bartlett Publishers: Canada (1999).
123. P. Linder and T. Zemb (Eds.), Neutron, X-ray and Light Scattering: North Holland, Amsterdam (1991).
124. J. S. Higgins and H. C. Benoit, Polymers and Neutron Scattering; Clarendon Press: Oxford (1994).
125. L. A. Feigin and D. I. Svergun, Structure Analysis by Small-Angle X-Ray and Neutron Scattering; Plentum Press: New York (1987).
126. H. Brumberger, Modern Aspects of Small-Angle Scattering; Springer (2010).
127. J. S. Pedersen, Adv. Colloid Interface Sci., **70**, 171 (1997).
128. O. Glatter, J. Appl. Crystallogr., **13,** 168 (1980).

129. M. Kotlarchyk, R.B. Stephens and J.S. Huang, J. Phys. Chem., **92**, 1533 (1988).
130. A. Guinier and G. Fournet, Small-Angle Scattering of X-Rays; John Wiley & Sons: New York (1955).
131. G. Porod, Kolloid Z., **124**, 83 (1951).
132. J. B. Hayter and J. Penfold, Mol. Phys., **42**, 109 (1981).
133. L. S. Ornstein and F. Zernike, Proc. Acad. Sci. Amsterdam, 17, 793 (1914).
134. J. K. Percus and G. Yevik, J. Phys. Rev., **110**, 1 (1958).
135. J. P. Hansen and J. B. Hayter, Mol. Phys., **46,** 3 (1982).
136. A. Perera, P. G. Kausalik and G. N. Patey, J. Chem. Phys., **87**, 1295 (1987).
137. N. W. Ashcroft and J. Lekner, Phys. Rev., **145**, 83 (1966).
138. R. J. Baxter, J. Chem. Phys., **49**, 2770 (1968).
139. S.-H. Chen and J. Teixeira, Phys. Rev. Lett., **57**, 2583 (1986).
140. J. Teixeira, J. Appl. Cryst., **21**, 781 (1988).
141. A. P. Radlinski, E. Z. Radlinska, M. Agamalian, G. D. Wignall, P. Lindner and O. G. Randl, Phys. Rev. Lett., **82**, 3078 (1999).
142. D. F. R. Mildner and P. L. Hall, J. Phys. D: Appl. Phys., **19**, 1535 (1986).
143. D. I. Svergun and M. H. J. Koch, Rep. Prog. Phys., **66**, 1735 (2003).
144. B. Jacrot, Rep. Prog. Phys., **39**, 911 (1976).
145. V. K. Aswal and P. S. Goyal, Curr. Sci. India, **79**, 947 (2000).
146. J. Kohlbrecher and W. Wagner, J. Appl. Cryst., **33**, 804 (2000).
147. G. Cicognani, Ed. The Yellow Book: Guide to Neutron Research Facilities; Institut Laue-Langevin: Grenoble, France (2008).
148. Y.-S. Han, S.-M. Choi, T.-H. Kim, C.-H. Lee, and H.-R. Kim, J. Appl. Cryst., **40**, S442 (2007).
149. O. Glatter, J. Appl. Crystallogr., **10,** 415(1977).
150. S. H. Chen and T. L. Lin, Colloidal Solutions. In Methods of Experimental Physics: neutron Scatterin; Price, D. L., Skold, K., Eds. Vol. **23B** , 489; Academic Press: New York (1987).
151. Y. Liu, E. Fratini, P. Baglioni, W.-R. Chen, and S.-H. Chen, Phys. Rev. Lett., **95**, 118102 (2005).
152. M. Granite, A. Radulescu, W. Pyckhout- Hintzen and Y. Cohen, Langmuir, **27**, 751 (2011).

153. S. Paria and K. C. Khilar, Adv. Colloid Interface Sci., **110**, 75−95 (2004).
154. M. J. Rosen, Surfactants in Emerging Technologies; Marcel Dekker: New York (1987).
155. V. C. Moore, M. S. Strano, E. H. Haroz,; R. H. Hauge and R. E. Smalley, Nano Lett., **3**, 1379 (2003).
156. K. Wong, B. Cabane, R. Duplessix and P. Somasundaran, Langmuir, **5**, 1346 (1989).
157. M. R. Böhmer, L. K. Koopal, R. Janssen, E. M. Lee, R. K. Thomas and A. R. Rennie, Langmuir, **8**, 2228 (1992).
158. J. Penfold, E. Staples and I. Tucker, Langmuir, **18**, 2967 (2002).
159. A. Maestro, E. Guzman, E. Santini, F. Ravera, L. Liggieri, F. Ortega and R. G. Rubio, Soft Matter, **8**, 837 (2012).
160. B. P. Binks and J. A. Rodrigues, Langmuir, **23**, 3626 (2007).
161. A. Zaccone, H. Wu, M. Lattuada, and M. Morbidelli, J. Phys. Chem. B, **112**, 1976 (2008).
162. R. Tuinier, G. A. Vliegenthart, and H. N. W. Lekkerkerker, J. Chem. Phys., **113**, 10768 (2000).
163. L. Qi, J. Fresnais, J.-F. Berret, J.-C. Castaing, F. Destremaut, J.-B. Salmon, F. Cousin, J.-P. Chapel, J. Phys. Chem. C., **114**, 16373 (2010).
164. J.-F. Berret, N. Schonbeck, F. Gazeau, D. E. Kharrat, O. Sandre, A. Vacher, M. J. Airiau, J. Am. Chem. Soc., **128** , 1755 (2006).
165. G. Despert, and J. Oberdisse, Langmuir, **19**, 7604 (2003).
166. S. Kumar and V. K. Aswal, J. Phys.: Condens. Matter, **23**, 035101 (2011).
167. S. Kumar, V. K. Aswal, and J. Kohlbrecher, Langmuir, **28**, 9288 (2012).
168. S. Kumar and V. K. Aswal, AIP Conf. Proc, **1313**, 183 (2010).
169. S. Kumar, V. K. Aswal and J. Kohlbrecher, AIP Conf. Proc., **1512**, 124-124 (2013).
170. S. Kumar and V. K. Aswal, AIP Conf. Proc., **1447**, 155-156 (2012).
171. C. G. Windsor, J. Appl. Cryst., **21**, 582 (1988).
172. J. S. Pedersen, J. Appl. Cryst., **33**, 637 (2000).
173. D. C. Pozzo and L. M. Walker, Colloids and Surfaces A: Phys. Eng. Asp., **294**, 117 (2007).
174. P.A. Hassan, G. Fritz, and E. W. Kaler, J. Colloid Interface Sci., **257**, 154 (2003).
175. M. Bergström and J. S. Pedersen, Phys. Chem. Chem. Phys., **1**, 4437 (1999).
176. V. K. Aswal and P. S. Goyal, Phys. Rev. E, **61**, 2947 (2000).

177. A. L. Galant, Kjøniksen, K. D. Knudsen, G. Helgesen, R. Lund, A. Laukkanen, H. Tenhu, B. Nyström, Langmuir, **21**, 8010 (2005).
178. F. Cousin, J. Gummel, D. Ung and F Boué, Langmuir, **21**, 9675 (2005).
179. B. Götzelmann, R. Evans and S. Dietrich, Phys. Rev. E., **57**, 6785 (1998).
180. J. Nygaard, H. K. Munch, P. W. Thulstrup, N. J. Christensen, T. Hoeg-Jensen, K. J. Jensen and L. Arleth, Langmuir, **28**, 12159 (2012).
181. Y.-C. Li, K.-B. Chen, H.-L. Chen, C.-S. Hsu, C.-S. Tsao, J.-H. Chen, and S.-A. Chen, Langmuir, **22**, 11009, (2006).
182. J. Oberdisse, Phys. Chem. Chem. Phys., **6**, 1557 (2004).
183. S. Chodankar, V. K. Aswal, J. Kohlbrecher, R. Vavrin, and A. G. Wagh, Phys. Rev. E, **79**, 021912 (2009).
184. I. Lynch and K. A. Dawson, Nano Today, **3**, 41, (2008).
185. J. Rauch, W. Kolch, S. Laurent and M. Mahmoudi, Chem. Rev., **113**, 3391, (2013).
186. N. A. Kotov, Science, **330**, 188 (2010).
187. J. Leszczynski, Nature Nanotechnol., **5**, 633 (2010).
188. M. Mahmoudi, I. Lynch, M. R. Ejtehadi, M. P. Monopoli, F. B. Bombelli and S. Laurent, Chem. Rev., **111**, 5610 (2011).
189. Y. Li, M. S. Budamagunta, J. Luo, W. Xiao, J. C. Voss and K.S. Lam, ACS Nano, **11**, 9485 (2012).
190. J. A. Brannigan, G. Dodson, H. J. Duggleby, P. C. E. Moody, J. L. Smith, D. R. Tomchick, and A. G. Murzin, Nature, **378**, 416 (1995).
191. K. Rezwan, A. R. Studart, J. Vörös and L. J. Gauckler, J. Phys. Chem. B, **109**, 14469 (2005).
192. A. A. Vertegel, R.W. Siegel and J. S. Dordick, Langmuir, **20**, 6800 (2004).
193. P. Roach, D. Farrar and C. C. Perry, J. Am. Chem. Soc., **128**, 3939 (2006).
194. H. Pan, M. Qin, W. Meng, Y. Cao, W. Wang, Langmuir, **28**, 12779 (2012).
195. A. A. Shemetov, I. Nabiev and A. Sukhanova, ACS Nano, **6**, 4585 (2012).
196. B. Bharti, J. Meissner, S. H. L. Klapp and G. H. Findenegg, Soft Matter, **10**, 718 (2014).
197. T. Stieger, T. M. Schoenab and T. R. Weikl, Soft Matter, **8**, 11737-11745 (2012).
198. A. Rimola, D. Costa, M. Sodupe, J.-F. Lambert and P. Ugliengo, Chem. Rev., **113**, 4216 (2013).

199. T. Stieger, M. Schoenab and T. R. Weikl, Soft Matter, **8**, 11737-11745 (2012).
200. G. S. Lee, Y.-J. Lee, S. Y. Choi, Y. S. Park, and K. B. Yoon, J. Am. Chem. Soc., **122**, 12151 (2000).
201. P. J. Costanzo, T. E. Patten and T. A. P. Seery, Chem. Mater., **16**, 1775 (2004).
202. L. Shi, F. Carn, F. Boué, G. Mosser and E. Buhler, Soft Matter., **9**, 5004 (2013).
203. D. Babayan, D. C. Chassenieux, F. Lafuma, L. Ventelon, J. Hernandez, Langmuir, **26**, 2279 (2010).
204. J. Wu, J. Silvent, T. Coradin and C. Aimé, Langmuir, **28**, 2156 (2012).
205. S. Kumar, V. K. Aswal and J. Kohlbrecher, Langmuir, **27**, 10167 (2011).
206. S. Kumar, V. K. Aswal and P. Callow, Langmuir, **30**, 1588 (2014).
207. S. Kumar, V. K. Aswal and J. Kohlbrecher, AIP Conf. Proc., **1349**, 222 (2011).
208. S. Kumar, V. K. Aswal, and P. Callow AIP Conf. Proc., **1591**, 161 (2014).
209. S. Kumar, V. K. Aswal and J. Kohlbrecher, AIP Conf. Proc., **1349**, 222 (2011).
210. E. Perevedentseva, C.-Y. Cheng, P.-H. Chung, J.-S. Tu, Y.-H. Hsieh and C.-L. Cheng, Nanotechnology, **18**, 315102 (2007).
211. X.-Z. Wang and Y. Huang, Phys. Rev. A., 46, 5038 (1992).
212. T. A. Jr. Witten and L. M. Sander, Phys. Rev. Lett., **47**, 1400 (1981).
213. C. Parneix, J. Persello, R. Schweins and B. Cabane, Langmuir, 25, 4692 (2009).
214. K. Rezwan, L. P. Meier, M. Rezwan, J. Vörös, M. Textor, and L. J. Gauckler, Langmuir, **20**, 10055 (2004)
215. A. J. Chinchalikar, V. K. Aswal, J. Kohlbrecher and A. G. Wagh, Phys. Rev. E, **87**, 062708 (2013).
216. R. C. Ball, D. A. Weitz, T. A.Witten and F. Leyvraz, Phys. Rev. Lett., **58**, 274-277 (1987).
217. P. Meakin and F. Family, Phys. Rev. A, **38**, 2110-2123 (1988).
218. H. Kang, F. A. Detcheverry, A. N. Mangham, M. P. Stoykovich, K. C. Daoulas, R. J. Hamers, M. Muller, J. J. de Pablo, and P. F. Nealey, Phys.Rev. Lett., **100**, 148303 (2008).
219. M. C. Orilall and U. Wiesner, Chem. Soc. Rev., **40**, 520 (2011).
220. Y. Lin, V. K. Daga, E. R. Anderson, S. P. Gido, and J. J. Watkins, J. Am. Chem. Soc., **133**, 6513 (2011).
221. A. Haryono and W. H. Binder, Small, **2**, 600 (2006).
222. F. H. Schacher, P. A. Rupar and I. Manners, Angew. Chem. Int. Ed., **51**, 7898 (2012)

223. W. R. Bowen and A. O. Sharif, Nature, **393**, 663 (1998).
224. A. M.-Molina, J. G. I.-Armenta, E. G.-Tovar, R. H.-Alvarez and M. Q.-Pérez, Soft Matter **7**, 1441 (2011).
225. A. Stradner, H. Sedgwick, F. Cardinaux, W. C. K. Poon, S. U. Egelhaaf and P. Schurtenberger, Nature, **432**, 492: London (2004).
226. V. J. Anderson, E. H. A. de Hoog and H. N. W. Lekkerkerker, Phys. Rev. E, **65**, 011403 (2001).
227. R. Wang, Y.-L. Chen, J. Hu and G. Xue, J. Chem. Phys., **29**, 044907 (2008).
228. D. Ray, V. K. Aswal and J. Kohlbrecher, Langmuir, **27**, 4048 (2011).
229. J. Galanis, R. Nossala and D. Harries, Soft Matter, **6**, 1026 (2010).
230. W. Agut, D. Taton, A. Brûlet, O. Sandre and S. Lecommandoux, Soft Matter, **7**, 9744 (2011).
231. T. Sato, T. Komatsu, A. Nakagawa and E. Tsuchida, Phys. Rev. Lett., **98**, 208101 (2007).
232. M. P.-Fernández, A. M.-Jordá and J. C.-Fernández, J. Chem. Phys., **134**, 054905 (2011).
233. G. M. Kepler and S. Fraden, Phy. Rev. Lett., **73**, 356 (1994).
234. J. E. Sader and D. Y. C. Chan, J. Colloid Interface Sci., **213**, 268 (1999).
235. E. E. Meyer, Q. Lin, T. Hassenkam, E. Oroudjev and J. N. Israelachvili, Proc. Natl. Acad. Sci., **102**, 6839 (2005)
236. S. Kumar, M.-J. Lee, V. K. Aswal and S.-M. Choi, Phys. Rev. E, **87**, 042315 (2013).
237. Y. Liu, W.-R. Chen and S.-H. Chen, J. Chem. Phys., **122**, 044507 (2005).
238. P. Alexandridis and T. A. Hatton, Colloids Surfaces A: Physicochem. Eng. Aspects, **96,** 1 (1995).
239. Y. Lin and P. Alexandridis, J. Phys. Chem. B, **106**, 10834 (2002).
240. S. A. Shah, S. Ramakrishnan, Y. L. Chen, K. S. Schweizer, and C. F. Zukoski, Langmuir, **19**, 5128 (2003).
241. A. Shukla , E. Mylonas, E. Cola, S. Finet, P. Timmins, T. Narayanan and D. Svergun, Proc. Nat. Acad. Sci. U.S.A., **105,** 5075 (2008).
242. R. Tuinier and A. Brûlet, Biomacromolecules, **4**, 28 (2003).
243. J. C. Crocker and D. G. Grier, Phys. Rev. Lett., **77**, 1897 (1996).
244. W. Knoben, N. A. M. Besseling and M. A. C. Stuart, Phys. Rev. Lett., **97**, 068301 (2006).

245. P. Alexandridis and T. A. Hatton, Colloids Surfaces A: Physicochem. Eng. Aspects, **96,** 1 (1995).
246. M. Zackrisson, A. Stradner, P. Schurtenberger, and J. Bergenholtz, Langmuir, **21**, 10835 (2005).
247. R. Tuinier, J. Rieger, and C.G. De Kruifa, Adv. Colloid Interface Sci., **103**, 1 (2003).
248. D. Ray and V. K. Aswal, J. Phys.: Condens. Matter, **26**, 035102 (2014).
249. J. M. Mendez-Alcaraz and R. Klein, Phys. Rev. E, **61**, 4095 (2000).
250. S. Ramakrishnan, M. Fuchs, K. S. Schweizer and C. F. Zukoski, J. Chem. Phys., **116**, 2201 (2002).
251. A. I. Chervanyov, Phys. Rev. E, **83**, 061801 (2011).
252. A. A. Shvets and A. N. Semenov, J. Chem. Phys., **139**, 054905 (2013).
253. D. Rudhardt, C. Bechinger, and P. Leiderer, J. Phys.: Condens. Matter, **11**, 10073(1999).
254. R. I. Feigin and D. H. Napper, J. Colloid Interface Sci., **75**, 525 (1980).
255. J. Y. Walz and A. Sharma, J. Colloid Interface Sci., **168**, 485 (1994).
256. G. K. James and J. Y. Walz, J. Colloid Interface Sci., **418**, 283 (2014).
257. P. B. Warren, S. M. Ilett, and W. C. K. Poon, Phys. Rev. E., **52**, 5203 (1995).
258. M. Schmidt, A. R. Denton, and J. M. Brader, J. Chem. Phys., **118**, 1541 (2003).
259. X. Ye, T. Narayanan, P. Tong, J. S. Huang, M. Y. Lin, B. L. Carvalho, and L. J. Fetters, Phys. Rev. E, **54**, 6500 (1996).
260. G. J. Fleer and J. Scheutjens, Croat. Chem. Acta, **60**, 477 (1987).
261. S. Kumar, D. Ray, V. K. Aswal and J. Kohlbrecher, Phys. Rev. E, 90, 042316 (1-10) (2014).
262. S. Kumar, A. J. Chinchalikar, V. K. Aswal and R. Schweins, AIP Conf. Proc., 1512, 152-153 (2013).
263. I. Yadav, S. Kumar, V. K. Aswal, and J. Kohlbrecher, Phys. Rev. E, **89**, 032304 (2014).
264. T. G. Shin, D. Müter, J. Meissner, O. Paris, and G. H. Findenegg, Langmuir, **27**, 5252 (2011).
265. S.H. Chen, E.Y. Sheu, J. Kalus and H. Hoffmann, J. Appl. Cryst., **21**, 751 (1988).
266. W. C. K. Poon, J. Phys.: Condens. Matter, **14**, R859 (2002).
267. X. Ye, T. Narayanan, P. Tong, and J. S. Huang, Phys. Rev. Lett., **76**, 4640 (1996).

268. A. J. Chinchalikar, V. K. Aswal, J. Kohlbrecher, and A. G. Wagh, Chem. Phys. Lett., **542**, 74 (2012).
269. P. J. Flory, J. Chem. Phys., **17**, 303 (1949).
270. G. Schmidt and M. M. Malwitz, Curr. Opin. Colloid Interface Sci., **8**, 103 (2003).
271. M. Ramanathan, L. K. Shrestha, T. Mori, Q. Ji, J. P. Hill and K. Ariga, Phys. Chem. Chem. Phys., **15**, 10580 (2013).